THE UNIVERSITY of ADELAIDE

Hadron Structure Using Feynman–Hellmann Theorem

Kim Yves Somfleth

Dr. Ross Young
Dr. James Zanotti

Doctorate of Philosophy
The Faculty of Sciences
The University of Adelaide

August, 2020

Abstract

Hadrons, such as protons and neutrons, are states that are formed through interactions of quarks and gluons, the fundamental building blocks of Quantum Chromodynamics (QCD). The role of non–perturbative effects in the emergent behaviour of QCD is a key ingredient in our understanding hadrons and hence the atoms formed thereof. These dynamics have important consequences for matter in the universe from the atomic scale to neutron stars and beyond.

We use an *ab initio* non–perturbative numerical path integral based approach to QCD, known as lattice QCD. Advancing computing resources have made possible rapid advances in hadronic studies in lattice QCD, but many challenges still remain. Two areas of vital importance to our understanding of QCD and future experiments are gluonic observables and structure functions. Gluonic observables are difficult to calculate on the lattice due to sensitivity to short distance gauge noise. Naïve structure function calculations suffer from rapidly increasing computational cost as the lattice grows to a size where discretisation systematics are under control, as well as problems matching onto Minkowski matrix elements.

A modification to the QCD action changes the energy eigenstates of hadrons. The shift in these eigenstates can be related to matrix elements with interactions introduced in the shifted action via the Feynman–Hellmann Theorem (FHT). We show how the FHT can be extended to second order to calculate two current hadronic matrix elements using only two–point function techniques. A detailed analysis on how to improve uncertainty and reduce computational requirements of any FHT calculation is given. Using the FHT the full Compton amplitude is calculated, which allow us to explore assumptions made in experimental parton studies in Deep Inelastic Scattering (DIS). The subtraction function, given in terms of the Compton amplitude is not experimentally extractable and is examined from first–principles for the first time.

Gluonic matrix elements are traditionally difficult to calculate on the lattice. By using Wilson flow to reduce short distance effects, forward matrix elements are determinable with reduced uncertainty. By classification of the Lorenz structure of off–forward gluonic matrix elements, the extraction of non–forward matrix elements were also made possible, providing further insight into the highly non–perturbative binding of hadrons.

Declaration

I certify that this work contains no material which has been accepted for the award of any other degree or diploma in my name, in any university or other tertiary institution and, to the best of my knowledge and belief, contains no material previously published or written by another person, except where due reference has been made in the text. In addition, I certify that no part of this work will, in the future, be used in a submission in my name, for any other degree or diploma in any university or other tertiary institution without the prior approval of the University of Adelaide and where applicable, any partner institution responsible for the joint-award of this degree.

I acknowledge that copyright of published works contained within this thesis resides with the copyright holder(s) of those works.

I also give permission for the digital version of my thesis to be made available on the web, via the University's digital research repository, the Library Search and also through web search engines, unless permission has been granted by the University to restrict access for a period of time.

I acknowledge the support I have received for my research through the provision of an Australian Government Research Training Program Scholarship.

Kim Somfleth

Aknowledgements

To the joys of science and the people who make it worth doing.

Contents

List of Figures

List of Tables

Chapter 1

Outline

One of the greatest achievements of physics is the formulation of the Standard Model (SM). The theory has great predictive power, having successfully described phenomena from interactions between individual quarks and gluons, all the way to neutron stars and beyond. Despite these achievements, the SM does not successfully predict all phenomena, such as the non–zero neutrino mass, and searches are under way for Beyond Standard Model (BSM) theories.

The interactions between quarks and gluons form QCD describes the strong sector of the SM and can be simply summed up as fascinating. From a simple Lagrangian

$$\mathcal{L}_{QCD}(x) := \overline{q}(x)\big(i\not{D}(x) - m\big)q(x) - \frac{1}{4}F_{\mu\nu}(x)F^{\mu\nu}(x) \tag{1.1}$$

many dynamic features arise; *confinement*, *asymptotic freedom*, *dynamical chiral symmetry breaking* and many more. Yet despite the simple equation and many years of studies, aspects of it's dynamics are yet to be understood or discovered. Protons and neutrons are examples of hadrons, composite objects made up of quarks and gluons. The structure of hadrons can be studied from the perspective of spatial and momentum distributions of the quarks and gluons that make up the hadron. The background to QCD and these hadronic structure are discussed in §2.

Due to the self–interaction of gluons, hadrons are highly non–perturbative objects. The only known non–perturbation *ab initio* determination of QCD, is the path integral based model-independent discretisation of QCD known as lattice QCD. As lattice QCD calculation continue to improve, fuelled by exponentially increasing computational resources, it provides more and more input into experiments. As lattices grow in size, computational costs increase, now more than ever improved lattice techniques become important. In §3 we provide a background introduction to lattice QCD necessary for subsequent chapters.

One of the short comings of lattice QCD is the direct calculations of hadronic matrix elements involving two currents. Using the FHT we can relate second order shifts of energy eigenstates to such matrix elements by introducing a new coupling to the action. In §4, we briefly describe the history of the FHT and followed by two proofs of second order FHT for path integrals that will allow us to calculate such matrix elements. The implementation of FHT for lattice QCD is described in §5, showing how using only hadron spectroscopy, we are able to extract matrix elements. Further improvements to the technique, reducing systematic uncertainty and computational costs are also presented.

The first FHT results examined are nucleon–delta transition form factors in §6. By using larger than physical masses the matrix elements from the FHT are approximately saturated by the lowest intermediate state, allowing us to test the FHT. This saturation allows one to relate the energy shifts to transition form factors, which are calculated and compared to other direct lattice calculations, quark models and phenomenology.

The Compton amplitude and the hadron tensor encode the longitudinal behaviour of partons inside hadrons. In §7 we present extraction of the Compton amplitude. The second order FHT is used calculate the Compton amplitude on the lattice in an unphysical region, matched through kinematics for the first time, without any rotations used by four–point techniques, or mixing

problems associated with Operator Product Expansion (OPE) methods. The Compton amplitude can be related to the moments of partonic momentum distributions, and these are compared to other results. These moments are calculated to a higher order than it was possible using lattice QCD before. The scaling behaviour of both the Compton amplitude and moments are presented, and show no significant deviations from the expected behaviour. Finally higher–twist effects were examined giving insights into many assumptions made in links to the partonic picture.

The proton–neutron mass difference is a highly tuned quantity, the make-up of our universe varies greatly if it is changed slightly. Part of the difference is determined from the *Cottingham self energy*, part of which is determined in terms of the Compton amplitude subtraction function, which is not extractable from experiment. Recent measurements of the proton charge radius using *Lamb shift* give different results when using different leptons, and one of the inputs to the experimental determination is the subtraction function. A long outstanding question is whether the subtraction function possesses a fixed–pole. We examine all these in §8, using multiple different vector operators and show that there is a possible fixed–pole term, and provide the necessary steps to fully resolve it.

Just as important as the study of the quark structure of the hadrons is the gluonic structure. However on the lattice the study of gluonic observable are plagued with high frequency gauge noise. Using smoothing techniques we study the gluonic contributions to the Energy Momentum Tensor (EMT) in §9 and are able to extract clean signal in the form factors associated with the gluonic mass and spin density of the nucleon, albeit on quenched lattices with larger than physical quark masses. These results are compared to their quark equivalent results and the gluonic radius is shown to be larger than it's quark EMT counterpart.

Finally in §10, all the results of this work are summarised, building a more complete picture of the hadron structure investigated.

Chapter 2

Hadron Structure

The scale at which we study matter has continuously expanded throughout history, both towards the large scale structures, of galaxy super-clusters, and to the other end of the scale towards the fundamental building blocks of matter; structures inside atoms. In 1896, the discovery of α, β, and γ radiation [1] gave physicists a lens for resolving structures on a finer level than possible before. In 1911 the nucleus was discovered inside the atom by scattering α and β–particles off gold [2]. In the following years many phenomena where found to be in contention with a point–like model of the nucleus, eventually leading to the proposal of quarks and gluons as the nucleus substructure in 1964 [3]. Eventually, after further theoretical and experimental advances, this lead to the formulation of QCD as the theory for these strong interactions [4, 5]. In each step these observations have been calibrated with the previous scale, leading to a rich description of matter over many different energy scales.

QCD eventually became part of the formulation of the SM, with the incorporation of electroweak interactions [6], and the Higgs mechanism [7–9] completing the theory [10, 11]. The SM is a Yang–Mills Gauge Field Theory (GFT) [12], with $SU(3)_C \times SU(2)_I \times U(1)_Y$ local gauge symmetry.

The theory has predicted, with great precision many interactions and particles. First the existence of a weak current [13–15] followed a few years later by the existence of weak bosons [16–19]. The gluons [20–25], and the charm quarks [26, 27], were also discovered in parallel. Then decades after the formulation, the existence of the top quark was verified [28, 29]. Finally, most recently the last piece, the Higgs was discovered at the LHC [30, 31]. With a large array of accurate predictions, it makes the SM as one of the most successful theories of modern physics.

The theory does not predict all observed phenomena however. Neutrinos where shown to have mass [32–35], although it is not yet excluded for one of the neutrinos to be massless. Another contention is the so called 'Hierarchy Problem', where the extreme difference in coupling constant, requires delicate cancellation in renormalisation to retain such a difference, although it has been argued that this is not a concern by itself [36]. However there are other contentions beyond non–vanishing neutrino mass, such as CP problems [37–40], and lepton universality [41], amongst others. The SM is not the end of theoretical physics, the search for physics beyond the standard model is under way in many areas, which requires a better understanding of the SM, particularly in the strong sector.

Throughout this work we focus primarily on the hadron structure of the strong sector, and electroweak interactions with strong sector composite objects; namely hadrons. Starting with a brief introduction into QCD §2.1, with a focus on it's symmetries. We follow with various formulations of describing the structure, with form factors §2.2, structure functions §2.3, and finally their combination in Generalised Parton Distributions (GPDs) §2.4. §2.2 is primarily used in §6 and §9, whereas §2.3 is used in §7 and §8.

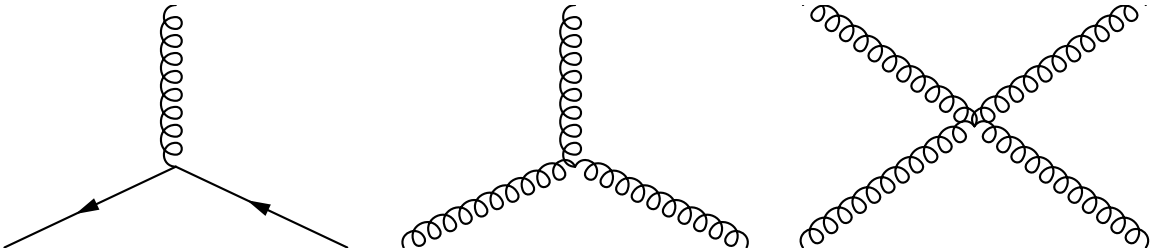

(a) Quark gluon vertex. (b) Three gluon vertex. (c) Four gluon vertex.

Figure 2.1: The three fundamental QCD Feynman diagrams.

2.1 Quantum Chromodynamics

QCD is a Yang–Mills [12] formulation of $SU(3)$, made up of quarks; as 3 generations of quark pairs, and gluons; as 8 spin-1 bosons, which carry colour and colour–anti–colour pairs respectively. With quarks taken to be massless, it is a beautiful parameter free theory, after the number of colours and flavours has been fixed. The lowest two quark flavours have very small mass, and as such many properties of QCD below energy scales at which the other flavours become active can be described by this massless prescription.

Ignoring the small quark mixing phase term the QCD Lagrangian can be written

$$\mathcal{L}_{QCD}(x) := \sum_f \overline{q}_f(x)^\alpha_a \Big(i\not{\mathcal{D}}(x)^{\alpha\beta}_{ab} - m_f \delta_{ab}\delta^{\alpha\beta} \Big) q_f(x)^\beta_b - \frac{1}{4} F_{\mu\nu}(x)^i F^{\mu\nu}(x)^i. \tag{2.1}$$

Defined in terms of the covariant derivative

$$\mathcal{D}_\mu(x)_{ab} := \delta_{ab}\partial_\mu - igt^i_{ab}A^i_\mu(x) \tag{2.2}$$

which includes the strong coupling g. Often we write

$$A_\mu(x)_{ab} := t^i_{ab}A^i_\mu(x). \tag{2.3}$$

where the eight $SU(3)$ generators t^i_{ab} are implicit, and represented by 3×3 traceless matrices, with unit determinant, acting in colour space.

The non–abelian skew–symmetric field strength tensor is given by

$$F^i_{\mu\nu} := \partial_\mu A^i_\nu - \partial_\nu A^i_\nu + g f^{ijk} A^j_\mu A^k_\nu \tag{2.4}$$

where f^{ijk} are $SU(3)$ Lie group structure constants. These equations determine three interaction vertices from which all QCD phenomena is formed Figure 2.1. The QCD action is formed from the Lagrangian by

$$S_{QCD} := \int d^4x \mathcal{L}_{QCD}(x). \tag{2.5}$$

Despite the simplicity of the QCD Lagrangian it encodes an extraordinarily rich set of phenomena. From high energy particle colliders, probing deep into nuclei, to the core of neutron stars and quark gluon plasmas. The most prominent feature of QCD is that it features both *confinement* at large distances, and *asymptotic freedom* at short distances. This naturally leads to a running coupling constant, which we can encode by the β function through use of the *Callan–Symanzik equation*, which relates a shift in renormalisation scale μ to the shift in coupling β.

The leading order form of β for an $SU(N)$ non–abelian gauge theory is given by

$$\beta(g) = -\frac{\beta_0 g^3}{(4\pi)^2} \tag{2.6}$$

$$\beta_0 := \frac{11}{3}N - \frac{2}{3}N_f \tag{2.7}$$

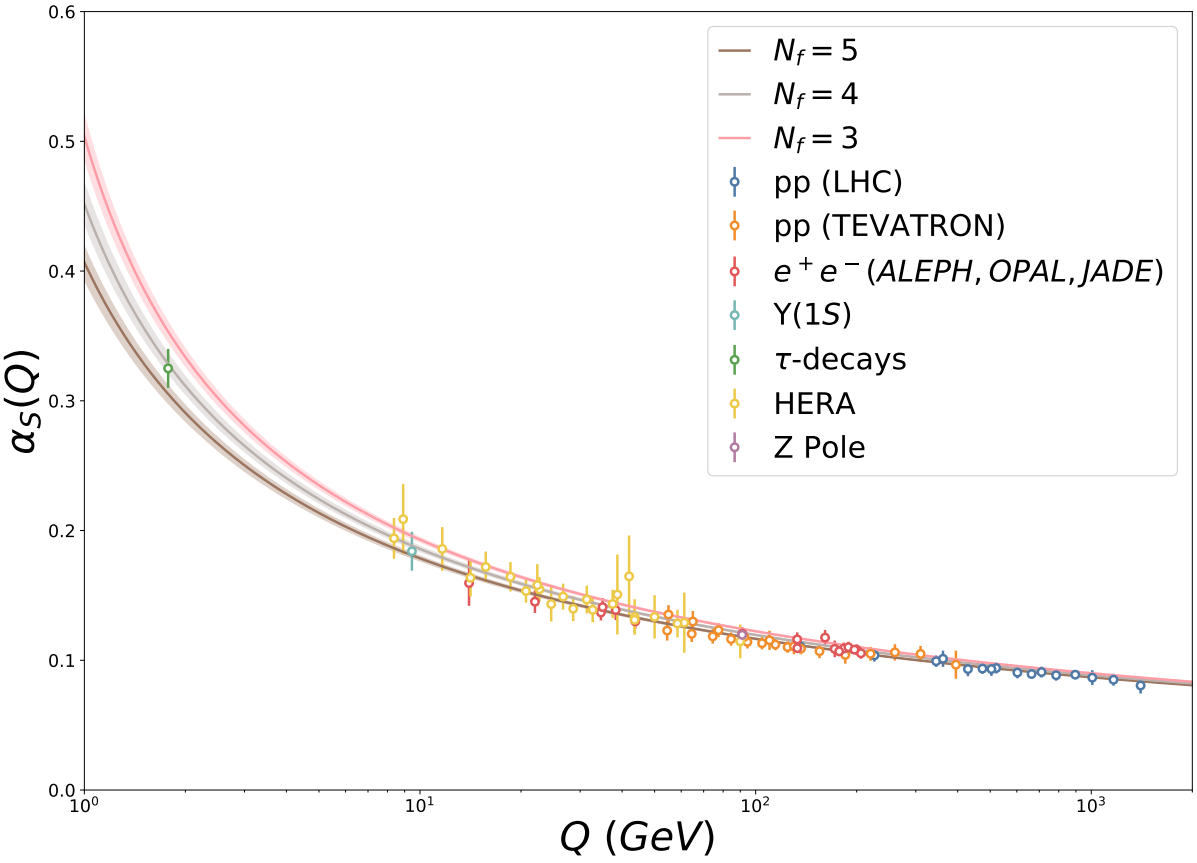

Figure 2.2: A selection of determinations of $\alpha_S(Q)$ from a variety of methods, as collated by [42], with the global average for fits obtained therein. The data includes Z pole fits methods from precision electroweak measurements [43], radiative $\Upsilon(1S)$ [44], and τ–decays [42]. Further data was taken from HERA [45–48], TEVATRON [49, 50], LHC [51–53], and various e^+e^- collider experiments [54–56]. The fits where taken at two loop order with N_f of 3, 4 and 5, with a Lambert function technique [57, 58]. All errors, including fit are shown to one standard deviation.

where N_f is the number of flavours of theory. For QCD $N = 3$ and N_f is the active flavours at the current energy scale. One can then write the QCD coupling constant

$$\alpha_S := \frac{g^2}{4\pi} \tag{2.8}$$

to leading order in Q in terms of β as

$$\alpha_S(Q) = \frac{2\pi}{\beta_0 \log\left(Q/\Lambda_{QCD}\right)}. \tag{2.9}$$

The QCD mass scale Λ_{QCD} can then be determined from experiments by matching *any* observable quantity involving the strong force, in powers of α_S with a Renormalisation Group Equations (RGE) via the *Callan–Symanzik equation*. The value is then determined by active quark flavours at that scale. Due to this ambiguity in the extraction of Λ_{QCD}, and that $\alpha_S(Q)$ is entirely characterised by knowledge of Λ_{QCD} or one value at some Q, it is standard practice to quote $\alpha_S(m_Z)$ instead. A collection of determinations of $\alpha_S(Q)$ is seen in Figure 2.2. The precise determination, of α_S over vastly different energy scales, is crucial evidence that QCD is the correct theory for the strong interactions.

The negative sign of β implies that as one heads to larger energy scales, the coupling constant tends to 0 and hence the theory has *asymptotic freedom*. At smaller scales Q or alternatively

large separation scales, the coupling constant becomes large, and non–perturbative effects come into play. At even larger distances due to the rise in coupling constant, quark/anti–quark pairs become energetically favourable and hence one observes only colour singlet states, known as *confinement*.

2.1.1 Symmetries

A symmetry of a theory says something fundamental about it's properties. Each symmetry can be linked via Noether's theorem to a conserved charge. We briefly introduce symmetries relevant to this work, namely gauge and chiral symmetry.

$SU(3)$ Gauge Invariance

The primary symmetry that QCD theory has been constructed with is gauge invariance. We require that the action is invariant under local transformation $\Omega(x)^{ab}$ under the special unitary group $SU(3)$, represented by unitary 3×3 matrices. Local meaning that the transformation can vary at each point in space–time x. This means that under a transformation, fermion and gluon fields transform

$$q_f(x)_a \to q'_f(x)_a = \Omega(x)_{ab} q_f(x)_b \tag{2.10}$$

$$\overline{q}_f(x)_a \to \overline{q}'_f(x)_a = \overline{q}_f(x)_b \Omega^\dagger(x)_{ba} \tag{2.11}$$

$$A_\mu(x)_{ab} \to A'_\mu(x)_{ab} = \Omega(x)_{ac} A_\mu(x)_{cd} \Omega^\dagger(x)_{db} + \frac{i}{g}(\partial_\mu \Omega(x)_{ac}) \Omega^\dagger(x)_{cd} \tag{2.12}$$

while the action remains unchanged

$$S\left[A'_\mu, \overline{q}'_f, q'_f\right] = S\left[A_\mu, \overline{q}_f, q_f\right]. \tag{2.13}$$

The covariant derivative and field strength tensor transform as

$$\mathcal{D}_\mu(x)_{ab} \to \mathcal{D}'_\mu(x)_{ab} = \Omega(x)_{ac} \mathcal{D}_\mu(x)_{cd} \Omega^\dagger(x)_{cb} \tag{2.14}$$

$$F_{\mu\nu}(x)_{ab} \to F'_{\mu\nu}(x)_{ab} = \Omega(x)_{ac} F_{\mu\nu}(x)_{cd} \Omega^\dagger(x)_{cb}. \tag{2.15}$$

The name covariant derivative comes from the fact that $\mathcal{D}_\mu q$ transforms like q. The conserved charge for the symmetry is colour.

Chiral Symmetries

One of the approximate symmetries the theory possess, is the vector symmetry, or isospin symmetry. For some constant α the action is constant under global transformations

$$q_{f_1}(x)_a \to q'_{f_1}(x)_a = e^{i\alpha t^i_{f_1 f_2}} q_{f_2}(x)_a \tag{2.16}$$

$$\overline{q}_{f_1}(x)_a \to \overline{q}'_{f_1}(x)_a = \overline{q}_{f_2}(x)_a e^{-i\alpha t^i_{f_1 f_2}} \tag{2.17}$$

where $t^i_{f_1 f_2}$ is one of the $N_f^2 - 1 = 8$ generators of $SU(3)$ and summation convention is used for f_2. The symmetry is broken by non–degenerate mass terms in (2.1). In addition to the above equations, there is also an additional flavour diagonal (flavour singlet) symmetry

$$q_f(x)_a \to q'_f(x)_a = e^{i\alpha} q_f(x)_a \tag{2.18}$$

$$\overline{q}_f(x)_a \to \overline{q}'_f(x)_a = \overline{q}_f(x)_a e^{-i\alpha} \tag{2.19}$$

which holds even for non–degenerate quark masses. Both of these symmetries' corresponding Noether currents are the vector currents, with the latter symmetries conserved quantity being baryon number.

Another symmetry is the axial–vector symmetry, which requires the action to be independent under the global transformations

$$q_{f_1}(x)_a \to q'_{f_1}(x)_a = e^{i\alpha\gamma_5 t^i_{f_1 f_2}} q_{f_2}(x)_a \tag{2.20}$$

$$\overline{q}_{f_1}(x)_a \to \overline{q}'_{f_1}(x)_a = \overline{q}_{f_2}(x)_a e^{i\alpha\gamma_5 t^i_{f_1 f_2}}. \tag{2.21}$$

and due to a non–invariant integration measure an extra symmetry

$$q_f(x)_a \to q'_f(x)_a = e^{i\alpha\gamma_5} q_f(x)_a \tag{2.22}$$

$$\overline{q}_f(x)_a \to \overline{q}'_f(x)_a = \overline{q}_f(x)_a e^{i\alpha\gamma_5} \tag{2.23}$$

These symmetries decouple left and right handed spinor components, which each separately observe the symmetry. The corresponding conserved quantity is axial charge, corresponding to the charge of the axial current.

The combination of both of these symmetries is known as chiral symmetry and is exact in the zero quark mass limit $m_f = 0$. The theory is implicitly broken by spontaneous chiral symmetry breaking, leading to 8 massless Goldstone bosons; the pseudoscalar meson octet. In addition the quark masses explicitly break the symmetry, which gives the octet mesons their mass. However as the three lightest quark flavours are small, the octet can still be considered approximately chiral.

2.2 Form Factors

While once the proton was thought of as an atom; indivisible, it is now known to be made of constituents. With the above discussion on *asymptotic freedom*, *confinement*, and the scaling of α_S (Figure 2.2), it is clear that QCD objects, such as the proton p and the positively charged pion π^+ are complicated objects. We need a method for encapsulating the complex structure that arises from the dynamics of QCD.

The most natural way to think about probing the internal structure of hadrons is the evolution of their Dirac structure's at different energy scales. Indeed the charge and magnetisation densities of the proton [59] were probed experimentally [60–62] more than a decade before the parton model was formulated [63]. To verify that the experimentally measured form factors are consistent with those predicted by QCD, precise predictions must be made. The only known model–independent formulation of form factors and other non–perturbative phenomena from QCD is lattice QCD [64].

A form factor encodes the effect of the composite nature of the object on interactions with it's constituents. The Quantum Electrodynamics (QED) quark–photon vertex

$$e_{q_f} \epsilon^\mu \overline{q}_f \gamma_\mu q_f \tag{2.24}$$

in terms of electric charge e_{q_f}, polarisation ϵ_μ, and quark fields q_f of flavour f is then affected by dynamics between the quarks inside a hadron. The nature of the effect gives rise to all possible Dirac structures that transform in the same way, with the constraint that it has to obey the same symmetries as the underlying interaction. In terms of vector current

$$V^f_\mu(x) := \overline{q}_f(x)\gamma_\mu q_f(x) \tag{2.25}$$

we have two form factors F_1 and F_2

$$\left\langle P, \vec{p}' \middle| V^f_\mu(0) \middle| P, \vec{p} \right\rangle = \overline{u}_P(p') \left[\gamma_\mu F^f_1(Q^2) + \frac{i\sigma_{\mu\alpha} q^\alpha}{2m} F^f_2(Q^2) \right] u_P(p) \tag{2.26}$$

where for convenience we have defined $Q^2 := -q^2$. Note the form factors are purely dependent on Q^2.

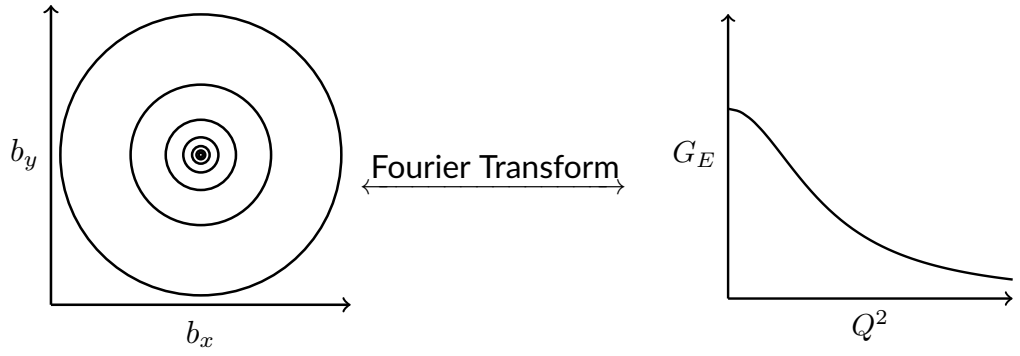

Figure 2.3: The relationship between form factors and their corresponding charge density. The charge density here is rotationally symmetric, but we have written it in terms of radial $b_\perp$ to link to §2.4.

These two form factors are just one choice of representation, the Dirac F_1 and Pauli F_2. The other representation commonly used is the Sachs electromagnetic form factors

$$G_E^f(Q^2) := F_1^f(Q^2) - \frac{Q^2}{4m_p^2} F_2^f(Q^2) \tag{2.27}$$

$$G_M^f(Q^2) := F_1^f(Q^2) + \qquad F_2^f(Q^2). \tag{2.28}$$

In this alternate form the form factors have simple non–relativistic interpretation in the infinite momentum frame; as two–dimensional Fourier transforms of the charge and magnetisation distribution respectively, as shown in Figure 2.3.

2.2.1 Generalised Form Factors

The electromagnetic form factors (2.26) are just one set of form factors, in general there are many more, presented usually in terms of towers of operators; Generalised Form Factorss (GFFs). Starting with motivation of GFFs for OPE methods we now present the GFFs relevant to this work.

GFFs are useful for the OPE; an expansion of a non–local operator in terms of local ones

$$\int d^4x e^{iq\cdot x} \mathcal{O}^1(x)\mathcal{O}^2(0) = \sum_n c_n^{12}(q,\mu)\mathcal{O}_n(0,\mu) \tag{2.29}$$

where the expansion is done at some scale μ. The so called Wilson coefficients c_n then encode the dependence on the separation

$$c_n(q,\mu) := \int d^4x e^{iq\cdot x} c_n(x,\mu). \tag{2.30}$$

In general, the factor $c_n(q,\mu)$ will carry a suppression factor

$$\left(\frac{1}{Q}\right)^{d-s-2} \tag{2.31}$$

in terms of the dimension d and spin s of the operator $\mathcal{O}_n$. It is natural then to define the twist τ of an operator as

$$\tau := d - s. \tag{2.32}$$

The matrix elements of a particular twist are then of interest to us. The tower of twist–two operators do not have any general Q suppression, and are defined as

$$\mathcal{O}^{qV}_{\mu\mu_1\cdots\mu_{n-1}} = \overline{q}\left[\gamma_{\{\mu} i\overleftrightarrow{\mathcal{D}}_{\mu_1}\cdots i\overleftrightarrow{\mathcal{D}}_{\mu_{n-1}\}} - \text{Traces}\right] q \tag{2.33}$$

$$\mathcal{O}^{qA}_{\mu\mu_1\cdots\mu_{n-1}} = \overline{q}\left[\gamma_{\{\mu}\gamma_5 i\overleftrightarrow{\mathcal{D}}_{\mu_1}\cdots i\overleftrightarrow{\mathcal{D}}_{\mu_{n-1}\}} - \text{Traces}\right] q \tag{2.34}$$

$$\mathcal{O}^{qT}_{\mu\nu\mu_1\cdots\mu_{n-1}} = \overline{q}\left[\sigma_{\mu\{\nu} i\overleftrightarrow{\mathcal{D}}_{\mu_1}\cdots i\overleftrightarrow{\mathcal{D}}_{\mu_{n-1}\}} - \text{Traces}\right] q \tag{2.35}$$

$$\mathcal{O}^{g}_{\mu\nu\mu_1\cdots\mu_{n-1}} = F_{\mu\alpha} i\overleftrightarrow{\mathcal{D}}_{\{\mu_1}\cdots i\overleftrightarrow{\mathcal{D}}_{\mu_{n-1}\}} F_\nu{}^\alpha - \text{Traces} \tag{2.36}$$

$$\mathcal{O}^{gd}_{\mu\nu\mu_1\cdots\mu_{n-1}} = F_{\mu\alpha} i\overleftrightarrow{\mathcal{D}}_{\{\mu_1}\cdots i\overleftrightarrow{\mathcal{D}}_{\mu_{n-1}\}} - i\widetilde{F}_\nu{}^\alpha - \text{Traces} \tag{2.37}$$

$$\mathcal{O}^{gT}_{\mu\nu\alpha\mu_1\cdots\mu_{n-1}} = F_{\mu\nu} i\overleftrightarrow{\mathcal{D}}_{\{\mu_1}\cdots i\overleftrightarrow{\mathcal{D}}_{\mu_{n-1}\}} F^{\alpha\beta} - \text{Traces}. \tag{2.38}$$

We use $\overleftrightarrow{\mathcal{D}} = \frac{1}{2}\left(\overrightarrow{\mathcal{D}} - \overleftarrow{\mathcal{D}}\right)$ and $\{\}$ indicates symmetrisation of indices. The first equation (2.33) with $n = 1$ reduces to the vector form factor (2.26). In the case $n = 2$ this becomes the operator for the EMT

$$\overline{q}\left[\gamma_{\{\mu} i\overleftrightarrow{\mathcal{D}}_{\nu\}} - \frac{1}{4} g_{\mu\nu}\gamma_\alpha i\overleftrightarrow{\mathcal{D}}^\alpha\right] q. \tag{2.39}$$

The general form factors for (2.33) and (2.36) can then be defined as

$$\begin{aligned}\left\langle N,\vec{p}'\middle|\mathcal{O}^{qV/g}_{\mu\mu_1\cdots\mu_{n-1}}\middle|N,\vec{p}\right\rangle = \overline{u}(p')\Bigg[&\sum_{i\ even}^{n-1}\gamma_{\{\mu} q_{\mu_1}\cdots q_{\mu_i} P_{i+1}\cdots P_{\mu-1\}} A^{q/g}_{n,i}(Q^2)\\ &-\sum_{i\ even}^{n-1}\frac{q^\alpha}{2M_N}\sigma_{\alpha\{\mu} q_{\mu_1}\cdots q_{\mu_i} P_{i+1}\cdots P_{\mu-1\}} B^{q/g}_{n,i}(Q^2)\\ &+\frac{(n+1)\%2}{M_N} q_{\{\mu} q_{\mu_1}\cdots q_{\mu-1\}} C^{q/g}_{n,0}(Q^2)\Bigg] u(p)\end{aligned} \tag{2.40}$$

where N represents a nucleon state with ingoing and outgoing momentum $\vec{p}$ and $\vec{p}'$ respectively and we have defined the average momentum

$$P_\mu := \frac{1}{2}(p'_\mu + p_\mu). \tag{2.41}$$

For the EMT ($n = 2$) dropping V labelling this becomes

$$\left\langle N,\vec{p}'\middle|\mathcal{O}^{q/g}_{\mu\nu}\middle|N,\vec{p}\right\rangle = \overline{u}(p')\left[\gamma_{\{\mu} p_{\nu\}} A^{q/g}_{20}(Q^2) + \frac{iq^\alpha\sigma_{\alpha\{\mu} P_{\nu\}}}{2m_p} B^{q/g}_{20}(Q^2) + \frac{q_\mu q_\nu}{m_p} C^{q/g}_{20}(Q^2)\right] u(p). \tag{2.42}$$

We shall look at the EMT in more detail in §9.1, but it can also be relevant to scaling of the Compton amplitude when gluonic moments aren't known as discussed in §7.2.

The form factor $A^{q/g}_{20}$ at $Q^2 = 0$ is the momentum fraction $\langle x\rangle_{q/g}$, so clearly for pure QCD

$$\sum_f A^{q_f}_{20}(0) + A^g_{20}(0) = 1. \tag{2.43}$$

This is the first of the sum rules of interest, used in §9.1.1.

2.3 Structure Functions

While form factors encode the spatial distributions of hadrons, structure functions encode light–cone momentum distributions. Experimentally DIS, e^+e^- *annihilation*, and the *Drell–Yan process* are all examples that exhibit behaviour that require structure functions. While the form factors

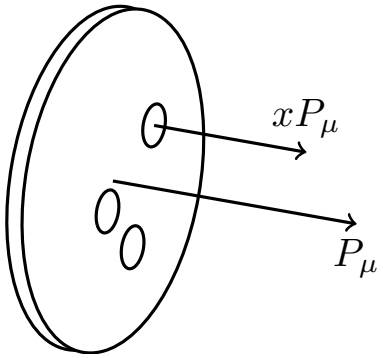

Figure 2.4: The Parton Model for a particle with momentum P_μ, that at high boost looks like a *pancake*, where each parton carries fractional momentum xP_μ of that momentum.

probe the elastic contributions, the structure functions also contain, among other contributions, the in–elastic contributions.

The structure functions can be linked to the parton model at large momentum transfers. The parton model as first proposed by Feynman in 1969 [63], describes the constituents of the proton as non–interacting at large boosts. In the infinite momentum frame the partons of a hadron (quarks and gluons) are effectively massless, and have no transverse momentum, the *pancake* picture, shown in Figure 2.4.

The structure functions then encode the x behaviour as well as the Q^2 behaviour, although generally the former is more prominent than the latter. We now present two examples of structure functions, the Compton amplitude §2.3.1 and the hadron tensor §2.3.2 as well as their relation §2.3.3. We finish with discussions on the weak charge of the proton §2.3.4 and two photon exchange §2.3.5, which motivate our study.

2.3.1 Forward Compton Amplitude

The forward Compton amplitude [65] is

$$T_{\mu\nu}(p,q,\rho) := i\rho_{s's}\left\langle p,s'\middle|\int d^4x e^{iq\cdot x}T\left\{J_\mu^\dagger(x)J_\nu(0)\right\}\middle|p,s\right\rangle \tag{2.44}$$

and at fixed Q^2 is analytic in $\nu := p\cdot q$, for nucleon mass m (alternatively $\omega := 2\nu/Q^2$). The time ordered product of electroweak currents J_μ in between nuclear states of momentum p, and spins s and s', with polarisation density matrix $\rho_{s's}$. We can divide the Compton amplitude into different structure functions by using Lorentz and time–reversal invariance

$$\begin{aligned}
T_{\mu\nu} = &\left(-g_{\mu\nu}+\frac{q_\mu q_\nu}{q^2}\right)T_1 + \frac{\left(p_\mu-\frac{1}{2}\omega q_\mu\right)\left(p_\nu-\frac{1}{2}\omega q_\nu\right)}{\nu}T_2 + \frac{q_\mu q_\nu}{\nu}T_4 + \frac{p_{\{\mu}q_{\nu\}}}{\nu}T_5 \\
&+ i\epsilon_{\mu\nu\alpha\beta}\left[\frac{q^\alpha p^\beta}{\nu}T_3 - q^\alpha\left(\frac{s^\beta}{\nu}G_1 + \frac{\left[\nu s^\beta-(s\cdot q)p^\beta\right]}{\nu^2}G_2\right) + \frac{p^\alpha s^\beta}{\nu}G_3\right] \\
&+ \frac{(s\cdot q)}{\nu}\left[\left(-g_{\mu\nu}+\frac{q_\mu q_\nu}{q^2}\right)X_1 + \frac{\left(p_\mu-\frac{1}{2}\omega q_\mu\right)\left(p_\nu-\frac{1}{2}\omega q_\nu\right)}{\nu}X_2 + \frac{q_\mu q_\nu}{\nu}X_4 + \frac{p_{\{\mu}q_{\nu\}}}{\nu}X_5\right] \\
&+ \frac{\left(s_{\{\mu}-\frac{1}{2}\frac{(s\cdot q)}{\nu}p_{\{\mu}\right)\left(p_{\nu\}}-\frac{1}{2}\omega q_{\nu\}}\right)}{\nu}Y_1 + \frac{\left(s_{\{\mu}-\frac{1}{2}\frac{(s\cdot q)}{\nu}p_{\{\mu}\right)p_{\nu\}}}{\nu}Y_2
\end{aligned} \tag{2.45}$$

although other representations and normalisations are possible. This choice of normalisation is for dimensionless structure functions, often called the *scaling* structure functions, chosen to

match the DIS results, which where in turn chosen to match to easily to Parton Distribution Functions (PDFs) at leading–twist in an OPE.

We now demonstrate the *crossing symmetry* of the Compton amplitude. Starting with switching μ and ν for the unpolarised $\rho = \frac{1}{2}I$ Compton amplitude, we can show the crossing symmetry by noting that the time ordering cares only about relative separation of the currents and redefining our unit of integration

$$T_{\nu\mu}(p,q) = i\left\langle p\left|\int d^4x e^{iq\cdot x} T\left\{J_\nu(x)J_\mu(0)\right\}\right|p\right\rangle \tag{2.46}$$

$$= i\left\langle p\left|\int d^4x e^{iq\cdot x} T\left\{J_\mu(-x)J_\nu(0)\right\}\right|p\right\rangle \tag{2.47}$$

$$= i\left\langle p\left|\int d^4x e^{-iq\cdot x} T\left\{J_\mu(x)J_\nu(0)\right\}\right|p\right\rangle \tag{2.48}$$

$$= T_{\mu\nu}(p,-q). \tag{2.49}$$

For the unpolarised Compton amplitude we can then separate into μ,ν even and odd terms

$$T_{\{\mu\nu\}}(p,q) = \left(-g_{\mu\nu} + \frac{q_\mu q_\nu}{q^2}\right)T_1 + \frac{\left(p_\mu - \frac{1}{2}\omega q_\mu\right)\left(p_\nu - \frac{1}{2}\omega q_\nu\right)}{\nu}T_2 + \frac{q_\mu q_\nu}{\nu}T_4 + \frac{p_{\{\mu}q_{\nu\}}}{\nu}T_5 \tag{2.50}$$

$$T_{(\mu\nu)}(p,q) = i\epsilon_{\mu\nu\alpha\beta}\frac{q^\alpha p^\beta}{\nu}T_3 \tag{2.51}$$

The symmetries in the structure function T_i forced by the crossing symmetry do not allow us to go further with simple kinematic symmetries.

2.3.2 Hadron Tensor

One of the most fundamental experimental probes of small distance hadron structure is the process of DIS. A lepton is scattered of a hadronic target via interchange of an electroweak boson. Figure 2.5 shows the process for electromagnetic DIS. For large momentum transfer, such a process yields a single electron and a collinear shower or jet of hadrons, which one can interpret the electron scattering off a single constituent particle of the hadron or parton. If this is the case the longitudinal momentum fraction is given by the Bjorken variable

$$x := \frac{Q^2}{2p\cdot q}. \tag{2.52}$$

The fractional electron energy transfer y is given by

$$y := \frac{p\cdot q}{p\cdot k} \tag{2.53}$$

where k is the incident photon momentum. Note that both x and y can be determined entirely from the scattered lepton.

Experimentally DIS allowed the discovery of partons. It was seen that after removing QED kinematic dependence the cross section was largely independent of Q^2 [66–68]. This phenomena, known as *Bjorken scaling*, implies that interactions during the scattering process can be ignored, so the constituents can be interpreted as free particles; *asymptotic freedom*. Conversely any deviation from this scaling has implications on our understanding of QCD. In addition the behaviour in y of the cross section established the fermion behaviour of these partons, the so called *Callan–Gross relation* [69] specifying that the cross section is proportional to $1 + (1-y)^2$.

One can relate the cross section of this inclusive lepton–hadron scattering rates to it's leptonic $L_{\mu\nu}$ and hadronic structure $W_{\mu\nu}$ separately

$$\frac{d^3\sigma}{dxdyd\phi} \propto L^{\mu\nu}W_{\mu\nu} \tag{2.54}$$

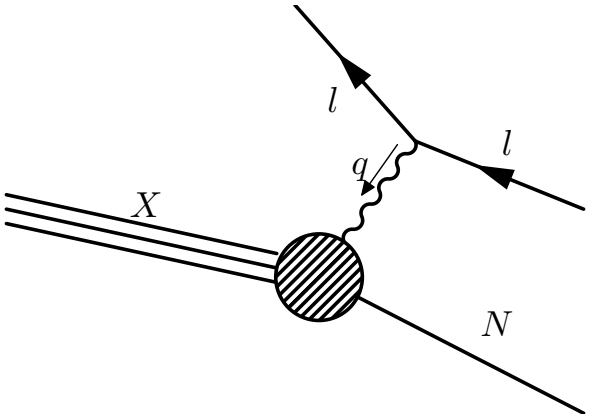

Figure 2.5: The deep inelastic scattering process for lepton l scattering off a hadron N via a photon with momentum transfer q to final state X.

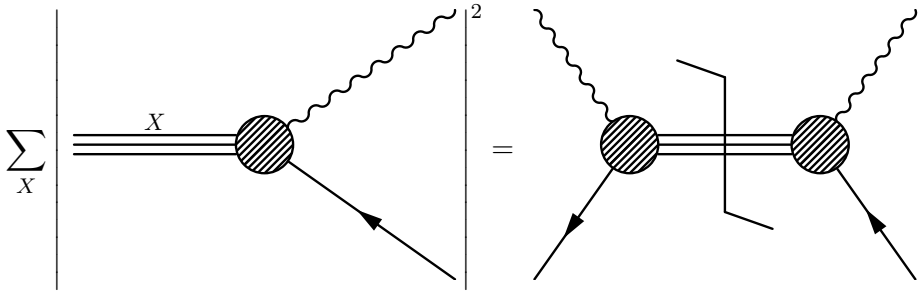

Figure 2.6: The relationship between the hadronic part of the lepton scattering process (left) and the hadron tensor (right).

where $L^{\mu\nu}$ encodes the Dirac structure of the scattered lepton

$$L_{\mu\nu} := \sum_{h''} \overline{u}(k,h')\Gamma^*_\mu u(k',h'')\overline{u}(k',h'')\Gamma_\nu u(k,h) \tag{2.55}$$

where h represents helicity, k electron momentum and $k' - k = q$. The forward hadron tensor is then defined

$$W_{\mu\nu}(p,q) := \int d^4x e^{iq\cdot x}\rho_{s's}\frac{1}{4\pi}\langle p,s'|[J_\mu(x),J_\nu(0)]|p,s\rangle. \tag{2.56}$$

The relationship can be described pictorially by Figure 2.6. Based on the current being probed Γ_μ and J_μ take their appropriate forms, for instance with

$$\Gamma_\mu = \gamma_\mu \tag{2.57}$$

then

$$J_\mu = J^\gamma_\mu \tag{2.58}$$

for the electric current, or

$$\Gamma_\mu = \left(\left[\frac{1}{2} - 2e_l \sin^2\theta_W\right] - \frac{1}{2}\gamma_5\right)\gamma_\mu \tag{2.59}$$

then

$$J_\mu = J^Z_\mu \tag{2.60}$$

for the neutral weak current, where e_l is the lepton's electric charge. The leptonic part of the cross section can be obtained from perturbation theory, so one is only left with the hadron tensor.

Kinematic Region	Scattering Process
$W^2 \approx m^2$	Quasi–elastic scattering region
$m^2 < W^2 \lesssim 4GeV^2$	Resonance region
$Q^2 \approx m^2 \quad W^2 \gtrsim 4GeV^2$	Regge region
$Q^2 > 4GeV^2 \quad W^2 \gtrsim 4GeV^2$	DIS region

Table 2.1: The different scattering process classification for differing kinematic regions for lepton–hadron scattering in terms of momentum transfer Q^2 and invariant final state mass $W^2 = m^2 + Q^2(1-x)/x$. The quasi–elastic region encodes both the elastic form factors as well as the proton–neutron transitions. The Resonance region contains contributions from various resonance outgoing states. The Regge region is of low x and fixed Q^2. Finally the DIS region is for smaller x as Q^2 becomes larger. The transition between regions, such as between quasi–elastic, resonance and DIS are well known, but other transitions such as those between Regge and DIS are not.

By using Lorentz and time–reversal invariance the hadron tensor can be decomposed into a series of structure functions

$$\begin{aligned} W_{\mu\nu} = &\left(-g_{\mu\nu} + \frac{q_\mu q_\nu}{q^2}\right) F_1 + \frac{\left(p_\mu - \frac{1}{2}\omega q_\mu\right)\left(p_\nu - \frac{1}{2}\omega q_\nu\right)}{\nu} F_2 + \frac{q_\mu q_\nu}{\nu} F_4 + \frac{p_{\{\mu} q_{\nu\}}}{\nu} F_5 \\ &+ i\epsilon_{\mu\nu\alpha\beta}\left[\frac{q^\alpha p^\beta}{\nu} F_3 - q^\alpha\left(\frac{s^\beta}{\nu} g_1 + \frac{\left[\nu s^\beta - (s\cdot q)p^\beta\right]}{\nu^2} g_2\right) + \frac{p^\alpha s^\beta}{\nu} g_3\right] \\ &+ \frac{(s\cdot q)}{\nu}\left[\left(-g_{\mu\nu} + \frac{q_\mu q_\nu}{q^2}\right) x_1 + \frac{\left(p_\mu - \frac{1}{2}\omega q_\mu\right)\left(p_\nu - \frac{1}{2}\omega q_\nu\right)}{\nu} x_2 + \frac{q_\mu q_\nu}{\nu} x_4 + \frac{p_{\{\mu} q_{\nu\}}}{\nu} x_5\right] \\ &+ \frac{\left(s_{\{\mu} - \frac{1}{2}\frac{(s\cdot q)}{\nu} p_{\{\mu}\right)\left(p_{\nu\}} - \frac{1}{2}\omega q_{\nu\}}\right)}{\nu} y_1 + \frac{\left(s_{\{\mu} - \frac{1}{2}\frac{(s\cdot q)}{\nu} p_{\{\mu}\right) p_{\nu\}}}{\nu} y_2. \end{aligned} \tag{2.61}$$

The F_i are the unpolarised structure functions, g_i are the parity–conserved polarised structure functions, x_i are the longitudinally–polarised parity–violating structure functions and y_i are the parity violating transversely polarised structure functions. In an electromagnetic process charge conservation implies that only F_1, F_2, g_1 and g_2 remain, but for a general current all are present.

As for the Compton amplitude, this decomposition is not the only such choice of decomposition. This decomposition was chosen to match onto the parton model for a leading order OPE calculation of F_2, which we shall demonstrate below.

These structure functions are valid for any x and Q^2, but DIS occurs only for sufficiently large Q^2 and small enough x. The relationship between kinematics is summarised in Table 2.1, but first we focus on the DIS region. For large enough Q^2 the *Callan–Gross* relation, can be used to relate the structure functions F_1 and F_2 for spin $\frac{1}{2}$ particles

$$F_2(x, Q^2) = 2xF_1(x, Q^2). \tag{2.62}$$

Experimentally the extraction of F_2 in the DIS region is known to astounding precision, while F_1 data is harder to extract, requiring larger scattering angles. A sample of available proton F_2^p data showing approximate *Bjorken scaling* is shown in Figure 2.7. Further information about the experimental DIS is available in §F.2.

At large Q^2 due to *asymptotic freedom* the constituents of the proton can be thought of as non–interacting over the interaction with the external current. These so called *partons* are naturally the quarks and gluons of the nucleon. In terms of twist, partons are of leading–twist, or twist–two, which has the so called "handbag" diagram Figure 2.8.

At lower Q^2 some part of the x region of the structure function are in the resonance region. A selection of F_2^p resonance data is shown in Figure 2.9. The fact that this data with all the

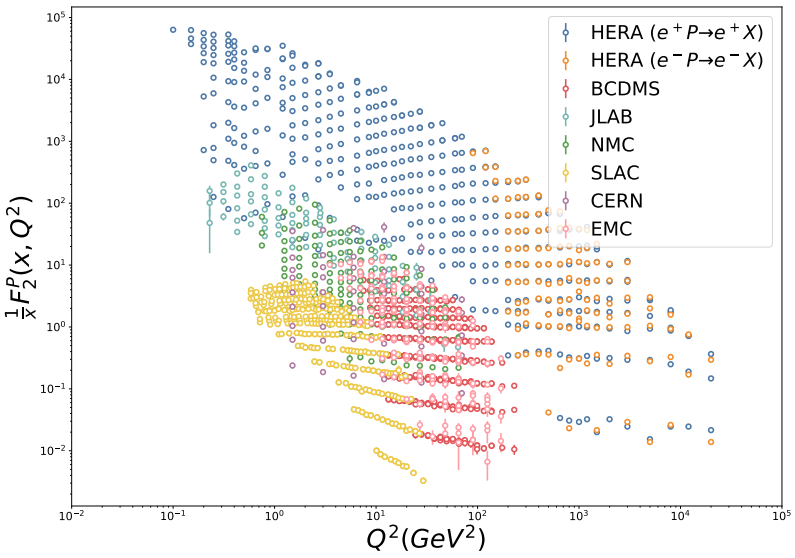

Figure 2.7: The determination of F_2^p scaled by x, with x ranging between 2.430×10^{-06} and 0.85. The scaling of the data by x effectively shifts the different x bins by a constant. The largest range of data come from HERA [70, 71] with both inclusive electron and positron scattering data. Further data come from various inclusive muon scattering experiments; BCDMS [72], JLAB [73], NMC [74], SLAC [75], CERN [76] and EMC [77]. The data shows great consistency between experiments and clearly shows *Bjorken scaling*. This plot was adapted from [78].

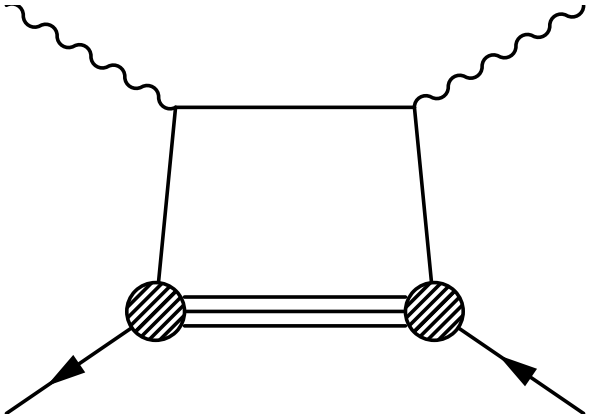

Figure 2.8: The "handbag" diagram, the leading–twist contribution to DIS, that one can relate to the parton model.

resonances is still described in average by fits taken at much higher energies in the DIS region is remarkable, which is known as *quark–hadron duality* (see [79, 80] for a more in depth discussion). As a consequence of this, structure functions from high Q^2 scattering experiments can be used to deduce moments at low energy.

We now show the relationship of the structure function F_2 and by extension F_1 to the parton model. Diagrams involving more than one quark, have higher twist and so have at least $\frac{1}{Q}$ suppression. Neglecting these terms, this means that at large Q^2 one can factorise F_2 as a sum of PDFs q_f

$$F_2(x, Q^2) = \sum_q e_q^2 x\big(q_f(x, \mu) + \overline{q}_f(x, \mu)\big) \tag{2.63}$$

where q_f is the probability of finding a parton of flavour f at momentum fraction x and similarly $\overline{q}_f$ for the anti–particle. This relationship naturally explains *Bjorken scaling*, as it does not have explicit Q^2 dependence, although the PDFs still have a scale dependence, which we denote μ.

This relationship can be formalised to $\mathcal{O}\left(\frac{1}{Q}\right)$ by OPE methods, but this assumption still requires some higher twist diagrams to be negligible. The diagrams neglected are those involving interaction between differing partons, such as those involving more than one quark line. One such diagram is the so–called *cat's ears* diagrams Figure 2.10, whose leading order twist contributions are twist $\tau = 4$.

Modern PDF extraction take into account such corrections, as well as accounting for contributions from higher twist. In addition to DIS data, they supplement the data with proton collider data to further constrain the PDFs, using weak bosons and jet production cross sections. Many different PDF extractions are available, one of which we show in Figure 2.11.

The following two sum rules then hold within the proton

$$\int_0^1 dx(u(x, \mu) - \overline{u}(x, \mu)) = 2 \tag{2.64}$$

$$\int_0^1 dx\big(d(x, \mu) - \overline{d}(x, \mu)\big) = 1 \tag{2.65}$$

These can be written in terms of structure functions, three of which we present now. The first is for neutrino–baryon scattering, the *Gross–Llewellyn–Smith sum rule* [90]

$$\int_0^1 dx F_3 = 3 \tag{2.66}$$

where the deviations from 3 measure asymmetry within the sea. The second, also for neutrino scattering is the *Adler sum rule* [91]

$$\int_0^1 \frac{dx}{x}(F_2^n - F_2^p) = 2 \tag{2.67}$$

with no QCD corrections. The third sum rule, now for electron scattering, the *Gottfried sum rule* [92] is

$$\int_0^1 \frac{dx}{x}(F_2^p - F_2^n) = \frac{1}{3} + \frac{2}{3}\int_0^1 dx\big(\overline{u}(x, \mu) - \overline{d}(x, \mu)\big) \tag{2.68}$$

whose deviation from $\frac{1}{3}$ measures the $\overline{u}$ and $\overline{d}$ asymmetry already seen in Figure 2.11.

We have discussed the relationship of the hadron tensor to the parton model, and the different kinematic contributions to the hadron tensor, notably the resonance and DIS regions. While we have discussed PDFs, most of these relationships, including the sum rules do not require partonic interpretation, being valid for the full hadron tensor directly.

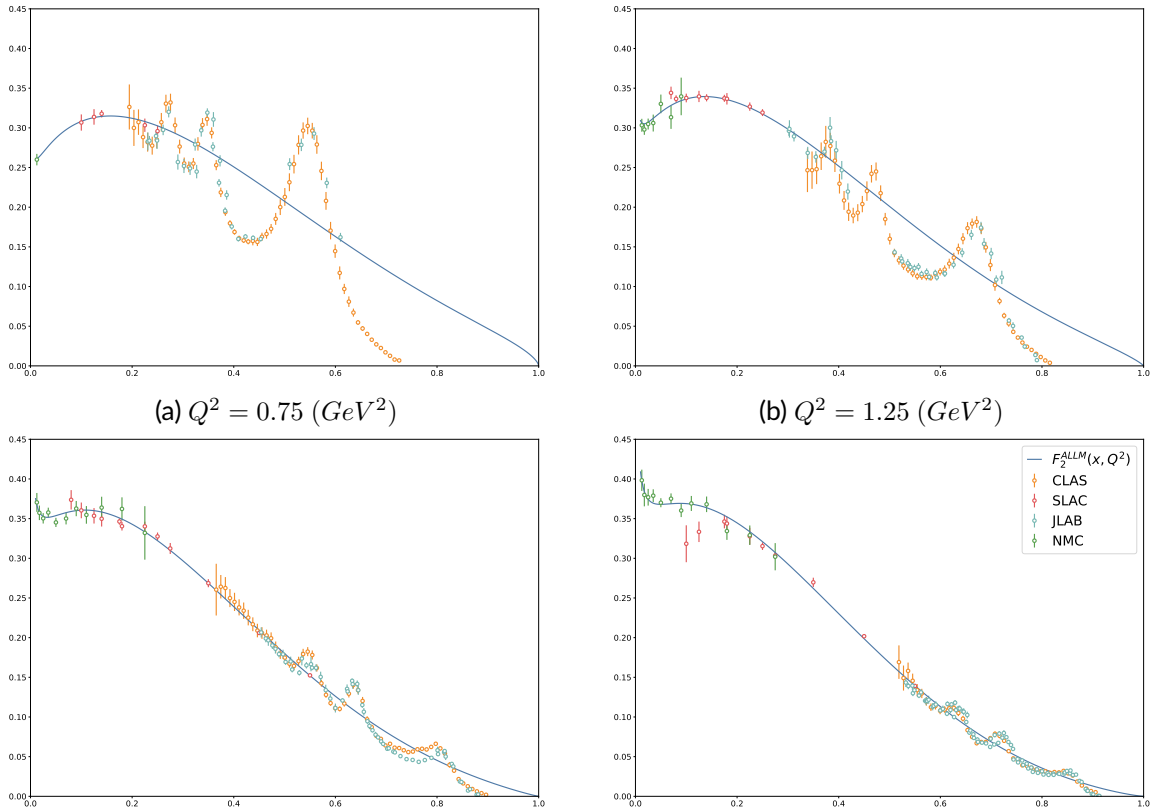

(a) $Q^2 = 0.75\ (GeV^2)$ (b) $Q^2 = 1.25\ (GeV^2)$

(c) $Q^2 = 2.5\ (GeV^2)$ (d) $Q^2 = 3.5\ (GeV^2)$

Figure 2.9: A selection of data for F_2^p (adapted from [81]) for Q^2 ranging from 0.75 to 3.5 GeV^2 chosen to coincide with CLAS Q^2 bins. This range puts a large fraction of the x region in the resonance region. All experimental data within 5% of the specified Q^2 was combined without correction. The data is taken from F_2 extractions from experiments; from CLAS [82], from which the Q^2 bins have been chosen, as they provide the largest set of x at these Q^2. Data reconstructed from cross section data available from JLAB [83] via model of R (see §F.2) as described in the same paper supplement the CLAS data. Further data from outside of the resonance region from SLAC [75] and NMC [74]. The fit [84] is constructed using data from various DIS experiments outside of the resonance region. As Q^2 grows, the resonance gets pushed closer and closer to $x = 1$, and hence it's effect disappears at large Q^2. The average Q^2 dependence of the data in the resonance region is still described by structure functions fits in the DIS region, which is known as *quark–hadron duality*.

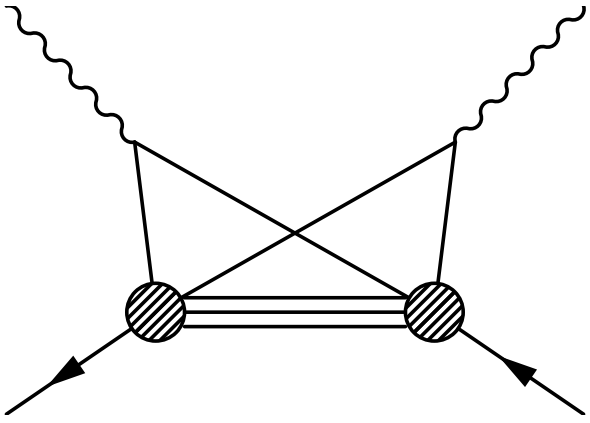

Figure 2.10: The cat's ears diagram, one of the diagrams corresponding to non–leading–twist contribution to DIS.

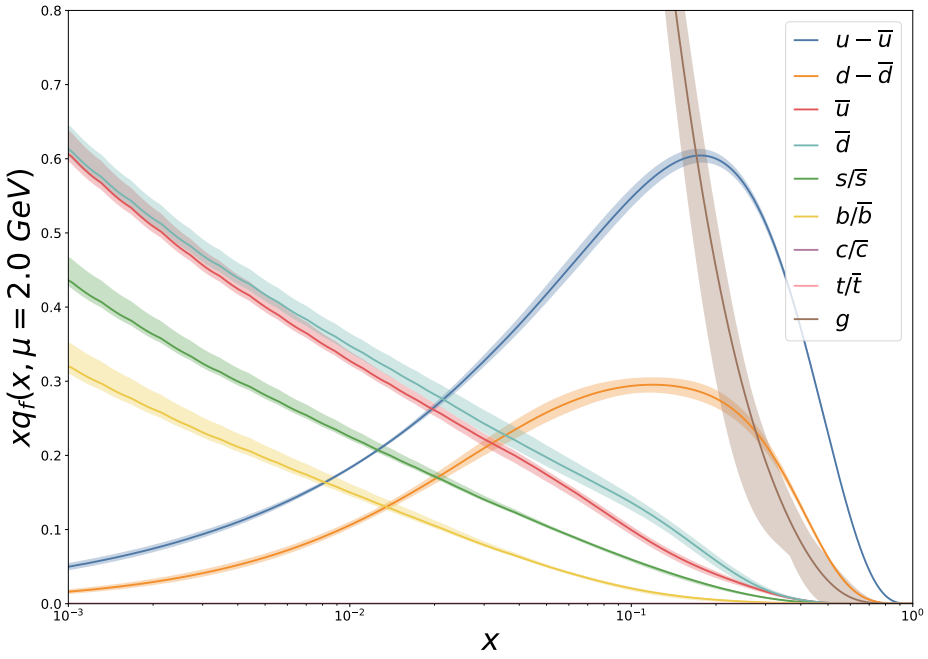

Figure 2.11: The $CJ15$ PDFs [85], shown weighted by x as all the PDFs diverge for small x. The flavour combination $u-\overline{u}$ and $d-\overline{d}$ represent the valence PDFs, show that their most likely carried momentum fraction is roughly $x=\frac{1}{3}$. The heavier quark flavours including the strange quark are assumed to be the same as their anti–particle counterparts. The errors bars where generated to one standard deviation as described in [86]. There is some light quark sea asymmetry, the $\overline{u}$ and $\overline{d}$ distributions, which converge again at small x. The gluon distribution is not determined directly, although inferable from gluon fusion and from DGLAP evolution [87–89].

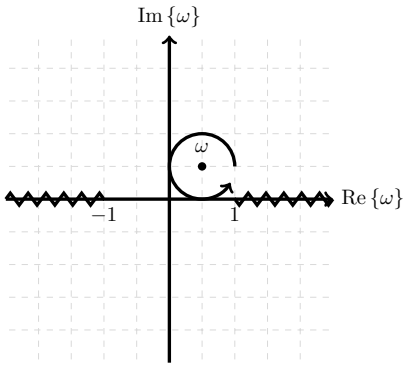

Figure 2.12: The dispersion integral of the Compton amplitude.

2.3.3 Dispersion Relation

We now form a relationship between the Compton amplitude and the hadron tensor, and by extension to the PDFs. The extraction relies on a dispersion relationship to map the unphysical parts of the Compton amplitude via optical theorem to the hadron tensor. The derivations for the dispersion relationship for T_1 and T_2 follow.

The Compton amplitude is real in the unphysical region below the elastic threshold $|\omega| = 1$, which we wish to relate to results to those experimentally reachable by DIS, $1 \leq \omega \leq \infty$. Suppose we had extracted T_1 at some ω and Q^2 we can then write down the a dispersion integral

$$T_1(\omega, Q^2) = \frac{1}{2\pi i} \oint_C \frac{T_1(\omega', Q^2)}{\omega' - \omega}. \tag{2.69}$$

Which is a dispersion integral of the form Figure 2.12. There is a cut on the real axis for $1 \leq \omega \leq \infty$, which we wrap around in the usual manner, which gives us a "Deathstar" dispersion integral Figure 2.13. Our dispersion integral in this form becomes

$$\begin{aligned} T_1(\omega, Q^2) = \frac{1}{2\pi i} \Bigg[& \int_1^{\infty} d\omega' \frac{T_1(\omega' + i\epsilon, Q^2)}{\omega' - \omega + i\epsilon} - \frac{T_1(\omega' - i\epsilon, Q^2)}{\omega' - \omega - i\epsilon} \\ & + \int_{-1}^{-\infty} d\omega' \frac{T_1(\omega' - i\epsilon, Q^2)}{\omega' - \omega - i\epsilon} - \frac{T_1(\omega' + i\epsilon, Q^2)}{\omega' - \omega + i\epsilon} \\ & + \int_{C'} \frac{T_1(\omega', Q^2)}{\omega' - \omega} \Bigg] \end{aligned} \tag{2.70}$$

where C' is the boundary integral of Figure 2.13. Using the *Schwarz reflection* principle this becomes

$$\begin{aligned} T_1(\omega, Q^2) = \frac{1}{2\pi} \Bigg[& 2 \int_1^{\infty} d\omega' \frac{\operatorname{Im} T_1(\omega' + i\epsilon, Q^2)}{\omega' - \omega} + 2 \int_{-1}^{-\infty} d\omega' \frac{\operatorname{Im} T_1(\omega' - i\epsilon, Q^2)}{\omega' - \omega} \\ & - i \int_{C'} \frac{T_1(\omega', Q^2)}{\omega' - \omega} \Bigg] \end{aligned} \tag{2.71}$$

where C' is the boundary term in Figure 2.13. The crossing symmetry (2.49) implies that the structure function $T_1(\omega, Q^2)$ is even in ω; $T_1(\omega, Q^2) = T_1(-\omega, Q^2)$. Applying this symmetry, after some algebra the dispersion integral becomes

$$T_1(\omega, Q^2) = \frac{1}{2\pi} \left[2 \int_1^{\infty} d\omega' \operatorname{Im} T_1(\omega' + i\epsilon, Q^2) \left(\frac{1}{\omega' - \omega} - \frac{1}{\omega' + \omega} \right) - i \int_{C'} \frac{T_1(\omega', Q^2)}{\omega' - \omega} \right]. \tag{2.72}$$

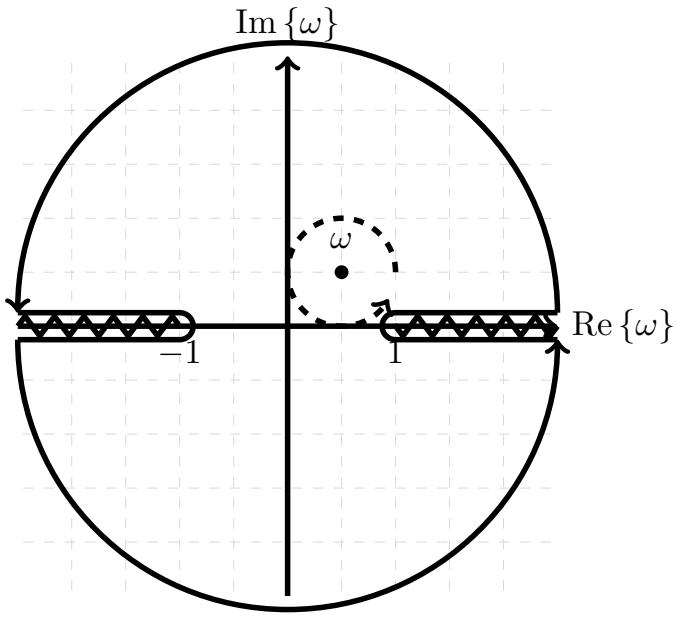

Figure 2.13: The "Deathstar" dispersion integral of the Compton amplitude with the usual shape around the branch cuts.

As discussed later in §8, the boundary term does not vanish as $|\omega| \to \infty$ and a subtracted dispersion relation needs to be formed. This subtracted dispersion integral Figure 2.14, with boundary term removed is

$$T_1(\omega, Q^2) - T_1(0, Q^2) = \frac{2}{2\pi} \int_1^\infty d\omega' \operatorname{Im} T_1(\omega' + i\epsilon, Q^2) \left(\frac{1}{\omega' - \omega} + \frac{1}{\omega' + \omega} - \frac{2}{\omega'} \right) \tag{2.73}$$

which simplifies to

$$T_1(\omega, Q^2) - T_1(0, Q^2) = \frac{4\omega^2}{2\pi} \int_1^\infty d\omega' \operatorname{Im} T_1(\omega' + i\epsilon, Q^2) \frac{1}{\omega'(\omega'^2 - \omega^2)}. \tag{2.74}$$

The imaginary part of the Compton amplitude structure function T_1 is related via optical theorem to the hadron tensor structure function F_1

$$\frac{1}{2\pi} \operatorname{Im} T_1(\omega, Q^2) = F_1(\omega, Q^2) \tag{2.75}$$

and ω' is related to the momentum fraction x by

$$\omega' = \frac{1}{x} \tag{2.76}$$

which then gives us

$$\boxed{T_1(\omega, Q^2) - T_1(0, Q^2) = 4\omega^2 \int_0^1 dx \frac{x F_1(x, Q^2)}{1 - (\omega x)^2}.} \tag{2.77}$$

The same steps can be performed for T_2, starting with the same dispersion integral Figure 2.12 the analogous equation to (2.69) is

$$T_2(\omega, Q^2) = \frac{1}{2\pi i} \oint_C \frac{T_2(\omega', Q^2)}{\omega' - \omega}. \tag{2.78}$$

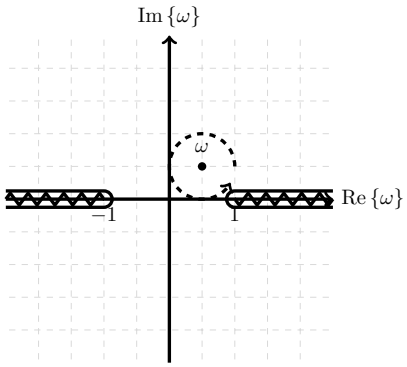

Figure 2.14: The subtracted dispersion integral for the Compton amplitude structure function T_2.

Unlike T_1, the boundary term for T_2 vanishes and hence T_2 does not require subtraction, as evident from it's skewness in ω. The *Callan–Gross* gross relationship (2.62) gives us an indication as to why, the limit $|\omega| \to \infty$, is roughly equivalent to $x \to 0$. More easily if one performs the subtraction the resultant dispersion relationship is unchanged due to the structure function being odd in ω, which we shall discuss in more depth in §8.1. Following the same steps as for T_1 the resulting dispersion relationship becomes

$$\boxed{T_2(\omega, Q^2) = 4\omega \int_0^1 dx \frac{F_2(x, Q^2)}{1 - (\omega x)^2}.} \tag{2.79}$$

In this section we have seen derivation of dispersion relationship for structure functions that are both even or odd in ω in terms of geometric sums

$$T_1(\omega, Q^2) - T_1(0, Q^2) = 4\omega^2 \int_0^1 dx \frac{x F_1(x, Q^2)}{1 - (\omega x)^2} \tag{2.80}$$

$$T_2(\omega, Q^2) = 4\omega \int_0^1 dx \frac{F_2(x, Q^2)}{1 - (\omega x)^2}. \tag{2.81}$$

2.3.4 Weak Charge of the Proton

The proton has a vector coupling G_V to the vector current, formed from the underlying vector charges of it's constituents. The same way we can define the weak charge Q_W of a composite object. In the case of the proton the weak charge is given at tree level by

$$Q_W^P = 1 - 4\sin^2\theta_W. \tag{2.82}$$

Coincidentally the weak mixing $\sin^2\theta_W \approx \frac{1}{4}$, so the weak charge of the proton is incredibly sensitive to $\sin^2\theta_W$, unlike the neutron which has approximate weak charge of -1. This natural SM suppression provides a natural test bed for the RGE scaling of the electroweak sector. The quantity would be sensitive to various parity violating BSM theories, notably SUSY, Z', and leptoquark theories [93].

With radiative corrections the weak charge of the proton becomes

$$Q_W^P = [\rho_{NC} + \Delta_e]\left[1 - 4\sin^2\theta_W + \Delta_e'\right] + \Box_{WW} + \Box_{ZZ} + \Box_{\gamma Z} \tag{2.83}$$

where ρ_{NC} renormalises the ratio of neutral and charged current interactions, Δ_e and Δ_e' correspond to Zee and γee couplings. The box diagrams are divided into purely electroweak box diagrams $\Box_{WW}$ and $\Box_{ZZ}$ whose contributions are perturbatively calculated using OPE methods.

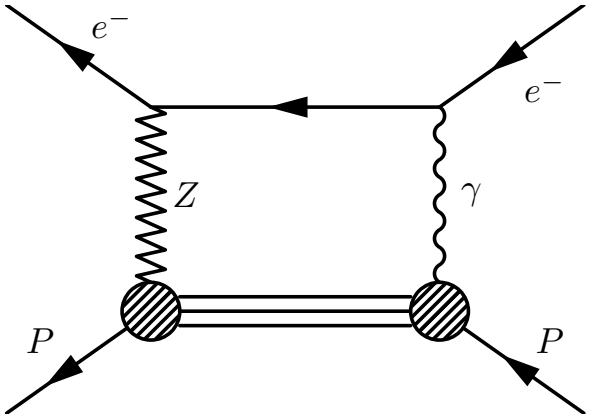

Figure 2.15: The γZ box diagram, with ingoing and outgoing proton P and electron e^-

The $\Box_{\gamma Z}$ box diagram (Figure 2.15) however includes significant long distance (small Q) contributions, that can't be determined with perturbative QCD.

Various model dependent determinations of $\Box_{\gamma Z}$ are available [94–99] and are in good agreement with each other. However their determination still has some contribution in the uncertainty when compared to state of the art experimental measurement of Q_W^P [100–102]. An improvement in the uncertainty in this quantity then increases the precision of our understanding of the scaling of $\sin^2\theta_W$ and hence constraints on BSM physics. In addition to the electroweak charge, such box diagrams are also inputs on atomic parity violating experiments.

Models of the $\Box_{\gamma Z}$ box diagram differ in technique, but are all built from integrals of structure functions. These structure functions are fitted from experiment, but some kinematic regions are not as precisely determined. The determination of any form of these structure functions whether integrated over x, or not, can lead to better constraints on the models, hence a better theoretical prediction of $\Box_{\gamma Z}$. The end result of such an improved calculation would be a better extraction of $\sin^2\theta_W$.

The accurate determination of $\sin^2\theta_W$ then allows us to test the RGE scaling properties against the SM predictions. Even if in agreement, the combined SM and experimental combination can be turned into bounds on different types of BSM particles. For instance current bounds from Q_W^P experiments give a mass exclusion for generic semi–leptonic parity violating BSM particles below $3.5\,TeV$ [102].

2.3.5 Two Photon Exchange

The ratio of proton electric (2.27) and magnetic (2.28) form factors

$$\mu_p \frac{G_E^p}{G_m^p} \tag{2.84}$$

where μ_p is the magnetic moment has two different apparent values when measured using two different techniques as shown in Figure 2.16. Using Rosenbluth separation [59] this value is approximately constant [103–105]. When the same ratio is extracted using recoil polarisation experiments [106–110], the value dies off linear with Q^2, although the fascinating question of whether there is a zero and it's nature has profound implications [111]. Currently both experiment and theory [112] are in the process of improving their determination of this ratio.

The deviation between the two methods has been largely attribute to a hard two photon exchange, although the effect is much larger for the Rosenbluth method [111]. In response the determination of two photon exchange has improved [113–115], largely resolving the discrepancy.

For the QCD prediction, only model dependent determinations are available. While some models predict the two photon exchange to remove the discrepancy [116–119], others do not

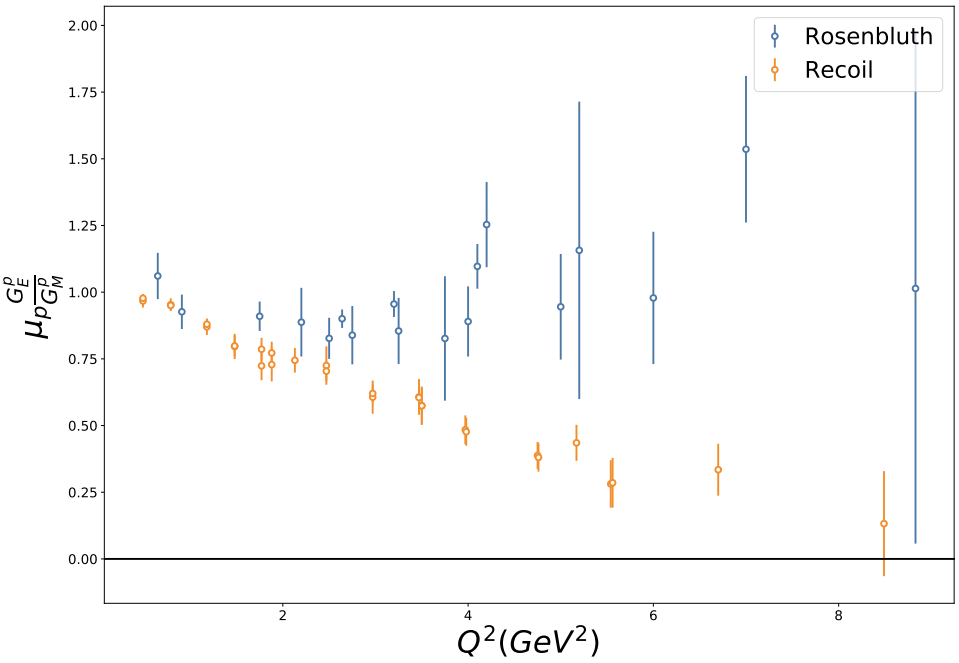

Figure 2.16: The ratio $\mu_p \frac{G_E^p}{G_M^p}$ shown against Q^2 extracted from Rosenbluth [103–105] (blue) and recoil polarisation [106–110] (orange) experiments.

[120, 121]. Such a discrepancy can be solved by providing an *ab initio* calculation, which in addition can be used to improve the sensitivity of affected experiments.

2.4 Generalised Parton Distribution Functions

We have encoded the spatial distributions within the hadron using form factors in §2.2 and the momentum distributions using structure functions in §2.3, but these two concepts can be combined in one function; the GPD. Where the structure functions encode diagonal operators, the GPDs additionally encode off–diagonal elements, of the very same matrix elements. The GPDs are defined in the same way as our GFFs shown in §2.2.1, but with quark longitudinal momentum fraction x dependence on the operators which are defined at leading–twist for the vector operator on a spin–half particle X

$$\left\langle X, \vec{p}' \middle| \mathcal{O}_\mu^{qV}(x) \middle| X, \vec{p} \right\rangle = \overline{u}_X(p') \left[\gamma_\mu H(x, \xi, Q^2) + \frac{i\sigma_{\mu\alpha} q^\alpha}{2m} E(x, \xi, Q^2) \right] u_X(p) + \mathcal{O}(\tau) \tag{2.85}$$

Here $\mathcal{O}(\tau)$ represents the higher twist contributions, x the momentum fraction and $\xi = -\frac{1}{2} n \cdot q$ the skewness as defined on the light–cone vector n satisfying $P \cdot n = 1$.

There are six additional GPDs defined for the axial and tensor currents, but we are only interested in the vector GPDs throughout this work. Like the vector current the GPDs can be separated by flavour to define flavour dependent GPDs $H^{q_f}(x, \xi, Q^2)$ and $E^{q_f}(x, \xi, Q^2)$. In the limit of zero skewness ξ and Q^2 the GPDs can be related to the PDFs by

$$H^{q_f}(x, 0, 0) = q_f(x) \tag{2.86}$$

$$H^g(x, 0, 0) = x g(x). \tag{2.87}$$

A PDF is the probability of finding the parton of momentum fraction x, with negative x typically corresponding to anti–quark distributions.

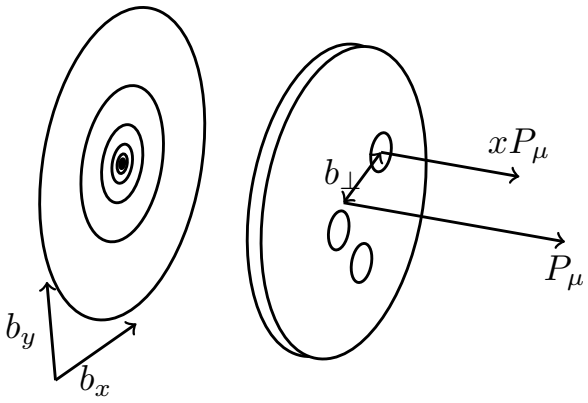

Figure 2.17: The information encoded in a GPD for a particle with momentum P_μ, that at high boost looks like a *pancake*, where each parton carries fractional momentum xP_μ of that momentum at transverse distance $b_\perp$ as encoded by $q = q_\perp$ for $\xi = 0$. The form factor (left) Figure 2.3 is shown to highlight how the GPD encapsulates the impact parameter $b_\perp$ distribution, and the partons are shown Figure 2.4, with their additional information.

The GPDs are relateable to the GFFs by

$$\int_{-1}^{1} dx x^{n-1} H\big(x,\xi,Q^2\big) = \sum_{i\ even}^{n-1} A_{n,i}\big(Q^2\big)(2\xi)^i + [(n+1)\%2]\, C_{n,0}\big(Q^2\big)(2\xi)^n \tag{2.88}$$

$$\int_{-1}^{1} dx x^{n-1} E\big(x,\xi,Q^2\big) = \sum_{i\ even}^{n-1} B_{n,i}\big(Q^2\big)(2\xi)^i - [(n+1)\%2]\, C_{n,0}\big(Q^2\big)(2\xi)^n. \tag{2.89}$$

Hence the Dirac and Pauli form factors defined in (2.26) are then given by integrals

$$\int_{-1}^{1} dx H\big(x,\xi,Q^2\big) = F_1\big(Q^2\big) \tag{2.90}$$

$$\int_{-1}^{1} dx E\big(x,\xi,Q^2\big) = F_2\big(Q^2\big) \tag{2.91}$$

This means that the GPDs encode not only the longitudinal structure of the partons, but also their internal distributions as well. For skewness $\xi = 0$, the momentum transfer is the purely in the transverse direction $q_\perp$. The Fourier transform with respect to $q_\perp$ leads to distribution in the impact parameter $b_\perp$. Hence GPDs encode the information of both the form factors and the PDFs, pictured in Figure 2.17.

We now have sufficient background in QCD for the work presented in subsequent chapters. We shall look at structure functions in §7 and §8, as well as GFFs, namely the EMT in §9.

Chapter 3

Lattice Quantum Chromodynamics

At large energy scales QCD is a perturbative theory, offering precise predictions that can be tested against experiment, but leaving gaps in understanding at smaller energy scales. For a more full understanding of the phenomena of QCD such gaps need to be filled with other methods. We shall explore one method in particular; lattice QCD.

Lattice QCD is a model–independent discretisation of QCD on a finite volume, first proposed by Wilson in 1974 [122]. It is the only known fundamental probe of QCD in the non–perturbative regime. At lower energies calculations in lattice QCD allow us to test the SM, whether directly in comparison to experiment or as complementary input to experiment or phenomenology. The approach can take advantage of modern high performance computational practices, improvable, in theory, to any desired accuracy. Underpinning lattice QCD is the path–integral formalism [123], on a finite extent four dimensional Euclidean space–time lattice of gauge fields and fermions. The finite volume provides an infrared cut-off and the discretisation an ultraviolet one, which with appropriate care can be compared to continuum results.

In this chapter we outline the mathematical formulation and terminology of QCD on a lattice, first by introducing the lattice §3.1, followed by reducing this to a finite volume §3.2, before finally looking at our reduced symmetry groups §3.3 and scale setting §3.4. To see this in practice we show how to calculate correlation functions §3.5, with some examples for states that shall be the focus throughout this work §3.6. For a more comprehensive background see [124, 125] and references therein.

3.1 Path Integrals

In practice to calculate observables on the lattice we use expectation values using the path integral formalism. We shall start with the Minkowski space–time path integral, discuss it's disadvantages and then Wick rotate it. The Minkowski path integral is

$$\langle \mathcal{O} \rangle := \frac{1}{Z} \int DA_\mu \prod_f D\overline{q}_f Dq_f \mathcal{O}\left[A_\mu, \overline{q}_f, q_f\right] e^{iS\left[A_\mu, \overline{q}_f, q_f\right]} \tag{3.1}$$

where the partition function Z is defined as

$$Z := \int DA_\mu \prod_f D\overline{q}_f Dq_f e^{iS\left[A_\mu, \overline{q}_f, q_f\right]} \tag{3.2}$$

with gluon gauge field A_μ, quark fields q_f for each flavour f, corresponding adjoint quark field $\overline{q}_f$, action S, and arbitrary time–ordered operator $\mathcal{O}$. The action is defined in the usual way as the integral of the Lagrangian density $\mathcal{L}$, as

$$S := \int d^4x \mathcal{L}(x). \tag{3.3}$$

The evaluation of (3.1) is problematic because of the so called *sign problem*. The origin of the problem is the oscillatory behaviour of the Boltzmann factor e^{iS}, causing large cancellation in the integral from different regions of phase space. To combat this problem we map the integral to Euclidean space, by performing a Wick rotation. There are multiple ways to perform the rotation and we choose the convention where our vectors are related by

$$x^{\mu}_{(M)} := \left(x^0_{(M)}, \quad \vec{x}_{(M)}\right) \to \left(\quad \vec{x}_{(M)}, ix^0_{(M)}\right) = \left(\vec{x}^{\,(E)}, x_4^{(E)}\right) =: x_{\mu}^{(E)} \tag{3.4}$$

$$x^{(M)}_{\mu} \;= \left(x^0_{(M)}, -\vec{x}_{(M)}\right) \to \left(-\vec{x}_{(M)}, ix^0_{(M)}\right) \tag{3.5}$$

and the corresponding Dirac matrix transforms

$$\gamma^{(M)}_{\mu} := \left(\gamma^{(M)}_0, \vec{\gamma}^{(M)}\right) \to \left(i\vec{\gamma}^{(M)}, \gamma^{(M)}_0\right) =: \gamma^{(E)}_{\mu}. \tag{3.6}$$

Here the super and sub–script (M) and (E) note Minkowski and Euclidean space values respectively. The rest of the Clifford algebra transformations are fixed once we have chosen

$$\gamma^{(M)}_5 := i\gamma_0\gamma_1\gamma_2\gamma_3 \tag{3.7}$$

$$\gamma^{(E)}_5 := \gamma_1\gamma_2\gamma_3\gamma_4 \tag{3.8}$$

such that $\gamma^{(M)}_5$ Wick rotates to $\gamma^{(E)}_5$. A consequence of these choices is that quantities such as a dot product will transform

$$(q \cdot x)^{(M)} \to -(q \cdot x)^{(E)} \tag{3.9}$$

The resulting properties of all the transformations, including of Clifford algebras and covariant derivatives are given in §C.1. Under the Wick rotation the Lagrangian density transforms

$$\mathcal{L}^{(M)} = -\mathcal{L}^{(E)} \tag{3.10}$$

where in terms of our quark and gluon on fields the Euclidean Lagrangian density reads

$$\mathcal{L}^{(E)}_{QCD} = \sum_f \overline{q}_f(\not{\partial} + m_f)q_f + \frac{1}{4}F_{\mu\nu}F_{\mu\nu} \tag{3.11}$$

Using (C.34) the path integral for Euclidean space now reads

$$\langle \mathcal{O} \rangle := \frac{1}{Z}\int DA_\mu \prod_f Dq_f D\overline{q}_f \mathcal{O}\left[A_\mu, \overline{q}_f, q_f\right] e^{-S\left[A_\mu, \overline{q}_f, q_f\right]} \tag{3.12}$$

with partition function

$$Z := \int DA_\mu \prod_f Dq_f D\overline{q}_f e^{-S\left[A_\mu, \overline{q}_f, q_f\right]}. \tag{3.13}$$

Now we no longer have the *sign problem*, caused by the Boltzmann factor, which now is precisely the Boltzmann weighting, which we will take advantage of with importance sampling later. The interpretation of a path integral is a summation of all possible paths, weighted by their action. We now have the necessary pieces to work towards Euclidean observables on a lattice, that can then be related back to Minkowski observables.

3.2 Lattice Quantum Field Theory in a Box

It was simple to express quantities of Quantum Field Theory (QFT) to those expressed in a still continuum Euclidean path integral, but to transform this into one with a finite set of points; as required by limits of computational resources, introduces a lot of obstacles. In this section, we present how to realise quark and gluon fields on an a lattice with infinite extent, then how to reduce it to a finite sized box, and finally we shall present some optimisations to make computations feasible.

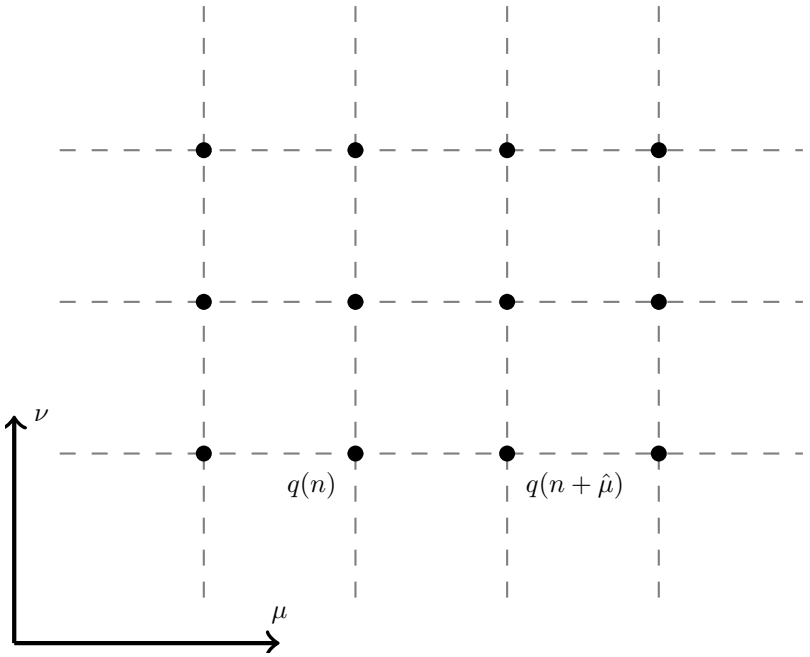

Figure 3.1: The graphical form of a discretised form of the naïve fermion part of the Lagrangian, where the quark fields q sit on each of the sites.

3.2.1 Discretisation

The first step in achieving a computationally solvable path integral is to introduce discretised space–time, separated by isotropic distance a in each dimension. Anisotropic lattices with a differing spacing in one direction have their uses [126], but are not the focus of this work. This lattice spacing a is usually of the order of tenths of a femtometre, and acts a natural regulator of ultraviolet divergences for the theory. In order to realise this we need to construct a lattice which has the correct continuum limit, we start with the naïve approach and demonstrate the need for link variables.

Fermion Lagrangian

Consider the non–interacting fermion part of the Euclidean action

$$\mathcal{L}_F^{NI}\left[\overline{q}_f, q_f\right](x) = \overline{q}_f(x)\left(\not{\partial} + m_f\right)q_f(x). \tag{3.14}$$

This puts each of our quark fields on the lattice, where they now depend on the lattice point $q(x) \to q(n)$ where $n \in \mathbb{Z}^4$, as seen diagrammatically as Figure 3.1. It should be noted that we implicitly use the lattice spacing $x = an$ to compare these fields. Now we shall drop the flavour level f where appropriate to simplify equations. We take the free fermion Lagrangian (3.14), convert it to these lattice fields, and then transform the derivative into an simple numerical approximation

$$\mathcal{L}_F^{NI}\left[\overline{q}, q\right](n) = \overline{q}(n)\left(\sum_\mu \gamma_\mu \frac{q(n+\hat{\mu}) - q(n-\hat{\mu})}{2a} + mq(n)\right). \tag{3.15}$$

Clearly as $a \to 0$ we recover the continuum form. This formulation however has a problem, the action will not be invariant under a local $SU(3)$ gauge transformation, to see this consider a transformation $\Omega(n)$ on $\overline{q}(n)q(n+\hat{\mu})$

$$\overline{q}(n)q(n+\hat{\mu}) \to \overline{q}(n)\Omega^\dagger(n)\Omega(n+\hat{\mu})q(n+\hat{\mu}) \tag{3.16}$$

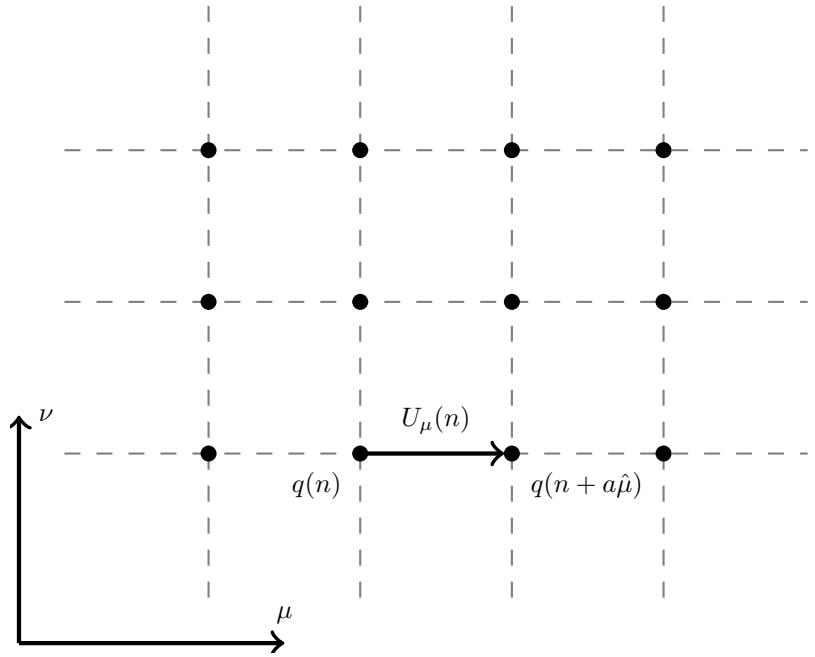

Figure 3.2: The representation of our lattice, with quark fields q on lattice sites and link variables U_μ, representing the gauge fields A_μ on links between the sites.

and as Ω can be chosen differently at each point in space–time this would break local $SU(3)$ symmetry. Just as in the continuum case where we needed to add a gauge field to the derivative to construct the covariant derivative, we add a term that transforms like

$$U_\mu(n) \to \Omega(n) U_\mu(n) \Omega^\dagger(n+\hat{\mu}). \tag{3.17}$$

Inserting these so called link variable U_μ into our Lagrangian yields an now gauge invariant expression, of the fermion part of the Lagrangian, now with interactions

$$\mathcal{L}_F\left[\overline{q}, q\right](n) = \overline{q}(n)\left(\sum_\mu \gamma_\mu \frac{U_\mu(n) q(n+\hat{\mu}) - U_{-\mu}(n) q(n-\hat{\mu})}{2a} + m q(n)\right) \tag{3.18}$$

where for convenience we have defined

$$U_{-\mu}(n) := U_\mu^\dagger(n-\mu). \tag{3.19}$$

In the continuum limit this operator is the so–called gauge transporter, a path–ordered integral along some curve that connect the two points

$$G(x,y) := P \exp\left(i \int_{C_{xy}} A \cdot ds\right). \tag{3.20}$$

These link variables encode the gluon fields, represented as elements of $SU(3)$ rather than elements of it's Lie algebra

$$U_\mu(n) = P e^{ig\int_0^a A_\mu(x+s\hat{\mu})ds} \approx e^{iaA_\mu(n)} \tag{3.21}$$

where

$$U_\mu(n) = G(n, n+\hat{\mu}) + \mathcal{O}(a). \tag{3.22}$$

With this in place we have the basic form of the lattice, diagrammatically presented by Figure 3.2. By using the fact that $U_\mu(n) = 1 + iaA_\mu(n) + \mathcal{O}\left(a^2\right)$ we can verify that in the continuum limit, we get the equivalent part of the QCD Lagrangian.

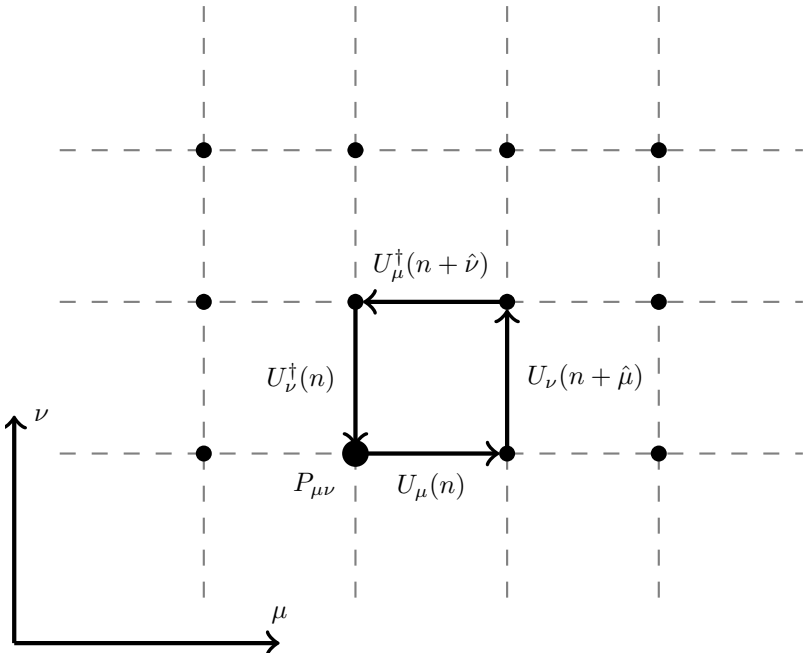

Figure 3.3: A lattice plaquette formed as the product of four gauge links, forming a closed loop on the lattice.

Gluon Lagrangian

To calculate the purely gluonic contribution to the action we need to introduce a particular Wilson loop, the plaquette

$$P_{\mu\nu} := U_\mu(n)U_\nu(n+\hat{\mu})U_\mu^\dagger(n+\hat{\nu})U_\nu^\dagger(n) \tag{3.23}$$

which we depict in Figure 3.3 and is clearly gauge independent after trace. By using the Baker–Campbell–Hausdorff formula for products of exponentials one can show that the action defined as

$$S_G\left[U_\mu\right] := \frac{2}{g^2}\sum_{n\in\mathbb{Z}^4}\sum_{\mu\leq\nu}\mathrm{Re}\,\mathrm{tr}\left[I - P_{\mu\nu}\right] = \frac{a^4}{2g^2}\sum_{n\in\mathbb{Z}^4}\sum_{\mu,\nu}\mathrm{tr}\left[F_{\mu\nu}(n)^2\right] + \mathcal{O}\big(a^2\big) \tag{3.24}$$

and has the correct $a \to 0$ continuum limit. It is clear that this term is also invariant under gauge transformations. With both the fermion and gluonic parts of our action we now have the discretised path integrals

$$\langle\mathcal{O}\rangle = \frac{1}{Z}\int\prod_{n\in Z^4}\left(DU_\mu(n)\prod_f Dq_f(n)D\overline{q}_f(n)\right)\mathcal{O}\left[U_\mu,\overline{q}_f,q_f\right]e^{-S_F\left[U_\mu,\overline{q}_f,q_f\right]-S_G[U_\mu]} \tag{3.25}$$

with partition function

$$Z = \int\prod_{n\in Z^4}\left(DU_\mu(n)\prod_f Dq_f(n)D\overline{q}_f(n)\right)e^{-S_F\left[U_\mu,\overline{q}_f,q_f\right]-S_G[U_\mu]} \tag{3.26}$$

and have seen that in the continuum limit we recover the continuum expression. We are now ready to put this expression into a box.

3.2.2 QCD in a Box

An infinite lattice is still impossible to fit into the memory of a computer and so unless an analytical solution is possible we must reduce our problem to a finite set of points. In addition to

making the equations computationally solvable, the restriction to a finite volume automatically regularises infrared divergences from our theory. Suppose we take (3.25) and limit the lattice to some hypercubic region $\Lambda \subset \mathbb{Z}^4$ of extent L in each direction, all our degrees of freedom in our path integral are now finite. This means we introduce additional artefacts into our resulting expectation values. The path integral for this system becomes

$$\langle \mathcal{O} \rangle = \frac{1}{Z} \int \prod_{n \in \Lambda} \left(DU_\mu(n) \prod_f Dq_f(n) D\overline{q}_f(n) \right) \mathcal{O}\left[U_\mu, \overline{q}_f, q_f\right] e^{-S_F\left[U_\mu, \overline{q}_f, q_f\right] - S_G[U_\mu]} \tag{3.27}$$

an evaluatable set of integrals, however the number of integration variables scales with the volume, which for typical lattices sizes range from order of millions to hundreds of millions of sites. Clearly more analytic reduction needs to be done. In order to reduce the problem to a solvable problem we introduce Grassmann variables and the Fermion determinant.

Fermion Determinant

As the fermionic degrees of freedom anti–commute with each other, care has to be made when introducing the interacting part of the fermion action. To perform such an integration we use so called Grassmann numbers, which display these very properties and relate these to the fermionic part of the lattice QCD action we denote q_i and $\overline{q}_i$. First we need the Matthew–Salam formula [127, 128]

$$\int dq_N d\overline{q}_N \dots dq_1 d\overline{q}_1 \exp\left(\overline{q}_i M_{ij} q_j\right) = \det\left(M\right) \tag{3.28}$$

where there is implicit summation of i and j. The other important tool we need is Wick's theorem, stated with only fermionic degrees of freedom

$$\begin{aligned} \left\langle q_{i_1} \overline{q}_{j_1} \dots q_{i_n} \overline{q}_{j_n} \right\rangle &= \frac{1}{Z} \int dq_N d\overline{q}_N \dots dq_1 d\overline{q}_1 q_{i_1} \overline{q}_{j_1} \dots q_{i_n} \overline{q}_{j_n} \exp\left(\overline{q}_i M_{ij} q_j\right) \\ &= (-1)^n \sum_P \operatorname{sign}\left(P\right) \left(M^{-1}\right)_{i_1 j_{P_1}} \dots \left(M^{-1}\right)_{i_n j_{P_n}} \end{aligned} \tag{3.29}$$

where P is the set of all permutations of n numbers in N. To realise this in our box we take our action

$$S_F\left[U_\mu, \overline{q}, q\right] = a^4 \sum_{n,m \in \Lambda} \overline{q}(n)^\alpha_a \mathcal{D}(n,m)^{\alpha\beta}_{ab} q(m)^\beta_b \tag{3.30}$$

with for instance if we take $\mathcal{D}$ of (3.18) we have

$$\mathcal{D}(n,m)^{\alpha\beta}_{ab} := \sum_\mu \left(\gamma_\mu\right)^{\alpha\beta} \frac{U_\mu(n)_{ab} \delta_{n+\hat{\mu},m} - U_{-\mu}(n)_{ab} \delta_{n-\hat{\mu},m}}{2a} + m(I)^{\alpha\beta} \delta_{ab} \delta_{n,m}. \tag{3.31}$$

Our inverses as defined in Wick's theorem are of fully contracted operators of fermions. To deal with the fact that our fermion action is dependent on the link variables we would then subsequently perform integration on our gluonic degrees of freedom, which transform our lattice observables (3.27) to

$$\langle \mathcal{O} \rangle = \frac{1}{Z} \int \prod_{n \in \Lambda} DU_\mu(n) \overset{\sqcap}{\mathcal{O}}\left[U_\mu\right] \prod_f \det\left(\mathcal{D}_f\left[U_\mu\right]\right) e^{-S_G[U_\mu]} \tag{3.32}$$

where $\overset{\sqcap}{\mathcal{O}}$ is our operator $\mathcal{O}$ with all possible Wick contractions performed, and are formed in our case by contracted quark propagators which can be calculated by

$$\left(S_f\right)^{\alpha\beta}_{ab}(n,m) = \mathcal{D}^{-1}_f(n,m)^{\alpha\beta}_{ab} \tag{3.33}$$

with inverse defined by

$$\sum_{m\in\Lambda} \mathcal{D}_f^{-1}(n,m)^{\alpha\beta}_{ab}\mathcal{D}_f(m,l)^{\beta\gamma}_{bc} = \delta^{\alpha\gamma}\delta_{ac}\delta^{(4)}(n-l). \tag{3.34}$$

As a consequence, the propagator inherits γ_5–Hermitticitty from the Dirac operator defined in §C.2.4.

Importance Sampling

We can now begin to statistically evaluate (3.32), by using Monte–Carlo techniques. Suppose we took N random samples of $U_\mu^{(i)}$, our expectation value can be approximated by

$$\langle\mathcal{O}\rangle \approx \frac{1}{Z}\sum_{i=1}^{N} \overset{\sqcap}{\mathcal{O}}\left[U_\mu^{(i)}\right]\prod_f \det\left(\mathcal{D}_f\left[U_\mu^{(i)}\right]\right)e^{-S_G\left[U_\mu^{(i)}\right]} \tag{3.35}$$

$$Z \approx \sum_{i=1}^{N}\prod_f \det\left(\mathcal{D}_f\left[U_\mu^{(i)}\right]\right)e^{-S_G\left[U_\mu^{(i)}\right]}. \tag{3.36}$$

The problem we are left with now is that the weighting factor

$$\rho\left(U_\mu^{(i)}\right) = \prod_f \det\left(\mathcal{D}_f\left[U_\mu^{(i)}\right]\right)e^{-S_G\left[U_\mu^{(i)}\right]} \tag{3.37}$$

will be small for almost all samples of $U_\mu^{(i)}$, which can be overcome by generating the samples with weighting (3.37) which reduces our problem to a simple sum

$$\langle\mathcal{O}\rangle \approx \frac{1}{N}\sum_{i=1}^{N} \overset{\sqcap}{\mathcal{O}}\left[U_\mu^{(i)}\right] \tag{3.38}$$

over such generated lattices.

There are two ways relevant to this body of work to generate lattices with such weighting, first is to set the fermion determinant to $\det(\mathcal{D}) = 1$, called 'quenched' and the other a hybrid Monte–Carlo algorithm [129] based approach. As the heavier quarks are expected to have minimal effect on hadron matrix elements, the c, b and t quarks have been absorbed into α_{QCD} at $N_f = 3$ in this work, but it should be noted that some quantities are reaching precisions where c sea effects are significant [130]. As the u and d masses are similar and very small, we can take them to be degenerate to further optimise computational cost.

With the basic implementation of QCD on a lattice proscribed, we now briefly go through some optimisations performed to systematically reduce artefacts, introduced by discretisation.

3.2.3 Wilson Fermions

As consequence to the discretisation unphysical poles are introduced into our momentum space fermion propagator. To see this we construct the free fermion ($U_\mu(n) = 1$) propagator

$$\tilde{S}(p) = \frac{m - ia^{-1}\sum_\mu \gamma_\mu \sin(ap_\mu)}{m^2 + a^{-2}\sum_\mu \sin^2(ap_\mu)}. \tag{3.39}$$

In the massless limit this becomes

$$\tilde{S}(p)\Big|_{m=0} = -ia\frac{\sum_\mu \gamma_\mu \sin(ap_\mu)}{\sum_\mu \sin^2(ap_\mu)} \tag{3.40}$$

which has 15 unphysical poles. The additional poles are referred to as 'doublers' and need to be removed. Fundamentally it is impossible to write a fermion discretisation that simultaneously is free from 'doublers', invariant under continuum chiral symmetry and has a local fermion operator while giving the correct continuum limit [131–133].

By including an extra term in the action (3.18), one possible solution to this problem is introducing an extra term that violates chiral symmetry

$$\mathcal{L}_W\left[\overline{q},q\right](n)=\overline{q}(n)\Big(\tfrac{1}{2a}\textstyle\sum_\mu\left[(r-\gamma_\mu)U_\mu(n)q(n+\hat{\mu})+(r+\gamma_\mu)U_{-\mu}(n)q(n-\hat{\mu})\right]+\big(m+\tfrac{4r}{a}\big)q(n)\Big) \tag{3.41}$$

which by freedom of choice of field normalisation can be defined

$$\mathcal{L}_W\left[\overline{q},q\right](n)=\overline{q}(n)\left(\kappa\sum_\mu\left[(r-\gamma_\mu)U_\mu(n)q(n+\hat{\mu})+(r+\gamma_\mu)U_{-\mu}(n)q(n-\hat{\mu})\right]+q(n)\right) \tag{3.42}$$

with

$$q\to\frac{q}{\sqrt{2a\kappa}} \tag{3.43}$$

$$\kappa:=\frac{1}{2ma+8r} \tag{3.44}$$

for any $r\in(0,1]$ typically chosen to be 1. We refer to κ as the *hopping parameter* and often use it as

$$am=\frac{1}{2}\left(\frac{1}{\kappa}-\frac{1}{\kappa_c}\right) \tag{3.45}$$

where $\kappa_c:=\frac{1}{8r}$ is the *critical hopping parameter*, that κ has in the chiral limit. With this improvement the mass of these 'doublers' receive extra contribution to their mass inversely proportional to a and hence tend to infinite mass in the continuum limit, decoupling from our theory entirely. The corresponding quark action is

$$S_W\left[\overline{q},q\right](n)=a^4\sum_{n\in\Lambda}\overline{q}(n)\left(\kappa\sum_\mu\left[(r-\gamma_\mu)U_\mu(n)q(n+\hat{\mu})+(r+\gamma_\mu)U_{-\mu}(n)q(n-\hat{\mu})\right]+q(n)\right). \tag{3.46}$$

3.2.4 Symanzik Improvement

The gluon action (3.24) and quark action (3.46) used have discretisation artefacts of order $\mathcal{O}(a^2)$ and $\mathcal{O}(a)$ respectively, meaning that calculations have to be performed at very fine computationally expensive lattice spacings in order to compare to continuum results. To allow simulation on coarser lattice spacings, it is standard to reduce discretisation errors through *Symanzik–improvement* [134], through introduction of higher order operators. We now present the improvement used for both fermions and gluons.

Clover Improved Fermions

To improve the Wilson fermion action (3.46) we use the *Sheikholeslami–Wohlert action* [135] which introduces a clover improvement term

$$S_{SW}\left[\overline{q},q\right](n)=S_W\left[\overline{q},q\right]+a^4\sum_{n\in\Lambda}\frac{arc_{SW}}{4}\overline{q}(n)\sigma_{\mu\nu}F_{\mu\nu}(n)q(n) \tag{3.47}$$

where the clover term is written

$$F_{\mu\nu}:=-\frac{i}{2}\left[C_{\mu\nu}-C_{\mu\nu}^\dagger\right] \tag{3.48}$$

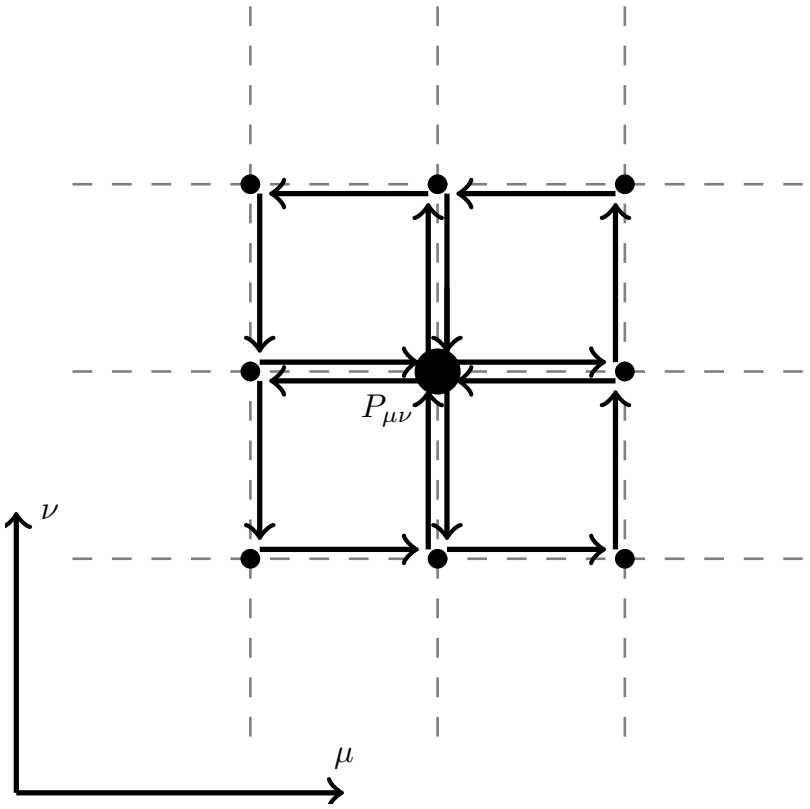

Figure 3.4: The clover plaquette, made up of four plaquette to form a staple.

where $C_{\mu\nu}$ is defined in terms of plaquettes (3.23)

$$C_{\mu\nu}(n) := \frac{1}{4a^2}\left[P_{\mu,\nu}(n) + P_{\nu,-\mu}(n) + P_{-\mu,-\nu}(n) + P_{-\nu,\mu}(n)\right] \tag{3.49}$$

which get their name from their shape, see Figure 3.4 The clover parameter c_{SW} is tuned to remove $\mathcal{O}(a)$ discretisation artefacts.

Lüscher-Weisz Gluons

The gauge parts of the action are improved by observing that for differently shaped Wilson loops in (3.24), different discretisation artefacts of order $\mathcal{O}(a^2)$ are obtained. Combinations of such different shapes can then be combined to construct a gauge action without errors at $\mathcal{O}(a^2)$. By using Wilson loops in the form

$$S_G\left[U_\mu\right] := \frac{2}{g^2}\sum_{n\in\mathbb{Z}^4}\left(c_1\sum \mathrm{Re\,tr}\left[I - P^{plaq}\right] + c_2\sum \mathrm{Re\,tr}\left[I - P^{rect}\right] + c_3\sum \mathrm{Re\,tr}\left[I - P^{parra}\right]\right) \tag{3.50}$$

with correct parameters c_i the action improves to $\mathcal{O}(a^4)$ [136]. The two new Wilson loops are the next simplest extensions to the plaquette, forming 2×1 rectangles and $1\times 1\times 1$ 'parallelograms', which are six sided in three dimensions. With only one term needing cancellation there is freedom in choice of c_i resulting in constraining equation

$$c_1 + 8c_2 + 8c_3 = 1. \tag{3.51}$$

A common choice for this action, as we shall use throughout this work is the tree–level improved action [137], corresponding to

$$c_1 = \frac{20}{12} \tag{3.52}$$

$$c_2 = -\frac{1}{12} \tag{3.53}$$

$$c_3 = 0. \tag{3.54}$$

3.3 Lattice Symmetries

Due to discretisation and finite volume we have broken many of our continuum symmetries. The Euclidianisation shifts the Lorentz group to the four–dimensional rotation group $O(4)$, before being further broken by discretisation to the group of hypercubic rotations $H(4)$. Due to this reduced symmetry, causing less stringent requirements for covariance, one has to be careful with extraction of operators on the lattice. By working with operators in a particular irreducible representation of $H(4)$ that avoid mixing with same or lower dimensional operators, continuum comparable matrix elements can be extracted. For a more in depth look at problems arising due to mixing see [138].

This reduction in symmetry shall become important in our calculations involving gluonic operators later in §9. We shall also investigate the higher moments of PDFs §7.2, where the mixing is important for the comparable conventional techniques.

Our discretised theory also inherits symmetries from the continuum theory. Euclidean space lacks distinguished directions present in Minkowski space, which split temporal and spatial directions. As any of the four dimensions can act as the temporal direction, the Euclidean theory must also have additional symmetries the Minkowski theory does not have. Of interest to us are parity and charge conjugation.

On the lattice a parity transformation P acts on fields as

$$Pq(\vec{n}, n_4) = \gamma_4 q(-\vec{n}, n_4) \tag{3.55}$$

$$P\overline{q}(\vec{n}, n_4) = \overline{q}(-\vec{n}, n_4)\gamma_4. \tag{3.56}$$

The lack of singled out direction means that there are three additional symmetries, collectively all four can be labelled P_μ with γ_μ instead of just γ_4. Consequently the product of three of them $P_1 P_2 P_3$ corresponds to the time reflection operator.

The form for time reflection has consequences for Hilbert space reconstructions, which are then only well defined when anti–periodic temporal boundary conditions are imposed on fermions. For this reason we use such boundary conditions in our formulation and periodic boundary conditions for all spatial, and non–fermionic temporal quantities.

The charge conjugation operator C, that transforms particles into their anti–particle counterpart, is defined by the relation to Dirac matrices

$$C\gamma_\mu C^{-1} = -\gamma_\mu^T \tag{3.57}$$

which determines it's form for a particular choice of representation for the Dirac matrices.

3.4 Quark Masses and Scale Setting

The formulation of the lattice QCD requires some calculations to be able to compare results to physical observables. We discuss *scale setting* and quark masses as they pertain to this work.

Lattice simulations are done at larger than physical quark masses, to improve inversion speed for the Dirac matrix (3.34). The common choice is to use heavy quark masses at their physical values and vary the u and d quark masses. Our simulations take a different approach, instead of

using the physical strange mass, the average mass of the three light quarks (with u and d quarks degenerate)

$$\overline{m} = \frac{1}{3}(2m_l + m_s) \tag{3.58}$$

is kept constant, at the physical value. This approach has several advantages [139], it constrains flavour–symmetry breaking expansions and keeps flavour–singlet quantities constant at leading order.

All quantities in lattice calculations are done in terms of the lattice spacing a. This spacing has not set directly, rather indirectly by bare coupling parameter β and so must be determined by *scale setting*. The *scale setting* has been performed for fixed β and varying κ by extrapolating a number of $SU(3)_{flav}$–singlet quantities to their physical values [137, 139–141]. The use of quark mass trajectory (3.58) then ensures that these flavour–singlet quantities are constant to leading order. The determined a from this procedure is then constant for fixed β.

3.5 Correlators

With a working theory of QCD in a box, we now shift focus on how to use this to calculate meaningful quantities, which for this body of work deals with n–point correlation functions. These correlators allow us to extract energies and matrix elements which we can relate to continuum phenomena. In this section, the basic two–point correlator is defined, and extended to include intermediate currents.

3.5.1 Two–point Correlator

To calculate the value of energy eigenstates on the lattice we use a two–point correlator. The basis of the two point function is a momentum projected pair of creation and annihilation interpolating operators $\chi^\dagger$ and χ, with quantum numbers corresponding to the state of interest. These operators create and annihilate a towers of states on a lattice, which have these quantum numbers. We start with the general form of a two–point correlation function

$$G^{(2)}_\chi(x,y) := \left\langle \chi(x)\chi^\dagger(y) \right\rangle := \left\langle \Omega \middle| \chi(x)\chi^\dagger(y) \middle| \Omega \right\rangle \tag{3.59}$$

with creation operator at space–time point y referred to as the source and annihilation operator at x referred to as the sink. In theory the interpolating operators on each end can be different but we shall restrict ourselves to a single interpolator with it's Hermitian conjugate.

The completeness relation on the lattice is

$$\mathbf{1} = \sum_X \int \frac{d^3p}{(2\pi)^3} \frac{1}{2E_{X,\vec{p}}} |X,\vec{p}\rangle\langle X,\vec{p}| \tag{3.60}$$

as determined by the normalisation

$$\left\langle Y,\vec{k} \middle| X,\vec{p} \right\rangle := 2E_{X,\vec{p}}\delta_{XY}(2\pi)^3\delta^{(3)}\left(\vec{p}-\vec{k}\right). \tag{3.61}$$

The state X of momentum $\vec{p}$ quantised to $\vec{p} = \frac{2\pi n}{L}$ for integer n, has energy $E_{X,\vec{p}}$. We often use lattice momenta and lattice momentum numbers interchangeably, which have been multiplied by $\frac{L}{2\pi}$ to turn them into integers.

On a lattice the integrals over space and momenta become sums, however we shall keep the notation of the continuum, the derivations in either form are equivalent and hence we can

calculate both forms at the same time. This correspondence is

$$\int \frac{d^3p}{(2\pi)^3} \to \frac{(2\pi)^3}{\left|\vec{\Lambda}\right|} \sum_{\vec{p}} \tag{3.62}$$

$$\int d^3x \to \sum_{\vec{x}} \tag{3.63}$$

$$(2\pi)^3 \delta^{(3)}\left(\vec{p} - \vec{k}\right) \to \frac{\left|\vec{\Lambda}\right|}{(2\pi)^3} \delta_{\vec{p}\vec{k}} \tag{3.64}$$

Using the continuum normalisation we can work out the spectral form of (3.59), by inserting a complete set of states

$$G_\chi^{(2)}(x,y) = \sum_X \int \frac{d^3k}{(2\pi)^3} \frac{1}{2E_{X,\vec{k}}} \frac{1}{2E_{X,\vec{k}}} \left\langle \Omega \middle| \chi(x) \middle| X, \vec{k} \right\rangle \left\langle X, \vec{k} \middle| \chi^\dagger(y) \middle| \Omega \right\rangle. \tag{3.65}$$

To use this to extract an energy we use translational invariance to identify a $x_4 - y_4$ varying term. Using the translation invariance we can redefine our interpolating fields using the four–momentum operator P

$$\chi(x) = e^{-iP\cdot x} \chi(0) e^{iP\cdot x} \tag{3.66}$$

where $P_4|X,\vec{p}\rangle = iE_{X,\vec{p}}|X,\vec{p}\rangle$ the two point function becomes

$$G_\chi^{(2)}(x,y) = \sum_X \int \frac{d^3k}{(2\pi)^3} e^{-E_{X,\vec{k}}(x_4-y_4)} e^{i\vec{k}\cdot(\vec{x}-\vec{y})} \frac{1}{2E_{X,\vec{k}}} \left\langle \Omega \middle| \chi(0) \middle| X, \vec{k} \right\rangle \left\langle X, \vec{k} \middle| \chi^\dagger(0) \middle| \Omega \right\rangle. \tag{3.67}$$

It is clear that the two point function only depends on the separation between the two interpolating fields and hence we define two–point function with source–sink separation x as

$$G_\chi^{(2)}(x) := G_\chi^{(2)}(x,0). \tag{3.68}$$

which can be diagrammatically represented by Figure 3.5. The momentum projected correlator, we define as

$$G_\chi^{(2)}(x_4,\vec{p}) = \int d^3x e^{-i\vec{p}\cdot\vec{x}} G_\chi^{(2)}(x) \tag{3.69}$$

which has form

$$G_\chi^{(2)}(x_4,\vec{p}) := \sum_X e^{-E_{X,\vec{p}}x_4} \frac{1}{2E_{X,\vec{p}}} \left\langle \Omega \middle| \chi(0) \middle| X, \vec{p} \right\rangle \left\langle X, \vec{p} \middle| \chi^\dagger(0) \middle| \Omega \right\rangle. \tag{3.70}$$

In the large separation limit $x_4 >> 0$, the lowest energy state with non–zero vacuum overlap saturates (3.70). The lowest energy state X, at large $x_4 >> 0$ then has form

$$G_\chi^{(2)}(x_4,\vec{p}) \to e^{-E_{X,\vec{p}}x_4} g_\chi^{(2)}\left[X,\vec{p}\right] \tag{3.71}$$

where the constant overlap $g_\chi^{(2)}\left[X,\vec{p}\right]$ is defined by

$$g_\chi^{(2)}\left[X,\vec{p}\right](x) := \frac{1}{2E_{X,\vec{p}}} \left\langle \Omega \middle| \chi(x) \middle| X, \vec{p} \right\rangle \left\langle X, \vec{p} \middle| \chi^\dagger(0) \middle| \Omega \right\rangle. \tag{3.72}$$

$$g_\chi^{(2)}\left[X,\vec{p}\right] := g_\chi^{(2)}\left[X,\vec{p}\right](0). \tag{3.73}$$

From (3.71), the energy $E_{X,\vec{p}}$ can then be extracted from the time dependence of the exponential. Using this we are able to calculate energies, such as nucleon energies.

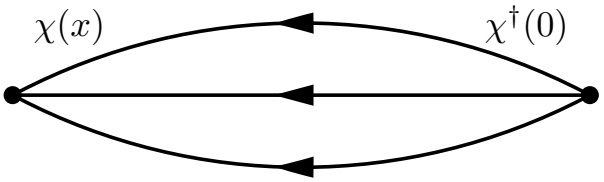

Figure 3.5: The two point function for interpolators χ, with source created at 0 and annihilated at x. The intermediate line represent quark propagators, of all possible contractions between the two interpolators.

3.5.2 Three and Four–Point Correlators

While the two–point correlators allow the extraction of energy eigenstates, the three and four–point correlators allow the extraction matrix elements. The derivation of forms equivalent to (3.71) use the same basics steps as for the two–point correlator and are presented in §A. We present a few of the results now.

The steps for the equivalent three–point correlator are presented in §A.1, the main definitions needed for later chapters are

$$G^{(3)}_{\chi,J}(x,y) := \left\langle \chi(x) J(y) \chi^\dagger(0) \right\rangle \tag{3.74}$$

$$g^{(3)}_{\chi J \chi^\dagger}\left[X,\vec{k}_1;Y,\vec{k}_2;x,y\right] := \frac{1}{2E_{X,\vec{k}_1}}\frac{1}{2E_{Y,\vec{k}_2}}\left\langle \Omega\middle|\chi(x)\middle|X,\vec{k}_1\right\rangle\left\langle X,\vec{k}_1\middle|J(y)\middle|Y,\vec{k}_2\right\rangle\left\langle Y,\vec{k}_2\middle|\chi^\dagger(0)\middle|\Omega\right\rangle \tag{3.75}$$

$$G^{(3)}_{\chi,J}(x_4,y_4,\vec{p},\vec{q}) := \int d^3x \int d^3y e^{-i\vec{p}\cdot\vec{x}} e^{i\vec{q}\cdot\vec{y}} G^{(3)}_{\chi,J}(x,y) tag3.76 \tag{3.76}$$

$$= \sum_{X,Y} e^{-E_{X,\vec{p}}x_4} e^{-\left(E_{Y,(\vec{p}-\vec{q})}-E_{X,\vec{p}}\right)y_4} g^{(3)}_{\chi J\chi^\dagger}\left[X,\vec{p};Y,(\vec{p}-\vec{q})\right]. \tag{3.77}$$

The same definitions have also been constructed for four–point correlators in §A.2, which in terms of

$$G^{(4)}_{\chi,J_1,J_2}(x,y,z,w) := \left\langle \chi(x) J_2(y) J_1(z) \chi^\dagger(w) \right\rangle \tag{3.78}$$

give

$$\begin{aligned} g^{(4)}_{\chi,J_1,J_2}\left[X,\vec{k}_1;Y,\vec{k}_2;Z,\vec{k}_3;x,y,z,w\right] := & \frac{1}{2E_{X,\vec{k}_1}}\frac{1}{2E_{Y,\vec{k}_2}}\frac{1}{2E_{Z,\vec{k}_3}} \\ & \times \left\langle \Omega\middle|\chi(x)\middle|X,\vec{k}_1\right\rangle\left\langle X,\vec{k}_1\middle|J_2(y)\middle|Y,\vec{k}_2\right\rangle \\ & \times \left\langle Y,\vec{k}_2\middle|J_1(z)\middle|Z,\vec{k}_3\right\rangle\left\langle Z,\vec{k}_3\middle|\chi^\dagger(w)\middle|\Omega\right\rangle. \end{aligned} \tag{3.79}$$

and

$$\begin{aligned} G^{(4)}_{\chi,J_1,J_2}(x_4,y_4,z_4,w_4,\vec{p},\vec{q}_1,\vec{q}_2) = & \int d^3x \int d^3y \int d^3z e^{-i\vec{p}\cdot(\vec{x}-\vec{w})} e^{i\vec{q}_2\cdot(\vec{y}-\vec{w})} e^{i\vec{q}_1\cdot(\vec{z}-\vec{w})} \\ & \times G^{(4)}_{\chi,J_1,J_2}(x,y,z,w). \end{aligned} \tag{3.80}$$

Useful also is a definition of (3.79) with no state specified in between currents

$$\begin{aligned} g^{(4,ph)}_{\chi J_i J_j \chi^\dagger}\left[X,\vec{k}_1;Z,\vec{k}_3;x,y,z,w\right] := \frac{1}{2E_{X,\vec{k}_1}}\frac{1}{2E_{Z,\vec{k}_3}} \\ \times\left\langle\Omega\middle|\chi(x)\middle|X,\vec{k}_1\right\rangle\left\langle X,\vec{k}_1\middle|J_2(y)J_1(z)\middle|Z,\vec{k}_3\right\rangle \\ \times\left\langle Z,\vec{k}_3\middle|\chi^\dagger(w)\middle|\Omega\right\rangle \end{aligned} \tag{3.81}$$

and current ordering swap

$$\begin{aligned} G^{(4)}_{\chi,J_{\{1},J_{2\}}}(x_4,y_4,z_4,w_4,\vec{p},\vec{q}_1,\vec{q}_2) := \frac{1}{2}\Big[\; G^{(4)}_{\chi,J_1,J_2}(x_4,y_4,z_4,w_4,\vec{p},\vec{q}_1,\vec{q}_2) \\ + G^{(4)}_{\chi,J_2,J_1}(x_4,y_4,z_4,w_4,\vec{p},\vec{q}_2,\vec{q}_1)\Big] \end{aligned} \tag{3.82}$$

where the momentum transfer q_1 and q_2 are properties of J_1 and J_2 rather than $y-w$ and $z-w$ respectively, which naturally arises from temporal integrals of time ordered pairs of currents.

One of the difficulties in calculating the three and four–point functions on the lattice arises from the fact that one has more than one temporal variable to deal with. For regular three–point functions inversions require either the source–sink or current–sink separation to be fixed for each simulation, requiring multiple simulations for different separations to determine adequate systematic control. In addition, the source–sink separation must be increased as the current must be inserted at a time the ground state dominates, which further decreases signal. In practice through prior knowledge of approximate required separations, and use of multiple simulations at different fixed separations this problem can be overcome.

However when we look at four–point functions there are now three different temporal separations, two of which must be fixed. First the source–sink separation must become even larger, which combined with the fact that one has to pick two separations ahead of time makes the calculation complicated. This is before the challenge presented converting Euclidean four–point function methods to their Minkowski counterparts [142, 143]. In this work we shall present new ways of calculating four–point functions §4.2.2 and use them to avoid this problem §7.

3.6 Hadron Spectroscopy

In §3.5 we defined correlators on the lattice, which we shall now use to demonstrate how to calculate pion and nucleon energies. In (3.70) we saw that any correlator comes with a tower of excited states, requiring us to fit our correlator at large source–sink separation x_4 to isolate the ground state. However except for the lowest energy hadronic state, the pion, fitting at large x_4 leads to fitting in areas of low signal–to–noise. The signal–to–noise for the nucleon n with N measurements has form [144]

$$\frac{\sigma_{G^{(2)}_\chi}}{G^{(2)}_\chi} \propto \frac{1}{\sqrt{N}} e^{\left(m_n-\frac{3}{2}m_\pi\right)x_4}. \tag{3.83}$$

To reduce the time required to saturate to the ground state, interpolators are smeared by replacing the delta function in (3.34) with an appropriate non–local function. It is expected that the ground state wave functions are approximately Gaussian, hence by tuning the smearing of the source, linking nearby lattice sites via some smooth function, to approximate the radius of our intended state we can fit earlier. The same step can be performed at the sink of the correlators, to further improve this method. Our method is to use gauge–invariant Jacobi smearing [145], with smearing tuned for the ground state nucleon size.

Much more sophisticated methods are possible, such as correlator matrix based techniques [146–150] that use multiple operators and smearing levels to construct almost perfect operators.

To drastically reduce the earlier onset of the signal–to–noise problem at higher momenta, modifying the smearing to better couple to high momentum states is also possible [151], but other methods have also been developed [152]

The two examples of two–point correlators we now present are of the pion §3.6.1 followed by the nucleon §3.6.2.

3.6.1 Example: Pion

As a consequence of spontaneous chiral symmetry breaking and the small explicit quark mass, the pion is a pseudo–Nambu–Goldstone boson. As the lowest mass hadronic state on the lattice, this means that it does not have problems with signal–to–noise, but instead the backwards propagating state affects our fits. The basic interpolator we can use to extract mesons is of the form

$$\chi_{f_1 f_2}(x) := \overline{q}_{f_1}(x)^{\alpha}_{a} \Gamma^{\alpha\beta} q_{f_2}(x)^{\beta}_{a} \tag{3.84}$$

for some γ_4–Hermitian (§C.2.3) element $\Gamma^{\alpha\beta}$ of the Clifford algebra .

By performing our calculation in the isospin–symmetric limit, the isospin triplet $\left(\pi^+, \pi^0, \pi^-\right)$ is mass degenerate, so we can work out pion masses by calculating any one of them. The π^+ interpolator has form

$$\chi_{\pi^+} = \overline{d}(x)^{\alpha}_{a} \gamma_5^{\alpha\beta} u(x)^{\beta}_{a}. \tag{3.85}$$

We note that under a parity transformation §3.3 our interpolator is transformed as

$$P\chi_{\pi^+}(\vec{x}, x_4) = -\chi_{\pi^+}(-\vec{x}, x_4). \tag{3.86}$$

If we restrict our case to $\vec{p} = 0$ then the mirroring of the spatial coordinates is not important, and the interpolator has parity of the pion state. Care has to be taken in analysis of non–zero momentum state parity mixing, especially for excited state analysis [147, 150].

We now construct our correlator from interpolator, using quark propagators. By using Wick's theorem on our correlator $G^{(2)}_{\chi}(x)$ we can construct our correlator in terms of quark propagators

$$\left\langle \chi_\pi(x) \chi^\dagger_\pi(0) \right\rangle = \langle \overline{d}(x)\gamma_5 \overbrace{u(x)\overline{u}(0)}\gamma_5 d(0) \rangle \tag{3.87}$$

which in terms of quark propagators (3.33) is

$$\left\langle \chi_\pi(x) \chi^\dagger_\pi(0) \right\rangle = -\langle \mathrm{tr}\left[\gamma_5 S_d(0,x) \gamma_5 S_u(x,0)\right] \rangle. \tag{3.88}$$

The problematic propagator is S_d, in order to calculate this correlator an all–to–all correlator is necessary, however due to the γ_5–Hermiticity (§C.2.4) of our quark propagators we can write this

$$S^\dagger_d(0,x) = \gamma_5 S_d(x,0) \gamma_5. \tag{3.89}$$

The momentum projected correlator form from this then has form

$$G^{(2)}_{\chi_\pi}\left(\vec{0}, x_4\right) = \sum_X g^{(2)}_{\chi_\pi}\left[X, \vec{0}\right] \left(e^{-E_{X,\vec{0}} x_4} + e^{-E_{X,\vec{0}}(T - x_4)}\right) \tag{3.90}$$

where the extra term when compared to (3.71) comes from the backwards propagating state introduced by the boundary conditions. We can rewrite the forwards and backwards propagating state together as a $\cosh$

$$G^{(2)}_{\chi_\pi}\left(\vec{0}, x_4\right) = \sum_X g^{(2)}_{\chi_\pi}\left[X, \vec{0}\right] e^{-E_{X,\vec{0}} \frac{T}{2}} \cosh\left[E_{X,\vec{0}}\left(x_4 - \frac{T}{2}\right)\right] \tag{3.91}$$

which for large enough x_4 and $T - x_4$ reduces to

$$G^{(2)}_{\chi_\pi}\left(\vec{0}, x_4\right) \to g^{(2)}_{\chi_\pi}\left[\pi\right] e^{-m_\pi \frac{T}{2}} \cosh\left[m_\pi\left(x_4 - \frac{T}{2}\right)\right]. \tag{3.92}$$

The fit is then guided by an effective mass ratio

$$R_{eff} = \ln\left[\frac{G^{(2)}_{\chi_\pi}(x_4)}{G^{(2)}_{\chi_\pi}(x_4+a)}\right] \tag{3.93}$$

which allows us to see visually when our fit is late enough for excited state artefacts.

We perform this calculation on our $\beta = 5.5$, $SU(3)_{flavour}$ symmetric, $32^3 \times 64$ ensemble from Table E.2. The results are taken from $N_s = 7001$ random sources evenly distributed over $N_{cfg} = 1763$ of the configurations, which accounts to roughly $N_{s/cfg} \approx 4$ sources per configuration. As we see in the correlator and effective mass Figure 3.6, with such high statistics, to have negligible systematic error from the excited states, a fairly late fitting range $x_4 \in [9, 55]$ had to be chosen. The resultant mass in lattice units is

$$am_\pi = 0.17534(23). \tag{3.94}$$

Scale setting §3.4 has been used on these lattice to calculate a [137, 139–141], which can use with appropriate factors of $\hbar c$ to get the corresponding pion mass in GeV

$$m_\pi = 0.467(12)\ \ GeV. \tag{3.95}$$

This is the simplest mass calculation possible on the lattice, which we shall build upon throughout this work.

3.6.2 Example: Nucleon

In §3.6.1, you might have noticed that we only formed our particle from quark propagators with single source locations. As the inversion is the most expensive part of the calculation, it is possible to calculate a nucleon correlator from the same quark propagators as well. A nucleon interpolator, naturally has three quark fields, with appropriate spin structure. The general form of particle operators are

$$\chi_{f_1 f_2 f_3}(x)^\alpha := e_{abc} q_{f_1}(x)^\alpha_a \left[q_{f_2}(x)^\beta_b \Gamma^{\beta\gamma} q_{f_3}(x)^\gamma_c\right] + \text{similar terms} \tag{3.96}$$

which ensures colour asymmetry and a spin degree of freedom. Just like in the pion case §3.6.1, the neutron and proton are mass degenerate in pure QCD with degenerate u and d quarks. One choice for nucleon interpolator is one that couples to the proton

$$\chi_N(x)^\alpha := e_{abc} u(x)^\alpha_a \left[u(x)^\beta_b (C\gamma_5)^{\beta\gamma} d(x)^\gamma_c\right]. \tag{3.97}$$

If we form a correlator then Wick's theorem will give us a correlator made up of quark propagators. The correlator

$$G^{(2)}_{\chi_N}(x)^{\alpha\beta} = \left\langle \chi_N(x)^\alpha \chi^\dagger_N(0)^\beta \right\rangle \tag{3.98}$$

has some Dirac dependency α and β, and use a projector $\Gamma^{\alpha\beta}$ (not the same Γ as (3.96)) in to project to the right spin and parity. For now we restrict ourselves to the unpolarised case, where we only project parity

$$\Gamma^\pm := \frac{1}{2}(I \pm \gamma_4). \tag{C.79}$$

We use both parity projections as the backwards propagating state will be the parity partner of the forward propagating state, so to maximise our statistics, we fit the forward propagating positive parity projected nucleon and the backwards propagating negative parity projected nucleon. With the forward and backward propagating states being much heavier, at early times, at least before the noise wall, the correlator is saturated by the forward propagating state. For sufficiently large x_4, but not too large we then have

$$G^{(2)}_{\chi_N}\left(\vec{0}, x_4\right) \to g^{(2)}_{\chi_N}[N]\, e^{-m_N x_4} \tag{3.99}$$

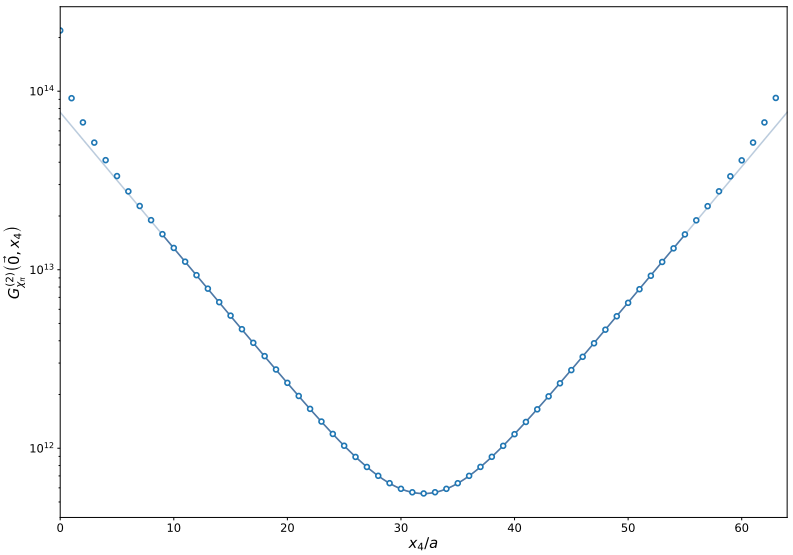

(a) Pion correlator

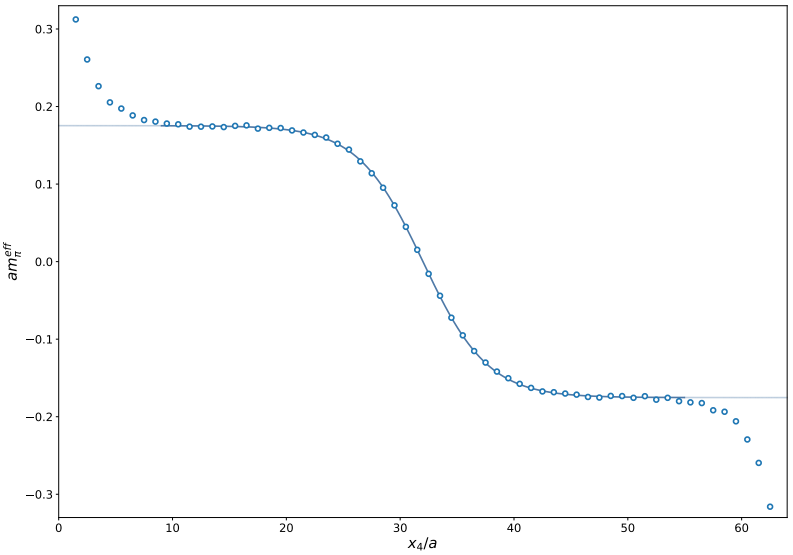

(b) Pion effective mass

Figure 3.6: Shown are the pion correlator (a) and corresponding effective mass (b). The data points are the raw correlator and effective mass values, shown with coshine fit of the correlator. The errors bars on the data points and the shaded error on the fit are too small to be visible by eye. The fit has chosen to be $x_4 \in [9, 55]$, as guided by χ^2_{dof} by varying start and end time symmetrically.

from which we can form an effective mass ratio (3.93), to fit on the same ensemble, from the same quark propagators as §3.6.1, which is summarised in Figure 3.7. We can clearly see the expected signal–to–noise reduction at large time steps in both the correlator and effective mass. The calculated nucleon mass in lattice and physical units respectively is then

$$am_N = 0.4698(56) \tag{3.100}$$

$$m_N = 1.250(39)\ \ GeV \tag{3.101}$$

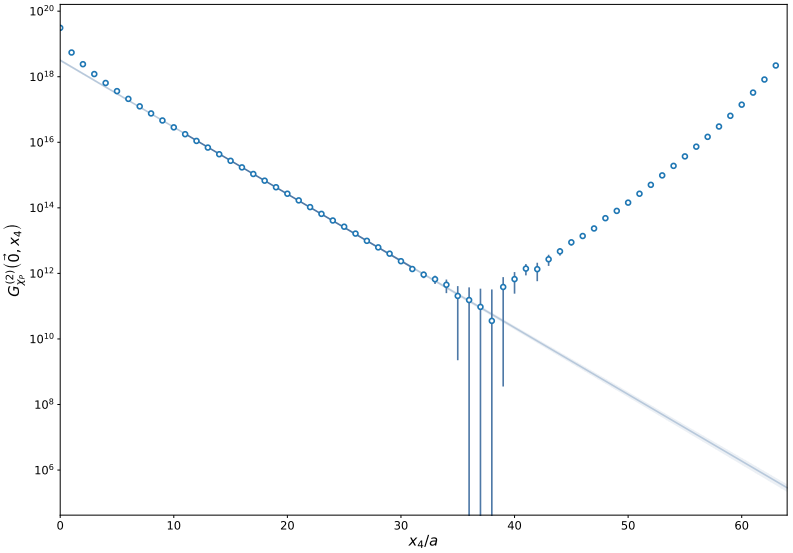

(a) Nucleon correlator

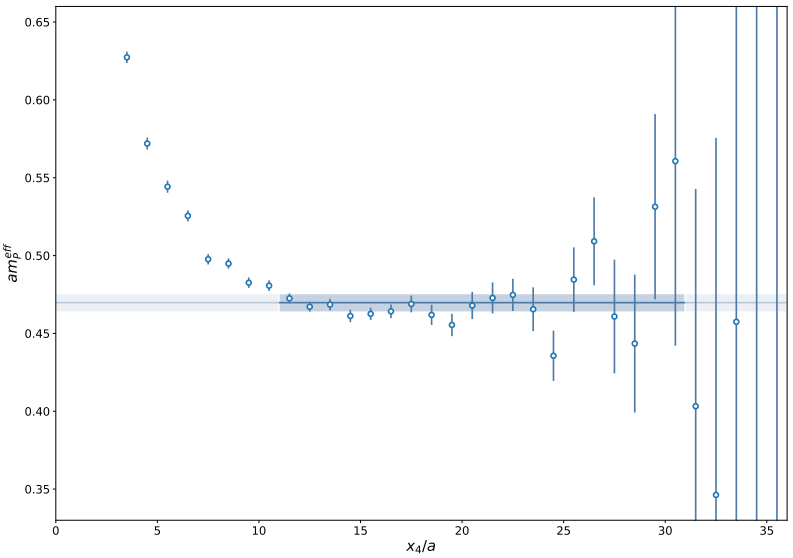

(b) Nucleon effective mass

Figure 3.7: The nucleon correlator (a) and corresponding effective mass (b). The data points are the raw correlator and effective mass values, where in both the line is an exponential fit to the correlator. Errors are shown to on standard deviation including shaded errors bars. From the slope of the backwards propagating state in (a), it is clear that the backwards propagating state has higher mass than the forward one, a consequence of the interpolator as described in the text. The fitting range $x_4 \in [11, 31]$, has been chosen by picking the starting slice such that χ^2_{dof} is close to 1.

3.7 Summary

In this chapter we presented the formulation of lattice QCD with various improvements that will be used in subsequent chapters. We showed how to extract masses from lattice two–point functions, which we shall use extensively throughout this work in all remaining chapters.

Chapter 4

The Feynman–Hellmann Theorem

The first formulations of the FHT were presented in the 1930s, first by Göttinger in 1932 [153], followed by Pauli in 1933 [154], finally in 1937 and 1939 by Hellmann [155] and Feynman [156] respectively, from which the theorem derives it's name. On the lattice it is widely used to calculate sigma terms [157–169]. Various similar methods are in use on the lattice as well, such as the background field method [170–172] to calculate polarisabilities [173–177], including with momentum transfer [178, 179], hadron vacuum polarisation [180], as well double–β decay [181, 182]. Other than the sigma terms, it has been used to calculate gluonic moments of the nucleon [183], by using anisotropy to provide an effective shift in the 'gluonic' magnetic and electric fields, via shifting temporal and spatial plaquettes. It can provide both connected [112, 184] and disconnected [185] form factors, as well as calculate renormalisation factors [186] and provide insight into resonance states [187].

The FHT is underpinned by a simple idea, a reverse of renormalisation. We renormalise a quantity, we expand it in terms of unperturbed diagrams, grouped by orders of powers of the introduced new Yukawa couplings. The renormalised propagators can be calculated to some order by calculating the appropriate diagrams. Suppose it were easier to calculate the renormalisation of a quantity, to all orders, than it was to calculate any of the diagrams involved in that renormalisation. If this were the case, then one could infer the value of the diagrams by changing the value of the coupling. The advantage of this is that one can calculate the renormalisation diagrams for non–perturbative objects, such as a low energy neutron or proton propagator. This is realised by introducing a weak external field to the Lagrangian and calculating the response to this field for various coupling strengths. We can determine the relation between a shift in Lagrangian to a shift in energy in multiple different spaces. In Quantum Mechanics (QM) the FHT relates shifts in the Hamiltonian, to matrix elements. In lattice QCD, this corresponds to shifts in Lagrangian density, with resultant shift in hadron energies.

Although alternative lattice approaches exist [188–191], we shall follow the approach of [112, 161, 183–185], deriving the FHT first for QM §4.1.1 and then extending it to second order §4.1.2. While the formulation of the theorem in QFT is possible [192], we shall derive it for path integrals directly §4.2, including to multiple forms at second order, each with their advantages and disadvantages. A short discussion is given on problems extending these results to a more general form §4.3. Finally we finish with some comments about Euclidean and Minkowski connections in §4.4.

4.1 For QM

The principle of the FHT is most easily shown in the form originally presented by Feynman, in QM, which we then compare to the result from perturbation theory.

To derive the FHT for QM we first define the unperturbed system of states as an inner–

product space, diagonalised with respect to the Hamiltonian H

$$\langle\psi_n|\psi_m\rangle = \delta_{nm} \tag{4.1}$$
$$H|\psi_n\rangle = E_n|\psi_n\rangle. \tag{4.2}$$

Suppose that one varies the Hamiltonian by some continuous parameter λ, the modified system obeys

$$\langle\psi_n(\lambda)|\psi_m(\lambda)\rangle_\lambda = \delta_{nm} \tag{4.3}$$
$$H(\lambda)|\psi_n(\lambda)\rangle_\lambda = E_n(\lambda)|\psi_n(\lambda)\rangle_\lambda \tag{4.4}$$

where the states and measure both vary with λ. The energy of any particle can easily be obtained by

$$E_n(\lambda) = \langle\psi_n(\lambda)|H(\lambda)|\psi_n(\lambda)\rangle_\lambda \tag{4.5}$$

which we shall now use to derive the FHT as presented in [156].

4.1.1 First Order

Taking derivatives of both sides of (4.5) gives

$$\frac{dE_n}{d\lambda} = \left\langle \psi_n(\lambda)\middle|\frac{dH}{d\lambda}\middle|\psi_n(\lambda)\right\rangle_\lambda + \left\langle \frac{d\psi_n}{d\lambda}\middle|H(\lambda)\middle|\psi_n(\lambda)\right\rangle_\lambda + \left\langle \psi_n(\lambda)\middle|H(\lambda)\middle|\frac{d\psi_n}{d\lambda}\right\rangle_\lambda \tag{4.6}$$

where we use shorthand

$$\left\langle \frac{d\psi_n}{d\lambda}\right| = \frac{d}{d\lambda}\langle\psi_n(\lambda)|_\lambda \tag{4.7}$$

Using (4.4) this becomes

$$\frac{dE_n}{d\lambda} = \left\langle \psi_n(\lambda)\middle|\frac{dH}{d\lambda}\middle|\psi_n(\lambda)\right\rangle_\lambda + E_n(\lambda)\left[\left\langle \frac{d\psi_n}{d\lambda}\middle|\psi_n(\lambda)\right\rangle_\lambda + \left\langle \psi_n(\lambda)\middle|\frac{d\psi_n}{d\lambda}\right\rangle_\lambda\right]. \tag{4.8}$$

The latter two terms can be transformed via the product rule giving

$$\frac{dE_n}{d\lambda} = \left\langle \psi_n(\lambda)\middle|\frac{dH}{d\lambda}\middle|\psi_n(\lambda)\right\rangle_\lambda + E_n(\lambda)\frac{d}{d\lambda}\langle\psi_n(\lambda)|\psi_n(\lambda)\rangle_\lambda \tag{4.9}$$

which disappears via (4.3) leaving just

$$\frac{dE_n}{d\lambda} = \left\langle \psi_n(\lambda)\middle|\frac{dH}{d\lambda}\middle|\psi_n(\lambda)\right\rangle_\lambda. \tag{4.10}$$

By evaluating this expression in the limit of $\lambda \to 0$, the FHT in QM is

$$\boxed{\left.\frac{dE_n}{d\lambda}\right|_{\lambda=0} = \left\langle \psi_n(0)\middle|\frac{dH}{d\lambda}\middle|\psi_n(0)\right\rangle_0} \tag{4.11}$$

It is obvious that this result is equivalent to the first order energy shift in perturbation theory for a linear shift in Lagrangian

$$\mathcal{L} = \mathcal{L}_0 + \lambda V. \tag{4.12}$$

Like perturbation theory it is straightforward to extend to the degenerate case.

4.1.2 Second Order

To extend this to second order we take the derivative of (4.10), dropping explicit λ dependence labels

$$\frac{d^2E_n}{d\lambda^2} = \left\langle \psi_n \middle| \frac{d^2H}{d\lambda^2} \middle| \psi_n \right\rangle + \left\langle \frac{d\psi_n}{d\lambda} \middle| \frac{dH}{d\lambda} \middle| \psi_n \right\rangle + \left\langle \psi_n \middle| \frac{dH}{d\lambda} \middle| \frac{d\psi_n}{d\lambda} \right\rangle. \tag{4.13}$$

The former term looks just like the (4.10) but for the quadratic shift of the Hamiltonian, so we first focus on the latter two terms. Inserting a complete set of states

$$\frac{d^2E_n}{d\lambda^2} = \left\langle \psi_n \middle| \frac{d^2H}{d\lambda^2} \middle| \psi_n \right\rangle + \sum_m \left[\left\langle \frac{d\psi_n}{d\lambda} \middle| \psi_m \right\rangle \left\langle \psi_m \middle| \frac{dH}{d\lambda} \middle| \psi_n \right\rangle + \left\langle \psi_n \middle| \frac{dH}{d\lambda} \middle| \psi_m \right\rangle \left\langle \psi_m \middle| \frac{d\psi_n}{d\lambda} \right\rangle \right]. \tag{4.14}$$

In the case where the $m = n$ the term inside the sum disappears. To see this consider the derivative

$$\frac{d}{d\lambda}\langle \psi_n | \psi_m \rangle = \left\langle \frac{d\psi_n}{d\lambda} \middle| \psi_m \right\rangle + \left\langle \psi_n \middle| \frac{d\psi_m}{d\lambda} \right\rangle = 0 \tag{4.15}$$

for any n and m including $n = m$, implying that those parts of (4.14) cancel, resulting in

$$\frac{d^2E_n}{d\lambda^2} = \left\langle \psi_n \middle| \frac{d^2H}{d\lambda^2} \middle| \psi_n \right\rangle + \sum_{m\neq n} \left[\left\langle \frac{d\psi_n}{d\lambda} \middle| \psi_m \right\rangle \left\langle \psi_m \middle| \frac{dH}{d\lambda} \middle| \psi_n \right\rangle + \left\langle \psi_n \middle| \frac{dH}{d\lambda} \middle| \psi_m \right\rangle \left\langle \psi_m \middle| \frac{d\psi_n}{d\lambda} \right\rangle \right]. \tag{4.16}$$

To relate the shifts of states to the shifts in the Hamiltonian we take the derivative of an off–diagonal term of the Hamiltonian $m \neq n$

$$\frac{d}{d\lambda}\langle \psi_m | H | \psi_n \rangle = \left\langle \psi_m \middle| \frac{dH}{d\lambda} \middle| \psi_n \right\rangle + \left\langle \frac{d\psi_m}{d\lambda} \middle| H \middle| \psi_n \right\rangle + \left\langle \psi_m \middle| H \middle| \frac{d\psi_n}{d\lambda} \right\rangle \tag{4.17}$$

which after applying H reduces to

$$\frac{d}{d\lambda}\langle \psi_m | H | \psi_n \rangle = \left\langle \psi_m \middle| \frac{dH}{d\lambda} \middle| \psi_n \right\rangle + E_n \left\langle \frac{d\psi_m}{d\lambda} \middle| \psi_n \right\rangle + E_m \left\langle \psi_m \middle| \frac{d\psi_n}{d\lambda} \right\rangle. \tag{4.18}$$

By utilising (4.15) the condition $m \neq n$ implies the LHS is 0, so the RHS can be rewritten, yielding

$$0 = \left\langle \psi_m \middle| \frac{dH}{d\lambda} \middle| \psi_n \right\rangle + [E_m - E_n] \left\langle \psi_m \middle| \frac{d\psi_n}{d\lambda} \right\rangle. \tag{4.19}$$

By using this with careful substitution of m and n of (4.16) we get

$$\frac{d^2E_n}{d\lambda^2} = \left\langle \psi_n \middle| \frac{d^2H}{d\lambda^2} \middle| \psi_n \right\rangle + \sum_{m\neq n} \frac{\left| \left\langle \psi_n \middle| \frac{dH}{d\lambda} \middle| \psi_m \right\rangle \right|^2}{E_m - E_n} \tag{4.20}$$

which evaluated at $\lambda = 0$ is the second order FHT for QM

$$\boxed{\left.\frac{d^2E_n}{d\lambda^2}\right|_{\lambda=0} = \left\langle \psi_n(0) \middle| \frac{d^2H}{d\lambda^2} \middle| \psi_n(0) \right\rangle_0 + \sum_{m\neq n} \frac{\left| \left\langle \psi_n(0) \middle| \frac{dH}{d\lambda} \middle| \psi_m(0) \right\rangle_0 \right|^2}{E_m(0) - E_n(0)}} \tag{4.21}$$

Like with the linear perturbation (4.12) we get the familiar result from perturbation theory, for the second order shift. This extension is useful as a demonstration of what we will find, but to fully understand what happens we would need to re–derive this for QFT, or GFT. A QFT formulation can be found in [192], so we shall focus on the latter with a direct derivation using path integrals.

4.2 For Path Integrals

To understand the structure of a modified Hamiltonian or equivalently action on the lattice, we need to know the form of the states on the lattice. We can infer this information by calculating the FHT for discretised path integrals. It will turn out that the second order shift requires knowledge of the first order amplitude shift. As it will be useful at second order to consider action modification involving multiple different currents at the same time, we consider action modifications with multiple λ. If we modify our action with an arbitrary number of λ

$$S \to S(\boldsymbol{\lambda}) := S(\lambda_1, \lambda_2, \cdots) \tag{4.22}$$

we can derive equivalent results for lattice QCD. Our normalisation condition (3.61) is now

$$\left\langle Y, \vec{k} \middle| X, \vec{p} \right\rangle_{\boldsymbol{\lambda}} := 2E_{X,\vec{p}}(\boldsymbol{\lambda})\delta_{XY}(2\pi)^3\delta^{(3)}\left(\vec{p} - \vec{k}\right) \tag{4.23}$$

and similar for the identity operator for the complete set of states (3.60). Starting with a basic momentum dependent two–point function in form (3.69) and (3.72) from §3.5.1 giving two equivalent forms of $G^{(2)}_{\chi\boldsymbol{\lambda}}(x_4, \vec{p})$, in terms of the vacuum expectation value this is

$$G^{(2)}_{\chi\boldsymbol{\lambda}}(x_4, \vec{p}) = \int d^3x e^{-i\vec{p}\cdot\vec{x}} \left\langle \chi(x)\chi^\dagger(0) \right\rangle_{\boldsymbol{\lambda}} \tag{4.24}$$

and in spectral form this is

$$G^{(2)}_{\chi\boldsymbol{\lambda}}(x_4, \vec{p}) = \sum_X g^{(2)}_{\chi\boldsymbol{\lambda}}\left[X, \vec{p}\right] e^{-E_{X,\vec{p}}(\boldsymbol{\lambda})x_4}. \tag{4.25}$$

By taking derivatives of both sides one can then relate energy shifts to matrix elements. We start with the first order case §4.2.1, before forming the extended FHT at second order §4.2.2, finally we shall look at a useful formulation of the second order FHT with momentum transfer §4.2.3, taking advantage of intricacies of the first order proof. Correlator notation used is defined in §3.5.

4.2.1 First Order

To start we construct pieces for a general shift in action. The action is present in the path integral (3.12) and partition function (3.13), the derivative of (4.24) is then

$$\frac{\partial}{\partial\lambda_i} G^{(2)}_{\chi\boldsymbol{\lambda}}(x) = \left\langle \frac{\partial}{\partial\lambda_i}\Big(\chi(x)\chi^\dagger(0)\Big) \right\rangle_{\boldsymbol{\lambda}} - \left\langle \chi(x)\chi^\dagger(0)\frac{\partial S}{\partial\lambda_i} \right\rangle_{\boldsymbol{\lambda}} + \left\langle \frac{\partial S}{\partial\lambda_i} \right\rangle_{\boldsymbol{\lambda}} \left\langle \chi(x)\chi^\dagger(0) \right\rangle_{\boldsymbol{\lambda}} \tag{4.26}$$

the first term being the shift in our choice of creation and annihilation operators with respect to λ_i, the second will contain the matrix element we are interested in. The third term is the vacuum correction to the operator in the second term arising from the partition function, which will vanish for our choice of operators, but is important later for §4.2.2. If one wanted to include this term one can simply redefine ones current in the Lagrangian to be vacuum subtracted. Under these assumptions we then have

$$\frac{\partial}{\partial\lambda_i} G^{(2)}_{\chi\boldsymbol{\lambda}}(x) = -\left\langle \chi(x)\chi^\dagger(0)\frac{\partial S}{\partial\lambda_i} \right\rangle_{\boldsymbol{\lambda}} \tag{4.27}$$

where we stress that there is implicit time ordering inside the expectation value. The derivative of (4.25) meanwhile reads

$$\frac{\partial}{\partial\lambda_i} G^{(2)}_{\chi\boldsymbol{\lambda}}(x_4, \vec{p}) = \sum_X \left[\frac{\partial}{\partial\lambda_i} g^{(2)}_{\chi\boldsymbol{\lambda}}\left[X, \vec{p}\right] - x_4 \frac{\partial E_{X,\vec{p}}}{\partial\lambda_i} g^{(2)}_{\chi\boldsymbol{\lambda}}\left[X, \vec{p}\right] \right] e^{-E_{X,\vec{p}}(\boldsymbol{\lambda})x_4}. \tag{4.28}$$

It is clear now that to find the energy shift one only needs to find the term in (4.27) which has the same energy dependency of the second term in (4.28), which we shall refer to as *time–enhancement* or x_4*–enhancement*. As it will turn out the important factor for this *time–enhancement* will be energy degeneracy, which we shall assume to be only in the case where the states are the same, in other words the states of interest for us to evaluate will be non–degenerate energy eigenstates, which we shall relax later. There are energy degenerate states in the tower of states, but these do not affect lower energy non–degenerate states in our proof, and so can be ignored. Despite only needing the x_4*–enhanced* terms for the first order FHT we will need the first term in (4.28) as well for calculation of the second order FHT in §4.2.2.

With a modification of our action of form

$$S(\lambda_i) = S(0) + \lambda_i \int d^4x e^{i\vec{q}_i\cdot\vec{x}} J_i(x) \tag{4.29}$$

for some translationally invariant J_i, then (4.27) becomes the time–ordered expression

$$\frac{\partial}{\partial\lambda_i} G^{(2)}_{\chi\boldsymbol{\lambda}}(x) = -\left\langle \int d^4y e^{i\vec{q}_i\cdot\vec{y}} T\left\{\chi(x)\chi^\dagger(0)J_i(y)\right\}\right\rangle_{\boldsymbol{\lambda}}. \tag{4.30}$$

First we resolve the time ordering

$$\begin{aligned} -\frac{\partial}{\partial\lambda_i} G^{(2)}_{\chi\boldsymbol{\lambda}}(x) = &\int_{x_4}^{\infty} dy_4 \int d^3y e^{i\vec{q}_i\cdot\vec{y}} \left\langle J_i(y)\chi(x)\chi^\dagger(0)\right\rangle_{\boldsymbol{\lambda}} \\ &+ \int_{0}^{x_4} dy_4 \int d^3y e^{i\vec{q}_i\cdot\vec{y}} \left\langle \chi(x)J_i(y)\chi^\dagger(0)\right\rangle_{\boldsymbol{\lambda}} \\ &+ \int_{-\infty}^{0} dy_4 \int d^3y e^{i\vec{q}_i\cdot\vec{y}} \left\langle \chi(x)\chi^\dagger(0)J_i(y)\right\rangle_{\boldsymbol{\lambda}}. \end{aligned} \tag{4.31}$$

The first and last terms look like re–definitions of our interpolating operator overlap with the vacuum, which makes us expect them to affect $\frac{\partial}{\partial\lambda_i} g^{(2)}_{\chi\boldsymbol{\lambda}}$, not the energy shift itself which we shall prove now. Dropping all explicit $\boldsymbol{\lambda}$ dependence labels, inserting a complete set of states on the first term of (4.31) gives

$$\sum_{X,Y} \int \frac{d^3k_1}{(2\pi)^3} \int \frac{d^3k_2}{(2\pi)^3} \int_{x_4}^{\infty} dy_4 \int d^3y e^{i\vec{q}_i\cdot\vec{y}} g^{(3)}_{J_i\chi\chi^\dagger}\left[X,\vec{k}_1;Y,\vec{k}_2;y,x,0\right]. \tag{4.32}$$

We then pull out the explicit operator space–time dependence referring to $k_1 = (\vec{k}, iE_{X,\vec{k}_1})$ and similar for k_2

$$\sum_{X,Y} \int \frac{d^3k_1}{(2\pi)^3} \int \frac{d^3k_2}{(2\pi)^3} \int_{x_4}^{\infty} dy_4 \int d^3y e^{ik_1\cdot y} e^{i(k_2-k_1)\cdot x} e^{i\vec{q}_i\cdot\vec{y}} g^{(3)}_{J_i\chi\chi^\dagger}\left[X,\vec{k}_1;Y,\vec{k}_2\right]. \tag{4.33}$$

which after integration of k_1 and $\vec{y}$ simplifies to

$$\sum_{X,Y} \int \frac{d^3k_2}{(2\pi)^3} \int_{x_4}^{\infty} dy_4 e^{-E_{X,-\vec{q}_i}y_4} e^{-\left(E_{Y,\vec{k}_2}-E_{X,-\vec{q}_i}\right)x_4} e^{i\vec{k}_2\cdot\vec{x}} g^{(3)}_{J_i\chi\chi^\dagger}\left[X,-\vec{q}_i;Y,\vec{k}_2\right]. \tag{4.34}$$

Now we can integrate over y_4

$$\sum_{X,Y} \int \frac{d^3k_2}{(2\pi)^3} \frac{1}{E_{X,-\vec{q}_i}} e^{-E_{Y,\vec{k}_2}x_4} e^{i\vec{k}_2\cdot\vec{x}} g^{(3)}_{J_i\chi\chi^\dagger}\left[X,-\vec{q}_i;Y,\vec{k}_2\right]. \tag{4.35}$$

In a similar fashion the last term of (4.31) becomes

$$\sum_{X,Y} \int \frac{d^3k_1}{(2\pi)^3} \frac{1}{E_{Y,\vec{q}_i}} e^{-E_{X,\vec{k}_1}x_4} e^{i\vec{k}_1\cdot\vec{x}} g^{(3)}_{\chi\chi^\dagger J_i}\left[X,\vec{k}_1;Y,\vec{q}_i\right] \tag{4.36}$$

which after reautorefling X, Y, k_1, k_2, as well as using $E_{X,\vec{q}_i} = E_{X,-\vec{q}_i}$ we can combine (4.35) and (4.36) into one expression

$$\sum_{X,Y} \int \frac{d^3k_1}{(2\pi)^3} \frac{1}{E_{Y,\vec{q}_i}} e^{-E_{X,\vec{k}_1} x_4} e^{i\vec{k}_1\cdot\vec{x}} \left(g^{(3)}_{\chi\chi^\dagger J_i} \left[X, \vec{k}_1; Y, \vec{q}_i \right] + g^{(3)}_{J_i\chi\chi^\dagger} \left[Y, -\vec{q}_i; X, \vec{k}_1 \right] \right). \tag{4.37}$$

As expected neither term has the required *time–enhancement*, instead they only provides a multiplicative factor to our vacuum overlap of χ.

We can insert a complete set of states into the middle term of (4.31)

$$\sum_{X,Y} \int \frac{d^3k_1}{(2\pi)^3} \int \frac{d^3k_2}{(2\pi)^3} \int_0^{x_4} dy_4 \int d^3y e^{i\vec{q}_i\cdot\vec{y}} g^{(3)}_{\chi J_i\chi^\dagger} \left[X, \vec{k}_1; Y, \vec{k}_2; x, y, 0 \right] \tag{4.38}$$

and pull out explicit space–time dependence

$$\sum_{X,Y} \int \frac{d^3k_1}{(2\pi)^3} \int \frac{d^3k_2}{(2\pi)^3} \int_0^{x_4} dy_4 \int d^3y e^{ik_1\cdot x} e^{i(k_2-k_1)\cdot y} e^{i\vec{q}_i\cdot\vec{y}} g^{(3)}_{\chi J_i\chi^\dagger} \left[X, \vec{k}_1; Y, \vec{k}_2 \right]. \tag{4.39}$$

Integration of $\vec{y}$ and $\vec{k}_2$ then reduces the momentum dependence to one momenta

$$\sum_{X,Y} \int \frac{d^3k_1}{(2\pi)^3} \int_0^{x_4} dy_4 e^{ik_1\cdot x} e^{-\left(E_{Y,(\vec{k}_1-\vec{q}_i)} - E_{X,\vec{k}_1}\right) y_4} g^{(3)}_{\chi J_i\chi^\dagger} \left[X, \vec{k}_1; Y, \left(\vec{k}_1 - \vec{q}_i\right) \right]. \tag{4.40}$$

Now we finally see a term with possible time dependence in the case where $E_{X,\vec{k}_1} = E_{Y,\vec{k}_1}$ then the integral over y_4 will give us an x_4*–enhancement*, for any degeneracies of energies. We can split our sum into degenerate and non–degenerate parts

$$\begin{aligned} &\sum_{\left\{X,Y | E_{X,\vec{k}_1} = E_{Y,(\vec{k}_1-\vec{q}_i)}\right\}} \int \frac{d^3k_1}{(2\pi)^3} \int_0^{x_4} dy_4 e^{ik_1\cdot x} g^{(3)}_{\chi J_i\chi^\dagger} \left[X, \vec{k}_1; Y, \left(\vec{k}_1 - \vec{q}_i\right) \right] \\ + &\sum_{\left\{X,Y | E_{X,\vec{k}_1} \neq E_{Y,(\vec{k}_1-\vec{q}_i)}\right\}} \int \frac{d^3k_1}{(2\pi)^3} \int_0^{x_4} dy_4 e^{ik_1\cdot x} g^{(3)}_{\chi J_i\chi^\dagger} \left[X, \vec{k}_1; Y, \left(\vec{k}_1 - \vec{q}_i\right) \right] e^{-\left(E_{Y,(\vec{k}_1-\vec{q}_i)} - E_{X,\vec{k}_1}\right) y_4}. \end{aligned} \tag{4.41}$$

By integrating over y_4 in each term the *time–enhancement* becomes apparent

$$\begin{aligned} &\sum_{\left\{X,Y | E_{X,\vec{k}_1} = E_{Y,(\vec{k}_1-\vec{q}_i)}\right\}} \int \frac{d^3k_1}{(2\pi)^3} e^{i\vec{k}_1\cdot\vec{x}} g^{(3)}_{\chi J_i\chi^\dagger} \left[X, \vec{k}_1; Y, \left(\vec{k}_1 - \vec{q}_i\right) \right] x_4 e^{-E_{X,\vec{k}_1} x_4} \\ + &\sum_{\left\{X,Y | E_{X,\vec{k}_1} \neq E_{Y,(\vec{k}_1-\vec{q}_i)}\right\}} \int \frac{d^3k_1}{(2\pi)^3} e^{i\vec{k}_1\cdot\vec{x}} g^{(3)}_{\chi J_i\chi^\dagger} \left[X, \vec{k}_1; Y, \left(\vec{k}_1 - \vec{q}_i\right) \right] \frac{e^{-E_{X,\vec{k}_1} x_4} - e^{-E_{Y,(\vec{k}_1-\vec{q}_i)} x_4}}{E_{Y,(\vec{k}_1-\vec{q}_i)} - E_{X,\vec{k}_1}}. \end{aligned} \tag{4.42}$$

This degeneracy yielding *time–enhancement* shall play out in a similar manner in our second order derivations. To finish this proof, we will need to match time dependence, which we do by relabelling terms to each include only a single exponential

$$\begin{aligned} &\sum_{\left\{X,Y | E_{X,\vec{k}_1} = E_{Y,(\vec{k}_1-\vec{q}_i)}\right\}} \int \frac{d^3k_1}{(2\pi)^3} e^{i\vec{k}_1\cdot\vec{x}} g^{(3)}_{\chi J_i\chi^\dagger} \left[X, \vec{k}_1; Y, \left(\vec{k}_1 - \vec{q}_i\right) \right] x_4 e^{-E_{X,\vec{k}_1} x_4} \\ + &\sum_{\left\{X,Y | E_{X,\vec{k}_1} \neq E_{Y,(\vec{k}_1-\vec{q}_i)}\right\}} \int \frac{d^3k_1}{(2\pi)^3} e^{i\vec{k}_1\cdot\vec{x}} g^{(3)}_{\chi J_i\chi^\dagger} \left[X, \vec{k}_1; Y, \left(\vec{k}_1 - \vec{q}_i\right) \right] \frac{e^{-E_{X,\vec{k}_1} x_4}}{E_{Y,(\vec{k}_1-\vec{q}_i)} - E_{X,\vec{k}_1}} \\ + &\sum_{\left\{X,Y | E_{X,(\vec{k}_1-\vec{q}_i)} \neq E_{Y,\vec{k}_1}\right\}} \int \frac{d^3k_1}{(2\pi)^3} e^{i\vec{k}_1\cdot\vec{x}} g^{(3)}_{\chi J_i\chi^\dagger} \left[Y, \vec{k}_1; X, \left(\vec{k}_1 - \vec{q}_i\right) \right] \frac{e^{-E_{X,(\vec{k}_1-\vec{q}_i)} x_4}}{E_{Y,\vec{k}_1} - E_{X,(\vec{k}_1-\vec{q}_i)}} \end{aligned} \tag{4.43}$$

Combining all these terms together we see the full shift in the two point correlator

$$\begin{aligned}-\frac{\partial}{\partial\lambda_i}G^{(2)}_{\chi\boldsymbol{\lambda}}(\vec{p}) = &\sum_{X,Y}\left(g^{(3)}_{\chi\chi^\dagger J_i}\left[X,\vec{p};Y,\vec{q}_i\right]+g^{(3)}_{J_i\chi\chi^\dagger}\left[Y,-\vec{q}_i;X,\vec{p}\right]\right)\frac{1}{E_{Y,\vec{q}_i}}e^{-E_{X,\vec{p}}x_4}\\ &+\sum_{\left\{X,Y|E_{X,\vec{p}}=E_{Y,(\vec{p}-\vec{q}_i)}\right\}} g^{(3)}_{\chi J_i\chi^\dagger}\left[X,\vec{p};Y,(\vec{p}-\vec{q}_i)\right]x_4e^{-E_{X,\vec{p}}x_4}\\ &+\sum_{\left\{X,Y|E_{X,\vec{p}}\neq E_{Y,(\vec{p}-\vec{q}_i)}\right\}} g^{(3)}_{\chi J_i\chi^\dagger}\left[X,\vec{p};Y,(\vec{p}-\vec{q}_i)\right]\frac{e^{-E_{X,\vec{p}}x_4}}{E_{Y,(\vec{p}-\vec{q}_i)}-E_{X,\vec{p}}}\\ &+\sum_{\left\{X,Y|E_{X,(\vec{p}-\vec{q}_i)}\neq E_{Y,\vec{p}}\right\}} g^{(3)}_{\chi J_i\chi^\dagger}\left[Y,\vec{p};X,(\vec{p}-\vec{q}_i)\right]\frac{e^{-E_{X,(\vec{p}-\vec{q}_i)}x_4}}{E_{Y,\vec{p}}-E_{X,(\vec{p}-\vec{q}_i)}}.\end{aligned} \tag{4.44}$$

Due to energy degeneracy requirements being dependent on $\vec{q}_i$ we look at the FHT in two cases; forward and non–forward.

Forward Case

Let us first consider the forward case, $\vec{q}_i=\vec{0}$. If we assume that there is no energy degeneracy in our state of interest then under our assumptions

$$E_{X,\vec{p}}=E_{Y,\vec{p}}\implies X=Y. \tag{4.45}$$

As the relationship (4.44) is true for all times we can use the time dependence to match up specific X terms. Consider the large time limits, only the lowest energy states contribute. By matching the lowest energy terms on both sides we can subtract these terms and repeat. In such a manner we can match up to arbitrary order. Alternatively one can think in terms of constructing perfect operators, in theory using correlator matrix techniques or similar other methods, an operator that overlaps with only one state can be constructed. Either way this matching allows us to get results, of a particular state X with momentum $\vec{p}$ for shift in overlap

$$\begin{aligned}-\frac{\partial}{\partial\lambda_i}g^{(2)}_{\chi\boldsymbol{\lambda}}\left[X,\vec{p}\right] = &\sum_{Y}\frac{1}{E_{Y,\vec{0}}(\boldsymbol{\lambda})}\left(g^{(3)}_{\chi\chi^\dagger J_i}\left[X,\vec{p};Y,\vec{0}\right]+g^{(3)}_{J_i\chi\chi^\dagger}\left[Y,\vec{0};X,\vec{p}\right]\right)\\ &+\sum_{Y\neq X}\frac{1}{E_{Y,\vec{p}}(\boldsymbol{\lambda})-E_{X,\vec{p}}(\boldsymbol{\lambda})}\left(g^{(3)}_{\chi J_i\chi^\dagger}\left[X,\vec{p};Y,\vec{p}\right]+g^{(3)}_{\chi J_i\chi^\dagger}\left[Y,\vec{p};X,\vec{p}\right]\right)\end{aligned} \tag{4.46}$$

and shift in energy

$$\frac{\partial E_{X,\vec{p}}}{\partial\lambda_i}=\frac{g^{(3)}_{\chi J_i\chi^\dagger\boldsymbol{\lambda}}\left[X,\vec{p};X,\vec{p}\right]}{g^{(2)}_{\chi\boldsymbol{\lambda}}\left[X,\vec{p}\right]}=\frac{1}{2E_{X,\vec{p}}(\boldsymbol{\lambda})}\langle X,\vec{p}|J_i(0)|X,\vec{p}\rangle_{\boldsymbol{\lambda}} \tag{4.47}$$

respectively.

By evaluating these expressions at $\lambda=0$ we then have the shift in the overlap

$$\boxed{\begin{aligned}-\frac{\partial}{\partial\lambda_i}g^{(2)}_{\chi\boldsymbol{\lambda}}\left[X,\vec{p}\right]\Big|_{\lambda=0} = &\sum_{Y}\frac{1}{E_{Y,\vec{0}}}\left(g^{(3)}_{\chi\chi^\dagger J_i}\left[X,\vec{p};Y,\vec{0}\right]+g^{(3)}_{J_i\chi\chi^\dagger}\left[Y,\vec{0};X,\vec{p}\right]\right)\\ &+\sum_{Y\neq X}\frac{1}{E_{Y,\vec{p}}-E_{X,\vec{p}}}\left(g^{(3)}_{\chi J_i\chi^\dagger}\left[X,\vec{p};Y,\vec{p}\right]+g^{(3)}_{\chi J_i\chi^\dagger}\left[Y,\vec{p};X,\vec{p}\right]\right)\end{aligned}} \tag{4.48}$$

while not explored in this work, also encodes interesting phenomena, the first term represents the redefinition of the two–point function overlap, while the second part matches an energy

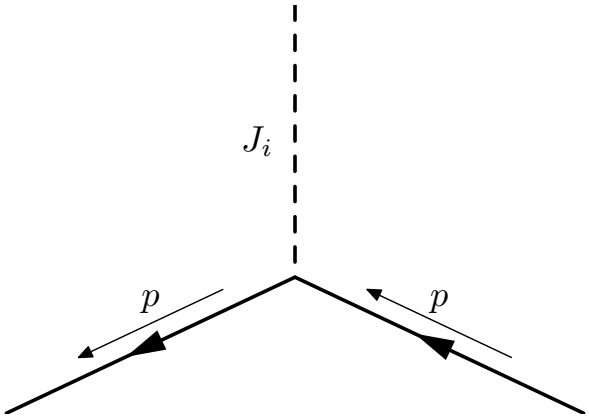

Figure 4.1: The diagram corresponding to the first order FHT without momentum transfer, that one can calculate from the first order energy shift

weighted set of all transition amplitudes from our state, which we shall see looks like a 'half–piece' of the second order FHT.

Now finally we can write the FHT for the linear forward case

$$\boxed{\left.\frac{\partial E_{X,\vec{p}}}{\partial \lambda_i}\right|_{\lambda=0} = \frac{1}{2E_{X,\vec{p}}}\langle X,\vec{p}|J_i(0)|X,\vec{p}\rangle_0.} \tag{4.49}$$

This relates the linear response of the energy, introduced by a weak external field to a matrix element of one operator, a three–point functions defined in §A.1 with external legs removed. This allows us to calculate simple vertex diagrams as depicted by Figure 4.1.

Non–forward Case

To extend this result to include the non–forward case we have to take care with our redefined states. Notice the energy exponential in the last term of (4.43), at non–zero q_i our states $|X,\vec{p}\rangle$ and $|X,(\vec{p}-\vec{q}_i)\rangle$ now mix. Before in our FHT we dealt with Hermitian modifications to our Hamiltonian, here the momentum transfer is off forward and so need to take a form which is Hermitian, by introducing a 'cosine' momentum transfer term

$$\frac{\partial S}{\partial \lambda_i} = \int d^4x \left(e^{i\vec{q}_i\cdot\vec{x}} + e^{-i\vec{q}_i\cdot\vec{x}}\right) J_i(x). \tag{4.50}$$

The observation that our states mix, is then equivalent to saying that we are dealing with energy degenerate states for non–zero x_4–*enhanced* terms. Assuming all energy degeneracies occur between the same state, choosing p and q_i such that $|\vec{p}| = |\vec{p}-\vec{q}_i|$, the term of interest is

$$\frac{\partial}{\partial \lambda_i} G^{(2)}_{\chi\boldsymbol{\lambda}}(\vec{p}) = -\sum_X g^{(3)}_{\chi J_i \chi^\dagger}\left[X,\vec{p};X,(\vec{p}-\vec{q}_i)\right] x_4 e^{-E_{X,\vec{p}}x_4} + \cdots \tag{4.51}$$

where the matrix element of each state $X,\vec{p}$ will mix with

$$g^{(3)}_{\chi J_i \chi^\dagger}\left[X,(\vec{p}-\vec{q}_i);X,\vec{p}\right] x_4 e^{-E_{X,(\vec{p}-\vec{q}_i)}x_4}. \tag{4.52}$$

To counteract this if we instead consider shifts of combinations of $G^{(2)}_{\chi\boldsymbol{\lambda}}(\vec{p})$ and $G^{(2)}_{\chi\boldsymbol{\lambda}}(\vec{p}-\vec{q}_i)$ then we can diagonalise the problem to get proper energy shifts free of mixing. Again assuming the degeneracy in energy only occurs in momenta, the combinations

$$\left|X^+_{\vec{q}_i},\vec{p}\right\rangle = \frac{1}{\sqrt{2}}\left(|X,\vec{p}\rangle + e^{i\theta}|X,(\vec{p}-\vec{q}_i)\rangle\right) \tag{4.53}$$

$$\left|X^-_{\vec{q}_i},\vec{p}\right\rangle = \frac{1}{\sqrt{2}}\left(|X,\vec{p}\rangle - e^{i\theta}|X,(\vec{p}-\vec{q}_i)\rangle\right) \tag{4.54}$$

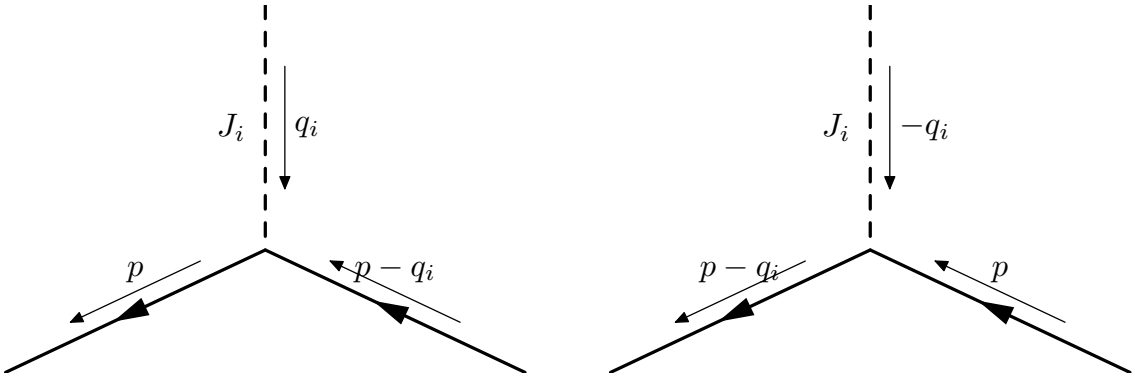

Figure 4.2: The diagrams corresponding to the first order FHT with momentum transfer, for the case where $|\vec{p}| = |\vec{p} - \vec{q}_i|$. Both these diagrams are calculated at once using the first order energy shift

will diagonalise the problem for any choice of relative phase $\theta \in \mathbb{R}$. While we are free to choose either of these states in our calculation, in practice we use the former with $\theta = 0$, as the latter will results in subtraction of correlation functions at $\lambda = 0$. The same setup occurs when the degenerate state is $|\vec{p}| = |\vec{p} + \vec{q}_i|$. Either way by modifying our completeness relation we then get matching

$$\boxed{\left.\frac{\partial E_{X^+_{\vec{q}_i},\vec{p}}}{\partial \lambda_i}\right|_{\lambda=0} = \frac{1}{2E_{X^+_{\vec{q}_i},\vec{p}}}\left\langle X^+_{\vec{q}_i},\vec{p}\right|J_i(0)\left|X^+_{\vec{q}_i},\vec{p}\right\rangle_0.} \tag{4.55}$$

Where the matrix element will be zero in cases where the magnitude of the momenta aren't the same. The corresponding diagrams are Figure 4.2. This form of the FHT is useful in reaching large momentum transfers on the lattice, but not the focus of this work, except for correct derivation of the second order FHT. For results using this to calculate electromagnetic form factors see [112], or for a more in depth derivation of the theory see [193].

In addition we can say something about the shift in the amplitude, but the strategy has to change. Consider the long time behaviour of the function, it will be dominated only by exponentials of the lowest energy states, that is the lowest energy states that mix with $|X, \vec{p}\rangle$ or $|X, (\vec{p} - \vec{q}_i)\rangle$. In our case, by construction, the lowest energy states are of momentum $\vec{p}$ and $\vec{p} - \vec{q}_i$ respectively. This means in this case, extraction of the shift in overlap is possible, through a similar manner as described in the forward case. For a second order derivation, we will avoid the Breit frame for intermediate momenta ($\frac{2p\cdot q}{Q^2} \neq 1$ in it's terminology), stepping around this issue.

4.2.2 Second Order

For the first order case we used first order derivatives of $G^{(2)}_{\chi\boldsymbol{\lambda}}(x_4, \vec{p})$ which we recall have forms

$$G^{(2)}_{\chi\boldsymbol{\lambda}}(x_4, \vec{p}) = \int d^3x e^{-i\vec{p}\cdot\vec{x}}\left\langle \chi(x)\chi^\dagger(0)\right\rangle_{\boldsymbol{\lambda}} \tag{4.24}$$

and

$$G^{(2)}_{\chi\boldsymbol{\lambda}}(x_4, \vec{p}) = \sum_X g^{(2)}_{\chi\boldsymbol{\lambda}}\left[X, \vec{p}\right] e^{-E_{X,\vec{p}}(\boldsymbol{\lambda})x_4}. \tag{4.25}$$

We shall now repeat the same steps, but taking second order derivatives of both sides, which

for (4.24) goes like

$$\begin{aligned}\frac{\partial^2}{\partial\lambda_i\partial\lambda_j}G^{(2)}_{\chi\boldsymbol{\lambda}}(x) = &\left\langle\frac{\partial^2}{\partial\lambda_i\partial\lambda_j}\Big(\chi(x)\chi^\dagger(0)\Big)\right\rangle_{\boldsymbol{\lambda}}\\ &-2\left\langle\frac{\partial}{\partial\lambda_i}\Big(\chi(x)\chi^\dagger(0)\Big)\frac{\partial S}{\partial\lambda_j}\right\rangle_{\boldsymbol{\lambda}}+2\left\langle\frac{\partial S}{\partial\lambda_j}\right\rangle_{\boldsymbol{\lambda}}\left\langle\frac{\partial}{\partial\lambda_i}\Big(\chi(x)\chi^\dagger(0)\Big)\right\rangle_{\boldsymbol{\lambda}}\\ &-2\left\langle\frac{\partial}{\partial\lambda_j}\Big(\chi(x)\chi^\dagger(0)\Big)\frac{\partial S}{\partial\lambda_i}\right\rangle_{\boldsymbol{\lambda}}+2\left\langle\frac{\partial S}{\partial\lambda_i}\right\rangle_{\boldsymbol{\lambda}}\left\langle\frac{\partial}{\partial\lambda_j}\Big(\chi(x)\chi^\dagger(0)\Big)\right\rangle_{\boldsymbol{\lambda}}\\ &-\left\langle\chi(x)\chi^\dagger(0)\frac{\partial^2 S}{\partial\lambda_i\partial\lambda_j}\right\rangle_{\boldsymbol{\lambda}}+\left\langle\chi(x)\chi^\dagger(0)\frac{\partial S}{\partial\lambda_i}\frac{\partial S}{\partial\lambda_j}\right\rangle_{\boldsymbol{\lambda}}\\ &-2\left\langle\frac{\partial S}{\partial\lambda_i}\right\rangle_{\boldsymbol{\lambda}}\left\langle\chi(x)\chi^\dagger(0)\frac{\partial S}{\partial\lambda_j}\right\rangle_{\boldsymbol{\lambda}}-2\left\langle\frac{\partial S}{\partial\lambda_j}\right\rangle_{\boldsymbol{\lambda}}\left\langle\chi(x)\chi^\dagger(0)\frac{\partial S}{\partial\lambda_i}\right\rangle_{\boldsymbol{\lambda}}\\ &+\left\langle\frac{\partial S}{\partial\lambda_i}\right\rangle_{\boldsymbol{\lambda}}\left\langle\frac{\partial S}{\partial\lambda_j}\right\rangle_{\boldsymbol{\lambda}}\left\langle\chi(x)\chi^\dagger(0)\right\rangle_{\boldsymbol{\lambda}}+\left\langle\frac{\partial^2 S}{\partial\lambda_i\partial\lambda_j}\right\rangle_{\boldsymbol{\lambda}}\left\langle\chi(x)\chi^\dagger(0)\right\rangle_{\boldsymbol{\lambda}}\end{aligned} \tag{4.56}$$

with the same conditions as before on (4.26), all derivatives of our interpolators are 0 by construction and the vacuum expectations values at first order are zero, giving a much reduced expression

$$\frac{\partial^2}{\partial\lambda_i\partial\lambda_j}G^{(2)}_{\chi\boldsymbol{\lambda}}(x) = -\left\langle\chi(x)\chi^\dagger(0)\frac{\partial^2 S}{\partial\lambda_i\partial\lambda_j}\right\rangle_{\boldsymbol{\lambda}}+\left\langle\chi(x)\chi^\dagger(0)\frac{\partial S}{\partial\lambda_i}\frac{\partial S}{\partial\lambda_j}\right\rangle_{\boldsymbol{\lambda}}+\left\langle\frac{\partial^2 S}{\partial\lambda_i\partial\lambda_j}\right\rangle_{\boldsymbol{\lambda}}\left\langle\chi(x)\chi^\dagger(0)\right\rangle_{\boldsymbol{\lambda}}. \tag{4.57}$$

The first term is present only if our action shift is not linear in $\boldsymbol{\lambda}$, relevant only for certain currents. It's derivation is identical to the first order case, but matching to the second order energy shift. The third term is a vacuum expectation value of a product of our currents and is non–zero in cases we shall look at, but as we only look at connected contributions at second order, neglect for this work. Finally the second order term, is the term we wish to extract. The derivative of (4.25) meanwhile becomes

$$\begin{aligned}\frac{\partial^2 G^{(2)}_{\chi\boldsymbol{\lambda}}}{\partial\lambda_i\partial\lambda_j}(x_4,\vec{p}) = \sum_X\Bigg[&\frac{\partial^2}{\partial\lambda_i\partial\lambda_j}g^{(2)}_{\chi\boldsymbol{\lambda}}[X,\vec{p}]\\ &-x_4\left(\frac{\partial}{\partial\lambda_i}g^{(2)}_{\chi\boldsymbol{\lambda}}[X,\vec{p}]\frac{\partial E_{X,\vec{p}}}{\partial\lambda_j}+\frac{\partial}{\partial\lambda_j}g^{(2)}_{\chi\boldsymbol{\lambda}}[X,\vec{p}]\frac{\partial E_{X,\vec{p}}}{\partial\lambda_i}+\frac{\partial^2 E_{X,\vec{p}}}{\partial\lambda_i\partial\lambda_j}g^{(2)}_{\chi\boldsymbol{\lambda}}[X,\vec{p}]\right)\\ &+x_4^2\frac{\partial E_{X,\vec{p}}}{\partial\lambda_i}\frac{\partial E_{X,\vec{p}}}{\partial\lambda_j}g^{(2)}_{\chi\boldsymbol{\lambda}}\Bigg]e^{-E_{X,\vec{p}}(\boldsymbol{\lambda})x_4}.\end{aligned} \tag{4.58}$$

There are now extra terms of different *time–enhancement* including two x_4*–enhanced* terms which have to be carefully treated. The first term of (4.57), the part of the first and all of the last term of (4.58) are expected terms purely from a redefinition of $\boldsymbol{\lambda}' = \sqrt{\boldsymbol{\lambda}}$. As part of our analysis we are only interested in energy shifts but one could possibly also look at the change in the overlap of the states, which as we shall see relates to transition amplitudes to all other states, with careful analysis of both $\frac{\partial}{\partial\lambda_i}G^{(2)}_{\chi\boldsymbol{\lambda}}$ and $\frac{\partial^2}{\partial\lambda_i\partial\lambda_j}G^{(2)}_{\chi\boldsymbol{\lambda}}$ could lead to useful results in the right circumstances.

This makes it clear also that in the x_4*–enhanced* terms we see terms involving first order terms. We modify the action with the form

$$S(\boldsymbol{\lambda}) = S(0)+\sum_i\lambda_i\int d^4x J_i(x) \tag{4.59}$$

where there is no momentum transfer. We then work with (4.57), the first term being identical formulation to the first order, and is usually 0. The latter term only becomes important for disconnected quantities, so we focus on the middle term. By substituting (4.59) into (4.57) we obtain

the expression

$$\frac{\partial^2}{\partial\lambda_i\partial\lambda_j}G^{(2)}_{\chi\boldsymbol{\lambda}}(x)=\left\langle\int d^4y\int d^4zT\left\{\chi(x)\chi^\dagger(0)J_i(y)J_j(z)\right\}\right\rangle_{\boldsymbol{\lambda}} \tag{4.60}$$

which we can split into 12 explicitly time ordered terms

$$\begin{aligned}\frac{\partial^2}{\partial\lambda_i\partial\lambda_j}G^{(2)}_{\chi\boldsymbol{\lambda}}(x)=&\int_{-\infty}^{0}dy_4\int_{-\infty}^{y_4}dz_4\int d^3y\int d^3z\Big\langle\chi(x)\chi^\dagger(0)J_i(y)J_j(z)+(i\leftrightarrow j)\Big\rangle_{\boldsymbol{\lambda}}\\&+\int_{0}^{x_4}dy_4\int_{-\infty}^{0}dz_4\int d^3y\int d^3z\Big\langle\chi(x)J_i(y)\chi^\dagger(0)J_j(z)+(i\leftrightarrow j)\Big\rangle_{\boldsymbol{\lambda}}\\&+\int_{x_4}^{\infty}dy_4\int_{-\infty}^{0}dz_4\int d^3y\int d^3z\Big\langle J_i(y)\chi(x)\chi^\dagger(0)J_j(z)+(i\leftrightarrow j)\Big\rangle_{\boldsymbol{\lambda}}\\&+\int_{0}^{x_4}dy_4\int_{0}^{y_4}dz_4\int d^3y\int d^3z\Big\langle\chi(x)J_i(y)J_j(z)\chi^\dagger(0)+(i\leftrightarrow j)\Big\rangle_{\boldsymbol{\lambda}}\\&+\int_{x_4}^{\infty}dy_4\int_{0}^{x_4}dz_4\int d^3y\int d^3z\Big\langle J_i(y)\chi(x)J_j(z)\chi^\dagger(0)+(i\leftrightarrow j)\Big\rangle_{\boldsymbol{\lambda}}\\&+\int_{x_4}^{\infty}dy_4\int_{x_4}^{y_4}dz_4\int d^3y\int d^3z\Big\langle J_i(y)J_j(z)\chi(x)\chi^\dagger(0)+(i\leftrightarrow j)\Big\rangle_{\boldsymbol{\lambda}}.\end{aligned} \tag{4.61}$$

We now systematically work through each line, one by one, inserting complete sets of states, starting with the first, third and last line. The first part of the first line is

$$\begin{aligned}&\sum_{X,Y,Z}\int\frac{d^3k_1}{(2\pi)^3}\int\frac{d^3k_2}{(2\pi)^3}\int\frac{d^3k_3}{(2\pi)^3}\int_{-\infty}^{0}dy_4\int_{-\infty}^{y_4}dz_4\int d^3y\int d^3z\\&\qquad\times g^{(4)}_{\chi\chi^\dagger J_iJ_j}\left[X,\vec{k}_1;Y,\vec{k}_2;Z,\vec{k}_3;x,0,y,z\right].\end{aligned} \tag{4.62}$$

Using translational–invariance to pull the explicit space–time dependence out of $g^{(4)}_{\chi\chi^\dagger J_iJ_j}$, with $k_1=\left(\vec{k}_1,iE_{X,\vec{k}_1}\right)$, and similar for k_2 and k_3

$$\begin{aligned}&\sum_{X,Y,Z}\int\frac{d^3k_1}{(2\pi)^3}\int\frac{d^3k_2}{(2\pi)^3}\int\frac{d^3k_3}{(2\pi)^3}\int_{-\infty}^{0}dy_4\int_{-\infty}^{y_4}dz_4\int d^3y\int d^3z\\&\qquad\times e^{ik_1\cdot x}e^{i(k_3-k_2)\cdot y}e^{-ik_3\cdot z}g^{(4)}_{\chi\chi^\dagger J_iJ_j}\left[X,\vec{k}_1;Y,\vec{k}_2;Z,\vec{k}_3\right].\end{aligned} \tag{4.63}$$

We can then perform all the spatial integrals reducing the expression to

$$\sum_{X,Y,Z}\int\frac{d^3k_1}{(2\pi)^3}\int_{-\infty}^{0}dy_4\int_{-\infty}^{y_4}dz_4e^{-E_{X,\vec{k}_1}x_4}e^{-\left(E_{Z,\vec{0}}-E_{Y,\vec{0}}\right)y_4}e^{E_{Z,\vec{0}}z_4}e^{i\vec{k}_1\cdot\vec{x}}g^{(4)}_{\chi\chi^\dagger J_iJ_j}\left[X,\vec{k}_1;Y,\vec{0};Z,\vec{0}\right] \tag{4.64}$$

which after integration of the temporal integrals reduces to

$$\sum_{X,Y,Z}\int\frac{d^3k_1}{(2\pi)^3}e^{i\vec{k}_1\cdot\vec{x}}\frac{1}{E_{Y,\vec{0}}E_{Z,\vec{0}}}g^{(4)}_{\chi\chi^\dagger J_iJ_j}\left[X,\vec{k}_1;Y,\vec{0};Z,\vec{0}\right]e^{-E_{X,\vec{k}_1}x_4}. \tag{4.65}$$

The other five terms have the same results, hence after relabelling states we get

$$\begin{aligned}\sum_{X,Y,Z}\int\frac{d^3k_1}{(2\pi)^3}\frac{1}{E_{Y,\vec{0}}E_{Z,\vec{0}}}e^{-E_{X,\vec{k}_1}x_4}e^{i\vec{k}_1\cdot\vec{x}}\Big(&g^{(4)}_{\chi\chi^\dagger J_iJ_j}\left[X,\vec{k}_1;Y,\vec{0};Z,\vec{0}\right]+g^{(4)}_{\chi\chi^\dagger J_jJ_i}\left[X,\vec{k}_1;Y,\vec{0};Z,\vec{0}\right]\\&+g^{(4)}_{J_iJ_j\chi\chi^\dagger}\left[Y,\vec{0};Z,\vec{0};X,\vec{k}_1\right]+g^{(4)}_{J_jJ_i\chi\chi^\dagger}\left[Y,\vec{0};Z,\vec{0};X,\vec{k}_1\right]\\&+g^{(4)}_{J_i\chi\chi^\dagger J_j}\left[Y,\vec{0};X,\vec{k}_1;Z,\vec{0}\right]+g^{(4)}_{J_j\chi\chi^\dagger J_i}\left[Y,\vec{0};X,\vec{k}_1;Z,\vec{0}\right]\Big).\end{aligned} \tag{4.66}$$

These terms just look like a second order multiplicative factor for our vacuum overlap with χ, contributing only to $\frac{\partial^2}{\partial\lambda_i\partial\lambda_j}g^{(2)}_{\chi\boldsymbol{\lambda}}$. If we then turn our attention to the second and second to last term of (4.61), we can use (4.35) to see that

$$\int_{-\infty}^{0} dz_4 \int d^3z \Big\langle \chi(x)J_i(y)\chi^\dagger(0)J_j(z)\Big\rangle = \sum_Z \frac{1}{E_{Z,\vec{0}}}\Big\langle\Omega\Big|\chi(x)J_i(y)\chi^\dagger(0)\Big|Z,\vec{0}\Big\rangle\Big\langle Z,\vec{0}\Big|J_j(0)\Big|\Omega\Big\rangle. \tag{4.67}$$

We can then use (4.41) to get

$$\begin{aligned}
&\sum_{X,Z}\frac{1}{E_{Z,\vec{0}}}\int\frac{d^3k_1}{(2\pi)^3}e^{i\vec{k}_1\cdot\vec{x}}g^{(4)}_{\chi J_i\chi^\dagger J_j}\Big[X,\vec{k}_1;X,\vec{k}_1;Z,\vec{0}\Big]\,x_4e^{-E_{X,\vec{k}_1}x_4}\\
&+\sum_{\{X,Y,Z|X\neq Y\}}\frac{1}{E_{Z,\vec{0}}}\int\frac{d^3k_1}{(2\pi)^3}e^{i\vec{k}_1\cdot\vec{x}}g^{(4)}_{\chi J_i\chi^\dagger J_j}\Big[X,\vec{k}_1;Y,\vec{k}_1;Z,\vec{0}\Big]\frac{e^{-E_{X,\vec{k}_1}x_4}}{E_{Y,\vec{k}_1}-E_{X,\vec{k}_1}}\\
&+\sum_{\{X,Y,Z|X\neq Y\}}\frac{1}{E_{Z,\vec{0}}}\int\frac{d^3k_1}{(2\pi)^3}e^{i\vec{k}_1\cdot\vec{x}}g^{(4)}_{\chi J_i\chi^\dagger J_j}\Big[Y,\vec{k}_1;X,\vec{k}_1;Z,\vec{0}\Big]\frac{e^{-E_{X,\vec{k}_1}x_4}}{E_{Y,\vec{k}_1}-E_{X,\vec{k}_1}}
\end{aligned} \tag{4.68}$$

for one order of J_i and J_j, and

$$\begin{aligned}
&\sum_{X,Z}\frac{1}{E_{Z,\vec{0}}}\int\frac{d^3k_1}{(2\pi)^3}e^{i\vec{k}_1\cdot\vec{x}}g^{(4)}_{J_j\chi J_i\chi^\dagger}\Big[Z,\vec{0}X,\vec{k}_1;X,\vec{k}_1;\Big]\,x_4e^{-E_{X,\vec{k}_1}x_4}\\
&+\sum_{\{X,Y,Z|X\neq Y\}}\frac{1}{E_{Z,\vec{0}}}\int\frac{d^3k_1}{(2\pi)^3}e^{i\vec{k}_1\cdot\vec{x}}g^{(4)}_{J_j\chi J_i\chi^\dagger}\Big[Z,\vec{0};X,\vec{k}_1;Y,\vec{k}_1\Big]\frac{e^{-E_{X,\vec{k}_1}x_4}}{E_{Y,\vec{k}_1}-E_{X,\vec{k}_1}}\\
&+\sum_{\{X,Y,Z|X\neq Y\}}\frac{1}{E_{Z,\vec{0}}}\int\frac{d^3k_1}{(2\pi)^3}e^{i\vec{k}_1\cdot\vec{x}}g^{(4)}_{J_j\chi J_i\chi^\dagger}\Big[Z,\vec{0};Y,\vec{k}_1;X,\vec{k}_1\Big]\frac{e^{-E_{X,\vec{k}_1}x_4}}{E_{Y,\vec{k}_1}-E_{X,\vec{k}_1}}
\end{aligned} \tag{4.69}$$

for the other ordering. Naturally as before the terms not x_4–*enhanced* will contribute to $\frac{\partial^2}{\partial\lambda_i\partial\lambda_j}g^{(2)}_{\chi\boldsymbol{\lambda}}$, but it is not yet clear where the x_4–*enhanced* terms will contribute, however they look like terms contributing to $\frac{\partial}{\partial\lambda_i}g^{(2)}_{\chi\boldsymbol{\lambda}}\frac{\partial E_{X,\vec{p}}}{\partial\lambda_j}+\frac{\partial}{\partial\lambda_j}g^{(2)}_{\chi\boldsymbol{\lambda}}\frac{\partial E_{X,\vec{p}}}{\partial\lambda_i}$, but to verify this we need also the terms in the last term of (4.61), the fourth line. The first term of this line, after inserting complete sets of states becomes

$$\begin{aligned}
&\sum_{X,Y,Z}\int\frac{d^3k_1}{(2\pi)^3}\int\frac{d^3k_2}{(2\pi)^3}\int\frac{d^3k_3}{(2\pi)^3}\int_0^{x_4}dy_4\int_0^{y_4}dz_4\int d^3y\int d^3z\\
&\qquad\times g^{(4)}_{\chi J_iJ_j\chi^\dagger}\Big[X,\vec{k}_1;Y,\vec{k}_2;Z,\vec{k}_3;x,y,z,0\Big].
\end{aligned} \tag{4.70}$$

Using translational invariance and defining $k_1=\Big(\vec{k}_1,iE_{X,\vec{k}_1}\Big)$, with similar definition for k_2 and k_3, this becomes

$$\begin{aligned}
&\sum_{X,Y,Z}\int\frac{d^3k_1}{(2\pi)^3}\int\frac{d^3k_2}{(2\pi)^3}\int\frac{d^3k_3}{(2\pi)^3}\int_0^{x_4}dy_4\int_0^{y_4}dz_4\int d^3y\int d^3z\\
&\qquad\times e^{ik_1\cdot x}e^{i(k_2-k_1)\cdot y}e^{i(k_3-k_2)\cdot z}g^{(4)}_{\chi J_iJ_j\chi^\dagger}\Big[X,\vec{k}_1;Y,\vec{k}_2;Z,\vec{k}_3\Big]
\end{aligned} \tag{4.71}$$

which becomes

$$\begin{aligned}
&\sum_{X,Y,Z}\int\frac{d^3k_1}{(2\pi)^3}\int_0^{x_4}dy_4\int_0^{y_4}dz_4e^{-E_{X,\vec{k}_1}x_4}e^{-\left(E_{Y,\vec{k}_1}-E_{X,\vec{k}_1}\right)y_4}e^{-\left(E_{Z,\vec{k}_1}-E_{Y,\vec{k}_1}\right)z_4}e^{i\vec{k}_1\cdot\vec{x}}\\
&\qquad\times g^{(4)}_{\chi J_iJ_j\chi^\dagger}\Big[X,\vec{k}_1;Y,\vec{k}_1;Z,\vec{k}_1\Big].
\end{aligned} \tag{4.72}$$

Under the same assumption as before where energy degeneracies occur only when the states are the same we can split this sum up into components using the identity

$$\begin{aligned}\sum_{X,Y,Z} f(X,Y,Z) = &\sum_{X} f(X,X,X) \\ &+ \sum_{\{X,Y|X\neq Y\}} \left(f(X,X,Y)+f(X,Y,X)+f(Y,X,X)\right) \\ &+ \sum_{\{X,Y,Z|X\neq Y,Y\neq Z,Z\neq X\}} f(X,Y,Z).\end{aligned} \tag{4.73}$$

Taking the case where all states are the same in (4.72), we get immediately

$$\sum_X \int \frac{d^3k_1}{(2\pi)^3} e^{i\vec{k}_1\cdot\vec{x}} g^{(4)}_{\chi J_i J_j \chi^\dagger}\left[X,\vec{k}_1;X,\vec{k}_1;X,\vec{k}_1\right]\frac{1}{2}x_4^2 e^{-E_{X,\vec{k}_1}x_4}. \tag{4.74}$$

For the term where there are no degeneracies we get, after relabelling

$$\begin{aligned}&\sum_{\{X,Y,Z|X\neq Y,Y\neq Z,Z\neq X\}} \int \frac{d^3k_1}{(2\pi)^3} e^{i\vec{k}_1\cdot\vec{x}} e^{-E_{X,\vec{k}_1}x_4} \\ &\Bigg[\frac{1}{E_{Z,\vec{k}_1}-E_{Y,\vec{k}_1}}\left(\frac{1}{E_{Y,\vec{k}_1}-E_{X,\vec{k}_1}}-\frac{1}{E_{Z,\vec{k}_1}-E_{X,\vec{k}_1}}\right) g^{(4)}_{\chi J_i J_j\chi^\dagger}\left[X,\vec{k}_1;Y,\vec{k}_1;Z,\vec{k}_1\right] \\ &+\frac{1}{\left(E_{Y,\vec{k}_1}-E_{X,\vec{k}_1}\right)\left(E_{Z,\vec{k}_1}-E_{X,\vec{k}_1}\right)} g^{(4)}_{\chi J_i J_j\chi^\dagger}\left[Y,\vec{k}_1;X,\vec{k}_1;Z,\vec{k}_1\right] \\ &-\frac{1}{\left(E_{Y,\vec{k}_1}-E_{X,\vec{k}_1}\right)\left(E_{Z,\vec{k}_1}-E_{X,\vec{k}_1}\right)} g^{(4)}_{\chi J_i J_j\chi^\dagger}\left[Z,\vec{k}_1;Y,\vec{k}_1;X,\vec{k}_1\right]\Bigg]\end{aligned} \tag{4.75}$$

another term contributing purely to the $\frac{\partial^2}{\partial\lambda_i\partial\lambda_j}g^{(2)}_{\chi\boldsymbol{\lambda}}$ term. The terms which are degenerate in the middle state gives, after relabelling

$$\begin{aligned}&\sum_{\{X,Y|X\neq Y\}} \int \frac{d^3k_1}{(2\pi)^3} e^{i\vec{k}_1\cdot\vec{x}} e^{-E_{X,\vec{k}_1}x_4} \\ &\Bigg[\frac{x_4}{E_{Y,\vec{k}_1}-E_{X,\vec{k}_1}}\left(g^{(4)}_{\chi J_i J_j\chi^\dagger}\left[X,\vec{k}_1;X,\vec{k}_1;Y,\vec{k}_1\right]+g^{(4)}_{\chi J_i J_j\chi^\dagger}\left[Y,\vec{k}_1;X,\vec{k}_1;X,\vec{k}_1\right]\right) \\ &+\frac{1}{\left(E_{Y,\vec{k}_1}-E_{X,\vec{k}_1}\right)^2}\left(g^{(4)}_{\chi J_i J_j\chi^\dagger}\left[X,\vec{k}_1;X,\vec{k}_1;Y,\vec{k}_1\right]+g^{(4)}_{\chi J_i J_j\chi^\dagger}\left[Y,\vec{k}_1;X,\vec{k}_1;X,\vec{k}_1\right]\right) \\ &-\frac{1}{\left(E_{Y,\vec{k}_1}-E_{X,\vec{k}_1}\right)^2}\left(g^{(4)}_{\chi J_i J_j\chi^\dagger}\left[Y,\vec{k}_1;Y,\vec{k}_1;X,\vec{k}_1\right]+g^{(4)}_{\chi J_i J_j\chi^\dagger}\left[X,\vec{k}_1;Y,\vec{k}_1;Y,\vec{k}_1\right]\right)\Bigg].\end{aligned} \tag{4.76}$$

The final term then is the one where the ingoing and outgoing states are degenerate, which after

relabelling yields

$$\sum_{\{X,Y|X\neq Y\}}\int\frac{d^3k_1}{(2\pi)^3}e^{i\vec{k}_1\cdot\vec{x}}e^{-E_{X,\vec{k}_1}x_4}\left[\frac{1}{\left(E_{Y,\vec{k}_1}-E_{X,\vec{k}_1}\right)^2}\left(g^{(4)}_{\chi J_iJ_j\chi^\dagger}\left[Y,\vec{k}_1;X,\vec{k}_1;Y,\vec{k}_1\right]-g^{(4)}_{\chi J_iJ_j\chi^\dagger}\left[X,\vec{k}_1;Y,\vec{k}_1;X,\vec{k}_1\right]\right)-\frac{x_4}{E_{Y,\vec{k}_1}-E_{X,\vec{k}_1}}g^{(4)}_{\chi J_iJ_j\chi^\dagger}\left[X,\vec{k}_1;Y,\vec{k}_1;X,\vec{k}_1\right]\right]. \tag{4.77}$$

There are also the terms with $(i\leftrightarrow j)$, but we now have all the terms to determine the second order energy and vacuum overlap shift. By adding all these expression together and subtracting the known parts (4.46), (4.47) from (4.58) we get relations

$$\begin{aligned}\frac{\partial^2}{\partial\lambda_i\partial\lambda_j}g^{(2)}_{\chi\boldsymbol{\lambda}}[X,\vec{p}] &= \sum_{Y,Z}\frac{1}{E_{Y,\vec{0}}E_{Z,\vec{0}}}\begin{pmatrix} g^{(4)}_{\chi\chi^\dagger J_iJ_j}\left[X,\vec{p};Y,\vec{0};Z,\vec{0}\right]\\ +g^{(4)}_{J_iJ_j\chi\chi^\dagger}\left[Y,\vec{0};Z,\vec{0};X,\vec{p}\right]\\ +g^{(4)}_{J_i\chi\chi^\dagger J_j}\left[Y,\vec{0};X,\vec{p};Z,\vec{0}\right]\end{pmatrix}\\ &+\sum_{\{Y,Z|X\neq Y\}}\frac{1}{E_{Z,\vec{0}}(E_{Y,\vec{p}}-E_{X,\vec{p}})}\begin{pmatrix} g^{(4)}_{\chi J_i\chi^\dagger J_j}\left[X,\vec{p};Y,\vec{p};Z,\vec{0}\right]\\ +g^{(4)}_{\chi J_i\chi^\dagger J_j}\left[Y,\vec{p};X,\vec{p};Z,\vec{0}\right]\\ +g^{(4)}_{J_j\chi J_i\chi^\dagger}\left[Z,\vec{0};X,\vec{p};Y,\vec{p}\right]\\ +g^{(4)}_{J_j\chi J_i\chi^\dagger}\left[Z,\vec{0};Y,\vec{p};X,\vec{p}\right]\end{pmatrix}\\ &+\sum_{\{Y|X\neq Y\}}\frac{1}{\left(E_{Y,\vec{p}}-E_{X,\vec{p}}\right)^2}\begin{pmatrix} g^{(4)}_{\chi J_iJ_j\chi^\dagger}[X,\vec{p};X,\vec{p};Y,\vec{p}]\\ +g^{(4)}_{\chi J_iJ_j\chi^\dagger}[Y,\vec{p};X,\vec{p};X,\vec{p}]\\ -g^{(4)}_{\chi J_iJ_j\chi^\dagger}[Y,\vec{p};Y,\vec{p};X,\vec{p}]\\ -g^{(4)}_{\chi J_iJ_j\chi^\dagger}[X,\vec{p};Y,\vec{p};Y,\vec{p}]\end{pmatrix}\\ &+\sum_{\{X,Y|X\neq Y\}}\frac{1}{\left(E_{Y,\vec{p}}-E_{X,\vec{p}}\right)^2}\begin{pmatrix} g^{(4)}_{\chi J_iJ_j\chi^\dagger}[Y,\vec{p};X,\vec{p};Y,\vec{p}]\\ -g^{(4)}_{\chi J_iJ_j\chi^\dagger}[X,\vec{p};Y,\vec{p};X,\vec{p}]\end{pmatrix}\\ &+\sum_{\{Y,Z|X\neq Y,Y\neq Z,Z\neq X\}}\frac{1}{\left(E_{Y,\vec{p}}-E_{X,\vec{p}}\right)\left(E_{Z,\vec{p}}-E_{X,\vec{p}}\right)}\begin{pmatrix} g^{(4)}_{\chi J_iJ_j\chi^\dagger}[Y,\vec{p};X,\vec{p};Z,\vec{p}]\\ -g^{(4)}_{\chi J_iJ_j\chi^\dagger}[Z,\vec{p};Y,\vec{p};X,\vec{p}]\end{pmatrix}\\ &+\sum_{\{Y,Z|X\neq Y,Y\neq Z,Z\neq X\}}\frac{1}{E_{Z,\vec{p}}-E_{Y,\vec{p}}}\frac{1}{E_{Y,\vec{p}}-E_{X,\vec{p}}}g^{(4)}_{\chi J_iJ_j\chi^\dagger}[X,\vec{p};Y,\vec{p};Z,\vec{p}]\\ &-\sum_{\{Y,Z|X\neq Y,Y\neq Z,Z\neq X\}}\frac{1}{E_{Z,\vec{p}}-E_{Y,\vec{p}}}\frac{1}{E_{Z,\vec{p}}-E_{X,\vec{p}}}g^{(4)}_{\chi J_iJ_j\chi^\dagger}[X,\vec{p};Y,\vec{p};Z,\vec{p}]\\ &+(i\leftrightarrow j)\end{aligned} \tag{4.78}$$

and

$$\frac{\partial^2E_{X,\vec{p}}}{\partial\lambda_i\partial\lambda_j}=\sum_{Y\neq X}\frac{\langle X,\vec{p}|J_i(0)|Y,\vec{p}\rangle_{\boldsymbol{\lambda}}\langle Y,\vec{p}|J_j(0)|X,\vec{p}\rangle_{\boldsymbol{\lambda}}+(i\leftrightarrow j)}{E_{X,\vec{p}}E_{Y,\vec{p}}\left(E_{X,\vec{p}}-E_{Y,\vec{p}}\right)} \tag{4.79}$$

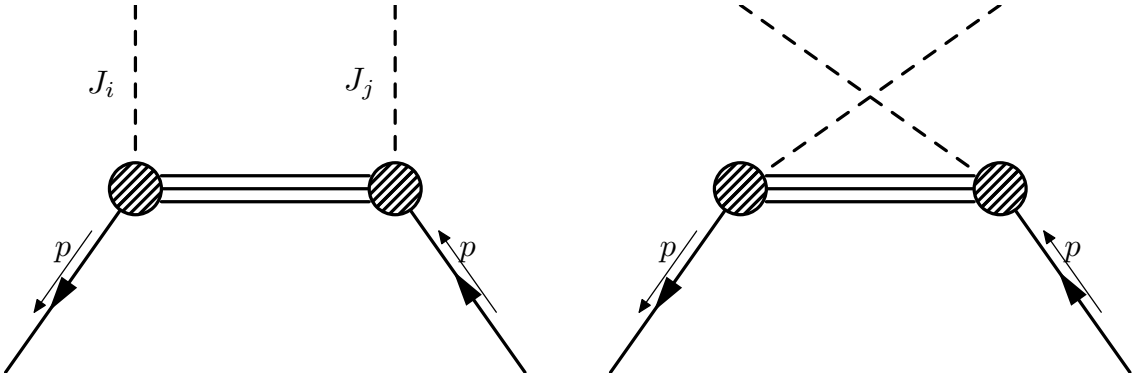

Figure 4.3: The two diagrams corresponding to the second order FHT without momentum transfer, that one can calculate from the second order energy shift

which at $\boldsymbol{\lambda} = \vec{0}$ gives

$$\boxed{\left.\frac{\partial^2 E_{X,\vec{p}}}{\partial\lambda_i\partial\lambda_j}\right|_{\boldsymbol{\lambda}=\vec{0}} = \sum_{Y\neq X}\frac{\langle X,\vec{p}|J_i(0)|Y,\vec{p}\rangle_0\langle Y,\vec{p}|J_j(0)|X,\vec{p}\rangle_0 + (i\leftrightarrow j)}{E_{X,\vec{p}}E_{Y,\vec{p}}\big(E_{X,\vec{p}}-E_{Y,\vec{p}}\big)}} \tag{4.80}$$

This relates the second order shift to the sum of transition amplitudes, or diagrams that look like Figure 4.3, which as in perturbation theory the denominator forces the lowest energy state to have negative second order energy shift. We can also state this in convenient form when working with only one current inserted twice

$$\boxed{\left.\frac{\partial^2 E_{X,\vec{p}}}{\partial{\lambda_i}^2}\right|_{\boldsymbol{\lambda}=\vec{0}} = 2\sum_{Y\neq X}\frac{\langle X,\vec{p}|J_i(0)|Y,\vec{p}\rangle_0\langle Y,\vec{p}|J_i(0)|X,\vec{p}\rangle_0}{E_{X,\vec{p}}E_{Y,\vec{p}}\big(E_{X,\vec{p}}-E_{Y,\vec{p}}\big)}} \tag{4.81}$$

This relation allows us to verify the second order FHT on the lattice. It doesn't however allow us to calculate the *Thomson term* of the Compton amplitude as it has some intricacies in order of limits $p\cdot q\to 0$ and $Q^2\to 0$ as discussed at length in §8.

4.2.3 Second Order in Partial Hilbert Space

By limiting ourselves to no momentum transfer, the lack of state mixing allowed us to easily compare terms that are x_4*-enhanced*, separating $\frac{\partial}{\partial\lambda_i}g^{(2)}_{\chi\boldsymbol{\lambda}}\frac{\partial E_{X,\vec{p}}}{\partial\lambda_j} + \frac{\partial}{\partial\lambda_j}g^{(2)}_{\chi\boldsymbol{\lambda}}\frac{\partial E_{X,\vec{p}}}{\partial\lambda_i}$ terms from our signal term $\frac{\partial^2 E_{X,\vec{p}}}{\partial\lambda_i\partial\lambda_j}$. Now in theory this should still be possible with momentum transfer, however the state mixing means that our technique of subtracting the known terms to get the second order energy shift via identifying shifts of specific states, requires us to diagonalise our system after the mixing at the interpolator vacuum overlap level, rather than just the energy level.

This small change has a far larger effect than is first apparent, the new eigenvectors of that system involve all momenta $\vec{p}\pm n\vec{q}_i$ for all $n\in\mathbb{Z}$, rather than just one other state. For more discussion on this problem see §4.3.1.

There is another way around this however, by restricting ourselves to cases where $\frac{\partial E_{X,\vec{p}}}{\partial\lambda_i}=0$, we do not need to separate time enhanced terms in our matrix elements, instead we can equate those with the second order energy shift directly.

We take the modified action with momentum transfer like (4.50), but with uniform momentum transfer

$$S(\boldsymbol{\lambda}) = S(0) + \lambda_i\int d^4x\Big(e^{i\vec{q}\cdot\vec{x}}+e^{-i\vec{q}\cdot\vec{x}}\Big)J_i(x). \tag{4.82}$$

and start by matching the remaining terms of (4.58) to

$$\frac{\partial^2 G^{(2)}_{\chi\boldsymbol{\lambda}}}{\partial\lambda_i\partial\lambda_j}(x_4,\vec{p}) = \sum_X\left[\frac{\partial^2}{\partial\lambda_i\partial\lambda_j}g^{(2)}_{\chi\boldsymbol{\lambda}}[X,\vec{p}] - x_4\frac{\partial^2 E_{X,\vec{p}}}{\partial\lambda_i\partial\lambda_j}g^{(2)}_{\chi\boldsymbol{\lambda}}[X,\vec{p}]\right]e^{-E_{X,\vec{p}}(\boldsymbol{\lambda})x_4}. \tag{4.83}$$

As we see we only have one term that is time enhanced, this means that after identifying terms with this enhancement, only mixing in energy shifts can occur. We will see however that in our case this does not occur, as our momentum transfer is uniform. We take the same equation as the momentum–transfer free case (4.57) and as before focus only on the middle term of (4.60), which we can divide into explicit time orderings (4.61). The only part that has *time–enhancement* parts that remains under the condition that $\frac{\partial E_{X,\vec{p}}}{\partial \lambda_i} = 0$ can be written

$$\int_0^{x_4} dy_4 \int_0^{x_4} dz_4 \int d^3y \int d^3z \left(e^{i\vec{q}\cdot\vec{y}} + e^{-i\vec{q}\cdot\vec{y}}\right)\left(e^{i\vec{q}\cdot\vec{z}} + e^{-i\vec{q}\cdot\vec{z}}\right)\left\langle \chi(x) T\left\{J_i(y)J_j(z)\right\}\chi^\dagger(0)\right\rangle_{\boldsymbol{\lambda}} \tag{4.84}$$

with both orderings of the current in one integral. We then perform the same steps as we did for no momentum transfer and insert a complete set of states, but not in between the current

$$\begin{aligned}\sum_{X,Z}\int \frac{d^3k_1}{(2\pi)^3}\int \frac{d^3k_3}{(2\pi)^3}\int_0^{x_4} dy_4 \int_0^{x_4} dz_4 \int d^3y \int d^3z \left(e^{i\vec{q}\cdot\vec{y}} + e^{-i\vec{q}\cdot\vec{y}}\right)\left(e^{i\vec{q}\cdot\vec{z}} + e^{-i\vec{q}\cdot\vec{z}}\right) \\ \times g^{(4,ph)}_{\chi J_i J_j \chi^\dagger}\left[X,\vec{k}_1;Z,\vec{k}_3;x,y,z,0\right]\end{aligned} \tag{4.85}$$

before pulling out explicit space–time dependence for ingoing and outgoing states

$$\begin{aligned}\sum_{X,Z}\int \frac{d^3k_1}{(2\pi)^3}\int \frac{d^3k_3}{(2\pi)^3}\int_0^{x_4} dy_4 \int_0^{x_4} dz_4 \int d^3y \int d^3z \left(e^{i\vec{q}\cdot\vec{y}} + e^{-i\vec{q}\cdot\vec{y}}\right)\left(e^{i\vec{q}\cdot\vec{z}} + e^{-i\vec{q}\cdot\vec{z}}\right) \\ \times e^{ik_1\cdot x} e^{i(k_3-k_1)\cdot z} g^{(4,ph)}_{\chi J_i J_j \chi^\dagger}\left[X,\vec{k}_1;Z,\vec{k}_3;0,y-z,0,0\right]\end{aligned} \tag{4.86}$$

with $k_1 = \left(\vec{k}_1, iE_{X,\vec{k}_1}\right)$ and similar for k_3. We now wish to perform one of the integrals, by changing system of coordinates to separate the integral inside the matrix element to the one outside. One of the coordinate transformations to do this is

$$Y = y - z \tag{4.87}$$

$$Z = y + z \tag{4.88}$$

which we can use to rewrite our expression as

$$\begin{aligned}\sum_{X,Z}\int \frac{d^3k_1}{(2\pi)^3}\int \frac{d^3k_3}{(2\pi)^3}\int_0^{x_4} dy_4 \int_0^{x_4} dz_4 \frac{1}{2^3}\int d^3Y \int d^3Z \left[\left(e^{i\vec{q}\cdot\vec{Y}} + e^{-i\vec{q}\cdot\vec{Y}}\right) + \left(e^{i\vec{q}\cdot\vec{Z}} + e^{-i\vec{q}\cdot\vec{Z}}\right)\right] \\ \times e^{ik_1\cdot x} e^{i(k_3-k_1)\cdot(Z-Y)/2} g^{(4,ph)}_{\chi J_i J_j \chi^\dagger}\left[X,\vec{k}_1;Z,\vec{k}_3;0,Y,0,0\right]\end{aligned} \tag{4.89}$$

where we haven't yet rewritten the temporal integrals in the new coordinate system. We can now however perform the $\vec{Z}$ spatial integral and look for *time–enhancement*. If we restrict ourselves to the case where $|\vec{p}| \neq |\vec{p} \pm 2\vec{q}|$ then the $\vec{Z}$ part of the momentum transfer will not give any *time–enhancement* and hence we get

$$\begin{aligned}\sum_{X,Z}\int \frac{d^3k_1}{(2\pi)^3}\int_0^{x_4} dy_4 \int_0^{x_4} dz_4 \int d^3Y \left(e^{i\vec{q}\cdot\vec{Y}} + e^{-i\vec{q}\cdot\vec{Y}}\right) \\ \times e^{ik_1\cdot x} e^{-\left(E_{Z,\vec{k}_1} - E_{X,\vec{k}_1}\right)(Z_4-Y_4)/2} g^{(4,ph)}_{\chi J_i J_j \chi^\dagger}\left[X,\vec{k}_1;Z,\vec{k}_1;0,Y,0,0\right]\end{aligned} \tag{4.90}$$

which clearly only has no *time–enhancement* for non–degenerate energy $E_{Z,\vec{k}_1} \neq E_{X,\vec{k}_1}$ or with our assumptions $X \neq Z$ which reduces us to

$$\sum_{X}\int \frac{d^3k_1}{(2\pi)^3}\int_0^{x_4} dy_4 \int_0^{x_4} dz_4 \int d^3Y \left(e^{i\vec{q}\cdot\vec{Y}} + e^{-i\vec{q}\cdot\vec{Y}}\right) e^{ik_1\cdot x} g^{(4,ph)}_{\chi J_i J_j \chi^\dagger}\left[X,\vec{k}_1;X,\vec{k}_1;0,Y,0,0\right]. \tag{4.91}$$

This leaves only the temporal integral which becomes

$$\int_0^{x_4} dy_4 \int_0^{x_4} dz_4 = \frac{1}{2}\int_{-x_4}^{0} dY_4 \int_{-Y_4}^{2x_4+Y_4} dZ_4 + \int_0^{x_4} dY_4 \int_{Y_4}^{2x_4-Y_4} dZ_4. \tag{4.92}$$

Our expression inside the integral is independent of Z_4 so we can freely perform that integral

$$\int_0^{x_4} dy_4 \int_0^{x_4} dz_4 = \int_{-x_4}^{x_4} dY_4 x_4 - |Y_4|\,. \tag{4.93}$$

giving us

$$\sum_X \int \frac{d^3k_1}{(2\pi)^3} \int_{-x_4}^{x_4} dY_4 (x_4 - |Y_4|) \int d^3Y \left(e^{i\vec{q}\cdot\vec{Y}} + e^{-i\vec{q}\cdot\vec{Y}}\right) e^{ik_1\cdot x} g^{(4,ph)}_{\chi J_i J_j \chi^\dagger} \left[X, \vec{k}_1; X, \vec{k}_1; 0, Y, 0, 0\right]. \tag{4.94}$$

The variable $|Y_4|$ is the current separation, which in small current separation expansions becomes negligible. Performing momentum projection and equating with (4.83) we then get

$$\frac{\partial^2 E_{X,\vec{p}}}{\partial\lambda_i \partial\lambda_j} = -\frac{\left\langle X,\vec{p}\right| \int_{-x_4}^{x_4} dY_4 \int d^3Y \left(e^{i\vec{q}\cdot\vec{Y}} + e^{-i\vec{q}\cdot\vec{Y}}\right) T\left\{J_i(Y) J_j(0)\right\} \left|X,\vec{p}\right\rangle_{\boldsymbol{\lambda}}}{2E_{X,\vec{p}}}. \tag{4.95}$$

Due to the exponential suppression on currents outside the range $|Y_4| \in [0, x_4]$, we can rewrite the integral

$$\frac{\partial^2 E_{X,\vec{p}}}{\partial\lambda_i \partial\lambda_j} = -\frac{\left\langle X,\vec{p}\right| \int d^4Y \left(e^{i\vec{q}\cdot\vec{Y}} + e^{-i\vec{q}\cdot\vec{Y}}\right) T\left\{J_i(Y) J_j(0)\right\} \left|X,\vec{p}\right\rangle_{\boldsymbol{\lambda}}}{2E_{X,\vec{p}}} \tag{4.96}$$

which finally gives us the partial Hilbert space FHT

$$\boxed{\left.\frac{\partial^2 E_{X,\vec{p}}}{\partial\lambda_i \partial\lambda_j}\right|_{\boldsymbol{\lambda}=\vec{0}} = -\frac{\left\langle X,\vec{p}\right| \int d^4y \left(e^{i\vec{q}\cdot\vec{y}} + e^{-i\vec{q}\cdot\vec{y}}\right) T\left\{J_i(y) J_j(0)\right\} \left|X,\vec{p}\right\rangle_0}{2E_{X,\vec{p}}}} \tag{4.97}$$

We now have a form of equation that looks like the Compton amplitude, the sum of four diagrams at once Figure 4.4, which we use in §7 and §8.

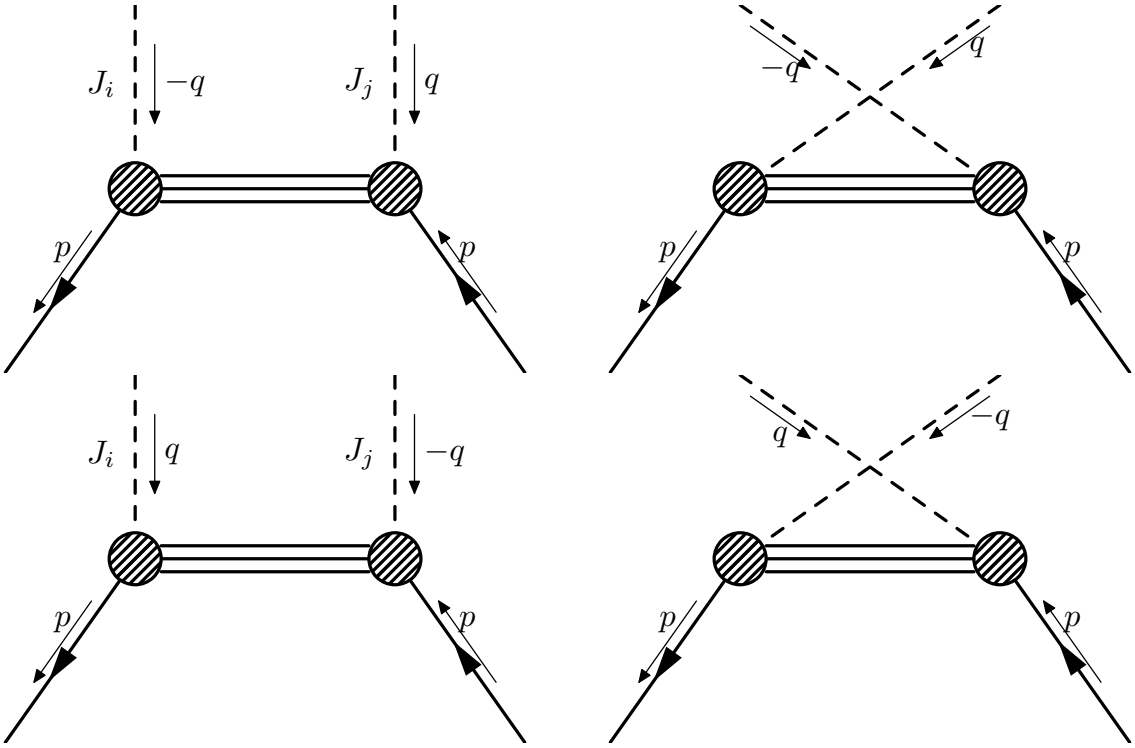

Figure 4.4: The four diagrams corresponding to the second order FHT with momentum transfer, that one can calculate the sum or difference thereof with 'cosine' and 'sin' overall momentum transfer combinations

4.3 State Mixing

So far we have only considered one case where states are non–degenerate, or degenerate only in pairs of momenta. We showed the prescription for a simple energy degeneracy (4.53), and (4.54), that diagonalises the system with respect to energy shifts. Other degeneracies could occur, for instance between unpolarised and polarised states, in this case though as the spin operator commutes with the modified Lagrangian and hence it is possible to resolve the degeneracy with additional operators. While it is very easy to avoid the same energy degeneracies in the second order case, with two different $\vec{q}_i$ it is very easy to arrive at cases where this can become problematic. This problem of differing momentum transfers $\vec{q}_i$ could allow one to generalise the extraction of the Compton amplitude (§7) to GPDs. To form a complete derivation of §4.2.2, with momentum transfer, one would need to account for state mixing at the overlap level.

4.3.1 Diagonalising Mixed Momentum States

In the off–forward FHT, we diagonalised energy degeneracies by redefining the states of interest in a closed form (4.53). Such a procedure could be generalised to more complicated degeneracies, like those that can occur between four states at $\vec{p}\cdot\vec{q}/Q^2 = 2$. However the mixing that occurs in the correlator is more problematic, a state $\vec{p}$ mixes to first order in λ with $\vec{p}+\vec{q}$ and $\vec{p}-\vec{q}$, regardless of energy. To illustrate the severity of the problem consider a system with degenerate

eigenvalues λ perturbed, represented by the $N \times N$ matrix

$$\begin{bmatrix} \lambda & \delta & 0 & & \delta \\ \delta & \lambda & \delta & & \\ 0 & \delta & \lambda & \ddots & \\ & & \ddots & \ddots & \delta \\ \delta & & & \delta & \lambda \end{bmatrix}. \tag{4.98}$$

This is a symmetric circulant matrix which has eigenvectors and eignevalues

$$e'_j = \frac{1}{\sqrt{N}}\left(1, R_j, R_j^2, \cdots, R_j^{N-1}\right) \tag{4.99}$$

$$\lambda'_j = \lambda + \delta\left(R_j + R_j^{N-1}\right) \tag{4.100}$$

where R_j is an N^{th} root of unity

$$R_j = e^{2\pi i \frac{j}{N}}. \tag{4.101}$$

We note that the eigenvalues are all real in such a perturbation and have a simple form, however the eigenvectors of the mixed states all depend on every other eigenvector. In fact if we take this to second order having two more diagonals non–zero, the mixing in this system, the eigenvectors, do not change at all. In the case where the diagonals are no longer constant, as is the case for our system, these expressions would get even more complicated. Nonetheless the problem remains that our matrix splits into equivalence classes $\vec{p} + n\vec{q}$ for $n \in \mathbb{Z}$, where the eigenvectors mix with every other state in their equivalence class, in a similar fashion to (4.98).

On a finite lattice this problem could possibly be circumvented by working with very large $\vec{q}$, which would reduce the size of each equivalence class to a manageable level. As the focus of the work is just on the energy shifts, we do not explore further. However there are many possible interesting finds with the shift in the overlap of the operators, which with correlator matrix techniques [146, 147, 149, 150], or AMIAS [148] could lead to some novel results.

4.4 For Minkowski Space

To perform calculations directly comparable to experimental results, in addition to discretisation artefacts, an extrapolation back to physical quantities must be managed. The FHT has one unique strong advantage over three and four–point methods, we are calculating energy eigenstates of the Hamiltonian, which you can extrapolate to physical mass and continuum limit before calculating the derivatives using a Taylor expansion and relating those to matrix elements in Minkowski space. The subtlety here is the discretisation and Euclidianisation that are responsible for *time–enhancement* have no continuum counterparts, but this only excludes some continuum diagrams, and the one calculable on the lattice can still be extrapolated to the continuum. The only reason the lattice derivation of the FHT is useful is to understand how one should go about fitting it, and to understand the excited state and time evolution of the correlators. This means that one could in theory only derive the relationship between energy shift and matrix elements in a continuum fashion.

There is a subtlety here, the extrapolation to the physical continuum has to be done at constant λ in physical units. As one varies a, as required for a continuum extrapolation the required lattice λ varies. However as we shall see smaller λ correlator are easily interpolated.

To calculate the FHT for Minkowski space, it is useful to think of determining renormalisation diagrams from dressed and undressed propagators with respect to the new term in the Lagrangian. We introduce extra terms into the Lagrangian, whose correction at some order, are the ones we are interested in. By expanding the renormalisation of a propagator we are interested

in interms of the coupling constant, and by calculating our renormalised propagator at different coupling constants we can infer those diagrams. To formalise this, consider a modification of Lagrangian

$$\mathcal{L}_{QCD}(x) \to \mathcal{L}_{QCD}(x) - \lambda \mathcal{O}(x) \tag{4.102}$$

and look at our dressed propagator S, in terms of unperturbed propagator S_0 of some particle N. We can write the new propagator in terms of the old one, in terms of one particle irreducible Σ as

$$S = S_0 + S_0 \Sigma S \tag{4.103}$$

or alternatively in terms of momentum p and unperturbed mass m_0, as a geometric sum

$$S = \frac{iZ}{\not{p} + m_0 + \Sigma(\not{p})}. \tag{4.104}$$

We can then expand Σ in terms of λ to find the terms of interest, the linear terms giving us single operator insertions of $\mathcal{O}$, and the quadratic giving $\sum_{N' \neq N} \mathcal{O} S_{N'} \mathcal{O}$. As one can see, these forms are much more easy to work with and vast literature is available for performing these sorts of calculations. This is an intriguing avenue to explore for future FHT calculations, as continuum extrapolation of energy eigenstates are well understood.

4.5 Summary

We have presented the FHT for QM and a form for use with lattice QCD. For the first time we presented a derivation of the second order FHT, including momentum transfer for path integrals. The continuum extrapolation prior to FHT calculations is particularly intriguing but is left for future studies.

We follow the FHT proofs with a guide on putting the FHT into practice, including methods of reducing statistical and systematics uncertainty, reducing simulation cost with a full method example in §5. This theory is then used in §6, §7 and §8.

Chapter 5

Lattice Implementation of the Feynman–Hellmann Theorem

The FHT in literature has so far been limited to first order local vector and axial–vector currents, which limits the available matrix elements. In the previous chapter the FHT was extended to second order §4.2.3, giving access to new types of matrix elements. By extending the range of operators available, the phenomina available to study using the FHT can be extended even further.

In this chapter we lead through concepts by use of a demonstrated example, that of quark counting in §5.1. From this lense we look at the lattice implementation of different operators §5.2, including both connected and disconnected contractions. Flavour decomposition and their relationship to physical counterparts are shown in §5.3. Correlator ratios are then constructed to reduce errors in extraction of lattice energy shifts in §5.4. By utilising unperturbed solutions and optimising λ size, inversion times are optimised in §5.5. Finally we look at the extracting the energy derivatives from discrete λ in §5.6 before summarising first the lattice FHT method §5.7 and then the chapter §5.8.

5.1 Example Setup: Quark Counting

To help us demonstrate all the intraquacies of the FHT, we will work upon realising an example calculationg; that of quark counting. The Euclidean space Dirac vector form factors for a spin half particle as defined in §C.1.4, are

$$\left\langle X,\vec{p}'\middle|V_\mu^f(0)\middle|X,\vec{p}\right\rangle = \overline{u}(p')\left[\gamma_\mu F_1^f\left(Q^2\right)+\frac{\sigma_{\mu\alpha}q_\alpha}{2m}F_2^f\left(Q^2\right)\right]\overline{u}(p) \tag{5.1}$$

where unlike Minkowski space $Q^2 := q^2$ for spacelike q^2. If we restrict ourselves to the temporal vector current in the forward case, we can use the Gordon identity §C.4 to reduce this to

$$\left\langle X,\vec{p}\middle|V_4^f(0)\middle|X,\vec{p}\right\rangle = \overline{u}(p)\gamma_4 F_1^f(0)\overline{u}(p) = 2E_{X,\vec{p}}F_1^f(0). \tag{5.2}$$

If we modify our action by

$$S(\lambda) = S(0) + \lambda\int d^4x V_4^f(n) \tag{5.3}$$

the FHT of form (4.49) then tells us that for nucleon state N

$$\frac{\partial E_{N,\vec{0}}}{\partial\lambda} = F_1^f(0). \tag{5.4}$$

Our example is only based on the simplest FHT we have but all our techniques hold for the other forms (4.55), (4.80) and (4.97), up to their respective caveats discussed in their sections.

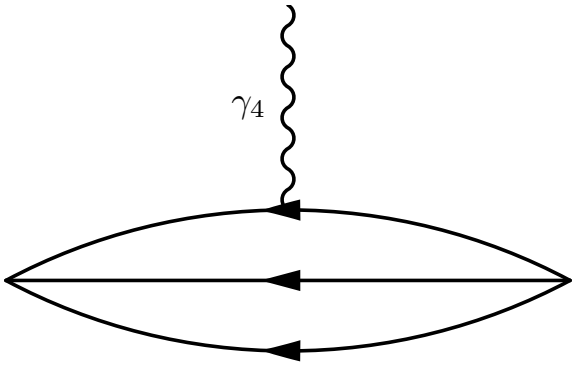

Figure 5.1: The diagram for the temporal photon vertex, used for quark counting

Charge conservation tells us that $F_1^f(0)$ is the total charge of flavour f, which is expected for a diagram of form Figure 5.1. Taking the same lattice as for our previous example (§3.6.1, §3.6.2), our $\beta = 5.5$, $SU(3)_{flavour}$ symmetric, $32^3 \times 64$ ensemble described in Table E.2, we only need a lattice implementation of $V_4^f(x)$ and choice of sufficiently many λ.

5.2 Lattice Operators

With this example in mind we discuss how to implement currents on the lattice. The simplest example is the connected local quark bilinear, which we discuss before showing other possibiities, both connected and disconnected.

5.2.1 Connected Local

The connected local current is the most common action shift used [112, 157–169, 184, 186], which include sigma, vector and axial–vector matrix elements. Recall that the we write our action as a quark bilinear

$$S_F\left[U_\mu, \overline{q}, q\right] = a^4 \sum_{n,m\in\Lambda} \overline{q}(n)_a^\alpha \mathcal{D}(n,m)_{ab}^{\alpha\beta} q(m)_b^\beta \tag{3.30}$$

and then invert $\mathcal{D}$ to obtain quark propagators to use in contractions. As a consequence if we modify the Dirac matrix prior to inversion, we can add an extra quark bilinear term to the connected part of the action. Specifically this modification in terms of the action is of the form

$$S \to S + \lambda_i \sum_n e^{i\vec{q}_i\cdot\vec{n}} \overline{q}(n)\Gamma q(n) \tag{5.5}$$

This modification is equivalent to modifying the diagonal of $\mathcal{D}$ to include an additional $e^{i\vec{q}_i\cdot\vec{n}}\Gamma$ term, where Γ is any element of the Clifford Algebra §C.1.2. For our purposes we focus on the vector and axial–vector currents

$$V_\mu^{loc}(n) := \overline{q}(n)\gamma_\mu q(n) \tag{5.6}$$

$$A_\mu^{loc}(n) := \overline{q}(n)\gamma_\mu\gamma_5 q(n). \tag{5.7}$$

with possible extra factors of i to keep the term Hermitian.

As the quark propagator is modified using this method, we are free to mix perturbed and unperturbed quark propagators in contraction. In the case of a meson this means that we can modify one or both connected quarks. In the case of baryons, we treat the quarks as either singly or doubly represented and can modify combinations of both of these. Either way as a consequence we can form four differnet current flavour decompositions discussed later in §5.3.

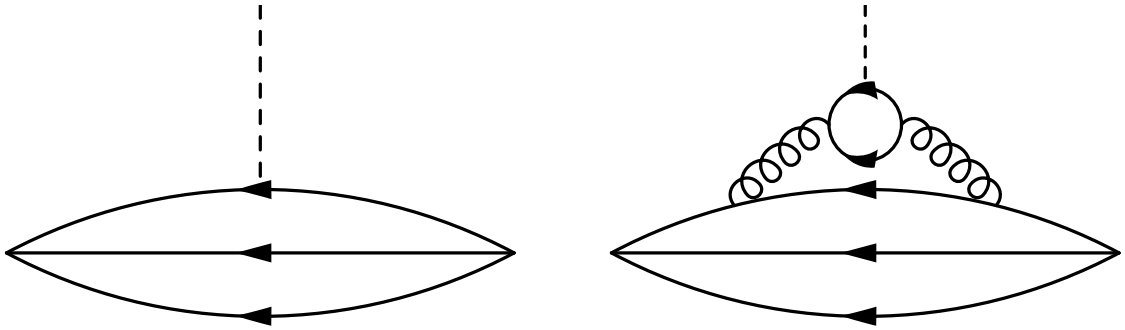

(a) Quark line connected diagram (b) Quark line disconnected diagram

Figure 5.2: The two possible cases for the FHT, (a) the connected contribution, where the current hits a valence quark and (b) the disconnected contribution, where the current hits a sea quark, only connected to the propagator via gluon lines.

As Grassmanian integration has already been performed on the gluonic degrees of freedom, we will only get the connected contributions for these matrix elements (Figure 5.2a).

This modification looks like an effective shift in the quark mass; the diagonal component of the Dirac matrix (3.31) contains the quark mass term, (5.5) also modifies the diagonal. Indeed for $\Gamma = 1$, the first order energy shift, the so called sigma terms is the shift in hadron mass due to shift in quark mass. For $\Gamma \neq 1$ this terms does not directly shift the quark mass but still causes the matrix to become more singular, a similar problem to the more singular matricies at near physical quark masses. As the matrix becomes more singular the larger λ is, this introduces a natural upper bound on λ. As we shall observe later §5.5, there is no actual advantage to large λ, so in practice we seek values well below this limit. This holds true as quark masses tend towards the physical point, where the window between κ and κ_c reduces.

Unlike it's continuum counterpart, due to discretisation the local current is not conserved on the lattice. However as the FHT gives us matrix elements of their n–point correlator method counterparts, the same renormalisation on matrix elements as described in §3.4 can be used. This requires us a multiplicative renormalisation factor Z_V, such that $Z_V V_\mu^{loc}(n)$ gives the renormalised matrix element at some fixed scal. Similar multiplicative renormalisation Z_A can be calculated for the axial current.

Coming back to our example, it is clear that we can then use V_4^{loc} as our lattice operator, as long as we also calculate Z_V for our lattice.

5.2.2 Connected Conserved

It is also possibly to implement the conserved vector current with minimal additional implementation. Recall the Wilson fermion action

$$\mathcal{L}_W\left[\overline{q},q\right](n) = \overline{q}(n)\Big(\tfrac{1}{2a}\textstyle\sum_\mu\left[(r-\gamma_\mu)U_\mu(n)q(n+\hat{\mu}) + (r+\gamma_\mu)U_{-\mu}(n)q(n-\hat{\mu})\right] + \big(m+\tfrac{4r}{a}\big)q(n)\Big) \quad (3.41)$$

it has a conserved current [124, 194, 195]

$$V_\mu^{con}(n) := \frac{1}{2}\left[\overline{q}(n+\hat{\mu})(r+\gamma_\mu)U_{-\mu}(n+\hat{\mu})q(n) - \overline{q}(n)(r-\gamma_\mu)U_\mu(n)q(n+\hat{\mu})\right]. \quad (5.8)$$

We are interested in transforming the Gauge Links

$$U_\nu \to U_\nu e^{i\lambda_\nu f(n)} \quad (5.9)$$

for some fixed ν, real constant λ_ν and a real function $f(n)$. We first rewrite the interacting fermion action, with some translation in elements of the sum

$$S_F^I\left[\overline{q},q\right] = a^4\sum_n\sum_\mu\left[\overline{q}(n+\hat{\mu})(r+\gamma_\mu)U_{-\mu}(n,\lambda_\nu) + \overline{q}(n)(r-\gamma_\nu)U_\mu(n,\lambda_\nu)q(n+\hat{\mu})\right] \quad (5.10)$$

where the first derivative in the action then becomes

$$\begin{aligned}\frac{\partial S_F}{\partial i\lambda_\nu} &= a^4 \sum_n \frac{1}{2}\Big[\overline{q}(n+\hat{\nu})(r+\gamma_\nu)(-f(n))U_{-\mu}(n) + \overline{q}(n)(r-\gamma_\nu)U_\mu(n)(f(x))q(n+\hat{\mu}) + \mathcal{O}(\lambda)\Big] \\ &= a^4 \sum_n \Big[- f(n)V_\nu^{con} + \mathcal{O}(\lambda)\Big]\end{aligned} \tag{5.11}$$

where we have absorved the λ dependence of U_μ into $\mathcal{O}(\lambda)$. Clearly this implies the second order derivative of this action is not zero, unlike all our other FHT cases

$$-\frac{\partial^2 S_F}{\partial \lambda_\nu^2} = a^4 \sum_n \frac{1}{2}\Big[\overline{q}(n+\hat{\nu})(r+\gamma_\nu)(f(n))^2 U_{-\mu}(n) + \overline{q}(n)(r-\gamma_\nu)U_\mu(n)(f(n))^2 q(n+\hat{\mu}) + \mathcal{O}(\lambda)\Big] \tag{5.12}$$

which is fermion action except with an additional $f^2(n)$ factor

$$a^4 \sum_n f^2 \overline{q}(n)\mathcal{D}_\nu \gamma_\nu q(n). \tag{5.13}$$

Now the second order derivative of the action term in the FHT requires *time–enhancement* just like the first order terms to modify the energy shifts. The matrix elements corresponding to the second order energy shift include a second order action shift matrix element, the first element of (4.57). Notice that (5.13) gives FHT current

$$J(n) = f^2(n)\overline{q}(n)\mathcal{D}_\nu\gamma_\nu q(n) \tag{5.14}$$

and the matrix element it is inserted to has just one instance of this current despite being of second order in λ. This means the derivation of the relationship between this matrix element and the energy shift is the same as the linear FHT, except the matching to second order energy shift

$$\left.\frac{\partial^2 E_{X,\vec{p}}}{\partial\lambda^2}\right|_{\lambda=0} = \frac{1}{2E_{X,\vec{p}}}\langle X,\vec{p}|J(0)|X,\vec{p}\rangle_0 + \left(\text{Regular } \frac{\partial S_F}{\partial i\lambda_\nu} \text{ Term}\right) \tag{5.15}$$

or

$$\left.\frac{\partial^2 E_{X^+_{\vec{q}},\vec{p}}}{\partial\lambda^2}\right|_{\lambda=0} = \frac{1}{2E_{X^+_{\vec{q}},\vec{p}}}\left\langle X^+_{\vec{q}},\vec{p}\right|J(0)\left|X^+_{\vec{q}},\vec{p}\right\rangle_0 + \left(\text{Regular } \frac{\partial S_F}{\partial i\lambda_\nu} \text{ Term}\right) \tag{5.16}$$

depending on momentum transfer.

This means the form of the matrix elements is determined by Breit frame conditions imposed on f^2. Take the case where $f(n) = \cos\vec{q}\cdot\vec{n}$ this is $f^2(n) = \frac{1}{2}(1+\cos 2\vec{q}\cdot\vec{n})$. The first term is a forward matrix element for any choice of $\vec{q}$ and the latter obeys Breit frame kinematics at $\vec{p} = \vec{p} \pm 2\vec{q}$, which can be expressed as

$$\left|\frac{2p\cdot q}{Q^2}\right| = 2. \tag{5.17}$$

This means this additional term is dependent on $\vec{p}$ only up to energy normalisation $2E_{X,\vec{p}}$ and completely independent of $\vec{q}$ outside of (5.17).

To implement this conserved current on the lattice, we introduce a $U(1)$ phase term to the guage links after smearing. Ideally this step would be performed before smearing but the Chroma software library [196] has many optimisations which this step would break, requiring extensive software developement. Another possible method would be to directly add the (3.31) equivalent of (5.11) to the non–diagonal parts of the Dirac matrix prior to inversion.

In either case we are calculating modified quark propagators like the local current §5.2.1 and the same contraction behaviours apply. We shall use V_4^{con} as the second vector current implementation for our example.

Disconnected Quarks

The calculations of self–contracted fermion lines has many challenges on the lattice. The problem in their calculation with established three–point function techniques on the lattice, naïvely requires the calculation of all–to–all propgataors. Recently there has been significant progress in stochastic estimation of such propgators [197–201] and [185] presented another complementary method which we summarise now.

In §5.2.1, we saw that a simple modification prior inversion due to our importance sampling (3.37) will only give the connected contribution to the energy shift. To generate the disconnected contributions with a FHT method we require modification of the configuration weighting $\rho\left(U_\mu^{(i)}\right)$ in the configuration generation. Lattices generated with an additional γ_5–Hermitian term in the Dirac matrix, yield the missing disconnected matrix elements. On these modified lattices one can also apply the modification for the connected local current to extract both connected and disconnected contribution at the same time. Such a modification has been used to give a better understanding of problems where the disconnected contribution is non–negligible [185] , in this case the proton spin problem §9.1.1. Note that for such problems the lattice spacing a is depedent on λ and quadratic at lowest order in λ in our case, see [193] for further details.

This technique has one major disadvantage, every single new discrete modification λ is accompanied by the generation of entirely new lattice ensembles. As lattices grow in volume, the work required to invert $\mathcal{D}$ becomes a larger contribution to the overall cost of computation. That is a larger part of the combination of generating general purpose lattice configurations and the combined computation performed on them. Despite this the disconnected calculation are still expensive enough to be limited by the need to generate single purpose lattice ensembles.

5.2.3 Future Operators

All the operators we have discussed do not break low–level Chroma software library [196] optimisations, which is why our local operators only modify the diagonal of the Dirac matrix §5.2.1. Such an addition for the local current already breaks even–odd preconditioning optimisations, which translates to slower inverters. The conserved current converted can use all existing inverters and such can use better inverters, such as domain decomposition [202].

By removing the constraint on modifying only the diagonal for local operators, more operators can be used for the FHT beyond those of the Clifford algebra. One such example would be a direct implementation of the conserved current, without including a shift beyond first order in the action. In fact this would allow any arbitrary quark billinears to be included into the Dirac matrix, such as the operators for quasi–distributions [203] and Ioffe time distributions [204], the latter of which already uses a different FHT approach for it's matrix elements [188].

5.3 Flavour Decomposition

In adding quark bilinears to the action prior to inversion in §5.2.1 and §5.2.2, we generate modified quark propagators, which we use to build up composite QCD objects. We are free to combine both modified and unmodified quark propagators to isolate flavour contribution to our matrix elements. We shall ignore the s flavour terms in our simulation as they are not present in our connected operator calculations but are straightforward to reinclude once disconnected quantities are studied.

Using two different λ we can construct any combination of flavour in hadron currents $\lambda_1 u + \lambda_2 d$. For technical reasons we shall go into later we always calculate λ and $-\lambda$ pairs for our quark and so without requiring extra inversion we can always form the u, d, $u-d$ and $u+d$ flavoured currents. For the linear case, their flavour decomposition is trivial, with only two independent quantities u and d shown diagramatically in Figure 5.3.

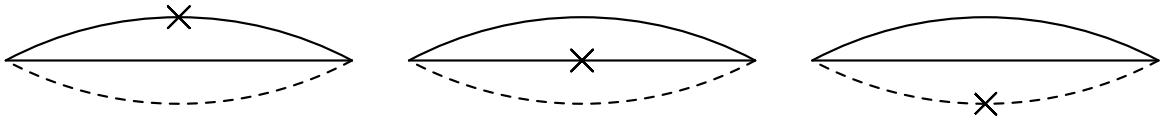

(a) (b) (c)

Figure 5.3: The three ways of inserting one current on a baryon with a doubly represented quark (plain) and a singly represented quark (dashed)

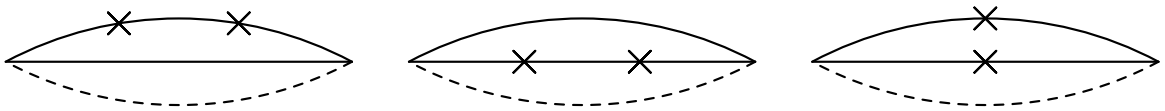

(a) (b) (c)

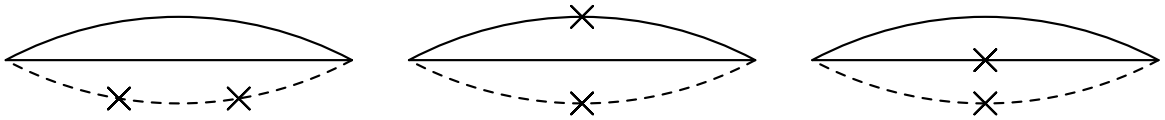

(d) (e) (f)

Figure 5.4: The six ways of inserting two currents on a baryon with a doubly represented quark (plain) and a singly represented quark (dashed)

At second order, there are two current insertions, so either one or two quark lines are hit with the current. Consider the information available from two simulation; one with just u currents Figure 5.4 (a)–(c) and the other with just d currents Figure 5.4d. This would miss an important class of insertions, those hitting two different flavoured currents Figure 5.4 (e)–(f). We shall label contributions by their quark flavour content, uu, dd and ud, which we shall use throughout this work and is summarised in Table 5.1. The normalisation ion the ud component is fixed such that two $(u + d)$ currents are split as $uu + dd + ud$.

Getting back to our quark counting example, we are dealing with the simpler linear energy shift, so only need to take u and d flavoured currents. The extra $u - d$ and $u + d$ contraction available without extra inversions are not statistically independent of u and d, so are not used. This means we can construct V_4^u and V_4^d giving us access to $F_1^u(0)$ and $F_1^d(0)$ respectively.

Insertions	Flavour Combination	Diagrams
Single	u	Figure 5.3 (a)–(b)
	d	Figure 5.3 (c)
Double	uu	Figure 5.4 (a)–(c)
	dd	Figure 5.4 (d)
	ud	Figure 5.4 (e)–(f)

Table 5.1: The contributing diagrams to our defined flavour combinations, which can be extended in the obvious manner to include disconnected terms as well.

5.4 Ratios

We now outline our method of extracting energy shifts from correlators modified as described above. The basic principle between a calculation is to shift the action at some finite discrete number of $\boldsymbol{\lambda}^{(1)}, \boldsymbol{\lambda}^{(2)}, \cdots$, calculating the correlator at each $\boldsymbol{\lambda}$, before fitting effective masses of two–point correlation functions as in §3.6. The energy extracted then follow a Taylor expansion

$$E_{X,\vec{p}}(\boldsymbol{\lambda}) = E_{X,\vec{p}}(0) + \sum_i \lambda_i \left.\frac{\partial E_{X,\vec{p}}}{\partial \lambda_i}\right|_{\boldsymbol{\lambda}=\vec{0}} + \sum_i \frac{{\lambda_i}^2}{2!} \left.\frac{\partial^2 E_{X,\vec{p}}}{\partial {\lambda_i}^2}\right|_{\boldsymbol{\lambda}=\vec{0}} + \sum_i \sum_{j<i} \left.\frac{\partial^2 E_{X,\vec{p}}}{\partial \lambda_i \partial \lambda_j}\right|_{\boldsymbol{\lambda}=0} + \mathcal{O}(\lambda^3). \tag{5.18}$$

By fitting to this expansion for our calculated two–point correlators at differing $\boldsymbol{\lambda}$ we can then extract the derivatives in energy, which we then relate to matrix elements via FHT. There are however some optimisations that can be performed on the simulation.

It is easiest to observe this improvement through our quark counting example. To extract modified hadron correlators we require definite or turned λ. Tuning λ however requires knowledge of the correct ratios to verify systematics, so we are left with a chicken and egg problem. As it will turn out in §5.5 the range of λ that gives the correct result is quite large $10^{-6} < |\lambda| < 10^{-1}$, so we shall use $\lambda \in \{\pm 10^{-4}, \pm 10^{-5}\}$ for our exploration.

The local vector current V_4^{loc} modified only for the u quark propagator inside a hadron is our example. With four λ and one unperturbed $\lambda = 0$, there are 5 different nucleon correlators $G^{(2)}_{\chi\lambda}$. The naïve expectation is that these correlators can be fit like a normal nucleon correlator, eg. §3.6.2 by using the effective masses to determine fitting range. The correlators and their effective masses are shown in Figure 5.5, with the modified correlator fit ranges chosen in the same way as the unmodified (see §3.6.2 for details). It is clear that the perturbations in energy caused by this modified action are not visible to the eye, however the correlators are highly correlated with each other, possessing the same lattice source sites. Using this high correlation we can extract a fit in λ, which gives a proton mass of

$$m_p(\lambda) = 0.923(19) + 2.31(18)\lambda. \tag{5.19}$$

The coeficient infront of λ is our first order energy shift using the FHT.

The first major optimisation one can perform is at this Taylor expansion fit step. By taking the ratios of modified and unmodified correlator

$$\frac{G^{(2)}_{\chi\lambda}}{G^{(2)}_{\chi}}(x_4, \vec{p}) \to \frac{g^{(2)}_{\chi\lambda}\left[X, \vec{p}\right]}{g^{(2)}_{\chi}\left[X, \vec{p}\right]} e^{-\left(E_{X,\vec{p}}(\lambda) - E_{X,\vec{p}}\right)x_4} \propto e^{-\Delta E_{X,\vec{p}}(\lambda) x_4}. \tag{5.20}$$

the constant in λ mass term, the first term of (5.18) from our fit is removed. This ratio is still includes $\mathcal{O}(\lambda^2)$ terms in general, so we can go even further than this by taking the ratio of two modified correlators

$$\frac{G^{(2)}_{\chi(+\lambda)}}{G^{(2)}_{\chi(-\lambda)}}(x_4, \vec{p}) \to \frac{g^{(2)}_{\chi\lambda}\left[X, \vec{p}\right]}{g^{(2)}_{\chi(-\lambda)}\left[X, \vec{p}\right]} e^{-\left(E_{X,\vec{p}}(\lambda) - E_{X,\vec{p}}(-\lambda)\right)x_4} \propto e^{-E^o_{X,\vec{p}}(\lambda) x_4} \tag{5.21}$$

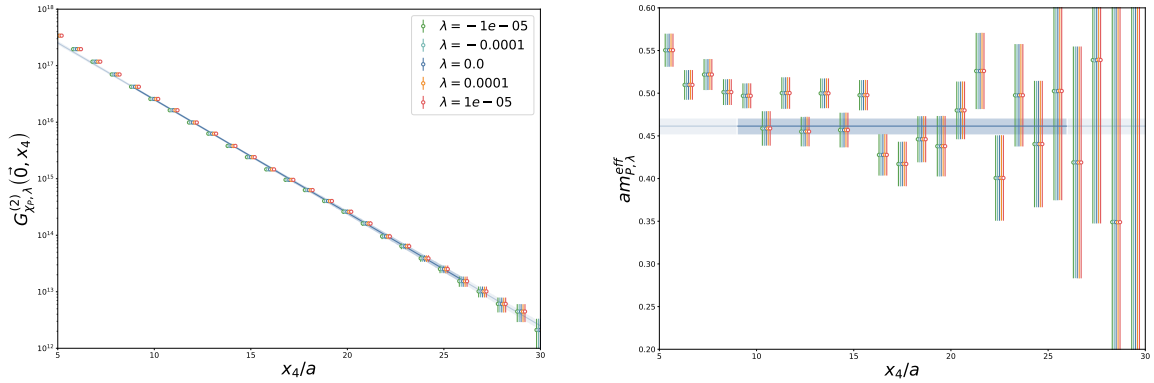

(a) Correlator

(b) Effective Mass

Figure 5.5: The modified and unmodified correlator comparison, the unmodified correlator (blue) is also shown with correlator fit. The points have been offset slightly for clarity. The inverters for the unperturbed correlator use even–odd preconditioning, while the modified correlators do not.

which only includes terms odd in λ, making the next–most significant precent term $\mathcal{O}(\lambda^3)$. We shall leave the systematic control of presence of such terms to §5.5.

Focusing on this ratio for our example we are left with fewer correlator ratios than there are modified correlators, see in Figure 5.6 that the both the different λ correlators have distinct signals and their effective mass Figure 5.6b, has two different distinct values.

The correlators are then fit by looking for constant effective mass behaviour, except with the correlator fit artificially later, the fit suggest starting at time–slice $x_4/a = 2$. This early plateaux is due to the excited states having the same value as the lowest order state, nevertheless prior first order FHT fits are earlier than their unmodified counterparts [184]. In later chapters we shall also calculate second order energy shifts using even ratios, which tend to plateaux later than their unmodified correlator counterpart.

The one parameter fit of the odd λ dependence of the mass with respect to λ then is

$$m^{odd}(\lambda) = 2.330(26)\lambda. \tag{5.22}$$

The precision of this fit is a magnitude smaller than when fitting each of the correlators separately, whose predominant contributions are from mass and momentum of the unperturbed ground state. Note that the method without ratios does not even attain the same precision if the ratio guided fitting range is used, hence for all future results we shall exclusively use the relevant ratios that we now define formally.

5.4.1 Single Modification

We can write the Taylor expansion of a λ dependent energy in one variable to all orders as

$$E_{X,\vec{p}}(\lambda) = E_{X,\vec{p}}(0) + E^e_{X,\vec{p}}(\lambda) + E^o_{X,\vec{p}}(\lambda) \tag{5.23}$$

where E^e denotes the even part of the energy with respect to λ and E^o the corresponding odd part. Then one can construct ratios in the same manner as (5.20), to extract pure odd or even energy shifts

$$R^o_{\chi\boldsymbol{\lambda}}(x_4, \vec{p}) := \frac{G^{(2)}_{\chi(+\lambda)}}{G^{(2)}_{\chi(-\lambda)}}(x_4, \vec{p}) \to g^{(o)}_{\chi\lambda} e^{-2E^o_{X,\vec{p}}(\lambda)x_4} \tag{5.24}$$

$$R^e_{\chi\boldsymbol{\lambda}}(x_4, \vec{p}) := \frac{G^{(2)}_{\chi(+\lambda)} G^{(2)}_{\chi(-\lambda)}}{\left(G^{(2)}_{\chi}\right)^2}(x_4, \vec{p}) \to g^{(e)}_{\chi\lambda} e^{-2E^e_{X,\vec{p}}(\lambda)x_4}. \tag{5.25}$$

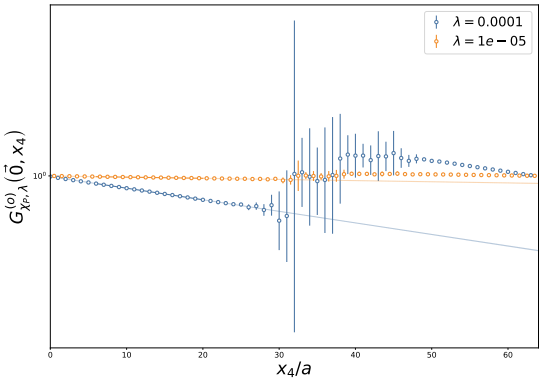

(a) Correlator

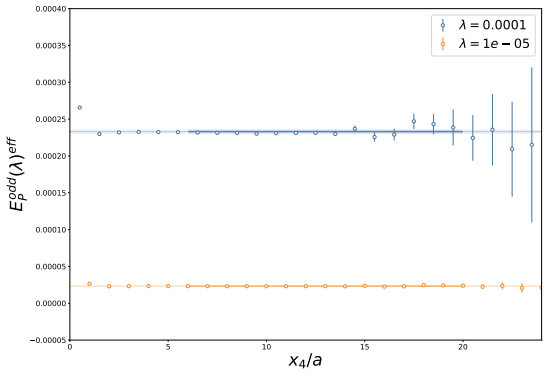

(b) Effective Mass

Figure 5.6: The correlator ratios for our quark couting example of both correlator (a) and effective mass Figure 5.6b.

Where we have defined

$$g^{(o)}_{\chi\lambda} := \frac{g^{(2)}_{\chi\boldsymbol{\lambda}}\left[X,\vec{p}\right]}{g^{(2)}_{\chi(-\lambda)}\left[X,\vec{p}\right]} \tag{5.26}$$

$$g^{(e)}_{\chi\lambda} := \frac{g^{(2)}_{\chi\lambda}\left[X,\vec{p}\right] g^{(2)}_{\chi(-\lambda)}\left[X,\vec{p}\right]}{g^{(2)}_{\chi}\left[X,\vec{p}\right]^2} \tag{5.27}$$

One can then simply fit these in exactly the same manner as a two–point correlation function, using effective masses to guide a fitting window, but the resultant Taylor expansions becomes simpler

$$E^{o}_{X,\vec{p}}(\lambda) = \lambda \left.\frac{\partial E_{X,\vec{p}}}{\partial\lambda}\right|_{\lambda=0} + \mathcal{O}\left(\lambda^3\right) \tag{5.28}$$

$$E^{e}_{X,\vec{p}}(\lambda) = \frac{\lambda^2}{2!} \left.\frac{\partial^2 E_{X,\vec{p}}}{\partial\lambda^2}\right|_{\lambda=0} + \mathcal{O}\left(\lambda^4\right). \tag{5.29}$$

As our strategy is to perform a fit with the lowest possible λ, in almost all cases, fits of the polynomial in λ are single parameter fits. As single parameter fits, with just with two different λ magnitudes for the ratios all higher order λ effects can demonstrated to be negligible.

5.4.2 Double Modification

The same principle can be extended to any number of different $\boldsymbol{\lambda}$ modifications, but the only other one of interest to us is two different action modifications $\boldsymbol{\lambda} = (\lambda_1, \lambda_2)$. We split the Taylor expansion into five pieces

$$E_{X,\vec{p}}(\boldsymbol{\lambda}) = E_{X,\vec{p}}(0) + E^{ee}_{X,\vec{p}}(\boldsymbol{\lambda}) + E^{eo}_{X,\vec{p}}(\boldsymbol{\lambda}) + E^{oe}_{X,\vec{p}}(\boldsymbol{\lambda}) + E^{oo}_{X,\vec{p}}(\boldsymbol{\lambda}). \tag{5.30}$$

where E^{oe} represent the energy odd in λ_1 and even in λ_2, and similar for E^{ee}, E^{eo}, E^{oo}. To extract these four ratios are formed

$$R^{oo}_{\chi\boldsymbol{\lambda}} := \frac{G^{(2)}_{\chi(+\lambda_1,+\lambda_2)} G^{(2)}_{\chi(-\lambda_1,-\lambda_2)}}{G^{(2)}_{\chi(+\lambda_1,-\lambda_2)} G^{(2)}_{\chi(-\lambda_1,+\lambda_2)}} \to g^{(oo)}_{\chi\lambda} e^{-4E^{oo}_{X,\vec{p}}(\boldsymbol{\lambda})x_4} \tag{5.31}$$

$$R^{oe}_{\chi\boldsymbol{\lambda}} := \frac{G^{(2)}_{\chi(+\lambda_1,+\lambda_2)} G^{(2)}_{\chi(+\lambda_1,-\lambda_2)}}{G^{(2)}_{\chi(-\lambda_1,-\lambda_2)} G^{(2)}_{\chi(-\lambda_1,+\lambda_2)}} \to g^{(oe)}_{\chi\lambda} e^{-4E^{oe}_{X,\vec{p}}(\boldsymbol{\lambda})x_4} \tag{5.32}$$

$$R^{eo}_{\chi\boldsymbol{\lambda}} := \frac{G^{(2)}_{\chi(+\lambda_1,+\lambda_2)} G^{(2)}_{\chi(-\lambda_1,+\lambda_2)}}{G^{(2)}_{\chi(-\lambda_1,-\lambda_2)} G^{(2)}_{\chi(+\lambda_1,-\lambda_2)}} \to g^{(eo)}_{\chi\lambda} e^{-4E^{eo}_{X,\vec{p}}(\boldsymbol{\lambda})x_4} \tag{5.33}$$

$$R^{ee}_{\chi\boldsymbol{\lambda}} := \frac{G^{(2)}_{\chi(+\lambda_1,+\lambda_2)} G^{(2)}_{\chi(-\lambda_1,-\lambda_2)} G^{(2)}_{\chi(+\lambda_1,-\lambda_2)} G^{(2)}_{\chi(-\lambda_1,+\lambda_2)}}{\left(G^{(2)}_{\chi}\right)^4} \to g^{(ee)}_{\chi\lambda} e^{-4E^{ee}_{X,\vec{p}}(\boldsymbol{\lambda})x_4} \tag{5.34}$$

which allow extraction of energy shifts

$$E^{oo}_{X,\vec{p}}(\boldsymbol{\lambda}) = \lambda_1\lambda_2 \left.\frac{\partial^2 E_{X,\vec{p}}}{\partial\lambda_1\partial\lambda_2}\right|_{\boldsymbol{\lambda}=\vec{0}} + \mathcal{O}\left(\lambda_1\lambda_2^3\right) + \mathcal{O}\left(\lambda_1^3\lambda_2\right) \tag{5.35}$$

$$E^{oe}_{X,\vec{p}}(\boldsymbol{\lambda}) = \lambda_1 \left.\frac{\partial E_{X,\vec{p}}}{\partial\lambda_1}\right|_{\boldsymbol{\lambda}=\vec{0}} + \mathcal{O}\left(\lambda_1\lambda_2^2\right) + \mathcal{O}\left(\lambda_1^3\right) \tag{5.36}$$

$$E^{eo}_{X,\vec{p}}(\boldsymbol{\lambda}) = \lambda_2 \left.\frac{\partial E_{X,\vec{p}}}{\partial\lambda_2}\right|_{\boldsymbol{\lambda}=\vec{0}} + \mathcal{O}\left(\lambda_1^2\lambda_2\right) + \mathcal{O}\left(\lambda_2^3\right) \tag{5.37}$$

$$E^{ee}_{X,\vec{p}}(\boldsymbol{\lambda}) = \sum_i \frac{\lambda_i^2}{2!} \left.\frac{\partial E_{X,\vec{p}}}{\partial\lambda_i}\right|_{\boldsymbol{\lambda}=\vec{0}} + \mathcal{O}\left(\lambda_1^2\lambda_2^2\right) + \mathcal{O}\left(\lambda_1^4\right) + \mathcal{O}\left(\lambda_2^4\right) \tag{5.38}$$

If one where interested in only higher order interference terms, where the terms includes non–interference terms, one can remove them by combing the ratios with appropriate one λ ratios.

5.4.3 Imaginary Shifts

The ratios of §5.4.1, §5.4.2, can be easily modified for extracting imaginary shifts by taking the phase of the ratio

$$\mathrm{Arg}\left\{R^{o}_{\chi\boldsymbol{\lambda}}\right\} = \to \mathrm{Arg}\left\{g^{(o)}_{\chi\lambda}\right\} - 2\,\mathrm{Im}\left\{E^{o}_{X,\vec{p}}(\lambda)\right\} x_4 \tag{5.39}$$

$$\mathrm{Arg}\left\{R^{e}_{\chi\boldsymbol{\lambda}}\right\} = \to \mathrm{Arg}\left\{g^{(e)}_{\chi\lambda}\right\} - 2\,\mathrm{Im}\left\{E^{e}_{X,\vec{p}}(\lambda)\right\} x_4 \tag{5.40}$$

$$\mathrm{Arg}\left\{R^{oo}_{\chi\boldsymbol{\lambda}}\right\} = \to \mathrm{Arg}\left\{g^{(oo)}_{\chi\lambda}\right\} - 4\,\mathrm{Im}\left\{E^{oo}_{X,\vec{p}}(\boldsymbol{\lambda})\right\} x_4 \tag{5.41}$$

$$\mathrm{Arg}\left\{R^{oe}_{\chi\boldsymbol{\lambda}}\right\} = \to \mathrm{Arg}\left\{g^{(oe)}_{\chi\lambda}\right\} - 4\,\mathrm{Im}\left\{E^{oe}_{X,\vec{p}}(\boldsymbol{\lambda})\right\} x_4 \tag{5.42}$$

$$\mathrm{Arg}\left\{R^{eo}_{\chi\boldsymbol{\lambda}}\right\} = \to \mathrm{Arg}\left\{g^{(eo)}_{\chi\lambda}\right\} - 4\,\mathrm{Im}\left\{E^{eo}_{X,\vec{p}}(\boldsymbol{\lambda})\right\} x_4 \tag{5.43}$$

$$\mathrm{Arg}\left\{R^{ee}_{\chi\boldsymbol{\lambda}}\right\} = \to \mathrm{Arg}\left\{g^{(ee)}_{\chi\lambda}\right\} - 4\,\mathrm{Im}\left\{E^{ee}_{X,\vec{p}}(\boldsymbol{\lambda})\right\} x_4. \tag{5.44}$$

Unlike the effective mass style ratios of the real shift counterparts, these ratios have a much simpler form to extract time depedence

$$\mathrm{Arg}\left\{R_{\chi\boldsymbol{\lambda}}(x_4)\right\} - \mathrm{Arg}\left\{R_{\chi\boldsymbol{\lambda}}(x_4+a)\right\} \propto \mathrm{Im}\left\{E_{X,\vec{p}}(\boldsymbol{\lambda})\right\} \tag{5.45}$$

for large enough x_4. As we use small λ any phase wrap around effects can be ignored, although nothing in theory is stopping their extraction with a slightly modified fit.

5.5 Inversion Optimisation

The FHT requires the calculation of additional propagators, which can be expensives when using many different λ. To make our extrapolation of energy shifts to zero λ well defined, we restrict ourselves to the smallest possible $\boldsymbol{\lambda}$, which allows us to perform a simple but effective improvement to the inversion time. This optimisation works on any inversions of perturbed propagators, in our case local and conserved currents. By using the unperturbed quark propagator, the inversion of the unperturbed Dirac matrix, as the initial guess to the inversion of a perturbed one, one can save substantially on inversion time. Additionally one can use combinations of prior guesses to get even better initial guess for the inversion by using a simple linear extrapolation. In all cases, as we care just determining the initial guess of the propagator solution, the resulting modified propagator with or without guess is the same, hence any improvement in inversion time is a pure gain. We now investigate the initial guess using our quark counting example.

The expected effect of a perturbation in λ depends on the magnitude. Theoretically one expect the entire perturbation to fail as λ tends to 1, as higher order energy shifts contribute more and more, thus extraction of some low order energy shifts becomes infeasible. In practice a more dominant bound on λ is given by increasingly singular Dirac matrix as $|\lambda|$ grows larger. If we look at the local vector current modification (5.5), a term that looks like the quark mass in (3.31) is introduced. This is an effective shift in the quark and anti–quark mass, so as the quark mass gets lighter one can get hit κ_c singularities. Additionally at large λ, higher order effects than of interest might become statistically significant. These give us both a hard and soft ceiling on λ.

Smaller λ have their own problems, due to finite machine precision. The IEEE 754 double precision float, most commonly implemented by hardware, has only approximately sixteen significant decimal digits. Thus for λ smaller than this, we expect no perturbation evident. One must also be careful due, only part of the perturbation might 'fall' through the correlator shift, which could lead to erroneous results. However our ratios §5.4, allows us to look at systematics in our perturbation by comparing multiple different λ. In the case where the perturbation 'falls' through the lattice we except to observe a rapid breakdown in leading order λ trend. In the case where λ is too large, their trend will also diverge from the dominant λ trend as λ gets bigger.

We now investigate different inversion guess strategies in a simple low statistics simulation to analyse the λ for the effects mentioned above. The calculation is performed on the $\beta = 5.5$ $SU(3)_{flavour}$ symmetric ensemble Table E.2, performed on a small subset of size $N_{cfg} = 27$. The action modification as the example was chosen to be a simple single flavour vector current

$$S(\lambda) = S(0) + \lambda \int d^4x \left(e^{i\vec{q}\cdot\vec{x}} + e^{-i\vec{q}\cdot\vec{x}} \right) V_3^{d,loc} \tag{5.46}$$

for $q = (4, 1, 0)$, in lattice units corresponding to a Q^2 of $4.64\ GeV^2$.

The λ where chosen with the machine precision and higher order perturbations in mind. Inversion times where recorded for each λ and shown in Figure 5.7. We first observe that no guess is significantly worse than the unperturbed inversion, as the unperturbed inverter has been optimised for the clover improved Wilson action. In addition the time of no guess is very unstable, which arises from the fact that the inverter does not initialise the initial guess to zero. This means that the trend towards smaller λ has more to do with the memory configuration of the used system. With a large difference between a guess and no guess inversions, an improved technique is clearly preferred.

We first look at the simplest inversion guess by looking at Figure 5.5, notice that the correlators are virtually unchanged, which means the quark propagator used are virtually the same too. The modified quark propagator was inverted off a slightly modified source, which means that for sufficiently small λ the solution of the perturbed quark propagator is almost identical to the unperturbed one. To this end we also run the same inversions with a starting perturbation, and observe due to the consistent starting perturbation that the result is much more stable between λ. We observe even for the larger λ, the inversion times are universally faster than no guess and can even beat the optimised inverter on the unperturbed inversion, once the unperturbed quark

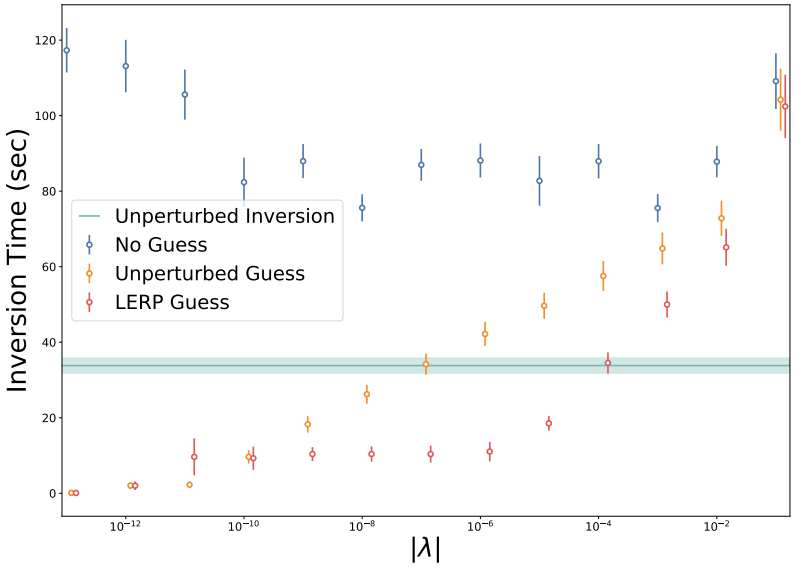

Figure 5.7: The inversion time in seconds for one colour and Dirac index, plotted against the absolute value of λ. The points in blue are the inversion done with no initial guess, the points in orange represent inversions with unperturbed correlator as initial guess for the solution and red the inversions with a linear extrapolation based initial guess. The teal band is the corresponding unperturbed correlator inversion time for reference, which we note uses a more optimised inverter. All error bars and bands are shown for one standard deviation.

propagator has been measured. In practice the unperturbed quark propagator needs to be calculated in every one of our simulations anyway, so this is effectively a free gain. This linear trend of inversion, is a good indication that no κ_c effects are hit for our choice of λ. Clearly a simple inversion guess is already better than none.

With the long linear inversion time trend we saw, it is natural to want to investigate what happens when we use simple Linear Interpolation (LERP) techniques. If one has an unperturbed and perturbed solution, one can form a initial guess by predicting the solution as only linear in λ. We observed that for a large range of λ the inversion time with this technique remains constant, until larger λ, it rises sharply in linear fashion. This improved technique has no significant implementation cost over inversion without guess, only storage in memory of prior solutions, and hence will be used throughout this work. Quadratic extrapolation and further techniques should also be possible, although improvements aren't expected to be as pronounced. Such extensions would be relevant for extracting cubic and quartic perturbation.

5.6 λ Tuning

Figure 5.7 shows that for very small $\lambda = 10^{-13}$ the solution to the perturbed quark propgator is indistinguishable from the unperturbed up to machine precision. This is when the entirety of the response from our action modification is definitely no longer measureable. We have to be more careful about this, we don't expect the perturbation to become invisible from one λ to the next, instead expecting a slower decline in signal which we investigate now. By calculating baryon correlators and ratios thereof to look at even energy shifts we can examine the λ trend. Again as this is a low statistics run we do not expect anything meaningful from these results, but we can look for λ consistency.

The results against λ of the even energy shift (5.29), as extracted using the even one–λ ratio (5.25) are shown in Figure 5.8. As we have divided by λ^2 we expect to observe constant behaviour where systematics are under control. For small λ we observe that not only is the result unstable,

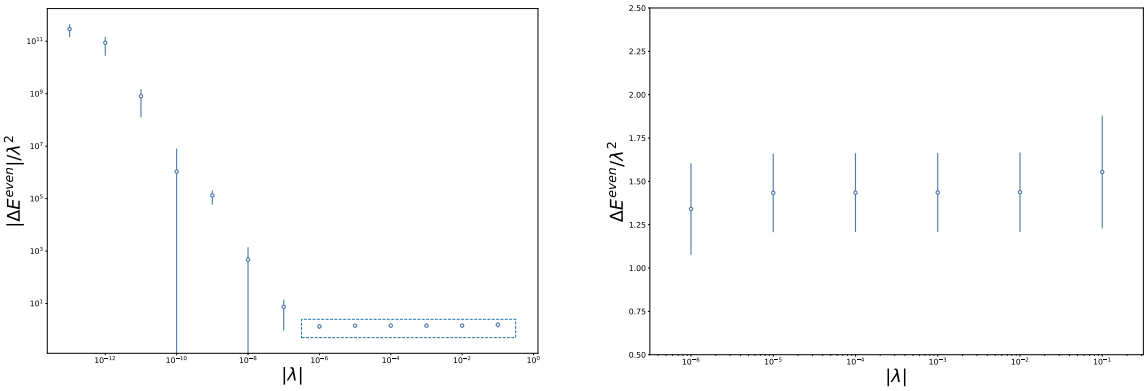

(a) Log Plot

(b) Zoomed Linear Plot

Figure 5.8: The even energy shift (5.29) divided by λ^2, as extracted from the ratio (5.25), given by the low statistics run as described in the text. For (a) the absolute value of the even energy shift was shown, to see the rapid decline in signal, with box showing the limits of zoomed figure (b), which is shown in linear scale and no absolute value.

it is certainly not consistent. Only for the largest λ do we not observe a consistent result. It is surprising how dramatic the falloff is from the consistent range of $\lambda \in \left[10^{-5}, 10^{-2}\right]$, to a slight inconsistency in $\lambda = 10^{-6}$, to completely different just one magnitude lower. This means that we must use large enough λ for our simulation.

To ensure that we observe the proper energy shift we can perform our calculation at multiple different values of λ, to see whether our ratios give consistent values. Due to the autocorrelation on the same source we observe that if our perturbation is invalid, even two very close λ values will show this difference, even if they differ by less than a magnitude.

The choice of λ then is limited for the problem, but is also changed based on the hardware at hand. As inversions can also be solved using GPGPU techniques and GPU hardware is often available at a cheaper cost, λ optimisation for them is also important. Inversions on such current readily available hardware is often done using single precision floating point. This lower precision does not change the inversion time characteristics much, but it does require us to use much larger λ. Future available GPUs however are designed for double precision calculations, so identical calculations can then be performed as for the CPU.

A typical three–point function techniques on the lattice have inversion equivalent in time to an unperturbed correlator. For properly tuned λ the computation of the equivalent matrix element is then faster than a sequential three point functions with the same operator, although the $\vec{q}$ extractable using FHT are more limited. In cases where both FHT and three point function are able to calculate the same matrix elements, this gives us an advantage in inversion time comparative to three point function techniques. Even without the inversion time improvement provided by using an initial guess the FHT method is already favourable [184].

We have shown how to optimise the λ chosen for inversions for extractions of second order energy shifts. This is keeping the λ small enough, that the inversion time is kept small and higher order effects are in check. As well as not letting it become to small that machine precision effects are noticeable. Throughout this work, 3 λ values are chosen for most simulation, with 2 chosen, when similar simulations with very close parameters have already been run.

In Figure 5.8 we saw that for a range of λ the ratio divided by λ^2 was constant, implying $\mathcal{O}(\lambda^4)$ terms were negligiable. This means we can verify that our λ are purely the energy shift of interest by comparing the effective masses divided by appropriate λ factors.

In the case of our quark counting example we want only linear λ terms in our ratio (5.24). The consistency is easily observed by looking at the odd energy shift with respect to λ and it's fit which we plot in Figure 5.9. Clearly there are no significant higher order terms present in each of the data points, if they were the straight line would not be consistent with all the points.

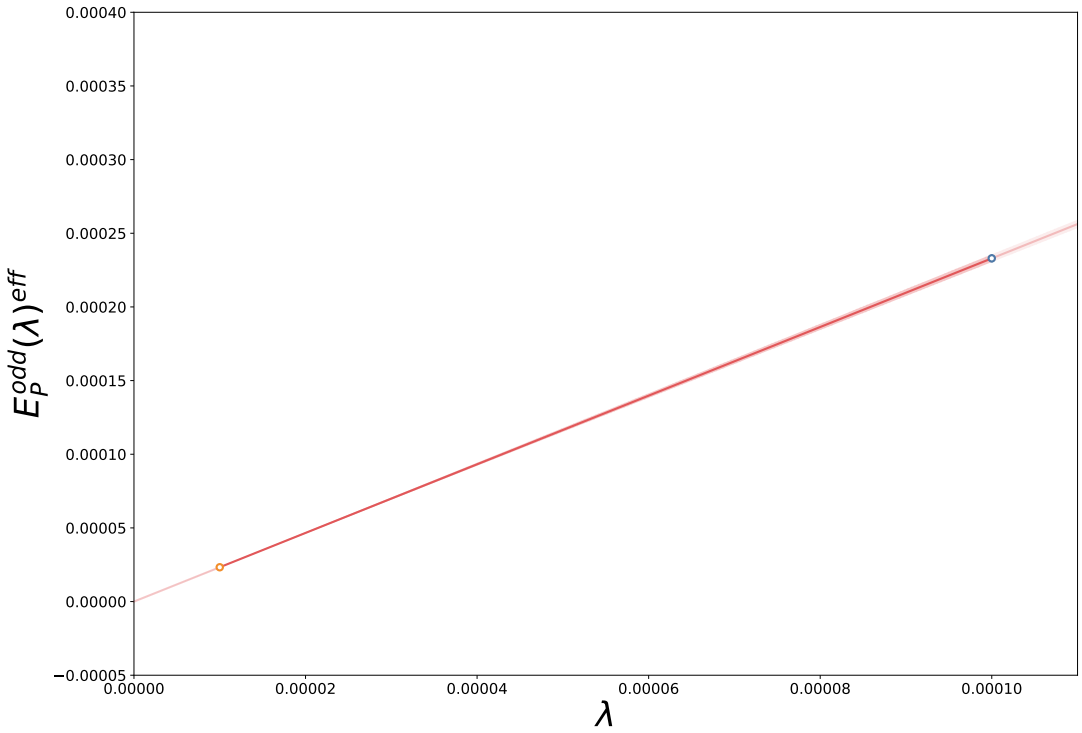

Figure 5.9: A linear fit in λ to the energy shift, showing no signs of other terms present, either constant or of higher order.

It turns out we can examine the fitting range and verify choice of λ at the same time. If we divide the effective mass by λ, then a linear trend in Figure 5.9 will exhibit itself as consistent effective masses. The resultant shifted effective mass observed in Figure 5.10 allows us to determine fitting range and presence of λ systematics in one plot qualitatively. Visually we see an exact agreement between the different λ, which means that the extracted energy divided by λ is a direct fit for the first order energy shift $\frac{\partial E_p^{odd}}{\partial \lambda}$, the quantity shown on the y–axis from this fit. In the case where the energy shift is imaginary, as is the case for quark counting with the conserved vector current, the same principle can be applied, dividing the effective phase by the corresponding λ factor.

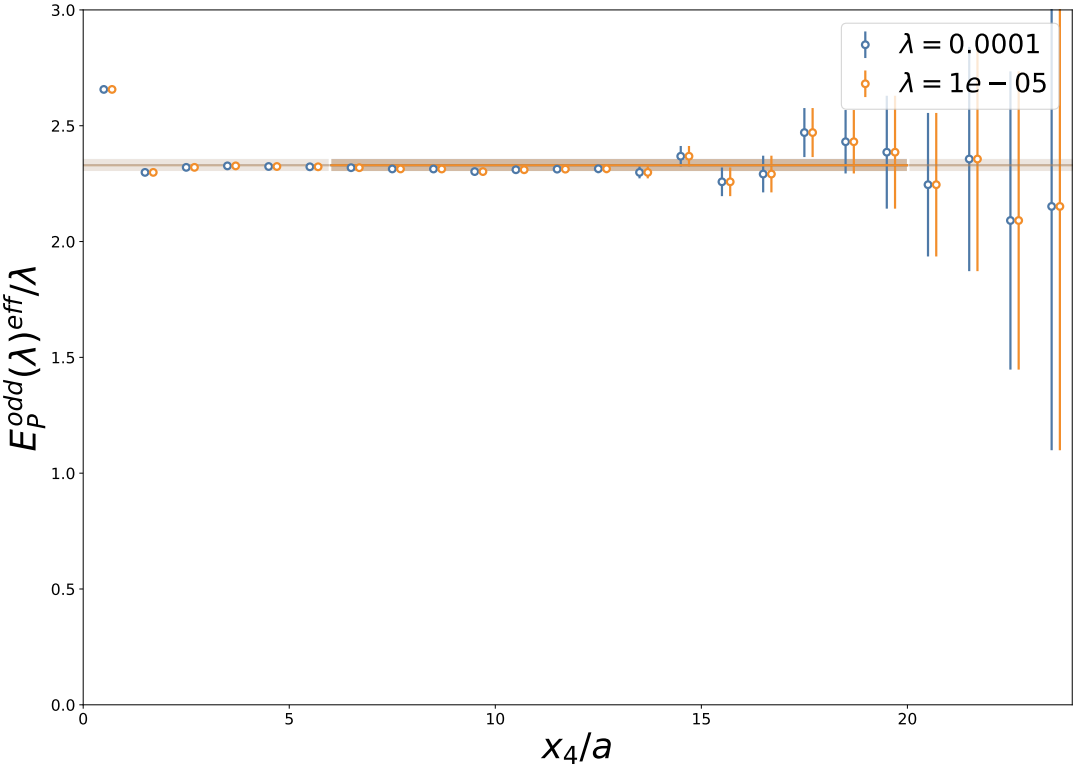

Figure 5.10: The shifted effective mass of the odd ratio (5.24), used to calculate the odd shift in energy for two different values of λ. The points have been offset slightly for clarity.

5.7 The Lattice Feynman–Hellmann Recipe

We now summarise the steps for a (connected) FHT calculation on the lattice.

1. Choose the FHT corresponding to the matrix element of interest (§4.2)
2. Choose the operators including any momentum transfer $\vec{q}$ (§5.2)
3. Identify the ratio (§5.4) for the matrix element and operator
4. Choose tuned λ (§5.6) for the choice of ratio and operators
5. Calculate modifed quark propagators
6. Contract quark propagators into hadrons to form modified correlators with chosen current flavour combination
7. Fit correlators using shifted effective masses to determine fitting ranges, fitting a polynomial with higher order terms if necessary
8. Perform flavour decomposition if not trivial (§5.3)
9. Renormalise matrix element if nessesary

Performing these steps for our quark counting example, also including the conserved vector current we can count the quarks inside the nucleon, summarised in Table 5.2. We observed an excellent aggreement between the two methods, although the conserved current is much more precise, which is expected as the symmetry is exact even trajectory by trajectory. For the vector

Current	Form Factor	Value
V_4^{loc}	$F_1^u(0)$	1.996(23)
	$F_1^d(0)$	0.993(11)
V_4^{con}	$F_1^u(0)$	1.9993(21)
	$F_1^d(0)$	0.99981(72)

Table 5.2: The summary for the calculation of proton $F_1^f(0)$, for two different flavours and two different currents.

current the multiplicative renormalisation factor Z_V was calculated already for this lattice, our calculation can also be used to fix this quantity instead giving a renormalisation constant of

$$Z_V = 0.8611(84) \tag{5.47}$$

which is used throughout this work.

5.8 Summary

We have presented implementable FHT operators, including a conserved current implementation. Using simple implementable steps, we showed how to reduce both statistical and systematic uncertainty, while at the same time reducing computational cost. By calculating precise vector charges of the proton using two different operators, including the first implementation of the conserved current using FHT in literature we have shown these steps in practice and calculated the vector renormalisation used throughout this work. This is put into practice in §6, §7 and §8.

Chapter 6

Transition Form Factors

In the case of the first order FHT, we have simple benchmark checks available in the form of quark counting §5.6. Additionally there are also many investigations with identical, or similar techniques that give us an understanding of the discretisation effects [112, 160–162, 165, 170–172, 180, 183–187].

Similar two current matrix elements have been studied on the lattice [173–177, 181, 182] and so now we present some results from the second order FHT. The result of the second order energy shift, is evidently a polarisability, in similar fashion to the electric and magnetic polarisabilities extracted using the background field technique. Due to the larger than physical pion mass we can consider the two current matrix element as being saturated by the Δ^+ intermediate state and compare the resultant derived transition form factor to other established lattice and phenomenological techniques.

The *Goldberger–Treiman relation*, links the strong pseudoscalar pion–nucleon coupling constant to the nucleon axial charge, via the partially conserved axial current. A similar result, the *off–diagonal Goldberger–Treiman relation* links the pion–nucleon–delta coupling constant to the longitudinal *Adler transition form factors* [205]. We first investigate how we are able to relate the second order FHT to transition form factors §6.1, followed by describing one such form factor we can gain some knowledge of the one of the *Adler transition form factors* §6.2 and finishing with some lattice calculations investigating this link §6.3, before summarising §6.4.

6.1 Lattice Spectrum

By taking advantage of the spectrum of lattice states at larger than physical masses, we can infer some behaviour of just one of them. Recall the second order FHT without momentum transfer

$$\left.\frac{\partial^2 E_{X,\vec{p}}}{\partial {\lambda_i}^2}\right|_{\boldsymbol{\lambda}=\vec{0}} = 2\sum_{Y\neq X}\frac{\langle X,\vec{p}|J_i(0)|Y,\vec{p}\rangle_0\langle Y,\vec{p}|J_i(0)|X,\vec{p}\rangle_0}{E_{X,\vec{p}}E_{Y,\vec{p}}\big(E_{X,\vec{p}}-E_{Y,\vec{p}}\big)} \tag{4.81}$$

and note that the contribution for each state Y is weighted by

$$E_{Y,\vec{p}}\big(E_{X,\vec{p}}-E_{Y,\vec{p}}\big). \tag{6.1}$$

This means that larger mass intermediate states are suppressed compared to the lighter ones. We saw in §3.6.1 and §3.6.2, that for those simulation parameters the masses where much large than their physical counterparts. In addition the gap in mass between the delta and proton is relatively unchanged. This means that for these parameters, the delta is the lowest energy state in the sum. As a consequence of $m_\Delta - m_p < m_\pi$, the delta particle is stable.

Diagrammatically we can look at the differences between the continuum and the unphysically heavier than physical lattice as Figure 6.1. As we expect the lowest energy $N\pi$ contributions to be small, we assume the energy shift (4.81) is saturated by just the delta contribution for a vector or axial current. Under these assumptions, we now relate the $p \to \Delta$ transition form factors to

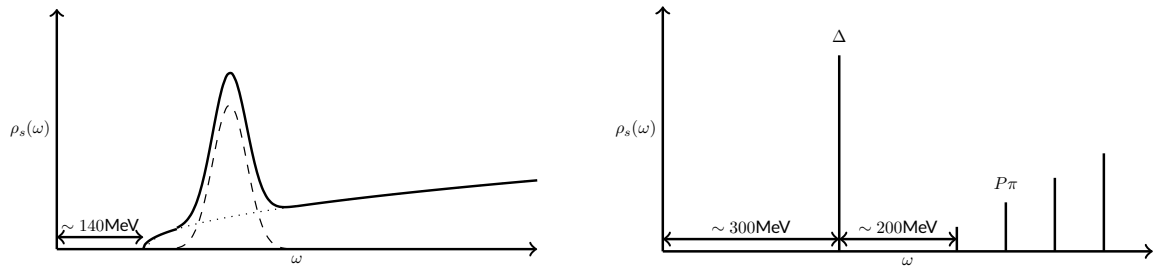

(a) Physical Point Continuum

(b) $SU(3)_{SYM}$ Point Lattice

Figure 6.1: A sketch of the spectral density function $\rho_s(\omega)$ of our state against energy difference $\omega = E_{Y,\vec{p}} - E_{X,\vec{p}}$. We have the continuum representation (a), where we see the pion production threshold at roughly 140 MeV, where $N\pi$ states (dotted) start contributing, the delta resonance (dashed) and with combined effect (solid). The lattice representation (b) for $m_\pi \approx 500\ MeV$ has discrete lattice states, a discrete Δ, followed by a discrete set of $N\pi$ states.

the FHT matrix element, and any deviations from these assumptions will lead to an overestimate of the transition form factors.

6.2 Adler Transition Form Factors

The matrix element of a $p \to \Delta^+$ transition form factor can be expressed in terms of four form factors [205–207]

$$\left\langle \Delta^+, \vec{p}' \middle| A_\mu^{u-d} \middle| p, \vec{p} \right\rangle = 2\overline{u}^\nu_{\Delta^+}(p') \Bigg[g_{\mu\nu} C_5^A(Q^2) + q_\mu q_\nu \frac{C_6^A(Q^2)}{M_N^2} + (q_\lambda g_{\mu\nu} - q_\nu g_{\mu\lambda}) \left(\gamma^\lambda \frac{C_3^A(Q^2)}{M_N} + p'^\lambda \frac{C_4^A(Q^2)}{M_N^2} \right) \Bigg] u_p(p). \tag{6.2}$$

The two form factors C_3^A and C_4^A are the transverse contributions. Conversely the form factors C_5^A and C_6^A encode the longitudinal part, which are dominant to the transverse part on the lattice [208]. Alternatively the Sachs transition form factor representation can be used [209–211], but for us the Adler form is used for comparison with the off–diagonal Goldberger–Treiman relationship.

Using the Rarita-Schwinger spin sum [210]

$$\sum_s u^{\nu'}_{\Delta^+}(p,s') \overline{u}^\nu_{\Delta^+}(p,s) = -\frac{\not{p}' + M_\Delta}{2M_\Delta} \left[g_{\nu'\nu} - \frac{1}{3}\gamma_{\nu'}\gamma_\nu - \frac{2p_{\nu'}p_\nu}{3M_\Delta^2} + \frac{p_{\nu'}\gamma_\nu - p_\nu\gamma_{\nu'}}{3M_\Delta} \right] \tag{6.3}$$

and the *Gordon identity* (§C.4), we can relate a FHT like matrix form to $C_5^A(0)$

$$\frac{\left\langle p, \vec{0} \middle| A_3^{u-d}(0) \middle| \Delta^+, \vec{0} \right\rangle_0 \left\langle \Delta^+, \vec{0} \middle| A_3^{u-d}(0) \middle| p, \vec{0} \right\rangle_0}{m_p m_\Delta (m_p - m_\Delta)} = \frac{16}{3} \left(C_5^A(0) \right)^2 \frac{1}{m_p m_\Delta (m_p - m_\Delta)}. \tag{6.4}$$

The diagonal *Goldberger–Treiman relationship* [212], links the pion–nucleon decay constant $g_{\pi NN}$ to the isovector axial charge g_A and pion decay constant F_π

$$g_{\pi NN} = \frac{g_A m_N}{F_\pi}. \tag{6.5}$$

The Adler C_5^A can be related exactly to the pion–nucleon–delta coupling constant $g_{\pi N\Delta}(Q^2)$ [205] by

$$C_5^A(0) = \sqrt{\frac{2}{3}} \left(\frac{g_{\pi N\Delta}(0) P_\pi(0)}{m_N m_\pi^2} - C(0) \right) \tag{6.6}$$

where $P_\pi(Q^2)$ is the psuedoscalar current coupling to the pion and $C(Q^2)$ encodes the non–pole contributions. Experimentally neither $g_{\pi N\Delta}$ or P_π are obtainable at $Q^2 = 0$, but can be obtained at $Q^2 = m_\pi^2$. We assume that neither of these quantities vary much with Q^2 and that the pion pole dominates the process, allowing us to neglect $C(Q^2)$. We can then write the *off–diagonal Goldberger–Treiman* relationship as

$$C_5^A(0) = \sqrt{\frac{2}{3}} \frac{g_{\pi N\Delta}(m_\pi^2) P_\pi(m_\pi^2)}{m_N m_\pi^2} (1 - \Delta_\pi) \tag{6.7}$$

where Δ_π the *off–diagonal Goldberger–Treiman discrepancy* is a measure of the breaking in our assumptions above.

We are now able to relate the $C_5^A(0)$ to the Δ intermediate part of the second order FHT, which we assume to saturate the even energy shift. With this relationship we now focus on calculating this energy shift on the lattice.

6.3 Lattice Results

If we modify our action by

$$S(\lambda) = S(0) + \lambda \int d^4x A_3^{u-d}(x) \tag{6.8}$$

the resultant axial–vector matrix elements allow us to calculate g_A and the *Adler transition form* factor C_5^A. These calculations are extracted using the same modified correlators with odd ratio (5.24) for g_A and even ratio for (5.25) for C_5^A.

We perform this calculation on our two $\beta = 5.5$ $SU(3)_{flavour}$ symmetric ensemble Table E.2 as summarised in Table 6.1. The resultant second order energy shift is shown in Figure 6.2. We note that $\lambda = 0.1$ is already too large for this simulation leading to significant inversion failures for this action modification, which are caused by too large effective κ shifts in the inversion of the Dirac matrix $\mathcal{D}$, causing it to be too singular. We then perform these energy shifts for the other volume and compare. In Figure 6.3 we observe that the λ^2 scaled even energy shifts are constant, which implies that the signal is entirely of second order with negligible corrections from higher order even powers of λ. The odd ratio also has no λ^3 terms, although the Δ^+ energy shift does. We also observe that the values between the two volumes are consistent with each other, although the smaller lattice has vastly increased statistics.

The values for the extrapolation back to zero λ are given by

$$\left.\frac{\partial E_{p,\vec{0}}^{24^3\times 48}}{\partial\lambda}\right|_{\lambda=0} = -26.9(29) \tag{6.9}$$

$$\left.\frac{\partial E_{p,\vec{0}}^{32^3\times 64}}{\partial\lambda}\right|_{\lambda=0} = -31.1(51) \tag{6.10}$$

which combined with (6.4) corresponds to

$$\left|C_5^A(0)^{24^3\times 48}\right| = 0.748(41) \tag{6.11}$$

$$\left|C_5^A(0)^{32^3\times 64}\right| = 0.803(67). \tag{6.12}$$

The effect of increasing volume would change the gap between spacing in the $N\pi$ states in Figure 6.1b while not changing the Δ contribution overly much. Roughly this would increase the contribution from unwanted intermediate states. The fact that we do not see significant volume dependence shows that for our lattices the Δ saturation assumption seems to hold. To compare to other results we assume the sign of C_5^A is positive.

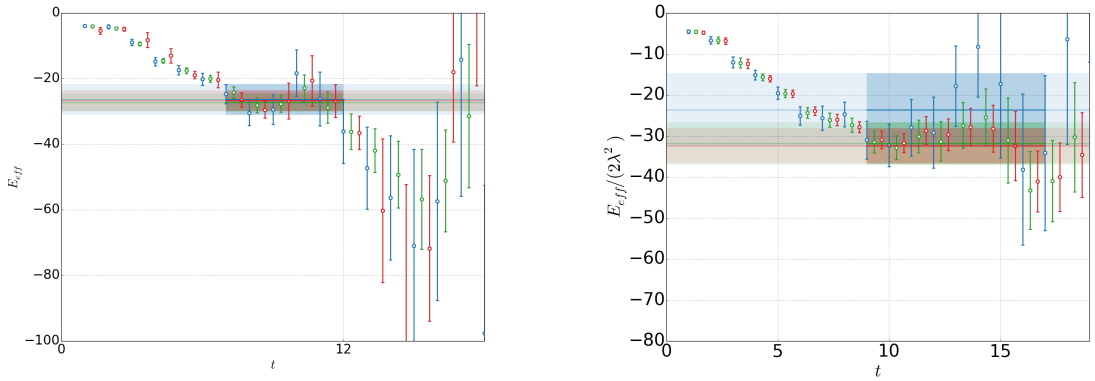

(a) $24^3 \times 48$ (b) $32^3 \times 64$

Figure 6.2: The effective mass of ratio Table 6.1 that provides the even energy shift against lattice time t/a, shifted by λ^2. The three different λ values are $\lambda = 0.0125$ (blue), $\lambda = 0.025$ (orange) and $\lambda = 0.0375$ (red). Each of these points have been offset for clarity.

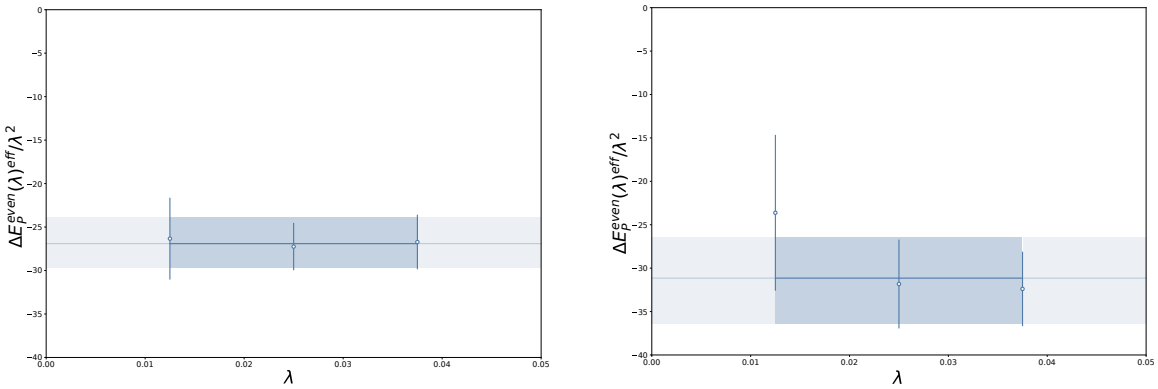

(a) $24^3 \times 48$ (b) $32^3 \times 64$

Figure 6.3: The even energy shifts for the forward axial current scaled by λ^2 against λ, with constant fit. The $\lambda = 0$ y–axis intercept then gives the value for the second order energy shift at $\lambda = 0$.

Dimensions	N_{cfg}	$N_{src/cfg}$	N_s
$24^3 \times 48$	3002	2	6003
$32^3 \times 64$	1080	1.4	1513

Table 6.1: The lattice details for the used transition form factors, with $\lambda \in [0.0125, 0.025, 0.0375]$. A subset N_{cfg} of the full ensemble was use with $N_{src/cfg}$ sources per trajectory resulting in N_s total sources.

The first result to compare to is a direct lattice extraction of C_5^A using conventional three–point functions [208, 213]

$$C_5^A(0)_{DWF} = 0.903(11). \tag{6.13}$$

This extraction was made from several lattices with differing lattice spacing with domain wall fermions with pion masses m_π of $0.297(5)$, $0.329(1)$ and $0.353(2)\ GeV$. The transition form factors were calculated at a finite series of non–zero Q^2, before being extrapolated back to $Q^2 = 0$. While the quark masses used are still larger than physical, they are smaller than the quark masses used in our simulation, so if C_5^A is mildly suppressed by hadron masses this result is still consistent with our value.

We can investigate the mass dependence by turning to a quark model. A quark model that uses the isovector–axial charge g_A, proton m_p and delta m_Δ mass [214] gives

$$C_5^A(0)_{QM} = \frac{1}{1.17}\frac{6}{5\sqrt{3}}\frac{2m_\Delta}{m_p + m_\Delta}g_A \tag{6.14}$$

for the *Adler transition form factor*. The prediction for the physical values for each parameter gives a value

$$C_5^A(0)_{QM}^{phys} = 0.87 \tag{6.15}$$

which is slightly larger than our result. We can extract g_A with the same correlators generated for C_5^A but with the odd ratio and combine with proton and delta masses as measured on our configurations to give values for $C_5^A(0)$ of

$$C_5^A(0)_{QM}^{24^3\times 48} = 0.888(77) \tag{6.16}$$

$$C_5^A(0)_{QM}^{32^3\times 64} = 0.854(35). \tag{6.17}$$

The errors come purely from errors in masses and g_A, not from the model. We see that for our parameters we observe a slightly smaller C_5^A for our lattices and hence expect our value to underestimate the physical value by a small amount.

Experimentally the transition form factor is obtainable from neutrino scattering of hydrogen and deuterium [215] to give a value of

$$C_5^A(0)_{\nu H/D} = 1.15(23). \tag{6.18}$$

One can also infer the value through pion pole dominance and χPT through the *off–diagonal Goldberger–Treiman relationship*

$$C_5^A(0)_{\chi PT} = 0.93(10) \tag{6.19}$$

however this assumes that the discrepancy Δ_π is zero. An alternative calculation using renormalised Berkeley and Argonne National Laboratory data for neutrino–induced $P_{33}(1232)$ resonance data [216] yielded

$$C_5^A(0)_{P_{33}(1232)} = 1.0. \tag{6.20}$$

In the original Adler parameterisation the Partially Conserved Axial–vector Current (PCAC) hypothesis was used to parameterise the transition form factors [215]. This model predicts at $Q^2 = 0$

$$C_5^A(0)_{PCAC} = \frac{g_{\pi N\Delta}F_\pi}{\sqrt{12}m_N} = 1.2. \tag{6.21}$$

Table 6.2 shows the summary of all these results. In combination these extractions suggest that this *Adler transition form factor* depends on the quark masses. In our case at larger than physical masses we predict a suppression compared to the experimental result of $1.15(23)$. Hence taking this into account our values are in broad agreement with the other results.

Source		$C_5^A(0)$
FHT (This Work)	$24^3 \times 48$	$0.748(41)$
	$32^3 \times 64$	$0.803(67)$
Alternative lattice QCD Technique [213]	$m_\pi = 0.297$–$0.353\ GeV$	$0.903(11)$
Quark Model [214]	physical masses	0.87
	$24^3 \times 48$ masses	$0.888(77)$
	$32^3 \times 64$ masses	$0.854(35)$
Original Adler parameterisation [215]	PCAC	1.2
Experiment [205, 216]	empirical νH/D scattering	$1.15(23)$
	low energy χPT pion scattering	$0.93(10)$
	$\nu P_{33}(1232)$ data	1.0

Table 6.2: A comparison of the extractions of $C_5^A(0)$ from multiple different techniques. The two FHT calculations are of the magnitude only, here present with positive sign.

6.4 Summary

We have demonstrated the second order FHT by using it to estimate transition form factors, with comparable results to other methods and experiment. While one could calculate the pion–nucleon–delta coupling constant $g_{\pi N\Delta}$ for a theoretical prediction for the *off–diagonal Goldberger–Treiman relationship discrepancy*, the technique would break down as the quark mass becomes lighter. However this provides confidence in the second order FHT proof §4.2.2, and we now move onto calculations with external momentum, the Compton amplitude in §7 and §8.

Chapter 7

Compton Amplitude

Earlier we introduced the notion of looking at hadronic structure in terms of structure functions §2.3. We showed how the hadron tensor is related via a dispersion relation to the Compton amplitude, which we will now examine in practice. In the extraction of PDFs, multiple experimental results using different techniques, including DIS are combined to improve accuracy. The same thing is possible for lattice QCD, the Compton amplitude can be combined with other lattice techniques, which in combination would improve the theoretical predictions for the PDFs or their moments.

The PDF is only the leading–twist component of the hadron tensor and hence the Compton amplitude contains more information about hadron dynamics, the higher twist components. Radiative corrections in the form of box diagrams are important model inputs for experiments. Currently these box diagrams are determined from model calculations. Knowledge of such diagrams play a crucial role in the precision of many experiments discussed in prior chapters §2.3.4, §2.3.5. A first principle of extraction here could provide improved understanding of QCD and improve the precision of experimental results.

Recently developed methods try to match onto the parton model directly on the lattice, through use of *Ioffe time distributions* [217]. By Fourier transform one can relate the *Ioffe time distributions* to PDFs directly, however they can also be related by different Fourier transforms to both quasi–PDFs [218] and pseudo–PDFs [219], which in turn can both be compared to PDFs by factorisation. The quasi–PDFs are calculated using Wilson line connected quark operators at large but non–infinite boost, roughly around $3\ GeV$ using momentum smearing techniques. By varying the boost to extrapolate to the infinite momentum frame the PDFs can be extracted, a selection of which are [203, 220–223] although renormalisation of such extractions are difficult [224–226]. Pseudo–PDFs are the off light-cone generalisations of PDFs and have similar success [204, 227–230]. A related method has also been proposed [231], referred to as *good lattice cross–sections*, although there are some objections to the correctness of the term [219], with the alternative *factorisable matrix elements* being suggested [232]. Regardless of the name, early results are available using this technique [233, 234].

The direct computation of structure functions, either for the hadron tensor or the Compton amplitude offer a complementary approach. Prior work has been done on extracting the structure functions directly from lattice QCD, including heavy quarks [235, 236], the Euclidean hadron tensor [237] and lattice OPE methods [238–240]. Some other methods have been proposed, by avoiding the problem of mixing [241] or a strategy similar to the one presented here [242]. We propose extracting the Compton amplitude directly using the second order FHT. Compared to heavy quark and Euclidean hadron tensor techniques, this avoids making a connection between Minkowski and Euclidean temporal coordinates instead exploiting physical kinematics so the current separation remains space–like. A similar use of space–like current separation was proposed to ensure analytic continuation in Minkoswki space for pion light–cone distribution amplitude [243]. The FHT renormalisation is as simple as for three–point techniques using the same operators, which are well understood.

The higher moments of the structure functions have problems with mixing with same or lower dimensional operators. While these terms are still present in our method, in the $a \to 0$ limit, the ultraviolet divergences in this limit should not be present as we are fundamentally determining our quantities from energy eigenstates. Some of the work in this chapter has been published [244].

In this chapter we first present how to extract the Compton amplitude including it's ω dependence in §7.1. These results are used to examine moments §7.2, scaling §7.3 and higher twist terms §7.4. Finally we conclude the results presented §7.5. Some of the work presented in this chapter has been published [244]

7.1 Subtracted Compton Amplitude

The unpolarised Euclidean counterpart to the Compton amplitude (2.45) reads

$$T_{\mu\nu}^{(E)}(p,q) = \left(\delta_{\mu\nu} - \frac{q_\mu^{(E)} q_\nu^{(E)}}{\left(q^{(E)}\right)^2}\right) T_1 - \frac{\left(p_\mu^{(E)} - \frac{1}{2}\omega q_\mu^{(E)}\right)\left(p_\nu^{(E)} - \frac{1}{2}\omega q_\nu^{(E)}\right)}{\nu^{(E)}} T_2. \tag{7.1}$$

To extract the Compton amplitude using the FHT we need to consider the action modification used. We have already seen an example where the isovector–axial–vector current was used in §6.3. For our calculation we will use

$$S(\lambda) = S(0) + \lambda_1 \int d^4x \left(e^{i\vec{q}\cdot\vec{x}} + e^{-i\vec{q}\cdot\vec{x}}\right) J_{1\mu}(x) + \lambda_2 \int d^4x \left(e^{i\vec{q}\cdot\vec{x}} + e^{-i\vec{q}\cdot\vec{x}}\right) J_{2\nu}(x) \tag{7.2}$$

for the general current J_i and external three–momenta $\vec{q}$. This 'cosine' external momentum transfer is required to make the action modification Hermitian, and a similar 'sin' combination is also possible, which has been tested, and gives the same results as the 'cosine' results. We can relate this action modification via the FHT relation (4.97) to the Compton amplitude

$$\left.\frac{\partial^2 E_{N,\vec{p}}}{\partial\lambda_1\partial\lambda_2}\right|_{\boldsymbol{\lambda}=0} = -\frac{T_{\mu\nu}(p,q) + T_{\mu\nu}(p,-q)}{2E_{N,\vec{p}}} \tag{7.3}$$

where the second term comes from our use of 'cosine' external momentum and

$$T_{\mu\nu}(p,q) = \left\langle p \middle| \int d^4x e^{iq\cdot x} T\left\{J_\mu(x) J_\nu(0)\right\} \middle| p \right\rangle. \tag{7.4}$$

J_μ can be any pair of V_μ^{loc} (5.6) and V_μ^{con} (5.8).

If we further limit ourselves to $\mu = \nu = 3$, $p_z = 0$ and $q_z = 0$ then we are able to directly extract T_1 from the energy shift

$$\left.\frac{\partial^2 E_{N,\vec{p}}}{\partial\lambda_1\partial\lambda_2}\right|_{\boldsymbol{\lambda}=0} = -\frac{T_1(\omega, Q^2)}{E_{N,\vec{p}}}. \tag{7.5}$$

Throughout this chapter, after demonstrating the extraction of the Compton amplitude at fixed ω, we will present results only for subtracted quantities (2.80). Due to this relationship, the ω dependence of the subtracted dispersion relationship gives us insight into the x dependence of the hadron tensor structure function F_1.

7.1.1 Analysis

We have already discussed in §6.3 how to extract and verify the quadratic regime for the second order energy shift with respect to one λ using the even ratio (5.25). As there are higher twist contribution to any Compton amplitude, it was thought by removing some of these by taking

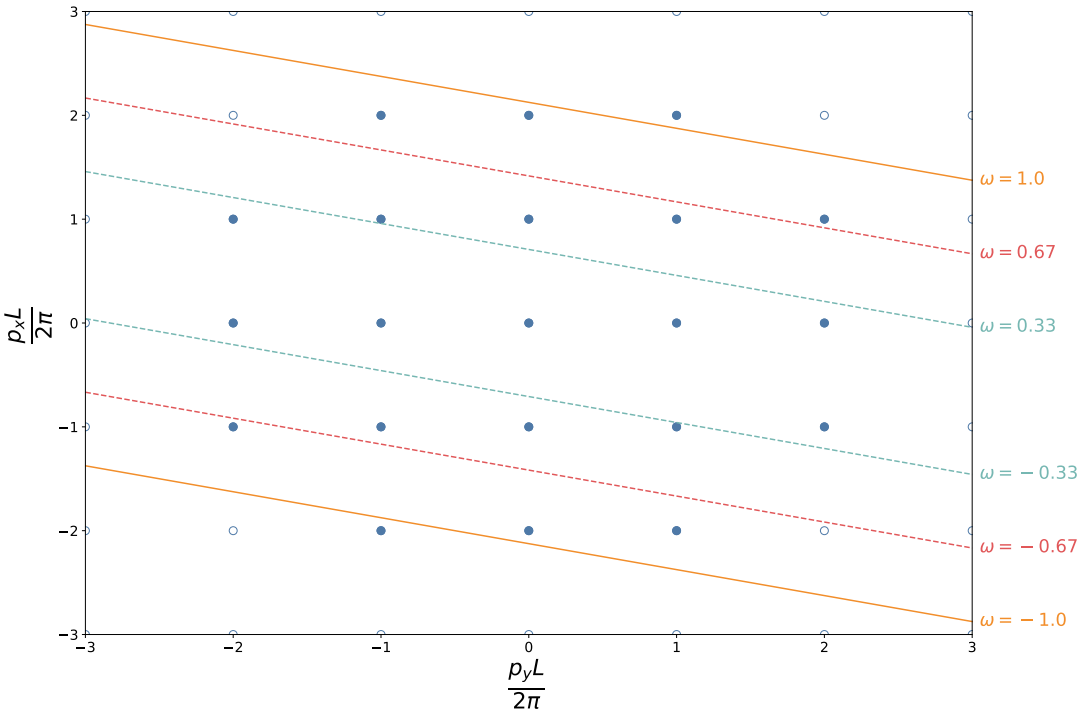

Figure 7.1: An illustration of the link between discretised $\vec{p}$ and ω for $\vec{q} = (4, 1, 0)$. The allowed momentum values for the x and y component are shown (blue), with the points that are extracted in our simulation shown using filled circles. On the plot are also shown the lines of constant ω, including our theory limiting line $|\omega| = 1$ (orange) which sandwiches the points where our FHT matching is valid.

averages of modified quark propagators and using different ratios the signal could be improved, however this did not turn out to be the case (for additional information see §F.1).

The interference current requires a similar process, but uses an imaginary energy shift due to the implementation of V_3^{con}. The ratio for the interference current (5.41) will allow one to extract energies odd in both λ_i

$$\Delta E^{oo} = \lambda_1 \lambda_2 \frac{\partial^2 E}{\partial \lambda_1 \partial \lambda_2} + \mathcal{O}(\lambda_1^3 \lambda_2) + \mathcal{O}(\lambda_1 \lambda_2^3). \tag{7.6}$$

If you divide the effective mass ratio by $\lambda_1 \lambda_2$ and the separate (highly correlated) $\boldsymbol{\lambda}$ correlators coincide with one another the bilinear regime is identified and the higher order terms are negligible.

Each simulation will extract multiple $\vec{p}$ results at the same time, which corresponds to the extraction of multiple ω. As an example, the ω extracted in a $\vec{q} = (4, 1, 0)$ and $|\vec{p}|^2 \leq 5$ simulation is given in Figure 7.1 and tabulated in Table 7.1. Note that there are at least two possible $\vec{p}$ values for each distinct ω, hence we present all T_1 results with same ω averaged to improve statistics. As p_x has a larger impact on ω than p_y for this choice of $\vec{q}$, ω is not proportional to $|\vec{p}|$, providing a good ω 'lever arm' for fits for co–prime q_x and q_y.

As discussed in §5.3, the contraction of modified and unmodified correlators allow us to choose u, d, $u+d$ and $u-d$ current flavour combinations for the action modification (7.2), which can be decomposed into uu, dd and ud flavour combinations. In the vector case, these are then related to the proton and neutron electromagnetic Compton amplitude by

$$T_1^p(\omega, Q^2) = \frac{4}{9} T_1^{uu}(\omega, Q^2) + \frac{1}{9} T_1^{dd}(\omega, Q^2) - \frac{2}{9} T_1^{ud}(\omega, Q^2) \tag{7.7}$$

$$T_1^n(\omega, Q^2) = \frac{1}{9} T_1^{uu}(\omega, Q^2) + \frac{4}{9} T_1^{dd}(\omega, Q^2) - \frac{2}{9} T_1^{ud}(\omega, Q^2). \tag{7.8}$$

p	17ω
$(-2,-1,0)$	-18
$(-2,0,0)$	-16
$(-2,1,0)$	-14
$(-1,-2,0)$	-12
$(-1,-1,0)$	-10
$(-1,0,0)$	-8
$(-1,1,0)$	-6
$(-1,2,0)$	-4
$(0,-2,0)$	-4
$(0,-1,0)$	-2
$(0,0,0)$	0
$(0,1,0)$	2
$(0,2,0)$	4
$(1,-2,0)$	4
$(1,-1,0)$	6
$(1,0,0)$	8
$(1,1,0)$	10
$(1,2,0)$	12
$(2,-1,0)$	14
$(2,0,0)$	16
$(2,1,0)$	18

Table 7.1: The momenta $\vec{p}$ and their corresponding ω values.

Note that experiment are only able to extract data from physical targets like a proton or neutron, which without further data does not allow them to decompose the quark flavour components, as this technique is able to.

Finally the $\omega = 0$ term is subtracted from the data, to match our subtracted dispersion relationship (2.80). The subtraction function of the Compton amplitude on it's own will be discussed in §8.

7.1.2 Simulation Details

As it is of much interest to study the Q^2 evolution, we are using lattices, with large set of different $\vec{q}$. For each lattice and $\vec{q}$ we use multiple λ as discussed in §5.6 to verify the quadratic or bilinear regime. The λ chosen vary in size as some of the results were generated either in single precision floating point on GPUs or before the λ tuning was well understood. Other simulations use small λ, as is done for all new simulations performed with double precision floating point. In some cases only one λ was generated, but in all those cases a very close simulation was also performed, giving us confidence in staying in the quadratic regime.

The action modifications used correspond to a $\{J_\mu, J_\nu\}$ of $\{V_\mu^{loc}, V_\nu^{loc}\}$, $\{V_\mu^{con}, V_\nu^{con}\}$, $\{V_\mu^{loc}, V_\nu^{con}\}$ and $\{A_\mu^{loc}, A_\nu^{loc}\}$. Prior calculated Z_V (5.47) and Z_A [186] were used to renormalise the local currents. The conserved current, by construction has $Z_V = 1$.

Multiple lattices are used in the calculation as different lattice spacings and volumes give us important information of our discretisation systematics. However as Q^2 is dependent on both β and L, such differing lattices do not give exact matching in Q^2. In some cases a different $\vec{q}$ can be picked that corresponds to an existing Q^2, but this causes the non–zero ω to not match in general. Instead we shall examine this in §8.5 and see that there are no significant effects.

The resulting simulation parameters are tabulated in Table 7.2, and additional information about the ensembles used are available in §E.2.

β	$L^3 \times T$	κ	$\{J_\mu, J_\nu\}$	$\vec{q}$	$a\lambda$	N_s	$N_{src/cfg}$
5.4	$32^3 \times 64$	$(0.11993, 0.11993)$	$\{V_3^{con}, V_3^{con}\}$	$(4,1,0)$	$[0.01, 0.001, 0.0001]$	194	1.0
5.5	$32^3 \times 64$	$(0.1209, 0.1209)$	$\{V_3^{con}, V_3^{con}\}$	$(1,0,0)$	$[0.001, 0.0001]$	1024	1.0
5.5	$32^3 \times 64$	$(0.1209, 0.1209)$	$\{V_3^{con}, V_3^{con}\}$	$(1,1,0)$	$[0.01, 0.001, 0.0001]$	928	1.0
5.5	$32^3 \times 64$	$(0.1209, 0.1209)$	$\{V_3^{con}, V_3^{con}\}$	$(2,0,0)$	$[0.001, 0.0001]$	802	1.0
5.5	$32^3 \times 64$	$(0.1209, 0.1209)$	$\{V_3^{con}, V_3^{con}\}$	$(4,0,0)$	$[0.001, 0.0001]$	761	1.0
5.5	$32^3 \times 64$	$(0.1209, 0.1209)$	$\{V_3^{con}, V_3^{con}\}$	$(4,1,0)$	$[0.01, 0.001, 0.0001]$	1517	1.4
5.5	$32^3 \times 64$	$(0.1209, 0.1209)$	$\{V_3^{loc}, V_3^{loc}\}$	$(1,0,0)$	$[0.025]$	1001	1.0
5.5	$32^3 \times 64$	$(0.1209, 0.1209)$	$\{V_3^{loc}, V_3^{loc}\}$	$(1,1,0)$	$[0.0125, 0.025]$	754	1.0
5.5	$32^3 \times 64$	$(0.1209, 0.1209)$	$\{V_3^{loc}, V_3^{loc}\}$	$(2,0,0)$	$[0.0125, 0.025]$	902	1.0
5.5	$32^3 \times 64$	$(0.1209, 0.1209)$	$\{V_3^{loc}, V_3^{loc}\}$	$(2,1,0)$	$[0.0125, 0.025, 0.0375]$	1758	1.0
5.5	$32^3 \times 64$	$(0.1209, 0.1209)$	$\{V_3^{loc}, V_3^{loc}\}$	$(3,1,0)$	$[0.0125, 0.025, 0.0375]$	8668	4.9
5.5	$32^3 \times 64$	$(0.1209, 0.1209)$	$\{V_3^{loc}, V_3^{loc}\}$	$(3,2,0)$	$[0.0125, 0.025, 0.0375]$	1234	1.0
5.5	$32^3 \times 64$	$(0.1209, 0.1209)$	$\{V_3^{loc}, V_3^{loc}\}$	$(4,0,0)$	$[0.0005, 5e-05]$	512	1.0
5.5	$32^3 \times 64$	$(0.1209, 0.1209)$	$\{V_3^{loc}, V_3^{loc}\}$	$(0,1,4)$	$[5e-05, 5e-06]$	1694	1.0
5.5	$32^3 \times 64$	$(0.1209, 0.1209)$	$\{V_3^{loc}, V_3^{loc}\}$	$(0,4,1)$	$[5e-05, 5e-06]$	1403	1.0
5.5	$32^3 \times 64$	$(0.1209, 0.1209)$	$\{V_3^{loc}, V_3^{loc}\}$	$(4,1,0)$	$[0.0125, 0.025]$	10461	5.9
5.5	$32^3 \times 64$	$(0.1209, 0.1209)$	$\{V_3^{loc}, V_3^{loc}\}$	$(4,2,0)$	$[0.0125, 0.025, 0.0375]$	1758	1.0
5.5	$32^3 \times 64$	$(0.1209, 0.1209)$	$\{V_3^{loc}, V_3^{loc}\}$	$(4,3,0)$	$[0.0125, 0.025, 0.0375]$	1758	1.0
5.5	$32^3 \times 64$	$(0.1209, 0.1209)$	$\{V_3^{loc}, V_3^{loc}\}$	$(5,1,0)$	$[0.025, 0.05]$	7036	4.0
5.5	$32^3 \times 64$	$(0.1209, 0.1209)$	$\{V_3^{loc}, V_3^{loc}\}$	$(5,1,0)$	$[5e-05, 5e-06]$	4313	2.5
5.5	$32^3 \times 64$	$(0.1209, 0.1209)$	$\{V_3^{loc}, V_3^{loc}\}$	$(3,5,0)$	$[0.0375, -0.075]$	1006	1.0
5.5	$32^3 \times 64$	$(0.1209, 0.1209)$	$\{V_3^{loc}, V_3^{loc}\}$	$(5,3,0)$	$[0.05]$	3052	3.0
5.5	$32^3 \times 64$	$(0.1209, 0.1209)$	$\{V_3^{loc}, V_3^{loc}\}$	$(6,3,0)$	$[0.025, 0.05]$	618	1.0
5.5	$32^3 \times 64$	$(0.1209, 0.1209)$	$\{V_3^{loc}, V_3^{loc}\}$	$(7,3,0)$	$[0.025, 0.05]$	602	1.0
5.5	$32^3 \times 64$	$(0.1209, 0.1209)$	$\{V_3^{loc}, V_3^{con}\}$	$(0,1,4)$	$[0.001, 0.0001]$	1767	1.5
5.5	$32^3 \times 64$	$(0.1209, 0.1209)$	$\{V_3^{loc}, V_3^{con}\}$	$(4,0,1)$	$[0.001, 0.0001]$	1915	1.5
5.5	$32^3 \times 64$	$(0.1209, 0.1209)$	$\{V_3^{loc}, V_3^{con}\}$	$(4,1,0)$	$[0.001, 0.0001]$	1507	1.4
5.5	$32^3 \times 64$	$(0.1209, 0.1209)$	$\{V_3^{loc}, V_3^{con}\}$	$(6,1,0)$	$[0.001, 0.0001]$	1153	1.3
5.65	$48^3 \times 96$	$(0.122005, 0.122005)$	$\{V_3^{loc}, V_3^{loc}\}$	$(1,0,0)$	$[0.01, 0.02]$	500	1.0
5.65	$48^3 \times 96$	$(0.122005, 0.122005)$	$\{V_3^{loc}, V_3^{loc}\}$	$(1,1,0)$	$[0.01, 0.02]$	500	1.0
5.65	$48^3 \times 96$	$(0.122005, 0.122005)$	$\{V_3^{loc}, V_3^{loc}\}$	$(2,0,0)$	$[0.0125, 0.025]$	498	1.0
5.65	$48^3 \times 96$	$(0.122005, 0.122005)$	$\{V_3^{loc}, V_3^{loc}\}$	$(2,1,0)$	$[0.0125, 0.025]$	498	1.0
5.65	$48^3 \times 96$	$(0.122005, 0.122005)$	$\{V_3^{loc}, V_3^{loc}\}$	$(3,1,0)$	$[0.0125, 0.0375]$	536	1.0
5.65	$48^3 \times 96$	$(0.122005, 0.122005)$	$\{V_3^{loc}, V_3^{loc}\}$	$(7,4,0)$	$[0.0125, 0.0375]$	536	1.0

Table 7.2: Parameters for the gauge–field ensembles §E.2 used as specified by coupling constant β, dimension $L^3 \times T$ and quark mass parameters κ. Each simulation is performed using even time currents J_μ and J_ν at specified momentum transfer $\vec{q}$ for a series of λ, with a total of N_s sources with $N_{src/cfg}$ average sources per used trajectory.

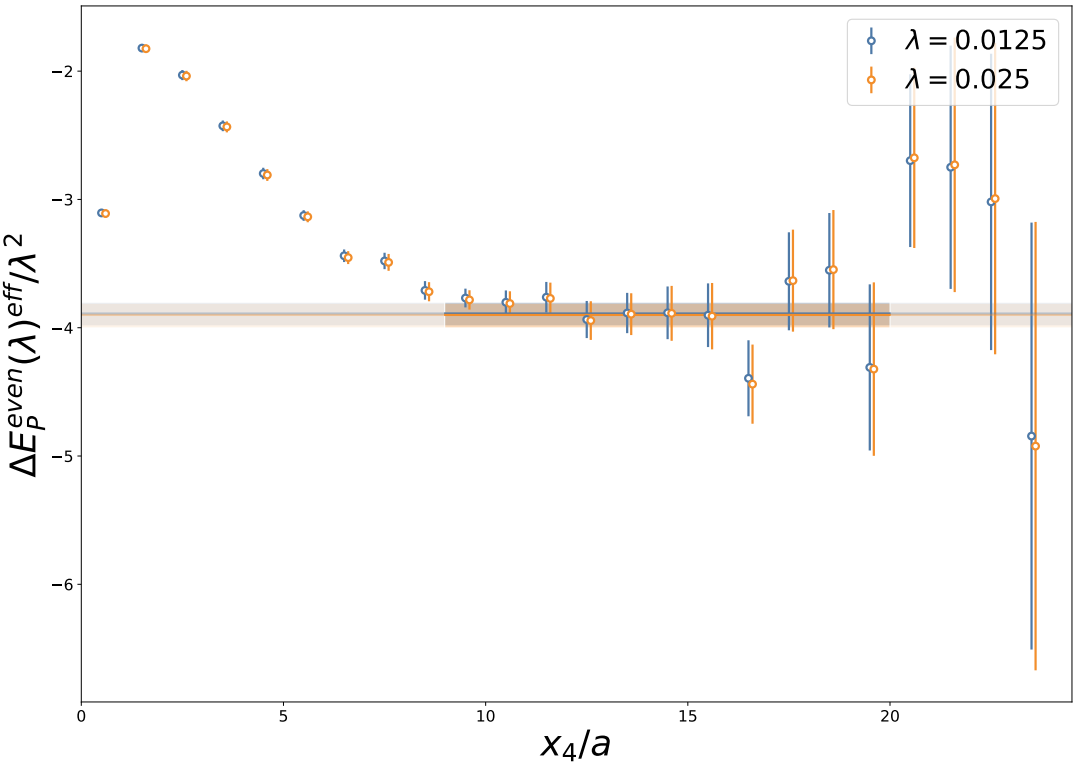

Figure 7.2: The effective mass of the ratio (5.25), which corresponds to the even energy shift ΔE^{even} shifted by λ^2 for the Compton amplitude T_{33} for d flavoured currents, $\vec{p} = \vec{0}$ and $\vec{q} = (4, 1, 0)$ for different λ. The fitting range $x_4 \in [11, 31]$, has been chosen by picking the starting slice such that χ^2_{dof} is closest 1.

7.1.3 Results

Figure 7.2 shows the effective mass for $\vec{p} = \vec{0}$ for the $\beta = 5.5$, $32^3 \times 64$, $SU(3)_{flav}$-symmetric ensemble with $\vec{q} = (4, 1, 0)$ which corresponds to $Q^2 = 4.64\ GeV^2$. We are able to identify a clean plateaux and both values of λ are consistent once scaled, which shows we are well within a quadratic regime; $\Delta E^{even}/\lambda^2 = \frac{\partial^2 E}{\partial \lambda^2}$, allowing us to determine T_1. The fitting range varies widely from the underlying two-point correlators (see Figure 3.7 for nucleon mass determination from the same data.)

After the remaining $\vec{p}$ with $\omega < 1$ from the same simulation are fit, we get the subtracted Compton amplitude at $Q^2 = 4.64\ GeV^2$ against ω. Figure 7.3 shows the results available from u and d action modifications. The FHT approach hence is able to extract a more complete ω behaviour for the Compton amplitude on the lattice than was available before. Unlike comparable techniques, the structure functions (after continuum and chiral extrapolation) are comparable directly to their continuum Minkowski space counterparts. The uncertainty in signal is not dependent on ω, rather it's dependent on $|\vec{p}|$.

We have implemented two different vector currents in three different combinations. As they each correspond to the same continuum current, they should give the same result and Figure 7.4 shows that they indeed do. However the relative uncertainty at each ω point differs between the techniques, the conserved current provides more precise results at low $|\vec{p}|$ and less precise at large $|\vec{p}|$ for the same statistics than the local current, and the interference current is somewhere between both. Due to the difference in implementation of the conserved and local vector currents, both have their use cases. The different vector results are somewhat statistically independent, so from here on out we will present only vector results, averaged over the different methods. Additional flavour comparisons are available in Figure B.1, Figure B.2 and Figure B.3.

With simulations taken from multiple different Q^2 we can perform a rough check on the

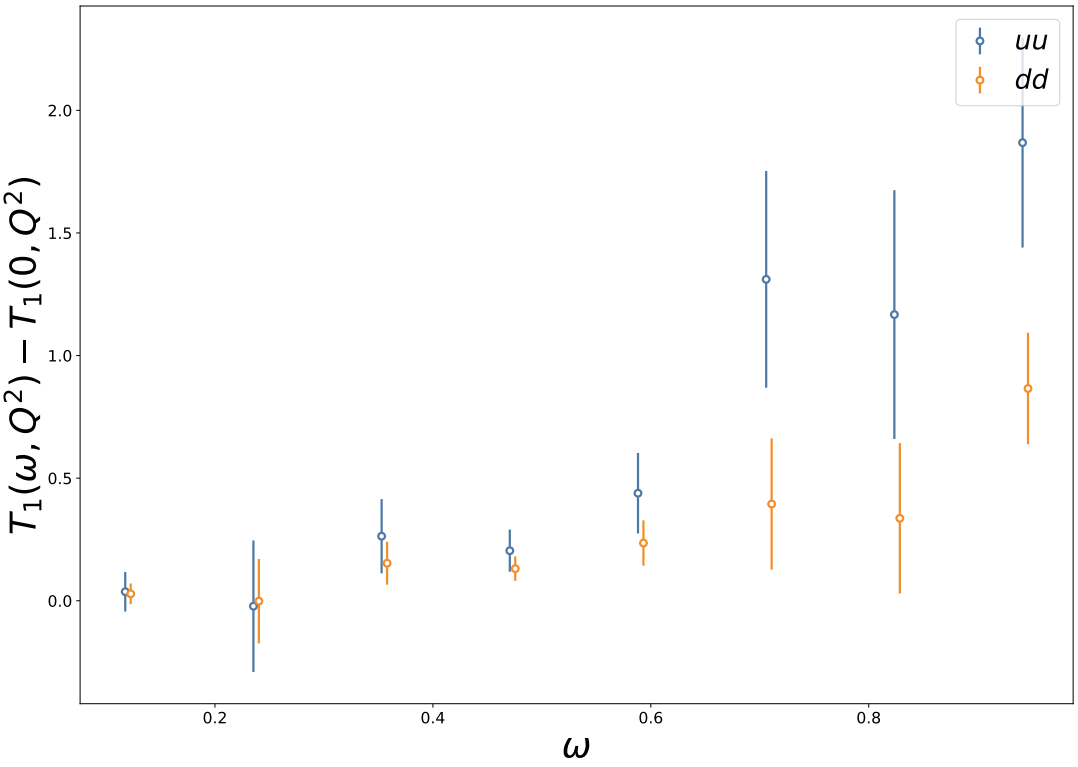

Figure 7.3: The subtracted and flavour decomposed Compton amplitude structure function $T_1^{uu/dd}(\omega, Q^2) - T_1^{uu/dd}(0, Q^2)$ for $\vec{q} = (4, 1, 0)$ which corresponds to $Q^2 = 4.64$ GeV^2. The points have been offset slightly for clarity.

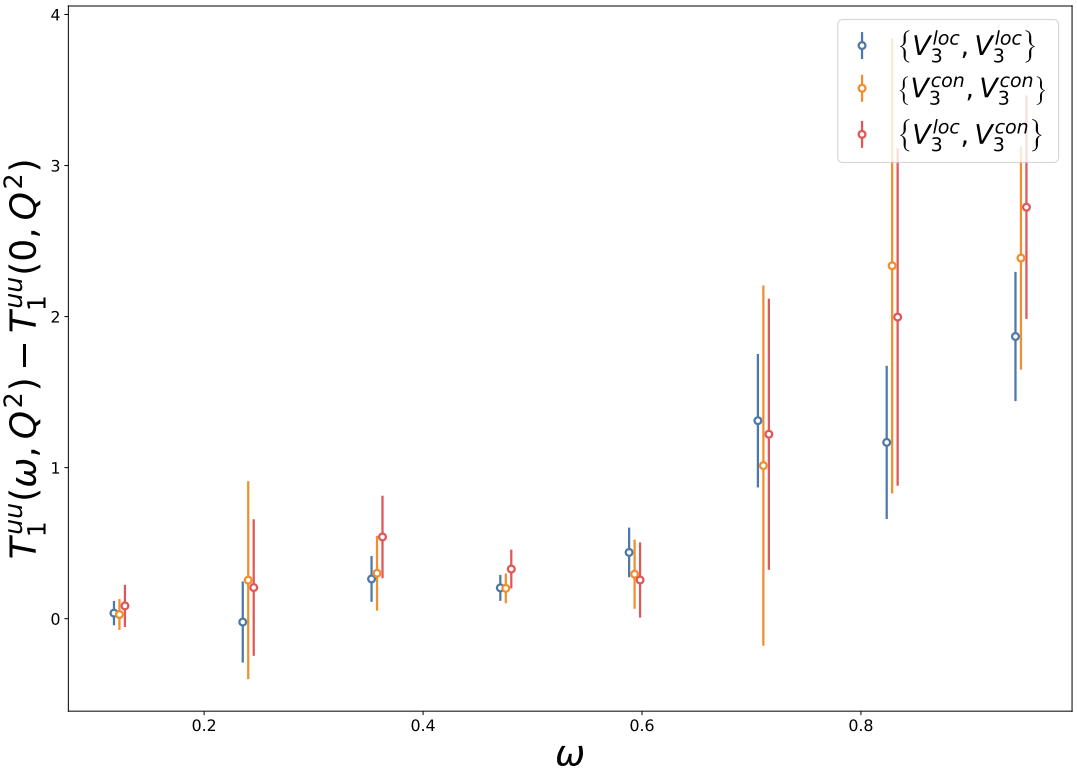

Figure 7.4: Operator comparison of the subtracted Compton amplitude $T_1^{uu}(\omega, Q^2) - T_1^{uu}(0, Q^2)$ for $\vec{q} = (4, 1, 0)$ for a set of different currents. Note that there is a large difference in the number of sources between the V_3^{loc} and the other currents (Table 7.2).

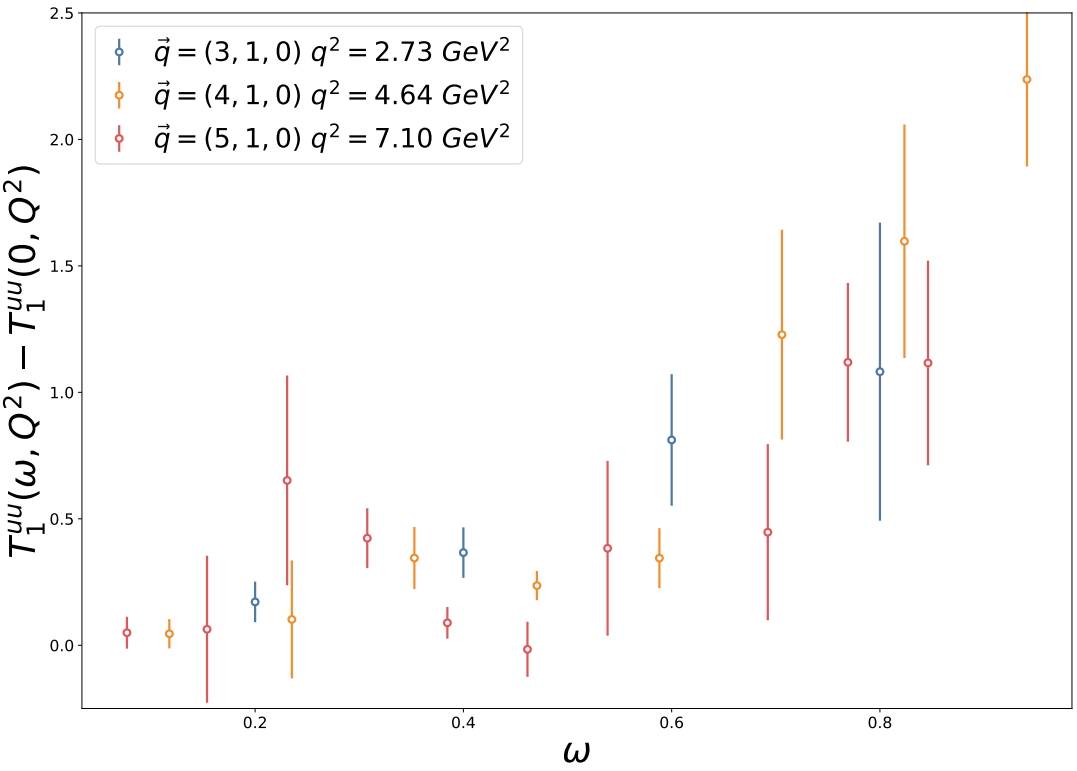

Figure 7.5: The subtracted Compton amplitude $T_1^{uu}(\omega, Q^2) - T_1^{uu}(0, Q^2)$. The points are the high statistics $N_s = \mathcal{O}(10000)$ simulations from Table 7.2.

scaling behaviour. The scaling behaviour itself is not expected to be strong, inheriting the logarithmic scaling behaviour from the hadron tensor. Figure 7.5 show the uu component for three high statistics runs on the same lattice as the prior results. No conclusive scaling can be seen from this, however if one were being generous, the smaller Q^2 points do appear to be systematically above the higher ones. Note that it is difficult to compare the structure functions against Q^2 directly at the same ω points, this is part of the motivations for looking at moments in §7.2, and we will partially get around this through clever choice of $\vec{q}$ in §7.3. Additional $\vec{q}$ comparisons for the other flavour combination are available in Figure B.5 and Figure B.6.

It is important to look at lattice volume and spacing effects, as the mixing problem associated with higher moments has not been entirely removed, just the ultra–violet divergences as $a \to 0$. However for our lattices, a reduction in a is also associated with an increase in L, which prohibits the comparison of differing a at the same Q^2. At large Q^2 the Q^2–dependence becomes small, so we could compare slightly differing $\vec{q}$ results more easily. However the lattice momenta required for that becomes more prohibitive, and the cost associated with the larger external momenta is compounded with the increased cost of larger lattices. In our case to have similar Q^2 to a $\beta = 5.5$, $32^3 \times 64$ lattice with $\vec{q} = (5,3,0)$ for a $\beta = 5.65$, $48^3 \times 96$ lattice is $\vec{q} = (7,4,0)$. We will see a rough test of this using moments §7.2 but a more definitive test is presented later in §8.5, where consistency between different β is seen more easily.

So far extractions have been limited to the uu and dd Compton amplitude, obtainable directly from the u and d flavoured currents. We also have the $u - d$ and $u + d$ flavoured currents, from which we can extract the ud component. Combing these three components allows us to reconstruct the photonic proton (7.7) and neutron (7.8) structure functions. Figure 7.6 shows the high statistics proton structure function. This sets the stage for future calculations, extrapolated to the continuum for comparison to the experimental hadron tensor. In principle the same reconstruction technique can be extended to other electroweak currents as well. The ud component required for the reconstruction is actually highly interesting by itself as it is a term of higher–twist, and will be discussed in §7.4.

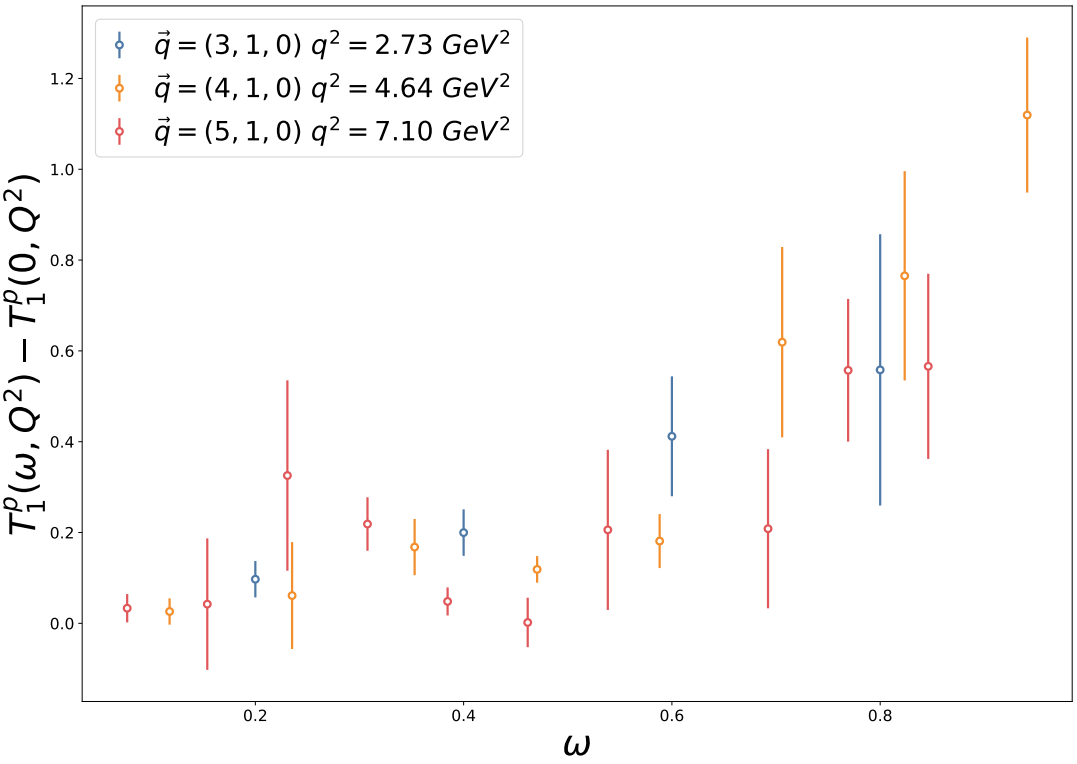

Figure 7.6: The reconstructed subtracted proton Compton amplitude $T_1^p(\omega, Q^2) - T_1^p(0, Q^2)$. The points are the high statistics subset of data points of our simulation Table 7.2. The neutron equivalent is shown in Figure B.4.

We have shown the first model–independent calculation of the subtracted Compton amplitude structure functions T_1 and are ready to examine these results further. In the remaining part of the chapter we cover extractions of moments §7.2, scaling §7.3 and higher twist behaviour §7.4 from these results.

7.2 Moments

The moments of the hadron tensor are defined

$$\mu_n^{f_1 f_2} := \int_0^1 dx x^{n-1} F_1^{f_1 f_2}(x, Q^2) \tag{7.9}$$

where f_i denote the quark flavours. When $f_1 = f_2 = f$ the Hadron tensor moments are related to quark moments in the parton model at sufficiently large Q^2 by

$$\mu_n^{ff} = \frac{1}{2}\langle x^{n-1} \rangle^f. \tag{7.10}$$

We will show that (2.80) allows us to extract such moments from the Compton amplitude.

While the lowest lying moments of the lattice are well understood [130], the higher moments are plagued with mixing problems due to the breaking of the continuum symmetry group $O(4)$ to the hyper-cubic group $H(4)$ §3.3. Some attempts have been made to take into account such moments to calculate higher order moments [245–249] although these are still limited to $\langle x^3 \rangle$ for baryons. By inferring the moments directly from the forward unpolarised Compton amplitude, we can extract the (even) moments, without having to account for ultraviolet divergent mixing. While quenched calculations of baryon $\langle x^3 \rangle$ have been performed [245], the renormalisation

for this method is difficult. As the divergence caused by the mixing is currently the main difficulty for extracting moments beyond $\langle x^2 \rangle$, this would lead to first *ab initio* determination of such quantities without this problem.

While many moments are required for a full reconstruction of the hadron tensor at low Q^2, even a few moments are useful in constraining hadron tensor models such as the model in [99] used to calculate the $\Box_{\gamma Z}$ box. In the DIS region, the moments can be used to reconstruct the PDFs, even with relatively few moments [244].

While different Q^2 lattice results do not share the same ω, they do share the same moments, so we can use the moments to investigate the scaling behaviour more directly. The operators associated with the moments in the DIS limit are expected to have *Bjorken scaling*, up to a small deviation due to operator scaling from the *Callan–Symanzik equation* governed by the anomalous dimension γ of the three–point current vertex. As each of the moments has been extracted at a different energy scale Q, this allows us to relate them to another scale μ by [250]

$$\langle x^n \rangle^f_\mu = \left(\frac{\log\left(\mu^2/\Lambda_{QCD}\right)}{\log\left(Q^2/\Lambda_{QCD}\right)} \right)^{a_n/(2\beta_0)} \langle x^n \rangle^f_Q. \tag{7.11}$$

Here β_0 is defined in (2.7) and a_n is the leading term in the γ function of $\langle x^n \rangle$

$$a_n = -\frac{8}{3}\left(1 - \frac{2}{n(n+1)} + 4\sum_{j=2}^{n}\frac{1}{j}\right). \tag{7.12}$$

This is all done under the assumption of no mixing with the equivalent twist gluonic operators, so we have to restrict ourselves to those operators without gluon mixing. As the gluon is flavour blind we can take our flavour combination $uu - dd$ combination, which corresponds to an isovector quark moment $\langle x^n \rangle^{u-d}$, to remove the mixing. To extend this result to include the mixing, one would require knowledge of either the gluon moments or the EMT.

7.2.1 Analysis

We showed that by using an optical theorem we can relate T_1 to a geometric sum of F_1 (2.80). We now relate this to the PDF quark moments through use of *Callan–Gross*. We can write (2.80) in terms of it's geometric series

$$T_1^{f_1 f_2}(\omega, Q^2) - T_1^{f_1 f_2}(0, Q^2) = 4\omega^2 \int_0^1 dx \frac{x F_1^{f_1 f_2}(x, Q^2)}{1 - (\omega x)^2} \tag{7.13}$$

$$= \sum_{n=1}^{\infty} 4\omega^{2n} \int_0^1 dx x^{2n-1} F_1^{f_1 f_2}(x, Q^2) \tag{7.14}$$

$$= \sum_{n=1}^{\infty} 4\omega^{2n} \mu_{2n}^{f_1 f_2} \tag{7.15}$$

We now use *Callan-Gross*

$$F_2(x, Q^2) = 2x F_1(x, Q^2). \tag{7.16}$$

our moments where $f_1 = f_2 = f$ are related to the PDFs using (2.63) at leading twist by

$$\mu_n^{ff} = \frac{1}{2}\int_0^1 dx x^n F_2^{ff}(x, Q^2) \tag{7.17}$$

$$= \frac{1}{2}\int_0^1 dx x^{n-1}\left(q_f(x) + \overline{q}_f(x)\right) \tag{7.18}$$

$$= \frac{1}{2}\langle x^{n-1} \rangle^f. \tag{7.19}$$

Relating all of these together we can rewrite the subtracted Compton amplitude as

$$\boxed{T_1^{ff}(\omega, Q^2) - T_1^{ff}(0, Q^2) = \sum_{n=1}^{\infty} 2\omega^{2n} \langle x^{2n-1} \rangle^f} \tag{7.20}$$

As $T_1^{p/n}$ come from cross–sections, they must be positive over the entire kinematic region. The same holds for uu and dd quark moments separately. As a consequence (7.9) implies that the corresponding moments must approach zero monotonically

$$\mu_0^{ff} \geq \mu_1^{ff} \geq \mu_2^{ff} \geq \cdots \geq 0. \tag{7.21}$$

The same is not true for μ_n^{ud}, although using the proton, neutron, uu and dd moments, they can be shown to tend to 0, just not monotonically. As we only extract the connected components, we miss the small disconnected component, and assume that monotonicity still holds.

As a consequence of (7.21), the series (7.20) converges and we can fit an even polynomial to extract the moments. However such a fit does not take into account the decreasing nature of the moments, while a Bayesian approach is in development [251] we pick a least square approach here. We can enforce the decreasing nature by fitting

$$P_{2n}^{con} = \sum_{m=1}^{n} c_2 \left(\prod_{l=2}^{m} e^{-c_{2l}} \right) \omega^{2m} \tag{7.22}$$

where we enforce positivity on c_n for $n \geq 4$. We now perform this analysis on the full data set of §7.1.2.

7.2.2 Results

Figure 7.7 shows even polynomial fits, truncated at several different powers of ω for $T_1^{uu}(\omega, Q^2) - T_1^{uu}(0, Q^2)$ at one fixed Q^2, where the fits are

$$P_2^{even} = 0.70(14)\omega^2 \tag{7.23}$$
$$P_4^{even} = 0.45(19)\omega^2 + 0.57(32)\omega^4 \tag{7.24}$$
$$P_6^{even} = 0.86(53)\omega^2 - 1.5(24)\omega^4 + 1.9(22)\omega^6 \tag{7.25}$$
$$P_{10}^{even} = 4.6(23)\omega^2 - 41(24)\omega^4 + 140(89)\omega^6 - 189(128)\omega^8 + 88(63)\omega^{10} \tag{7.26}$$

which is clearly not a well constrained fit.

We now investigate the use of constrained polynomial fits (7.22), to enforce monotonicity. Figure 7.8 shows these fits to $T_1^n(\omega, Q^2) - T_1^n(0, Q^2)$. It is straight away evident that the fits exhibit more consistent behaviour with $n > 2$ fits. The resulting fit coefficients are

$$P_2^{con} = 0.416(78)\omega^2 \qquad \chi^2_{dof} = 2.49 \tag{7.27}$$
$$P_4^{con} = 0.335(58)\omega^2 + 0.326(59)\omega^4 \qquad \chi^2_{dof} = 1.41 \tag{7.28}$$
$$P_6^{con} = 0.297(62)\omega^2 + 0.260(64)\omega^4 + 0.207(96)\omega^6 \qquad \chi^2_{dof} = 1.19 \tag{7.29}$$
$$P_8^{con} = 0.289(70)\omega^2 + 0.208(63)\omega^4 + 0.178(65)\omega^6 + 0.152(76)\omega^8 \qquad \chi^2_{dof} = 1.66 \tag{7.30}$$
$$P_{10}^{con} = 0.289(75)\omega^2 + 0.187(67)\omega^4 + 0.158(60)\omega^6 + 0.126(63)\omega^8 + 0.100(65)\omega^{10} \qquad \chi^2_{dof} = 2.61. \tag{7.31}$$

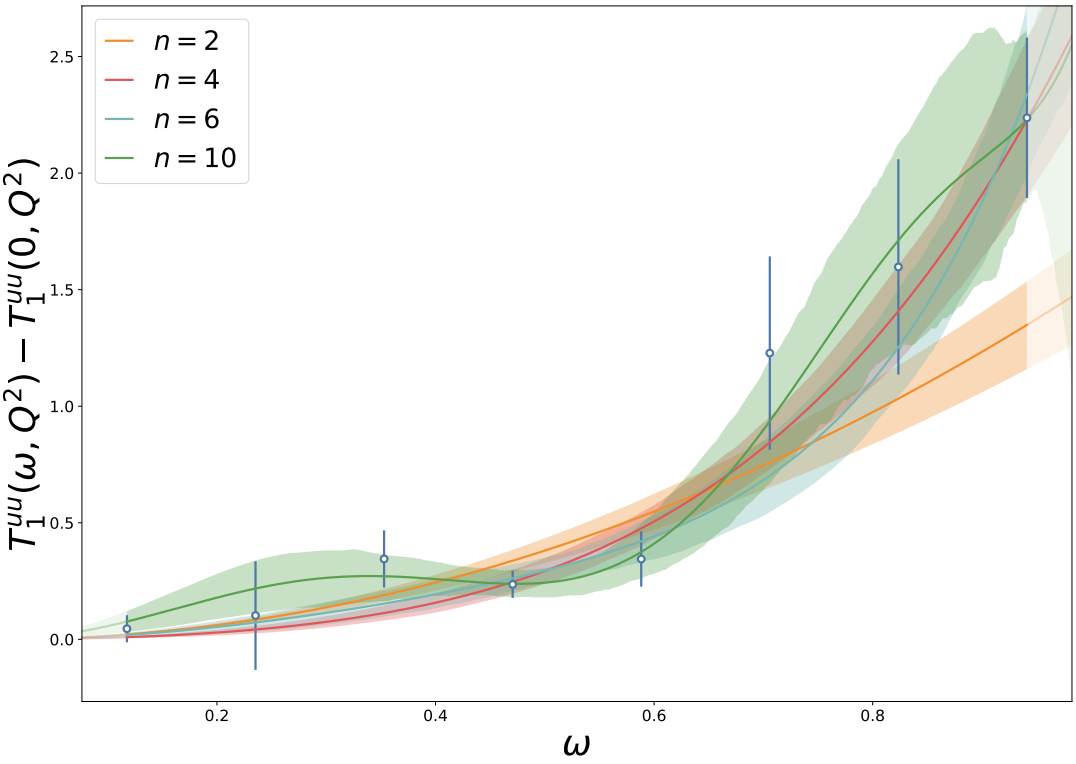

Figure 7.7: We show the subtracted Compton amplitude $T_1^{uu}(\omega, Q^2) - T_1^{uu}(0, Q^2)$ for $\vec{q} = (4, 1, 0)$ with a number of simple even polynomial fits without an ω^0 component for $\omega < 1$, the valid region for our derived dispersion relationship (2.80). The lack of description of these unconstrained polynomials has lead to modified fits as described in §7.2.

First we note the coefficients are more stable, all the coefficients at each order are consistent with each other, but the P_6^{con} has the closest χ^2_{dof} to one, so we shall use this fit in our analysis. The exact same story plays out with the other flavours too, however their best polynomial order differs.

To compare the result to experiment, we can use these moments to construct $uu - dd$ flavour components, which correspond to the isovector quark moments $\langle x^n \rangle^{u-d}$. The resulting inferred fit is

$$T_1^{uu-dd}(\omega, Q^2) - T_1^{uu-dd}(0, Q^2) = 0.513(100)\omega^2 + 0.57(13)\omega^4 + 0.47(30)\omega^6 \tag{7.32}$$

which corresponds to

$$\langle x \rangle^{u-d}_{\mu=2.16GeV} = 0.257(50). \tag{7.33}$$

It is standard in literature to quote the isovector momentum fraction value at $\mu = 2.0\,GeV$, so we use a fit to the expected scaling behaviour to determine this quantity. Figure 7.9 shows all our isovector momentum fractions for a range of Q. Our extracted moments are consistent with the expected scaling behaviour (7.11), although with this precision in measurement over this range of Q we do not expect to be able to observe small deviations from such scaling. The fit is (7.11) for points $Q > 1.5\,GeV$, as at low Q scaling breaks down and we cannot link our moments and the parton model. There is some tension starting to show from the deviation of this scaling, the values smaller than $Q = 2.0\,GeV$ are systematically higher, and the values larger are systematically lower, however the signal quality is not yet good enough to resolve this. Quoted at $\mu = 2.0\,GeV$ the fit gives

$$\langle x \rangle^{u-d}_{\mu=2.0\ GeV} = 0.293(29). \tag{7.34}$$

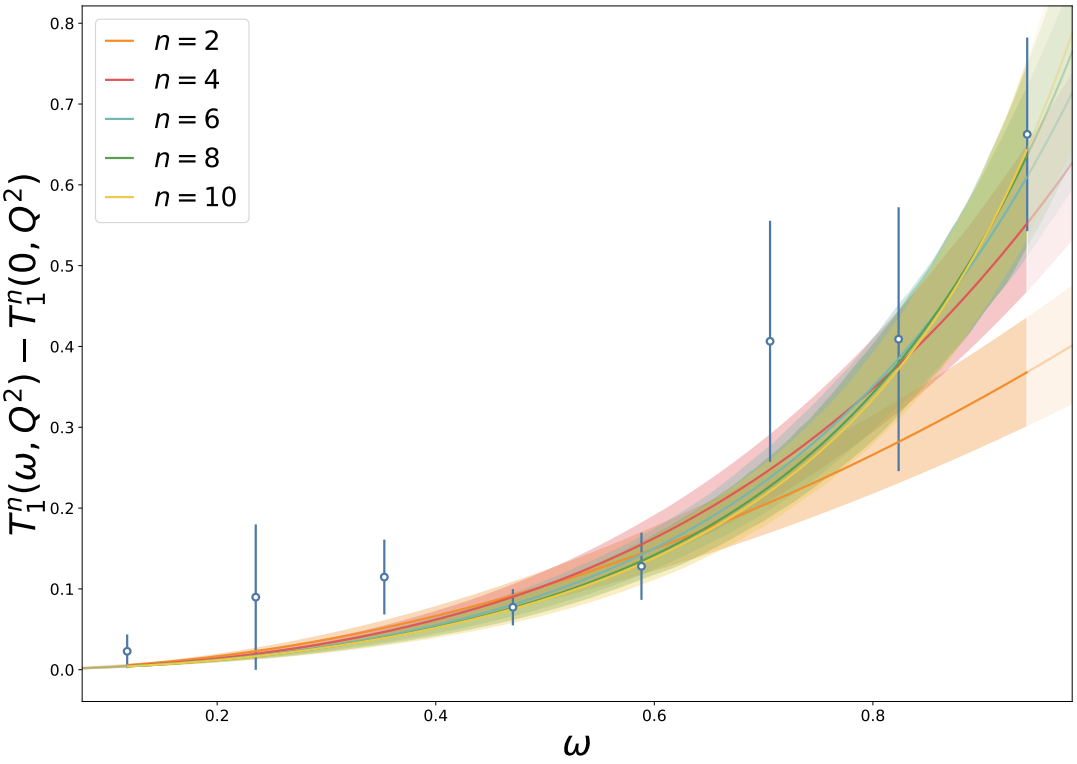

Figure 7.8: The constrained polynomials fits to the Compton amplitude $T_1^n(\omega, Q^2) - T_1^n(0, Q^2)$ for $\vec{q} = (4, 1, 0)$ of the neutron. The different fits are for different orders as described in the text, with ω points fitted only for $\omega < 1$, in the region valid for the derived dispersion relationship (2.80).

This value is comparable to other results in literature but this extraction was done at larger than physical pion masses. As many lattice collaborations calculate this value as a benchmark calculation we can compare our results to theirs at equivalent pion masses. The comparative results are shown in Figure 7.10, where our point is larger than some other lattice results, but consistent with others. The larger uncertainty is because this is an indirect calculation of the momentum fraction, where the others calculate them directly using three point functions. Nevertheless we observe broad agreement within errors with other lattice results at our pion mass.

The first and third point in Figure 7.9 are from the $\beta = 5.65$ simulation, however due to the separation in Q from the low uncertainty $\beta = 5.5$ results we can only conclude that the difference is not large, we will examine whether it is significant in §8.5.

Combining the proton, neutron, uu and dd moments allow us to infer the ud moments. However performing this for our highest statistics simulations yields

$$T_1^{ud}(\omega, Q^2) - T_1^{ud}(0, Q^2) = -0.016(56)\omega^2 - 0.09(10)\omega^4 - 0.03(31)\omega^6 \tag{7.35}$$

clearly indeterminable using this technique. Using the proton, uu and dd moments as bounds an improved method could be devised, but we keep our focus on higher moments of $uu - dd$.

Figure 7.11 shows the extraction of μ_4^{u-d}, demonstrating the strength of the second order FHT approach. There are fewer μ_4^{uu-dd} moments than there were μ_2^{uu-dd} moments, but an extraction of $\langle x^3 \rangle$ is still possible. The resultant $\mu = 2.0\ GeV$ quark moment is

$$\langle x^3 \rangle^{u-d}_{\mu=2.0\ GeV} = 0.186(31). \tag{7.36}$$

The next higher moments were not extractable. The fit to our highest statistics (7.32) gave the most non–zero of the μ_6^{uu-dd}, but in combination the final result is too close to zero for comfort.

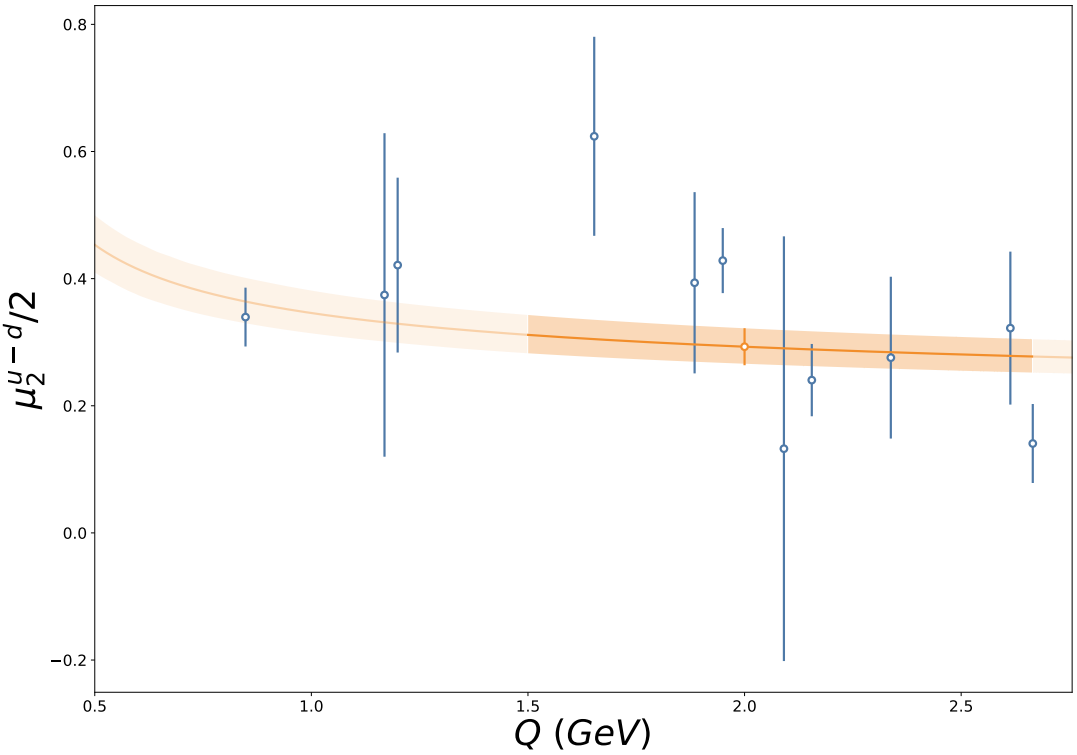

Figure 7.9: The second isovector quark moment $\mu_2^{u-d}/2$ (blue) extracted from the Compton amplitude as described in the next. The data needs to be fit when we can link the moments to the parton model and so fit using the points $Q > 1.5\ GeV$ with the expected scaling behaviour (7.11). The extracted $\langle x \rangle_Q^{u-d}$ with corresponding point at $\mu = 2.0\ GeV$ (orange) is shown.

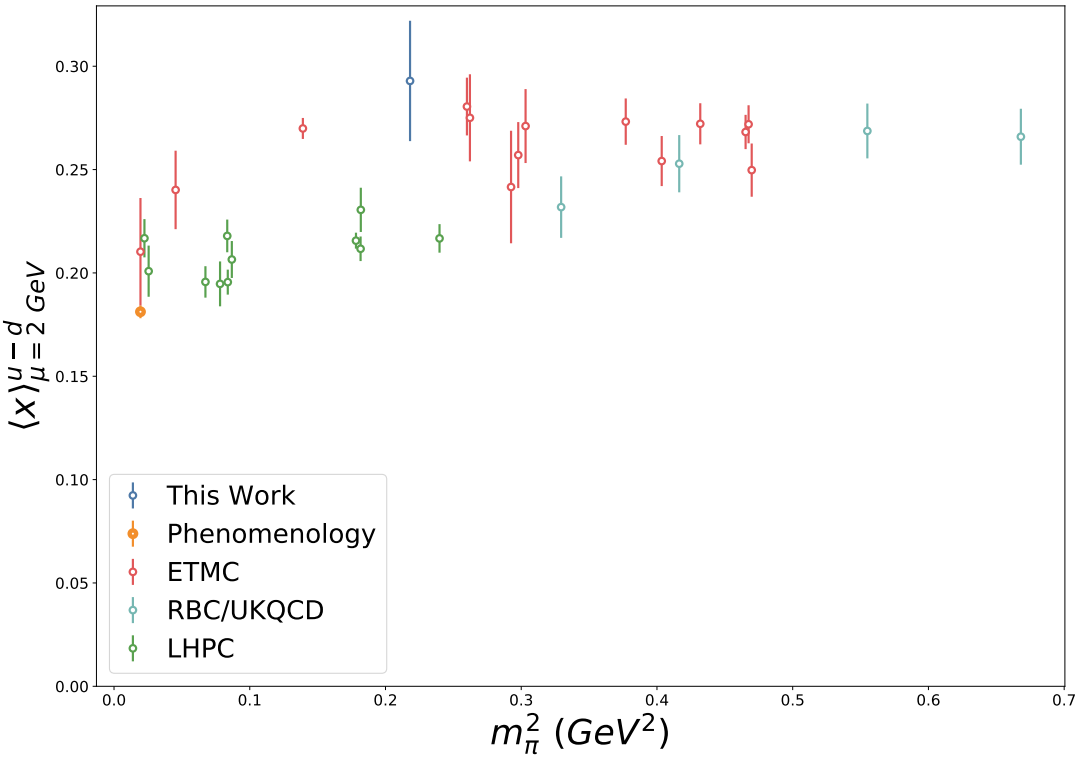

Figure 7.10: The comparison between different lattice results of $\langle x \rangle^{u-d}_{\mu=2\ GeV}$ for different m_π. The results have differing techniques, as well as lattice spacing and chiral trajectories. The results include the phenomenological extraction from experimental data (orange) [252]. Also shown are results from ETMC for $N_f = 2$ and $N_f = 2+1+1$ results (red) [253, 254] and $N_f = 2 + 1$ results; RBC/UKQCD (teal) [255], LHPC (green) [256]. Other simulations have been done but intermediate pre–chiral extrapolation data was not found [257, 258].

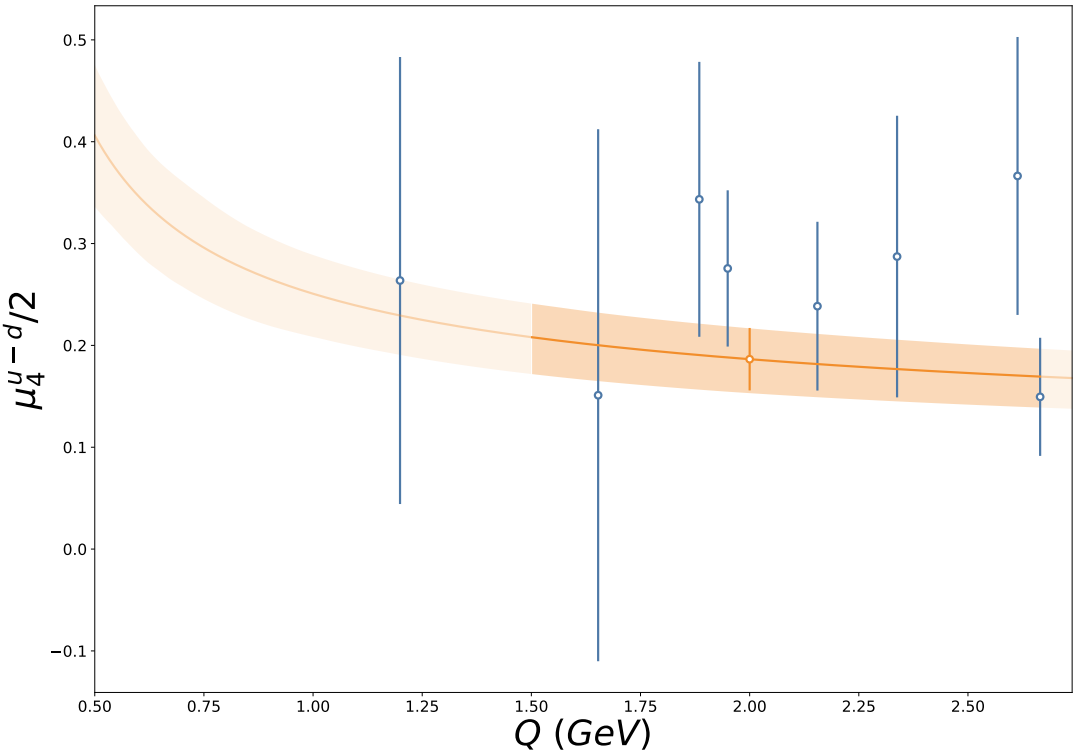

Figure 7.11: The fourth moment $\mu_4^{u-d}/2$ (blue) extracted from the Compton amplitude as described in the next. The data is fit using the points $Q > 1.5\ GeV$ with the expected scaling behaviour (7.11) and it's resultant extraction for $\langle x^3 \rangle_Q^{u-d}$ (orange) with corresponding result at $\mu = 2.0\ GeV$ shown.

As there are fewer simulations with more than two moments, many of the data points did not contribute to the μ_6^{uu-dd} extraction.

In summary we have presented the first *ab initio* extraction of the higher quark moments of the nucleon on a dynamical lattice. The observed power scaling behaviour of the moments was consistent with theory, however seen only over a small range of Q, which warrants future investigation at larger Q^2. The technique is extendible in principle to even higher moments.

7.3 Scaling

In the DIS region at constant x the proton structure function F_2 is approximately constant in Q^2, up to $\log Q^2$ scaling, which is seen in the 'fan plots' Figure 2.7. Due to the *Callan-Gross relation* the same result holds for F_1. One would think that moments, which are integrals over x of such data would exhibit the same approximate scaling behaviour. Another way to look at the same data would be to look for scaling behaviour within the Compton amplitude T_1 at unphysical x which as

$$x = \frac{1}{\omega} \tag{7.37}$$

will correspond to $x > 1$. Due to the dispersion relationship (2.80), both these scaling behaviours are the two ways of looking at the same problem. We now investigate the scaling of the Compton amplitude T_1 directly, rather than looking at moments.

The equivalent test at constant x in our case is constant ω. Our $\vec{q}$ were specifically setup (Table 7.2) to allow this direct constant ω comparison at different Q^2 to be possible. We look at a number of ω bins, where the results from $T_1(\omega, Q^2) - T_1(0, Q^2)$ are taken when ω is within 10.0% of the ω bin. In combinations with this data, we can use the fits performed of the moments to

interpolate values to the ω bins. While our data is not as precise as the equivalent experimental data for T_2, this is still a fundamental test for the behaviour predicted for the theory.

The combinations of $T_1(\omega, Q^2) - T_1(0, Q^2)$ data and our fits are shown in Figure 7.12. The larger ω is, the larger $|\vec{p}|$ is in general to obtain that ω at the same Q^2, hence the smaller ω have a better relative determination. At these small ω we see that the fits show broad consistency over the range of Q^2, except maybe at the smallest Q^2 point. The data points by themselves are not as precise as the points generated from our fits. Quantitatively no deviation from a power correction can be seen from this data, but more statistics would be need to verify this. Additional plots for smaller and larger ω are presented in Figure B.7.

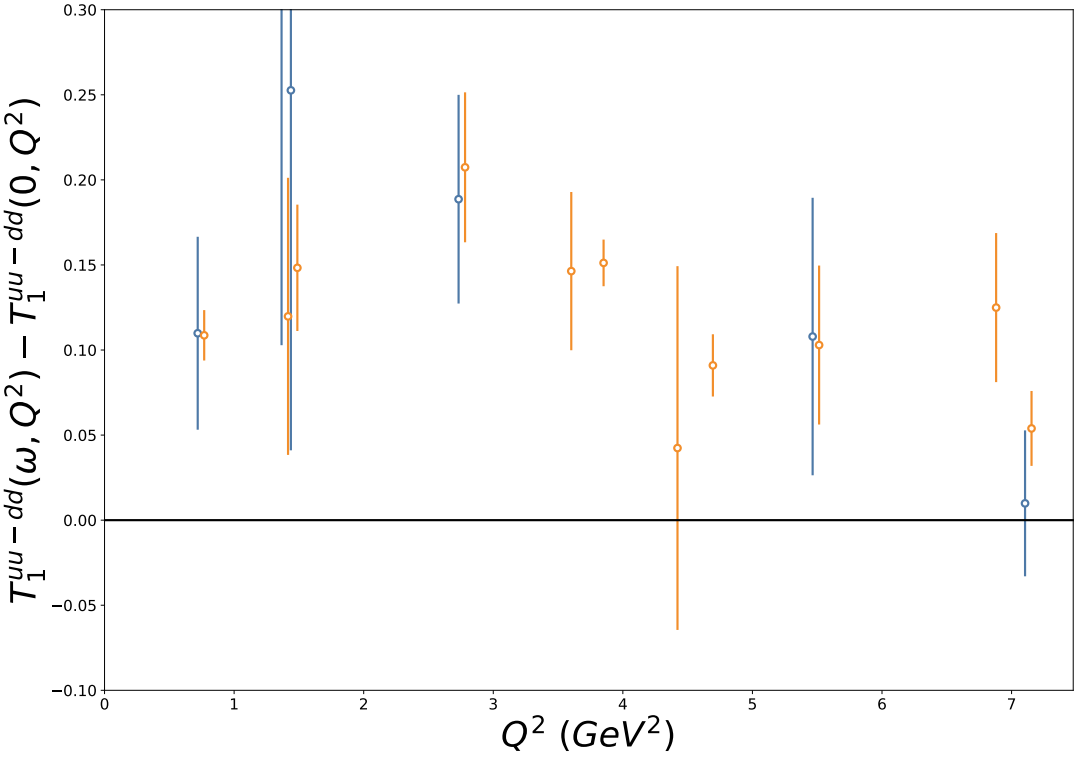

(a) $\omega = 0.4$

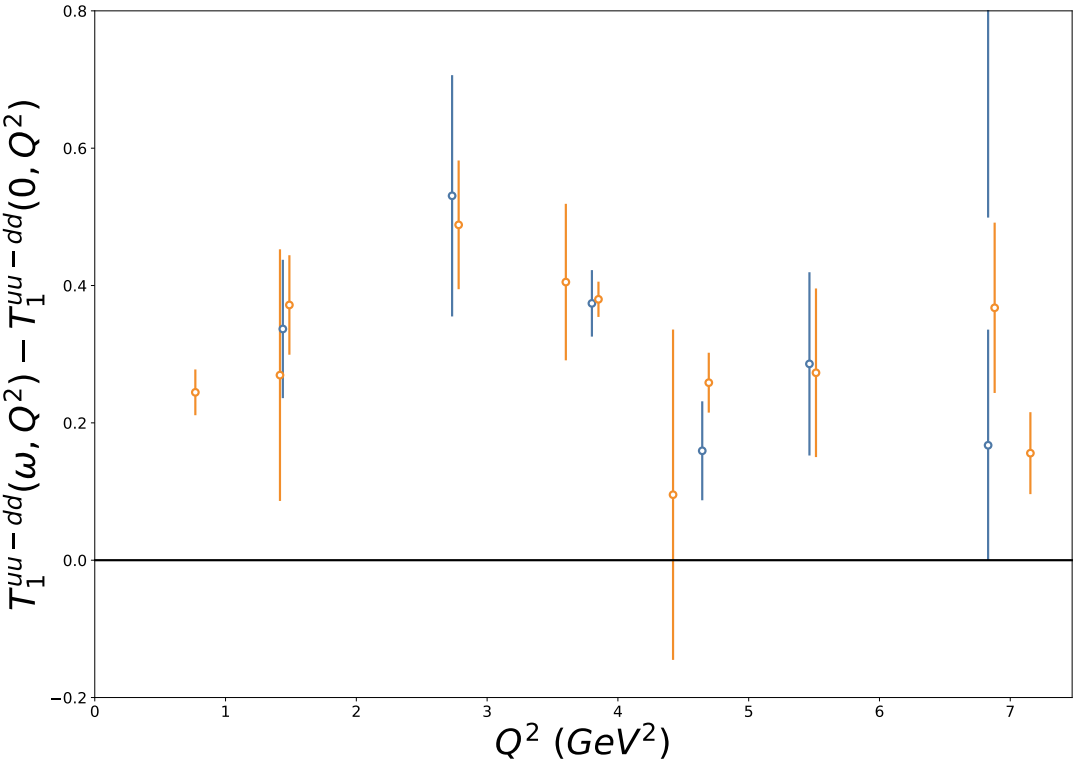

(b) $\omega = 0.6$

Figure 7.12: The scaling at constant ω of the subtracted Compton amplitude $T_1^{dd}(\omega, Q^2) - T_1^{dd}(0, Q^2)$ for $\omega = 0.4$ (a) and $\omega = 0.6$ (b). These points include direct calculations at these ω (blue), whose ω are within 10.0% of this value. The constrained fit values for each simulation have been used to generate points (orange) at these ω, offset slightly for clarity.

7.4 Higher Twist

Throughout this chapter we have focused on the proton, neutron, uu, dd and $uu-dd$ quark flavour quantities with only a brief mention of ud. By looking at either moments §7.2 or at constant ω §7.3, we can observe hints that the dominant contribution to these terms scales as logarithms in Q^2. Other than this scaling there seems to be no more Q dependence, which implies this dominant contribution is twist-2 or leading–twist (2.32). We briefly discuss higher twist diagrams, before showing how we can access these terms from the ud component.

The leading–twist terms consist of the *handbag* terms Figure 2.8. Quark and gluon lines introduce extra twist, with an example twist-3 term being the handbag diagram with gluon line connecting the interacting quark before and after one interaction. We have already shown the simplest example of higher twist, the *cat's ears* diagram Figure 2.10, whose lowest twist contributions are twist-4. These higher twist terms are important in collinear factorisation [259] and pseudo-PDFs [260], to determine whether higher twist corrections are under control.

The lowest twist contributions to the ud contribution are the twist-4 contributions from the *cat's ears* diagram, and hence has no leading twist. Thus this allows direct study of the higher twist effects within the Compton amplitude. Three high statistics results from Table 7.2, all from the $\beta = 5.5$, $32^3 \times 64$, $SU(3)_{flav}$–symmetric ensemble are shown in Figure 7.13. We clearly see the power suppression of purely higher twist terms, the Compton amplitude rapidly dies off as Q^2 increases.

The remarkable thing about the extraction of the ud term is how accurate such a higher twist extraction is. While there are methods of calculating some higher twist contributions to some quantities (see for instance [234]), direct higher twist extraction ordinarily requires the use of higher dimensional operators §2.2.1, which are harder extract quantities from on the lattice. The Q^2 dependence of the ud subtraction function is studied in §8.5.

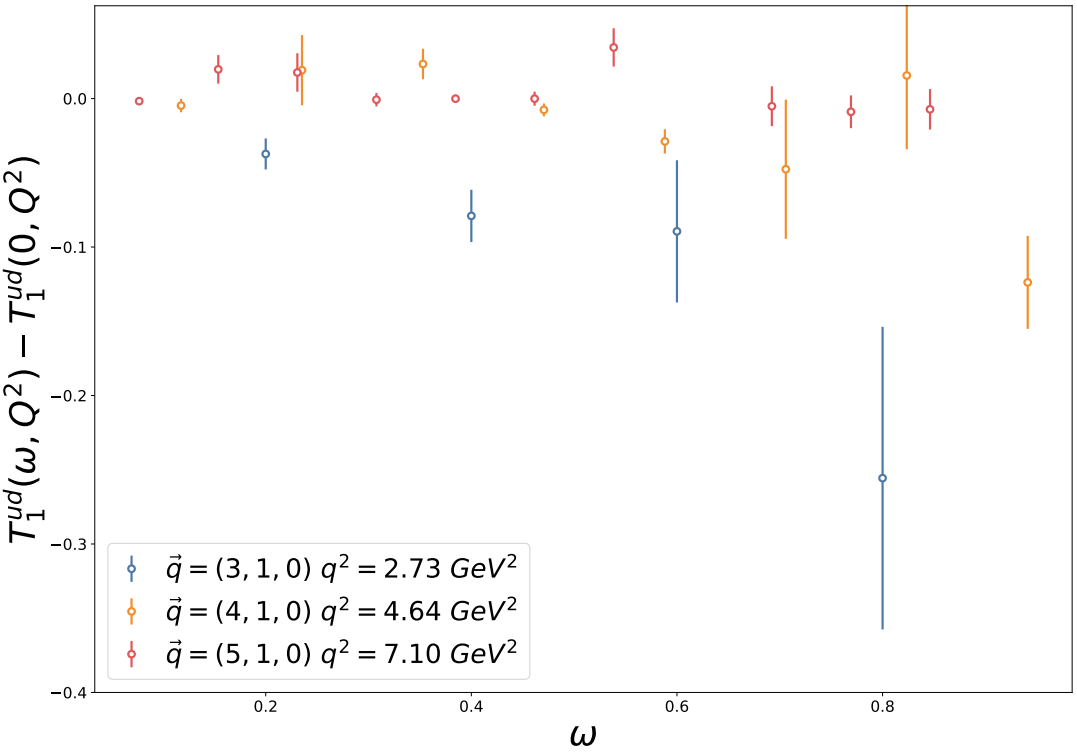

Figure 7.13: The ud extraction $T_1^{ud}(\omega, Q^2) - T_1^{ud}(0, Q^2)$ shown for three values of $\vec{q}$ corresponding to three different Q^2 values.

7.5 Summary and Outlook

We have investigated the Compton amplitude at unphysical ω, related it to the hadron tensor via dispersion relationship and hence via OPE to the PDFs. We showed for the first time that the full Compton amplitude structure function T_1 is calculable on the lattice for arbitrary lattice $\vec{q}$ and a variety of different vector currents, the summary of our simulations performed are available in Table 7.2. This method unlike comparable methods does not require complicated operator renormalisation or handling of mixing. We then used this to calculate the moments of structure functions using constrained fits, getting results for moments difficult to obtain using conventional lattice techniques.

We looked at the flavour decomposition allowed by the FHT (§5.3), to extract separate u and d quark terms, as well as proton–neutron different term $uu - dd$ and the flavour diagonal component ud, and used them to construct proton and neutron photonic Compton amplitudes. Furthermore this can be extended to reconstructions of the full electroweak structure functions.

These results set the stage for calculations that will help reduce model uncertainty of box diagram and two–photon exchange calculation in non–perturbative QCD, pending chiral and continuum extrapolation. Those same results could also then be combined with other PDF determination procedures to improve the theoretical determination of PDFs from first principles. In addition they can be used to test the PDF extractions' control of higher twist systematics. Work is under way for an improved fitting method, which will be able to extract even higher moments from the data presented here [251, 261].

With the extraction of T_1, this sets the stage for future extractions of the other structure functions, but require modification of the technique. To get at the equivalent T_2 result to T_1 at fixed ω, in our simulation with $q_z = 0$ one or more units of momentum must be introduced to the z direction, before decomposing a linear system, leading to reduced signal. However future simulations, using methods such as momentum smearing could allow extraction of T_2. Another possible extension is for the extraction of terms odd in μ and ν required to extract T_3, G_1 and

G_2. If the external momentum on one current is changed from a 'cosine' to a 'sin' in (7.5), then these structure functions would be extractable. The extraction of T_3 would allow the separation of quark and anti–quark PDFs. The extraction of G_1 and G_2, gives us further insight into the spin structure of hadrons. This would allow investigation into the spin PDFs but there are also some predictions for the relationship between $T_{1/2}$ and $G_{1/2}$ to investigate [262].

The off forward Compton amplitude gives information on the full GPDs [263]. The technique can also be extended to such terms by introducing more than one momentum transfer term to the off–forward Compton amplitude but care would have to be taken with energy degeneracies, analogous to the off–forward first order FHT §4.2.1. Work is currently on–going into extracting the GPDs with this technique [264].

In the calculation of the subtracted dispersion relationship we have not looked more deeply at the subtraction function, which we shall investigate in the next chapter §8.

Chapter 8

Subtraction Function

In §2.3.3 we determined a relationship between the Compton amplitude structure functions and their hadron tensor counterparts, in particular we used a once subtracted dispersion relationship (2.80) to extract ω dependence of the Compton amplitude in §7. Unlike the imaginary part of the Compton amplitude for $\omega \geq 1$, the $\omega = 0$ subtraction function is not directly obtainable from experiment. As such, an alternative determination is crucial to the understanding of sub–atomic structure. While it has been predicted to be obtainable from the background field methods [179], no actual calculation has been performed to verify this. We shall now examine the Compton amplitude in unsubtracted form, focusing on the subtraction function, the $\omega = 0$ structure function.

Theoretically some values are known. Using low energy theories [265, 266], one predicts the subtraction function in the *Thomson limit* $Q^2 \to 0$ to be

$$T_1^{p/n}(\nu = 0, 0) = -2e_{p/n}^2 \tag{8.1}$$

which is the so called *Thomson term*. We use $\nu = p \cdot q$ instead of $\omega = \frac{2\nu}{Q^2}$ as the former is well defined at $Q^2 = 0$. Part of the leading Q^2 behaviour is known from elastic form factors, but still includes contributions from unknown functions [267].

We can also examine the prediction at large Q^2, the leading asymptotic behaviour constrained by the OPE is [268]

$$T^{p/n}(0, Q^2) \sim \frac{1}{Q^2}. \tag{8.2}$$

The asymptotic behaviour of the proton–neutron difference can be shown to be [269]

$$T_1^{p-n}(0, Q^2) \approx \frac{1}{Q^2}\left(-4m_N\left(\frac{4}{9}\sigma_u^{p-n} + \frac{1}{9}\sigma_d^{p-n}\right) + \frac{2m_N^2}{3}\langle x\rangle^{u-d}\right). \tag{8.3}$$

Naturally as we expect the proton and neutron to asymptote to zero at large Q^2, by extension uu and dd must as well.

The requirement for a subtracted dispersion relationship is predicted by *Regge theory* [270–272] and the requirement has strong implications for the presence of fixed pole terms. Another argument exists as well for the need of subtraction term, from electric polarisability [273]. Alternatively it is proposed that one can avoid the subtraction term by using the longitudinal structure function [274]. Another low energy relation is that for real photon Compton scattering one can relate the slope of T_2 at $Q^2 = 0$ to T_1 at $Q^2 = 0$

$$\left|\frac{1}{Q^2}\frac{\partial}{\partial Q^2}T_2(\omega, Q^2)\right|_{Q^2=0} = \frac{T_1(\omega, 0) - T_1(0, 0)}{\omega^2} \tag{8.4}$$

or a similar relation using *Regge theory* and current algebra [262]. We have mentioned *Regge theory* multiple times, which due to the experimentally indeterminable subtraction function plays an important role for it's model determination.

In this chapter we start by providing context of the subtraction in literature from *Regge theory* §8.1, proton–neutron mass splitting §8.2 and muonic hydrogen *Lamb shifts* §8.3. We then discuss discretisation of the current §8.4 and lattice results of the subtraction function §8.5, before concluding §8.6.

8.1 Fixed Pole and Regge Theory

Analytic continuation is a common tool in physics, indeed we have used just such a technique to calculate dispersion relationships for the Compton amplitude in §2.3.3. We shall now discuss the analytic continuation of orbital angular momentum and it's consequences for the subtraction function.

Classically the idea of using complex angular momentum was first established for harmonic oscillator problems [275, 276]. The actual first use in a quantised theory, was by Regge for a complex orbital angular momentum [277, 278], from where it derives the name *Regge theory*. *Regge theory* describes an interaction in terms of an exchange of a fictitious particle, a so called *Regge pole*, sometimes referred to as a *Reggeon*, that has varying Q^2–dependent complex spin. The Q^2 dependence of this particle is referred to as the *Regge trajectory*, which can be used to relate the high energy s–channel process to bound states and resonances in the t–channel through use of the complex spin.

Regge theory is used to model interactions for high energy particle accelerators where not all hard interactions can be described in terms of free particle systems. Soft processes are one such interaction, two examples being $ep \to eXp$ at HERA [279] or $pp \to Xp$ among others at the LHC [280]. These diffractive processes are modelled using the exchange of strongly interacting colour neutral particles called *Pomerons* [281]. This means that *Regge theory* plays an important role in modern experiments to model backgrounds.

Part of the electromagnetic self–energy depends on the $\nu \to \infty$ limit of the Compton amplitude. This can be analysed in terms of *Regge trajectories* [270], which allow us to determine bounds for the Compton amplitude structure function in the large ν limit, in terms of ν^α where α is referred to as the *Regge trajectory* intercept. The existence of a boundary term, the non–vanishing of the Compton amplitude as $|\nu| \to \infty$ can then be determined from the sign of the intercept α. If $\alpha < 0$ then the dispersion integral will converge without subtraction, however if $\alpha > 0$ then it will not. For the pion $\alpha < 0$, so no subtracted dispersion relationship is needed, however for the proton $0 < \alpha < 1$ a (once) subtracted dispersion relationship is needed.

If we assume the hadron tensor structure function F_1 is fully defined by a *Regge* model, denoted F_1^R, then it can be written as [282–284]

$$F_1^R(\nu, Q^2) = \sum_{\alpha>0} \beta_\alpha(Q^2)\nu^\alpha \tag{8.5}$$

for *Regge poles* α and corresponding residues β. The dispersion relationship between the hadron tensor and the Compton amplitude §2.3.3, prior to subtraction and in terms of ν not ω, then predicts a definite form for the *Regge* structure of the Compton amplitude

$$T_1^R(\nu, Q^2) = \sum_{\alpha>0} \frac{\pi\beta_\alpha(Q^2)}{\sin\pi\alpha} \left[(-\nu - i\epsilon)^\alpha + (\nu - i\epsilon)^\alpha\right]. \tag{8.6}$$

In the case where α is an integer we have *pomerons* but in other cases a branch cut in the positive real axis.

The Compton amplitude contains non–*Regge* contributions but the *Reggeon dominance hypothesis* states that in the large ν limit only the *Regge* components survive, formally

$$\lim_{\nu\to\infty} \left(T_1(\nu, Q^2) - T_1^R(\nu, Q^2)\right) = 0. \tag{8.7}$$

Hence the need for a subtracted dispersion relationship assuming *Reggeon dominance hypothesis* is wholly determined from *Regge theory*. Furthermore any deviations from this form must be ν–independent, a pole with zero angular momentum. One possible such fixed pole would be a term independent of Q^2, which has implications for small x behaviour for partons. For further discussion of such a fixed pole see [285, 286] and references therein.

8.2 Cottingham Self Energy

The proton–neutron mass difference plays an important role in the particle make–up of the universe. Assuming degenerate light quark flavours, the mass difference at leading order is purely determined by QED effects and predicts $m_p > m_n$. In reality the small isospin breaking due to $m_d > m_u$ provides a slightly larger opposite effect resulting in $m_p < m_n$. Experimentally the mass splitting has been measured to extraordinary accuracy [42]

$$m_n - m_p = 1.29333205\ (51)\ MeV \tag{8.8}$$

which is less than the difference in m_u and m_d. This mass splitting is in fact finely tuned, with only a narrow band of less than $3\ MeV$ allowed values. In the case where this mass splitting were only $1\ MeV$ larger, deuterium would no longer be a bound nuclear state, leading to a hydrogen dominated universe. Conversely if the neutron was light enough to favour inverse β decay $e^- + m_n < m_p$ then the universe would be neutron dominated. As such, improvements in our understanding of the mass difference is important to our understanding of the universe.

At leading order the mass difference is

$$m_p - m_n = \delta m^{m_d - m_u} + \delta m^{\gamma} \tag{8.9}$$

where the first term is the contribution due to quark mass splitting and the latter them the electromagnetic self energy. The quark mass splitting term requires calculation of low–energy hadronic effects, which have been calculated using lattice QCD [287]. The latter term can be obtained by the *Cottingham self energy* [267, 288] pictured in Figure 8.1. The *Cottingham formula* relates the electromagnetic self energy to the Compton amplitude, part of which requires the forward Compton amplitude subtraction function [287]

$$\delta m^{\gamma}_{sub} = -\frac{3\alpha}{16\pi m}\int dQ^2 T_1^{p-n}(0, Q^2). \tag{8.10}$$

Theoretical determination of this electromagnetic self energy has been made and summarised in Table 8.1. It is clear that improved determinations of the Q^2 dependence of the subtraction function then will improve our understanding of fundamental sub–atomic physics.

δm^{γ}	Source
0.76(30)	[289]
1.30(50)	[287]
1.04(35)	[290]

Table 8.1: Theoretical determinations of the electromagnetic self energy contribution to the proton–neutron mass difference. These are the long standing *Cottingham self energy* based calculation [289] and proposed modern improvement [287], as well as inference from $\delta m^{m_u - m_d}$ [290].

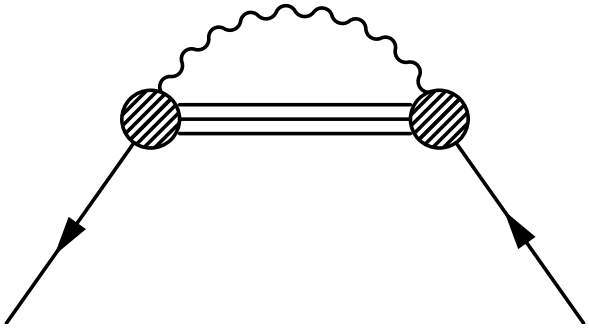

Figure 8.1: The Cottingham self energy, which can be related via dispersion relation to the Compton amplitude subtraction function.

8.3 Muonic Hydrogen Lamb Shift

From the difference in binding energy between the $2P$ and $2S$ states of hydrogen; the *Lamb shift* [291] can be used to infer the proton charge radius. Using lepton scattering experiments the root–mean–square proton charge radius can be determined, however the values obtained by different leptons are not consistent. The value determined from eH *Lamb shifts* [292] averaged from multiple sources is

$$\sqrt{\langle r_p^2 \rangle} = 0.8768(69)\ fm. \tag{8.11}$$

As the Born radius of lepton orbits are inversely proportional to their mass, a muon in $2P$ and $2S$ orbit much closer to the atom than an electron. Hence $2P$ and $2S$ are more sensitive to the finite size of the proton when the electron is replaced by a muon. Such measurements have recently become feasible [293] and yield a charge radius of

$$\sqrt{\langle r_p^2 \rangle} = 0.84184(67)\ fm. \tag{8.12}$$

This muonic Lamb shift differs by about 5 standard deviations from the electron measurement. One of the inputs into the determination in muonic hydrogen is two photon exchange [294], such determination uses analysis that requires knowledge of pole contributions to F_1 to write the Born term in terms of vector boson form factors and subtract it from the Compton amplitude [269]. Thus for the same reason as for *Cottingham self energy*, further understanding of the properties of the subtraction function are needed.

8.4 Lattice Integral Discretisation

In §7.1.3 we examined purely–local, purely–conserved and interference vector currents a showed they were statistically equivalent after subtraction for $\omega < 1$ (Figure 7.4). As the subtraction function, is a short distance function, it may be more sensitive to discretisation. The different implementation of the vector current have different short distance structure, so by examining these we can improve our understanding of the continuum limit.

Recall the second FHT in partial Hilbert form

$$\left.\frac{\partial^2 E_{X,\vec{p}}}{\partial\lambda_i\partial\lambda_j}\right|_{\boldsymbol{\lambda}=\vec{0}} = -\frac{\left\langle X,\vec{p}\right|\int d^4y\left(e^{i\vec{q}\cdot\vec{y}}+e^{-i\vec{q}\cdot\vec{y}}\right)T\left\{J_i(y)J_j(0)\right\}\left|X,\vec{p}\right\rangle_0}{2E_{X,\vec{p}}}. \tag{4.97}$$

On the lattice the continuum integral will be turned into a discrete sum, meaning the weight of the $y_4 = 0$ term in the integral does not represent a set of measure zero. This present new

term would lead to a contact term that has non–infinitesimal contribution to the second order matrix element. This extra term behaves properly in the continuum limit $a \to 0$, as in this limit the offending term in the integrand will have zero measure, however is still present at finite a.

We can gain some insight into this phenomena by looking into the conservation of the vector current on the lattice. By using Noether current for the discrete symmetries of QCD on the lattice the conserved vector current can also be constructed (see §5.2.2), which then does not require renormalisation. By comparing local and conserved vector currents, some insights into the contact term can be inferred.

The local (non–conserved) vector operator can be improved using a Symanzik scheme in the same manner as §3.2.4. From this perspective at leading order in a the breaking of conservation can be thought of as a derivative, which we consider in terms of an improved local current V_μ^{imp} which has form [295]

$$V_\mu^{imp} := (1 + am_q c_0)V_\mu^{loc} - \frac{1}{2}ac_1\overline{q}\mathcal{D}_\mu q + \frac{1}{2}aic_2\partial_\lambda(\overline{q}\sigma_{\mu\lambda}q). \tag{8.13}$$

Through careful choice of c_0, c_1 and c_2 this allows the cancellation of $\mathcal{O}(a)$ errors. Conversely this allows us to look at the interplay of two V_μ^{loc} current insertions. Neglecting the c_2 component, the interplay of two different currents would look like the derivative term $\overline{q}\mathcal{D}_\mu q$ interacting with $\overline{q}\gamma_\mu q$ of the other current, introducing an artefact into our calculation, a contact term.

The presence of contact term for interference current is not unique to the second order FHT, in Hadron Vacuum Polarisation (HVP) this term is present as well [296]. In HVP there are various ways to remove this term, one of which removes the contact term by constructing a projection onto the conserved component of your matrix element [296]. Another way of removing the contact term is to use a mixture of the lattice local and conserved currents. The local current $V_\mu^{loc}(n)$ (§5.2.1) is as the name suggests an operator which lives on lattice site n, whereas the conserved current $V_\mu^{con}(n)$ (§5.2.2) effectively lives on lattice site $n + \frac{1}{2}\hat{\mu}$. Thus the contact term should not be present for the interference current.

We can take advantage of this in our technique, both the conserved and local vector currents are implementable using the FHT and so it is possible to construct the interference of them. The interference current has one further improvement over the conserved current, the explicit contact term due to the non–zero second order shift in the action, is also not present. We have of course seen the interference current already in subtracted form Figure 7.4, where each of the methods provide consistent results, once subtracted. This naturally predicts that a discrepancy found in the Compton amplitude is independent of ω and so our once subtracted dispersion relationship is valid without any changes. The question still remains what level of contribution these contact terms have to the FHT extracted result in our subtraction function. By utilising the three different vector current combinations, we should be able to infer more about presence of any contact term.

8.5 Lattice Results

We have already shown the method to extract results for $T_1(\omega, Q^2) - T_1(0, Q^2)$ in §7. In this section we focus on the subset $\omega = 0$, from our simulations Table 7.2.

Figure 8.2 shows the subtraction function for pure V_3^{loc} currents for different flavour combinations. The FHT is capable of extracting the subtraction function for an extraordinarily large range of Q^2, both very close to zero using larger lattice volumes as well as out to approximately $Q^2 = 16\ GeV^2$. We observe differing behaviour between the different flavour combinations. The uu and dd flavours both rapidly decrease at small Q^2, however dip in uu is preceded by a sudden rise. The ud combination rapidly approaches zero as Q^2 increases.

We have attempted to look at the lattice spacing and volume dependence of the Compton amplitude in §7.1.3, §7.2.2, §7.3 and §7.4, however no clean comparisons were possible. Here however, as we have so many Q^2 values and the trends, especially for the ud term are so clean we can

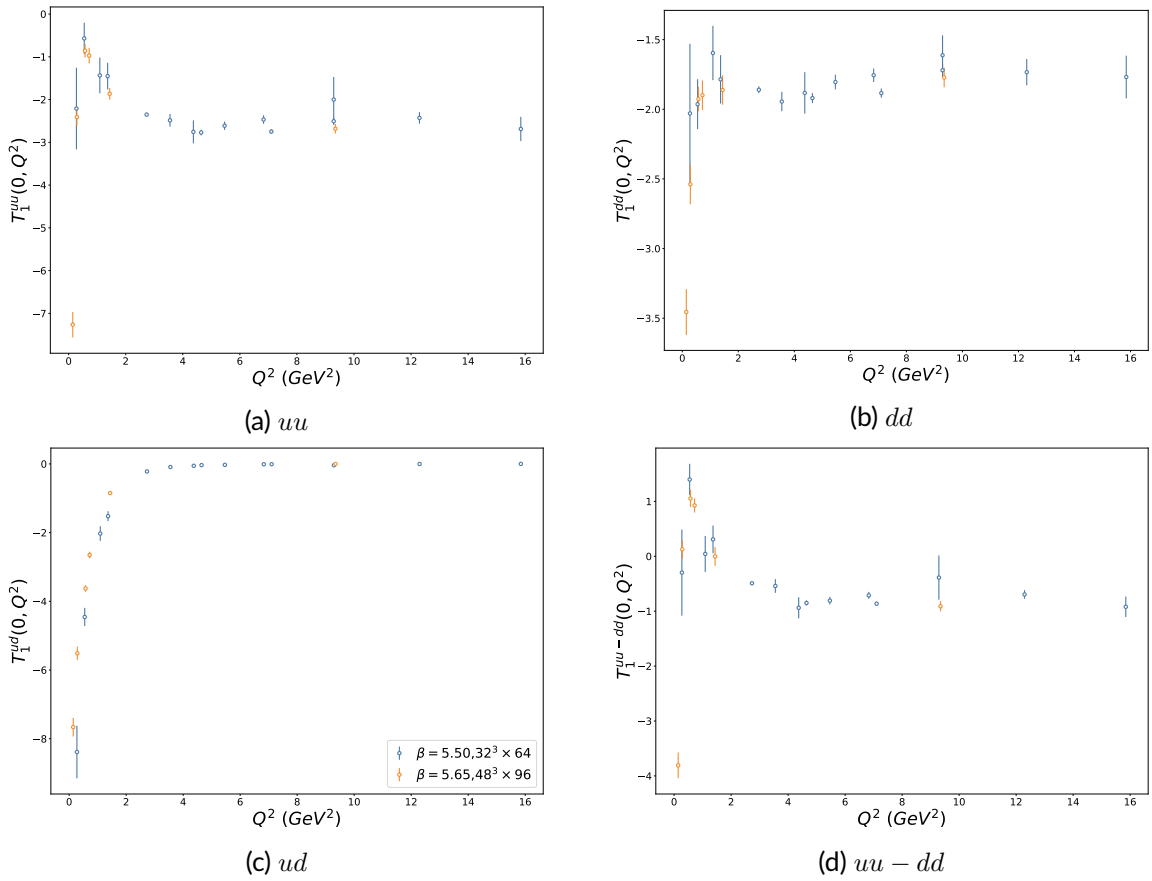

(a) uu (b) dd

(c) ud (d) $uu - dd$

Figure 8.2: The subtraction function for the Compton amplitude structure function $T_1(\omega = 0, Q^2)$ for V_3^{loc} against Q^2 for a variety of flavour combinations.

compare two different lattices, with differing spacing and volume side by side. Figure 8.2 shows no significant deviation except for a small shift in the ud component. Since this term strongly tends to zero we can be confident that there are no significant volume effects at larger Q^2 and only a small effect at smaller Q^2.

Neither the uu, dd or $uu - dd$ combinations vanish as $\frac{1}{Q^2}$ as predicted by (8.2), instead are approximately flat for $Q^2 \gtrsim 3\ GeV^2$, which suggest a fixed pole term is present. This fixed pole would cause a quadratic divergence in the *Cottingham formula* with no obvious SM operators available to renormalise. However other possibilities due to discretisation and contact terms have to be explored. We fill now look at the difference in the subtraction function between our different vector operators because this may offer some insight into possible discretisation artefacts.

8.5.1 Vector Operator Subtraction Functions Comparison

Earlier we discussed the nuances of Q^2–independent contributions to the subtraction function §8.4, which we now discuss using multiple different operators; $\{J_\mu, J_\nu\}$ of $\{V_3^{loc}, V_3^{loc}\}$, $\{V_3^{con}, V_3^{con}\}$ and $\{V_3^{loc}, V_3^{con}\}$. Figure 8.3 shows the difference between operators for the proton subtraction functions. We see a large differences in behaviour between them, most easily seen at $Q^2 = 4.64$ GeV^2. As the ω–dependent part of the Compton amplitude remains rather insensitive to the operator form, we expect that any contact terms that are present to also be ω–independent.

The pure local and pure conserved vector currents differ at larger Q^2 by an apparent constant offset. They are expected to be differ as the pure conserved vector current has an extra explicit contact term introduced by the non–zero second order action shift (5.12), the correction of which has not yet been performed. The pure local and interference vector currents also seem to differ at larger Q^2 by a constant. The interference of currents does not have a contact term, so the

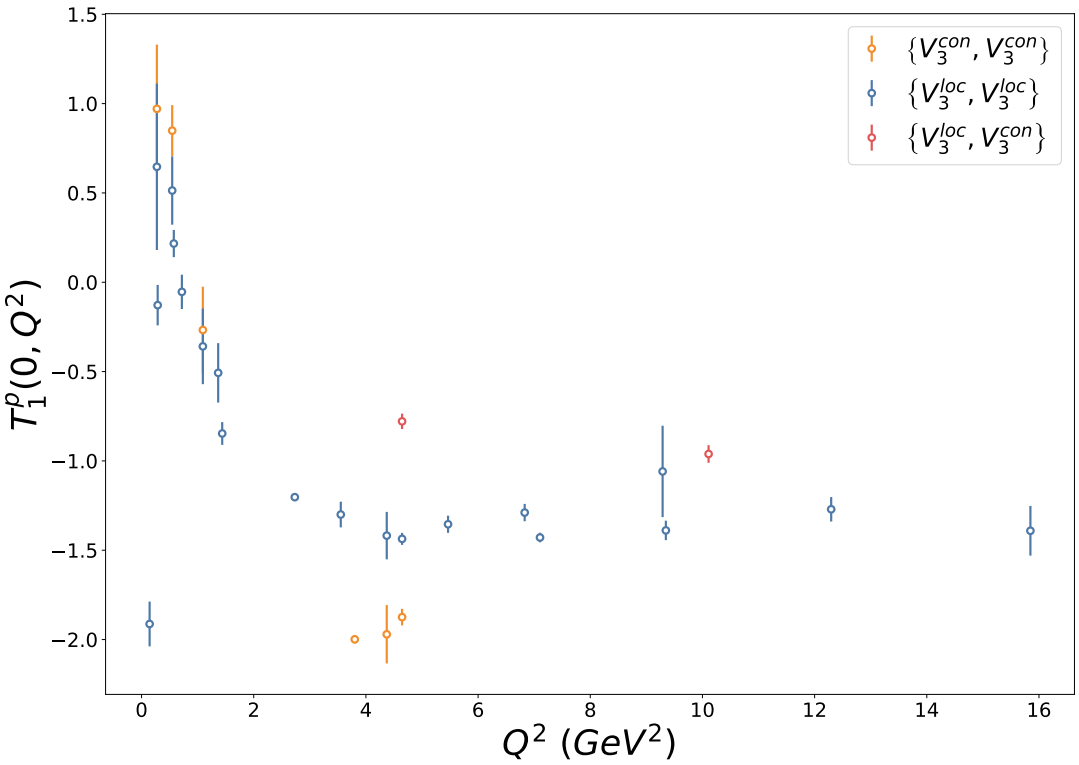

Figure 8.3: Operator comparison of the subtraction function for the Compton amplitude structure function $T_1^p(\omega = 0, Q^2)$ against Q^2. Note that the conserved current $\{V_3^{con}, V_3^{con}\}$ has not had the second order action shift term (5.12) removed and so strictly isn't purely $T_1^p(\omega = 0, Q^2)$.

difference should be the local contact term. This suggests that the purely local and probably the purely conserved currents contains contact terms arising from the discretisation.

As contact terms involve only one quark line the ud component of the subtraction function is not sensitive to them. Figure 8.4 shows no difference between operators for the ud flavour combination. Hence we conclude that the difference between the operators likely stems from contact terms.

The large Q^2 behaviour is important for the presence or lack of fixed pole like terms discussed earlier. As the interference of currents also does not exhibit asymptotic $\frac{1}{Q^2}$ behaviour, there is still a possible fixed pole. However the difference between the different discretisation structure of the currents suggests that this observable could be highly sensitive to the lattice cut–off, warranting a more careful $a \to 0$ study to see if it persists before drawing conclusions. To resolve this the contact and seagull terms present in the pure local and conserved currents need to be calculated, to conclude whether their differences do in fact come from contact terms in the subtraction function. Finally the interference of currents needs to be studied for volume and lattice spacing dependence. Resolving these issues would allow one to conclude whether there is a fixed pole in the subtraction function.

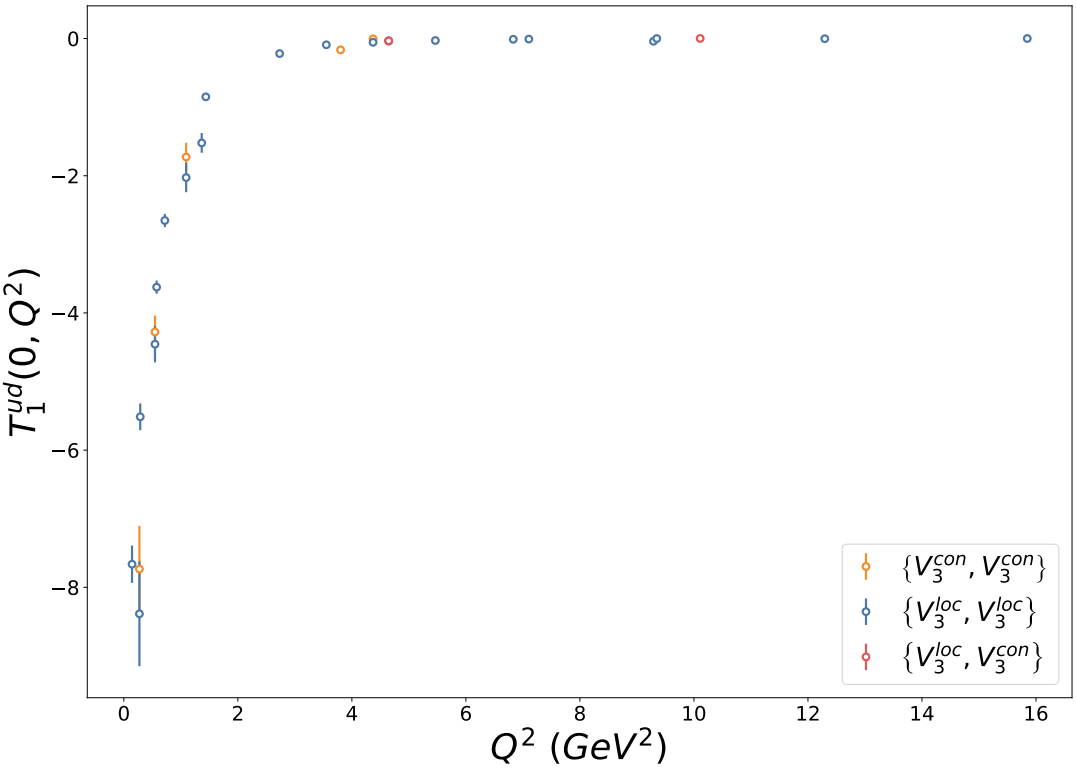

Figure 8.4: Operator comparison of the subtraction function for the Compton amplitude structure function $T_1^{ud}(\omega = 0, Q^2)$ against Q^2.

8.6 Summary and Outlook

In this chapter we have presented further insight into the nature of the subtraction function. Presented was an *ab initio* calculation of the Compton amplitude subtraction for the first time, with possible remaining unresolved lattice artefacts, a fixed pole or a mixture thereof. Multiple operators were examined and a prescription presented for resolving this question, including a use of a interference currents, the current most free of these artefacts. This sets the stage for future calculations, offering the potential to resolve the long standing question of whether a fixed pole is present in the Compton amplitude.

Chapter 9

Gluons

As one of the fundamental building blocks of hadrons, gluons play an important role in the emergent behaviour of QCD. Just as we study the quark structure of hadrons, we also need to understand the gluon structure of hadrons. While many of the dynamics of gluons can be inferred from quark form factors, we can look at gluons directly from the lense of gluonic GFFs or more specifically the EMT ($n = 2$ GFFs in the terminology of §2.2.1).

The coupling of gravity and matter is described by the EMT, which allows us to probe the fundamental properties of such matter [297]; mass, spin and the so called *D–term*, which characterises the stresses inside the hadron. As a consequence, understanding of the EMT is important for a wide array of phenomena, from matter in strong gravitational fields to hard scattering processes and exotic matter.

On the lattice the extraction of matrix elements using gluonic operators has been plagued by their sensitivity to short range gauge noise. Nevertheless some earlier lattice determinations of $Q^2 \neq 0$ gluonic operators are available [257, 298]. By utilising smoothing to reduce such noise, it has become possible to extract gluonic matrix elements at larger Q^2 [299–303].

9.1 Energy Momentum Tensor

In §2.2.1 we introduced GFFs and noted that (2.33) with $n = 2$ is the operator for the EMT (2.39). Recall the EMT for a nucleon N

$$\left\langle N,\vec{p}'\middle|\mathcal{O}^{q/g}_{\mu\nu}\middle|N,\vec{p}\right\rangle = \overline{u}(p')\left[\gamma_{\{\mu}p_{\nu\}}A^{q/g}_{20}(Q^2) + \frac{iq^\alpha\sigma_{\alpha\{\mu}P_{\nu\}}}{2m_p}B^{q/g}_{20}(Q^2) + \frac{q_\mu q_\nu}{m_p}C^{q/g}_{20}(Q^2)\right]u(p). \tag{2.42}$$

This decomposition is just one of the decompositions commonly used, the other being

$$\left\langle N,\vec{p}'\middle|\mathcal{O}^{q/g}_{\mu\nu}\middle|N,\vec{p}\right\rangle = \overline{u}(p')\left[P_\mu P_\nu M^{q/g}_2(Q^2) + \frac{iq^\alpha\sigma_{\alpha\{\mu}P_{\nu\}}}{4m}J^{q/g}(Q^2) + \frac{q_\mu q_\nu}{m}d^{q/g}_1(Q^2)\right]u(p). \tag{9.1}$$

The relationship between these two forms can be derived from the *Euclidean Gordon identity* (C.96) and are related by

$$M^{q/g} = A^{q/g}_{20} \tag{9.2}$$

$$J^{q/g} = \frac{1}{2}\left(A^{q/g}_{20} + B^{q/g}_{20}\right) \tag{9.3}$$

$$d^{q/g}_1 = C^{q/g}_{20}. \tag{9.4}$$

This latter representation is commonly chosen for physical interpretation of each of the GFFs.

The first of which is M (A_{20}), which at $Q^2 = 0$ is the momentum fraction. The slope of M encodes the gravitational radius, an interesting open question in physics is whether the gluon or quark radius is larger. The size of such radii are important to the dynamics of the binding of

atoms (see for instance [304] and references therein). In addition the axis intercept determines the gluon or quark momentum fractions.

The second term, the spin form factor $J^{q/g}$, encodes the spin distribution, which at $Q^2 = 0$ gives the quark and gluon contributions to the spin of the proton. The corresponding GFF $B_{20}^{q/g}$ is known as the anomalous gravitomagnetic moment, which is a measure of how much the spin contribution proportions differs from the momentum fraction ones. Some hints exists that this term is non–zero [257].

The third term d_1 (C_{20}), often called the D term [297], encodes 'pressure' inside the proton [305]. The combination of proton and gluons provide information of strong shear and pressure distributions inside the nucleon.

For the individual quark and gluon EMT components, there is an additional form factor in both (2.42) and (9.1), a $g_{\mu\nu}$ term. For the (2.42) decomposition this becomes

$$\begin{aligned}\left\langle p,\vec{p}'\middle|\mathcal{O}_{\mu\nu}^{q/g}\middle|p,\vec{p}\right\rangle = \overline{u}(p')\Bigg[&\gamma_{\{\mu}p_{\nu\}}A_{20}^{q/g}(Q^2) + \frac{iq^\alpha\sigma_{\alpha\{\mu}P_{\nu\}}}{2m}B_{20}^{q/g}(Q^2)\\ &+ \frac{q_\mu q_\nu - q^2 g_{\mu\nu}}{m}C_{20}^{q/g}(Q^2) + mg_{\mu\nu}\overline{C}^{q/g}(Q^2)\Bigg]u(p)\end{aligned} \tag{9.5}$$

satisfying

$$\overline{C}^{g}(Q^2) + \sum_q \overline{C}^{q}(Q^2) = 0. \tag{9.6}$$

However due to the breaking of the continuum rotational group, no trace terms are extractable with our technique so we shall omit it, for a discussion on this term see [297].

9.1.1 Sum Rules

We can relate the EMT GFFs to sum rules formally through use of GPDs. The second Mellin moments of the GPDs defined in §2.4 can be related to the GFFs by (2.88) and (2.89)

$$\int_{-1}^{1} dx x H(x,\xi,Q^2) = A_{20}(Q^2) + (2\xi)^2 C_2(Q^2) \tag{9.7}$$

$$\int_{-1}^{1} dx x E(x,\xi,Q^2) = B_{20}(Q^2) - (2\xi)^2 C_2(Q^2) \tag{9.8}$$

which at $Q^2 = 0$ can be related to the parton spin contributions [306]

$$J^{q/g} = \frac{1}{2}\left[A_{20}^{q/g}(0) + B_{20}^{q/g}(0)\right] \tag{9.9}$$

$$\frac{1}{2} = J^q + J^g. \tag{9.10}$$

Note the use of spin contribution $J^{q/g}$ and Q^2 dependent spin form factor $J^{q/g}(Q^2)$, which are related by $J^{q/g} = J^{q/g}(0)$. In combination with (2.43), (9.9) predicts

$$\sum_f B_{20}^{q_f} + B_{20}^{g} = 0. \tag{9.11}$$

If one of the B_{20} is zero, then this would mean that the fraction of momentum is the same fraction of contribution to the proton spin and conversely the deviation from this a measure of dynamical effects inside the hadron affecting the spin contribution.

To understand (9.10) we need to decompose the spin contribution to quark and gluonic parts. The first decomposition we will look at is the *Ji decomposition* [307]

$$\frac{1}{2} = \frac{1}{2}\Delta\Sigma + \sum_q L_q + J_g \tag{9.12}$$

where $\Delta\Sigma$ is the contribution to the spin of the proton from the spin of the quarks, L_q the contribution to the spin due to the orbital angular momentum of the quarks and J_g is the remaining contributions due to the gluons defined above. The *Ji decomposition* is gauge invariant.

The second decomposition is the *Jaffe–Manohar decomposition* [308]

$$\frac{1}{2} = \frac{1}{2}\Delta\Sigma + \sum_q \mathcal{L}_q + \Delta G + \mathcal{L}_g \tag{9.13}$$

where $\mathcal{L}_{q/g}$ are the light cone orbital angular momenta of quarks and gluons respectively, and ΔG is the contribution to spin due to gluon spin. Unlike the *Ji decomposition*, this decomposition is not gauge invariant. This has lead to another light–cone method with partonic picture [309, 310], that specifies a preferred direction and argue that experiments are performed at large boost, making such a preferred direction fairly natural.

On the lattice greats strides have been taken to calculate all these components. The quark spin contributions can be calculated with three point function methods (see for instance [64]) but recently methods to extract the others have been published. Both *Ji* and *Jaffe–Manohar* quark orbital angular momenta are extractable using the same lattice technique [311] by varying the shape of used gluon 'staple'. Using a gluon spin density operator [312], ΔG has also been calculated [313]. This means that if $\mathcal{L}_g$ can be extracted directly from the lattice, both spin sum rules can be verified *ab initio*.

Experimentally $\Delta\Sigma$ has been measured [314, 315], providing around a third of the total spin of the proton, often referred to as the 'spin problem' [316]. The other contributions, including the contributions from the gluons are less well determined [317]. Proposals for experiments at both JLab and BNL are under way for future experiments for determining the gluon contributions more precisely [304].

The conservation of the EMT implies that the total sum of all quark and gluon components to a GFF is scale invariant. Individually however the quark and gluon GFFs have renormalisation scale dependence μ which we only highlight when necessary.

9.2 Lattice Method

To calculate the gluonic EMT, we need the corresponding gluon operator

$$T_{\mu\nu} = \mathrm{tr}_c \left[G_{\mu\alpha} G_\nu{}^\alpha \right]. \tag{9.14}$$

On the lattice our continuous rotational symmetry group $O(4)$ is broken into the hypercubic group $H(4)$, so to avoid mixing we restrict to the components of (9.14) that transform irreducibly under $H(4)$. Two such operator combinations are

$$\mathcal{O}_{1i} = T_{4i} \tag{9.15}$$

$$\mathcal{O}_2 = T_{44} - \frac{1}{3} T_{ii} \tag{9.16}$$

where in the second line summation convention is used over the spatial indices. These operators have interpretations as gluonic equivalents of electromagnetic fields, $\mathcal{O}_{1i}$ is the gluonic $(E \times B)_i$ and $\mathcal{O}_2$ the gluonic $\left(B^2 - E^2\right)$ where the sign of the latter comes from Euclidianisation. These two operators correspond to $v_{2,a}$ and $v_{2,b}$ in [183, 238, 239] or $\tau_3^{(6)}$ and $\tau_1^{(3)}$ in [318].

Due to the integrated gluonic degrees of freedoms, the resulting three–point correlators (3.74) are constructed source–by–source on each configuration

$$G^{(3)}_{\chi,\mathcal{O}}(x, y) = G^{(2)}_\chi(x)\mathcal{O}(y) \tag{9.17}$$

which means that the momentum dependent three–point function (3.76) is then

$$G^{(3)}_{\chi,\mathcal{O}}\left(x_4, y_4, \vec{p}', \vec{q}\right) = \int d^3y e^{-i\vec{q}\cdot\vec{y}} G^{(2)}_\chi\left(x_4, \vec{p}'\right)\mathcal{O}(y). \tag{9.18}$$

As a consequence three–point functions can be generated from lattice two point functions without need for additional inversions. This means that calculating all combinations of $y_4, \vec{p}'$ and $\vec{q}$ are relatively cheap to compute. The three–point functions are then vacuum subtracted to improve signal

$$\left\langle \hat{G^{(3)}}_{\chi,\mathcal{O}}(x_4, y_4, \vec{p}', \vec{q}) \right\rangle = \left\langle G^{(3)}_{\chi,\mathcal{O}}(x_4, y_4, \vec{p}', \vec{q}) \right\rangle - \left\langle G^{(2)}_{\chi}(x_4, \vec{p}') \right\rangle \langle \mathcal{O}(y_4, \vec{q}) \rangle. \tag{9.19}$$

The gluon operator (9.14) is implemented using the Clover staple (3.48), with gradient flow [319] applied to the gauge links in the staple to a flow–time 5 in lattice units in steps sizes of 0.01.

9.2.1 Feynman–Hellmann Re–weighting

Prior work has been done using the FHT to calculate the forward gluon matrix elements [183]. We now briefly discuss a new FHT based method.

It is known that re–weighting Monte Carlo samples [320, 321] can effectively generate samples with a different action on the lattice [322]. If one has some small perturbation in action $S(0) \to S(\lambda)$ then one can re–weight existing path integral expectation values by

$$\langle \mathcal{O}(\lambda) \rangle = \frac{1}{\left\langle e^{-(S(\lambda)-S(0))} \right\rangle} \left\langle \mathcal{O}(0) e^{-(S(\lambda)-S(0))} \right\rangle \tag{9.20}$$

Initially it was attempted to use reweighting in terms of varying small $\lambda\mathcal{O}$ as the reweighting term and using the FHT to get the EMT. This method has one problem for the gluon operator. Due to the decomposition (9.17), any FHT calculation is forced to be equivalent to the summation method. Consider operator two–point correlator operator $\mathcal{O} = G^{(2)}_{\chi}(x) = \chi(x)\chi^{\dagger}(0)$ and action modification

$$S(\lambda) = S(0) + \lambda \int_0^{x_4} dy_4 \int d^3y T_{4i}(y) \tag{9.21}$$

then the resulting operator becomes

$$\left\langle G^{(2)}_{\chi\lambda}(x) \right\rangle = \frac{1}{\left\langle e^{-\lambda \int_0^{x_4} dy_4 \int d^3y T_{4i}(y)} \right\rangle} \left\langle G^{(2)}_{\chi}(x) e^{-\lambda \int_0^{x_4} dy_4 \int d^3y T_{4i}(y)} \right\rangle. \tag{9.22}$$

For very small λ and neglecting the λ dependence of the first term, this becomes

$$\left\langle G^{(2)}_{\chi\lambda}(x) \right\rangle \approx \left\langle G^{(2)}_{\chi}(x) \right\rangle - \lambda \left\langle G^{(2)}_{\chi}(x) \int_0^{x_4} dy_4 \int d^3y T_{4i}(y) \right\rangle \tag{9.23}$$

the derivative of the operator just forming the summation method. This method would still be relevant for non–gluonic operators to calculate other disconnected matrix elements, but we shall look at regular three–point methods for our gluon calculation.

9.2.2 Form Factors

In FHT calculations the matrix element $\langle X, \vec{p} | \mathcal{O} | X, \vec{p} \rangle$ is determine directly, however for regular three–point functions we extract terms of form

$$F_3(\Gamma, J) := \Gamma_{\alpha\beta} \left\langle \Omega \middle| \chi_\beta \middle| X, \vec{p} \right\rangle \left\langle X, \vec{p} \middle| \mathcal{O} \middle| X, \vec{p} \right\rangle \left\langle X, \vec{p} \middle| \chi^{\dagger}_{\alpha} \middle| \Omega \right\rangle \tag{9.24}$$

some appropriate projector Γ an element of the Clifford algebra.

These trace terms need to be taken into account when matching onto the GFFs. For polarised T_{4i} we have

$$\begin{aligned} F_3\big(\Gamma^+\Gamma_{\hat{s}}, 2T_{4i}\big) = &\left\{-iP_4\left[(E+m)\big(\vec{p}'\times\hat{s}\big)_i + \big(E'+m\big)(\vec{p}\times\hat{s})_i\right] + P_i\big(\vec{p}\times\vec{p}'\big)\cdot\hat{s}\right\} A_{20}\big(Q^2\big) \\ &+ \left\{-P_i\left[(E+m)\big(\vec{p}\times\vec{p}'\big)\cdot\hat{s} + \big(E'+m\big)\big(\vec{p}\times\vec{p}'\big)\cdot\hat{s}\right]\right. \\ &\quad -iP_4\left[\big(E'+m\big)(E+m) + \vec{p}\cdot\vec{p}'\right](\vec{q}\times\hat{s})_i - iP_4\big(\vec{p}\times\vec{p}'\big)_i(\vec{q}\cdot\hat{s}) \\ &\quad \left.-P_i\left[(E+m)\big(\vec{p}\times\vec{p}'\big)\cdot\hat{s} - \big(E'+m\big)\big(\vec{p}\times\vec{p}'\big)\cdot\hat{s}\right]\right\} B_{20}\big(Q^2\big) \\ &+ \left\{\frac{q_4 q_i}{m}\big(\vec{p}\times\vec{p}'\big)\cdot\hat{s}\right\} C_{20}\big(Q^2\big) \end{aligned} \tag{9.25}$$

where $\Gamma^+\Gamma_{\hat{s}} = \frac{1}{2}(I+\gamma_4)i\vec{\gamma}\cdot\hat{s}\gamma_5$ to project onto the positive parity state with spin vector $\hat{s}$. Similar forms can be calculated for other operator and unpolarised cases, and are presented in §D.

The polarisation vector $\hat{s}$ is then chosen for the polarised projected three–point functions. We define

$$F_3\big(\Gamma^+\Gamma_{\hat{s}}, \mathcal{O}\big) =: a_{\hat{s}}A_{20} + b_{\hat{s}}B_{20} + c_{\hat{s}}C_{20} \tag{9.26}$$

and unit vectors $\hat{i}$, $\hat{j}$, $\hat{k}$ in the three spatial direction. For results satisfying $\vec{p}\times\vec{p}' = \vec{0}$ we use

$$\hat{s} = \frac{(a_{\hat{i}}, a_{\hat{j}}, a_{\hat{k}})}{\left|(a_{\hat{i}}, a_{\hat{j}}, a_{\hat{k}})\right|} \tag{9.27}$$

and for $\vec{p}\times\vec{p}' \neq \vec{0}$ use

$$\hat{s} = \frac{\vec{p}\times\vec{p}}{|\vec{p}\times\vec{p}|} \tag{9.28}$$

or

$$\hat{s} = \hat{P}. \tag{9.29}$$

The constructed three–point function (9.19) has dependence in fit on both sink and operator insertion time where we need $x_4 >> y_4 >> 0$ sufficiently apart to remove excited state effects. Just as for two–point functions we form an effective mass to guide fitting ranges, we construct a ratio that once excited states are suppressed is constant in x_4 and y_4. While many such ratios exist we use

$$R_{\chi,\mathcal{O}}\big(x_4, y_4, \vec{p}', \vec{q}\big) = \frac{\hat{G^{(3)}}_{\chi,\mathcal{O}}(x_4, y_4, \vec{p}', \vec{q})}{G^{(2)}_\chi(x_4, \vec{p}')}\sqrt{\frac{G^{(2)}_\chi(x_4-y_4, \vec{p})G^{(2)}_\chi(y_4, \vec{p}')G^{(2)}_\chi(x_4, \vec{p}')}{G^{(2)}_\chi(x_4-y_4, \vec{p}')G^{(2)}_\chi(y_4, \vec{p})G^{(2)}_\chi(y_4, \vec{p})}} \tag{9.30}$$

from [64], which has the required properties. As the construction of new $G^{(3)}_{\chi,\mathcal{O}}$ just requires multiplication by two–point correlators (9.19), unlike normal methods we can construct all source–sink and operator insertion time combinations for all $\vec{p}'$ and $\vec{q}$ at no significant additional cost, except for the storage space required.

9.3 Results

A quenched lattice ensemble was generated for this project, with details summarised in Table E.1. Two–point correlators were generated with $(\kappa_l, \kappa_s) = 0.132$ which corresponds to $m_\pi = 754.8(3)$, with $N_s = 20000$ random sources evenly distributed over $N_{cfg} = 2000$ of the configurations, which corresponds to $N_{s/cfg} = 10.0$.

Ratios with the same combinations of the GFFs were averaged before fitting. One such a three–point function fit is presented in Figure 9.1 and Figure 9.2, whose simultaneously varying x_4 and y_4 allows us to verify control of excited states.

Fits were chosen by choosing first minimum operator insertion time y_4, then the source–sink separation range x_4 was picked for this operator insertion time ($y_4/a = 6$ in Figure 9.2). The maximum operator insertion time for minimum and maximum source–sink separation were then picked (x_4/a of 15 and 21 in Figure 9.1). The maximum operator insertion times for source–sink separation in-between source–sink minima and maxima are then taken to be linear interpolation of this. This forms a discrete approximation to a right trapezoid. Finally these fits are checked for consistency, and if necessary y_4 was changed and the process repeated again. In the case were no consistent fitting range was found, the data was discarded.

A total of 157 independent ratios were extracted, Q^2 ranging from 0.0 to $1.1\ GeV^2$.

9.3.1 Quark Comparison

To interpret the gluon results, we need the quark GFFs as well. Regular three–point function techniques were used to obtain the EMT GFFs for the quarks in [323]. Using the operator (2.33), these results for the form factor using sequential sources are shown in Figure 9.3. Note that B_{20}^{u+d} is small while B_{20}^{u-d} is not, this implies that the spin contribution of each of the quarks differs from their proportional momentum fraction. On the other hand the C_{20} contributions from each of the quarks are approximately equal, implying that they feel the same shear forces within the nucleon.

Dipole fits

$$f^{dip}(Q^2) = \frac{A}{1 + \frac{Q^2}{\Lambda^2}} \tag{9.31}$$

are then performed on each of these GFFs except for C_{20}^{u-d} and B_{20}^{u+d}, which are approximately zero. The corresponding unrenormalised momentum fraction extracted from this is

$$\langle x \rangle^{u+d} = 0.590(61). \tag{9.32}$$

9.3.2 Gluon Momentum Fraction and Renormalisation

While the un–flowed gluon renormalisation factor Z_g has been calculated for the lattice for both $\mathcal{O}_{1i}$ and $\mathcal{O}_2$ [183, 245], the flow changes this factor.

One could calculate this factor from first principles, but there is a subtlety. As the gluon operator has been calculated using flowed links, it is unclear whether to use flowed links in the operator only or for every link in the action as well. Instead we shall use the momentum sum rule to determine Z_g for this flow time.

We take the renormalisation prescription of [183], where the 'bare' parameters are written in terms of the extracted lattice results as

$$\langle x \rangle^{g,bare} = Z^g \langle x \rangle^g \tag{9.33}$$

$$\langle x \rangle^{q,bare} = Z^q \langle x \rangle^q \tag{9.34}$$

where $\langle x \rangle^{g,bare}$ and $\langle x \rangle^{q,bare}$ satisfy the momentum sum rule (2.43) to $\mathcal{O}(a^2)$. These results can be changed to $\overline{MS}$ scheme at scale μ, which for quenched lattices are related by

$$\langle x \rangle_\mu^{g,\overline{MS}} = \langle x \rangle^{g,bare} + \left(1 - Z^{\overline{MS}}_{\mu,bare\ qq}\right) \langle x \rangle^{q,bare} \tag{9.35}$$

$$\langle x \rangle_\mu^{q,\overline{MS}} = Z^{\overline{MS}}_{\mu,bare\ qq} \langle x \rangle^{q,bare} \tag{9.36}$$

which conserve the momentum sum rule. The quark renormalisation factors are taken to be [183, 245]

$$Z^q = 1.0(1) \tag{9.37}$$

$$Z^{\overline{MS}}_{\mu,bare\ qq} = 1.06(1). \tag{9.38}$$

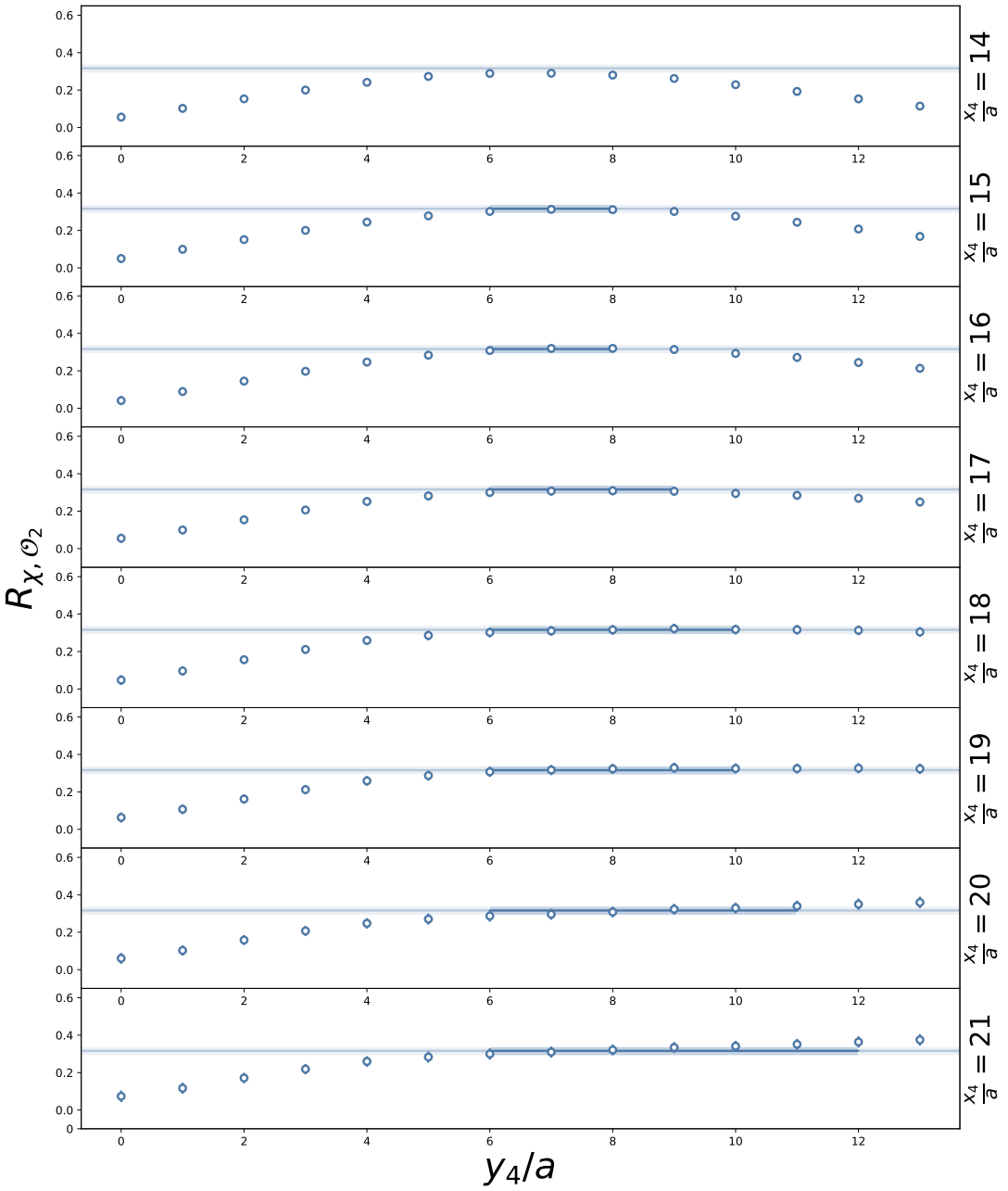

Figure 9.1: An example of a gluon three–point function fit for $Q^2 = 0$ and $\vec{p}^2 = 0$. The different slices shown vary the sink location x_4 and the x axis is y_4. For the same plot with x_4 and y_4 flipped see Figure 9.2. The fit was chosen as described in the text, and the value of the fit corresponds to the value of $A_{20}(0)$.

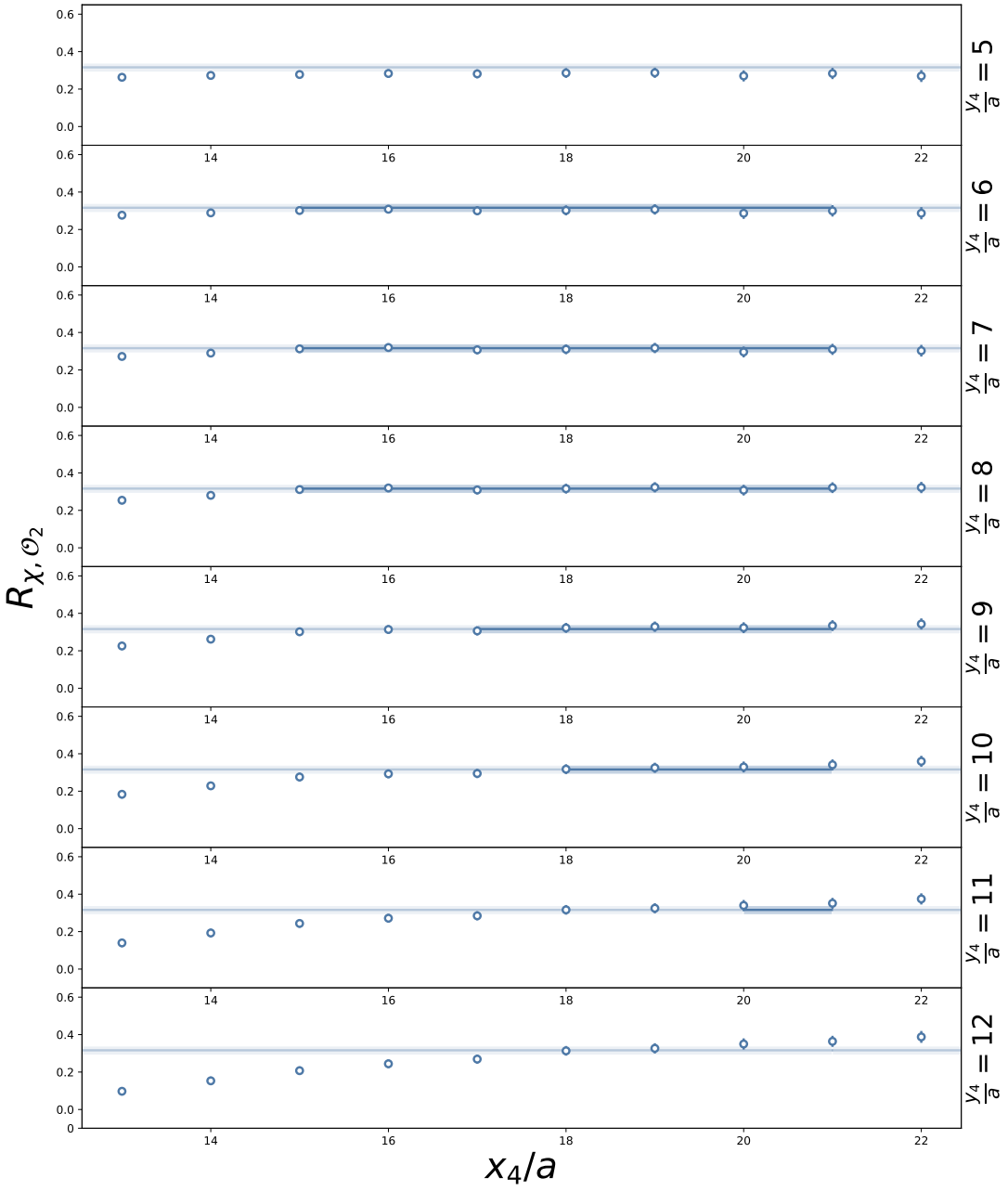

Figure 9.2: The same plot as Figure 9.1, with the slices and x axis flipped, now the slices differ by y_4 and the x axis is x_4.

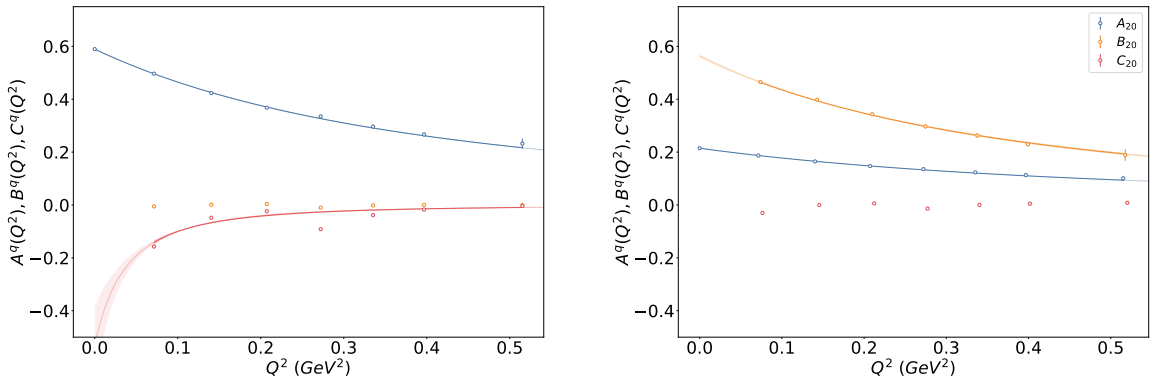

(a) $u + d$ (b) $u - d$

Figure 9.3: The quark EMT GFFs calculated on the same lattice, using conventional three–point function techniques. Dipole fits are shown for each GFF except for B_{20}^{u+d} and C_{20}^{u-d}. The uncertainty on many points is too small to see by eye.

As we are using the momentum sum rule to fix the renormalisation we fix $\langle x \rangle^{g,bare}$ from (9.32)

$$\langle x \rangle^{g,bare} = 0.410(61). \tag{9.39}$$

In the $\overline{MS}$ scheme at $\mu = 2\ GeV$ the quark and gluon momentum fractions then are

$$\langle x \rangle^{g,\overline{MS}}_{\mu=2\ GeV} = 0.374(65) \tag{9.40}$$

$$\langle x \rangle^{u+d,\overline{MS}}_{\mu=2\ GeV} = 0.626(65). \tag{9.41}$$

consistent with the other method in [183] performed on lattices generated with the same parameters. The gluon momentum fraction is smaller than the continuum counterpart [324], however these calculations have been performed on a quenched lattice with very large quark masses, so this is to be expected.

We now calculate the renormalisation constants from our data. As the two operators in use are in different representations of $H(4)$ it is not necessary for the renormalisation factors to be the same, however they are expected to be close as they must both tend to 1 in the continuum. The lattice momentum fractions calculated from the data are

$$\langle x \rangle^{g}_{\mathcal{O}_{1i}} = 0.328(45) \tag{9.42}$$

$$\langle x \rangle^{g}_{\mathcal{O}_{2}} = 0.339(27) \tag{9.43}$$

which differ from [183] due to the Wilson flow. Using the momentum sum rule one can then calculate the bare renormalisation factors for each operator

$$Z^{g}_{\mathcal{O}_{1i}} = 1.27(27) \tag{9.44}$$

$$Z^{g}_{\mathcal{O}_{2}} = 1.22(20). \tag{9.45}$$

The consistency between different representations is good, as they need to converge in the continuum. All of the remaining results in the chapter are presented in 'bare' form.

9.3.3 Spin Form Factor $J^g(Q^2)$

The spin GFF can be examined directly from (9.1). Using a polarised projector for kinematics satisfying $\vec{p} \times \vec{p}' = \vec{0}$, for the operator $\mathcal{O}_{1i}$, $J^g(Q^2)$ is accessed directly. As the condition is easily satisfied for almost every possible Q^2 except $Q^2 = 0$, many points have been extracted. The resulting form factor is shown in Figure 9.4, the dipole fit (9.31) gives coefficients

$$A = 0.255(73) \tag{9.46}$$

$$a\Lambda = 0.503(43) \tag{9.47}$$

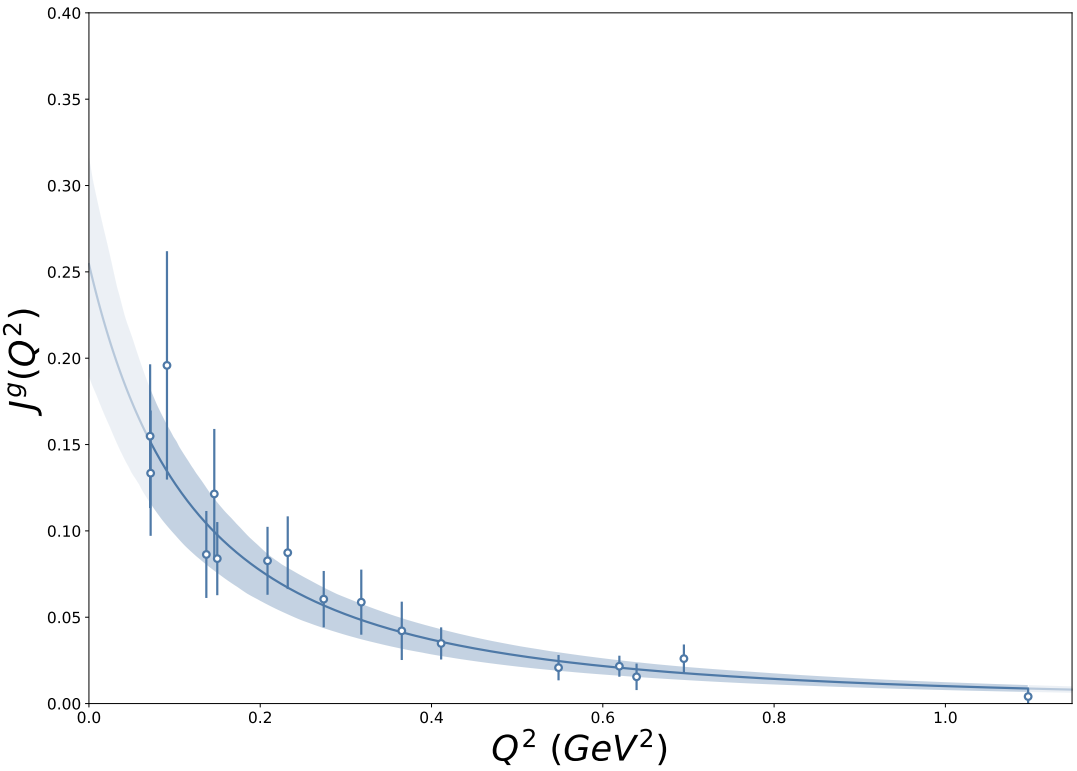

Figure 9.4: The spin form factor $J^g(Q^2)$ as extracted using polarised projector for kinematics satisfying $\vec{p} \times \vec{p}' = 0$ for operator $\mathcal{O}_{1i}$, which fix the three–point functions to be purely $J^g(Q^2)$.

The precision in the extracted Λ is quite clean, which provides a cleaner picture into the spin density distribution inside the nucleon. Using $J^g(0)$ and the gluon momentum fraction predicts

$$B_{20}(0) = 2J^g(0) - A^g_{20}(0) = 0.10(12). \tag{9.48}$$

This is consistent with zero, hence there is no apparent deviation from $J(Q^2) = \frac{1}{2}A_{20}(Q^2)$.

9.3.4 Separation of $A^g_{20}(Q^2)$ and $B^g_{20}(Q^2)$

As almost every non–zero Q^2 point has extractable $J^g(Q^2)$, each of these only require one more independent point for operator $\mathcal{O}_{1i}$ with kinematics satisfying $q_i = 0$ in order to separate J into A_{20} and B_{20}. The second condition, on the momentum transfer ensures zero coefficient for C_{20}. In addition we take the $Q^2 = 0$ points from both operators, which correspond to $A^g_{20}(0)$. Each Q^2 where this decomposition is possible is shown in Figure 9.5.

There are fewer points than Figure 9.4, this is because the requirement is more stringent on the possible momenta involved. Nevertheless the $A^g_{20}(Q^2)$ extraction is clean, but the $B^g_{20}(Q^2)$ extraction remains noisy, although consistent with zero. To this end a dipole is fit to $A^g_{20}(Q^2)$ giving

$$A = 0.356(33) \tag{9.49}$$
$$a\Lambda = 0.600(43). \tag{9.50}$$

No non–zero signal was evident in the $B^g_{20}(Q^2)$ signal. While we haven't ruled out a small B^g_{20}, a very precise simulation would have to be performed to determine this. With no indication of how small this term would be we treat it as equivalent to zero.

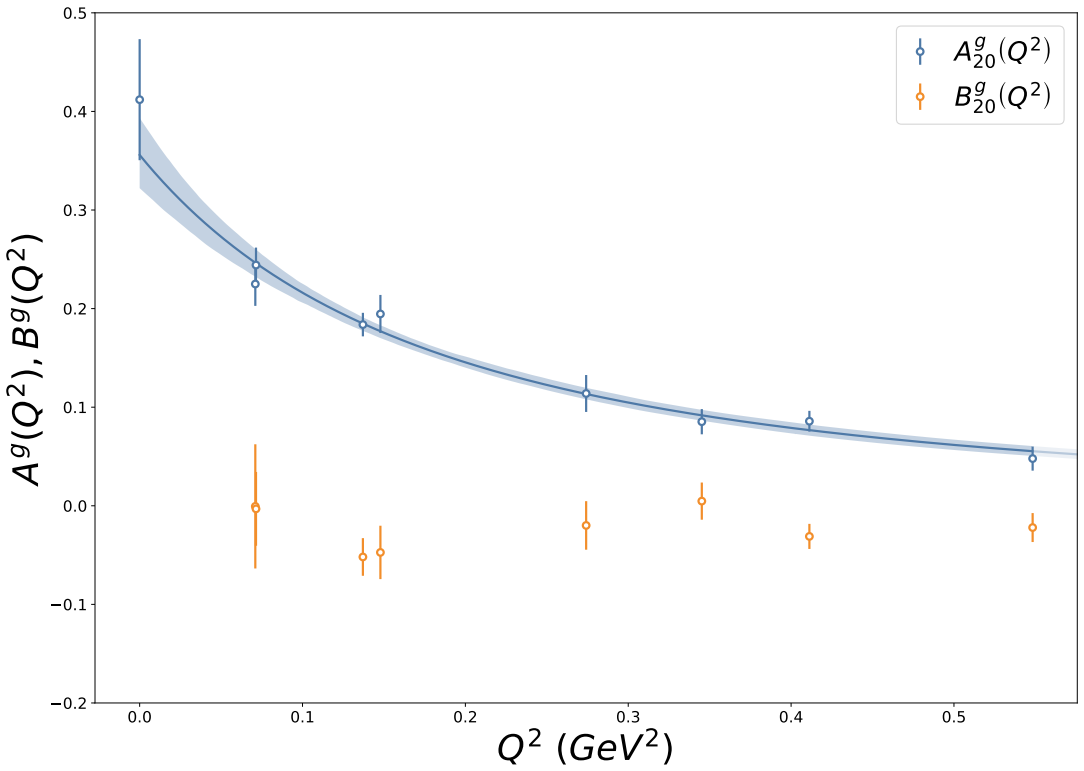

Figure 9.5: The gluon spin GFF decomposed into gluon momentum form factor $A^g_{20}(Q^2)$ (blue) and gluonic anomalous gravitomagnetic form factor $B^g_{20}(Q^2)$ (orange), as extracted using polarised projected operator $\mathcal{O}_{1i}$ with kinematic satisfying $\vec{p} \times \vec{p}' = 0$ or $q_i = 0$ as well as forward results from both operators at $Q^2 = 0$.

9.3.5 Full Decomposition: $A^g_{20}(Q^2)$, $B^g_{20}(Q^2)$ and $C^g_{20}(Q^2)$

To extract C_{20} as well we need three independent points at fixed Q^2. By utilising all the data available, the Q^2 where it is possible to extract each GFF are shown in Figure 9.6, with dipole fit for $A^g_{20}(Q^2)$.

The dipole fit on $A^g_{20}(Q^2)$ gives

$$A = 0.369(31) \tag{9.51}$$
$$a\Lambda = 0.602(33). \tag{9.52}$$

The extra data points have not been able to increase the precision of axis intercept A from §9.3.4, as this point is mainly fixed by the $Q^2 = 0$ point, common between these two. However the Λ term is improved in precision slightly, which we shall use to compare the gluonic radii of the quark and gluon GFFs in §9.3.6.

Despite the new data points in the extraction, the anomalous gravitomagnetic moment is still consistent with zero.

Finally the D term $C^g_{20}(Q^2)$ was not yet extractable with these statistics.

9.3.6 Gravitational Radius Comparison

One can relate A_{20} to the gravitational radii via the first derivative of the form factor [64], i.e. Λ in (9.31). We can determine relative radii visually alone, as sharper slopes imply larger radii. By plotting the Q^2 evolution of the dipole fits without the A factor we can observe this difference, from both data and fit, shown in Figure 9.7. Clearly the gluonic form factor drops much faster which implies it's gravitational radius is larger.

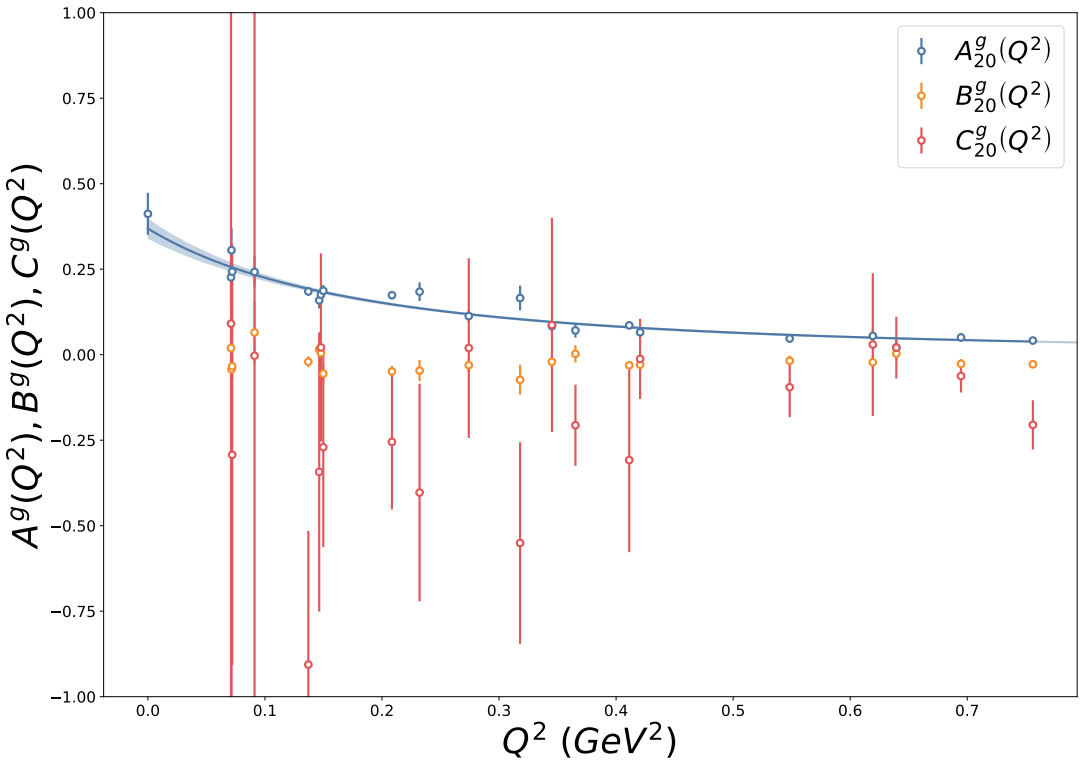

Figure 9.6: The full EMT GFF extraction, decomposed from the full data set, with $A^g_{20}(Q^2)$ (blue), $B^g_{20}(Q^2)$ (orange) and $C^g_{20}(Q^2)$ (red).

Note the much larger than physical masses, the heavier quarks have natural suppression on their radii. As one heads towards the physical limit, one expects the gravitational radius of the quark to increase. This method will then with sufficient statistics be able to determine which of the radii are larger.

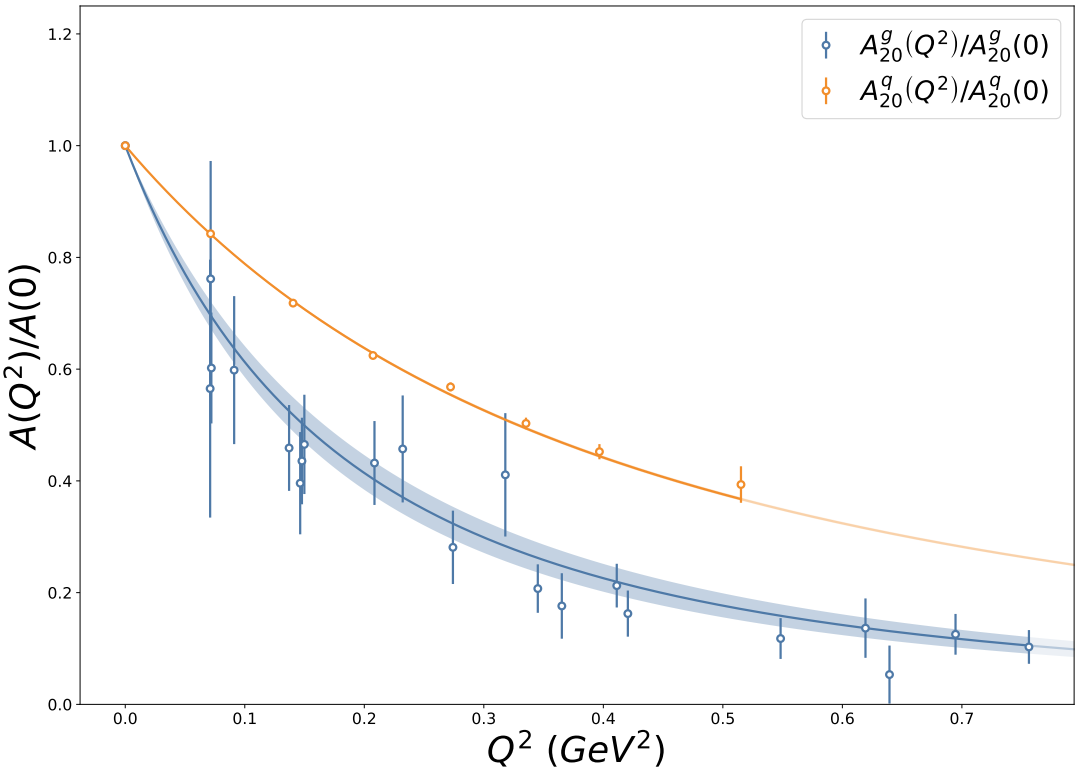

Figure 9.7: A comparison between gluon (blue) and quark (orange) radius, $A^g_{20}(Q^2)$ and $A^{u+d}_{20}(Q^2)$ have been scaled to start at 1.

9.4 Summary and Outlook

We showed how one can use Wilson flow to calculate the EMT GFFs on the lattice. Through careful choice of $\vec{q}$ and $\hat{s}$ the spin form factor was extracted directly. Using progressively more of data, first A^g_{20} and B^g_{20} were separated, before extracting C^g_{20} as well with the full data set. No deviation was found from $J^{g/q} = \frac{1}{2}A^{g/q}_{20}$, implying the spin contributions are determined entirely by momentum fractions. For these statistics no C^g_{20} signal was extractable.

Finally these gluon results were compared to the quark contributions to the EMT and showed that the gluon gravitational radius was larger than it's quark counterpart. Although this was at larger than physical masses, but sets the stage for future physical mass calculations.

Chapter 10

Summary and Outlook

Studies in hadron structure are at the forefront of the fundamental processes that underpin the structure of all matter in the universe. Lattice QCD is at the cutting edge of hadronic studies, with many observables now calculated at the percent level. Other quantities however, are not as well understood through the lens of lattice QCD, but work is on going to bridge these gaps. In this work we have shown through the use of the FHT how to calculate hadron matrix elements involving two external currents, normally extremely difficult on the lattice. Additionally gluonic spin and momentum structures were studied. as well as gluonic observables.

The cost of lattice calculations prohibits the breadth of studies with limited computing resources. In our proof of the FHT we presented two second order proofs, usable with lattice QCD that provide a new way of calculating hadron matrix elements with two currents on the lattice. Furthermore improvements to the FHT were shown, improving control of excited state systematics through the use of ratios and dramatically reducing computational costs through λ tuning and initial inverter conditions. This new FHT based tool-set allows us to examine new areas of the QCD from first principles for the first time.

Calculations of transition form factors are an interesting recent addition to the capabilities of lattice QCD. As a consequence of the parameters of the lattices used we are able to use the FHT approximate nucleon to delta transition form factors. With this simple approach the Adler transition form factor was approximated on two different lattice volumes to be $\left|C_5^A(0)^{24^3\times 48}\right| = 0.748(41)$ and $\left|C_5^A(0)^{32^3\times 48}\right| = 0.803(67)$, consistent with other lattice data and slightly smaller but still consistent with current experimental determinations.

The forward Compton amplitude in the unphysical region is related to the hadron tensor in terms of a sum of moments of the structure functions, which historically have been plagued by mixing, making extraction only possible for the lowest lying moments. We used the FHT to calculate the Compton amplitude $T_1\left(\omega, Q^2\right)$, for $\omega < 1$ and Q^2 between 0.72 and $15.85\ GeV^2$. The subtracted dispersion relationship was shown to be insensitive to the vector operator form. From this data, moments were extracted for the nucleon. These and related extensions offer the possibility to further constrain the models such as two–photon exchange and $\Box_{\gamma Z}$ calculations. In addition we showed the ω dependence of higher twist components of the structure function.

The subtraction function for the Compton amplitude has important implications for hadron structure. One open question remaining is the presence of a fixed–pole term, a term independent of Q^2. While it is not possible with current simulation data to determine whether a fixed pole is present, future simulations have been outlined to improve on this investigation. With this question resolved, these results could be used to calculate or challenge the existence of the *Cottingham formula*.

The EMT characterises the mass, spin and 'pressure' inside a hadron. Gluonic components are difficult to calculate on the lattice due to the short distance fluctuations present in the gauge links. Using gradient flow these operators were extracted, presenting the Q^2 dependency of the EMT GFFs. A direct calculation of the spin density $J^g\left(Q^2\right)$ was also achieved and showed no

deviation from $J^g = \frac{1}{2}A^g_{20}$. The EMT gluonic radius was determined to be greater than it's quark counterpart, albeit on a quenched lattice with large quark masses.

The study of the Compton amplitude in this work has been primarily limited to $T_1(\omega, Q^2)$, with the other structure functions extractable in principle. Momentum smearing could improve the extraction of the ω dependence of $T_1(\omega, Q^2)$, and allow determination of $T_2(\omega, Q^2)$. The structure function $T_3(\omega, Q^2)$ requires the use of mixed 'cosine' and 'sin' momentum combinations, rather than the pure 'cosine' combination shown here, and can be used to improve model calculation of box diagrams even further. The method can be further generalised to polarised or non–forward Compton amplitude and efforts are already under way to use the latter to extract GPDs. The future of FHT has exciting potential, both for our understanding of QCD and for it's impact on experiments.

Appendix A

Three and Four–Point Correlator Definitions

A.1 Three–point Correlator

The three–point correlator we will define differs from that of a two–point correlator by an extra operator applied in between the source and sink. Like the two–point case, it is easily shown that translational invariance implies the three–point correlator is only sensitive to separation between operators, not their absolute positions. Hence we have defined the three–point correlator

$$G^{(3)}_{\chi,J}(x,y) := \left\langle \chi(x) J(y) \chi^\dagger(0) \right\rangle. \tag{3.74}$$

We have restricted ourselves to the temporal ordering $x_4 > y_4 > 0$ for simplicity. As with the two–point correlator, we insert a complete set of states in between each operator

$$\begin{aligned} G^{(3)}_{\chi,J}(x,y) = \sum_{X,Y} \int \frac{d^3k_1}{(2\pi)^3} \int \frac{d^3k_2}{(2\pi)^3} \\ \times \frac{1}{2E_{X,\vec{k}_1}} \frac{1}{2E_{Y,\vec{k}_2}} \left\langle \Omega \middle| \chi(x) \middle| X, \vec{k}_1 \right\rangle \left\langle X, \vec{k}_1 \middle| J(y) \middle| Y, \vec{k}_2 \right\rangle \left\langle Y, \vec{k}_2 \middle| \chi^\dagger(0) \middle| \Omega \right\rangle \end{aligned} \tag{A.1}$$

and use translational invariance to simplify to

$$G^{(3)}_{\chi,J}(x,y) = \sum_{X,Y} \int \frac{d^3k_1}{(2\pi)^3} \int \frac{d^3k_2}{(2\pi)^3} e^{ik_1\cdot x} e^{i(k_2-k_1)\cdot y} g^{(3)}_{\chi J\chi^\dagger} \left[X, \vec{k}_1; Y, \vec{k}_2; 0, 0 \right] \tag{A.2}$$

where

$$g^{(3)}_{\chi J\chi^\dagger} \left[X, \vec{k}_1; Y, \vec{k}_2; x, y \right] := \frac{1}{2E_{X,\vec{k}_1}} \frac{1}{2E_{Y,\vec{k}_2}} \left\langle \Omega \middle| \chi(x) \middle| X, \vec{k}_1 \right\rangle \left\langle X, \vec{k}_1 \middle| J(y) \middle| Y, \vec{k}_2 \right\rangle \left\langle Y, \vec{k}_2 \middle| \chi^\dagger(0) \middle| \Omega \right\rangle. \tag{3.75}$$

and we often use shorthand

$$g^{(3)}_{\chi J\chi^\dagger} \left[X, \vec{k}_1; Y, \vec{k}_2 \right] := g^{(3)}_{\chi J\chi^\dagger} \left[X, \vec{k}_1; Y, \vec{k}_2; 0, 0 \right]. \tag{A.3}$$

The momentum space version then is

$$G^{(3)}_{\chi,J}(x_4, y_4, \vec{p}, \vec{q}) = \int d^3x \int d^3y e^{-i\vec{p}\cdot\vec{x}} e^{i\vec{q}\cdot\vec{y}} G^{(3)}_{\chi,J}(x,y) \tag{3.76}$$

$$= \sum_{X,Y} e^{-E_{X,\vec{p}} x_4} e^{-\left(E_{Y,(\vec{p}-\vec{q})} - E_{X,\vec{p}}\right) y_4} g^{(3)}_{\chi J\chi^\dagger} \left[X, \vec{p}; Y, (\vec{p}-\vec{q}); 0, 0 \right]. \tag{3.77}$$

In a similar manner to two–point functions in the large x_4 and y_4 time limit with $x_4 >> y_4 >> 0$ yields

$$G^{(3)}_{\chi,J}(x_4, y_4, \vec{p}, \vec{q}) \to e^{-E_{X,\vec{p}}x_4} e^{-\left(E_{X,(\vec{p}-\vec{q})} - E_{X,\vec{p}}\right)y_4} g^{(3)}_{\chi J \chi^\dagger}\left[X, \vec{p}, Y, (\vec{p}-\vec{q}); 0, 0\right] \tag{A.4}$$

where X is the lowest energy states for $\vec{p}$ and $\vec{p}-\vec{q}$ with $g^{(3)}_{\chi J \chi^\dagger} \neq 0$. This gives us a three–point function which we can use to calculate matrix elements. We use three–point correlators for our FHT proofs in §4 and directly on the lattice for our gluon calculations §9.

A.2 Four–point Correlator

We look at four–point correlators with two interpolators and two currents. As we see by increasing the number of operators in our expectation value, the complexity of the calculations increases. The four–point correlator is defined in position space by

$$G^{(4)}_{\chi,J_1,J_2}(x, y, z, w) := \left\langle \chi(x) J_2(y) J_1(z) \chi^\dagger(w) \right\rangle. \tag{3.78}$$

Unlike the two and three–point case, we have not redefined our result in terms of separation variables $x-w$, $y-w$ and $z-w$, as this form is useful only to our proof in §4. As before we pick time ordering for our operators $x_4 > y_4 > z_4 > w_4$ and insert complete sets of states

$$\begin{aligned} G^{(4)}_{\chi,J_1,J_2}(x, y, z, w) = \sum_{X,Y,Z} \int \frac{d^3k_1}{(2\pi)^3} \int \frac{d^3k_2}{(2\pi)^3} \int \frac{d^3k_3}{(2\pi)^3} \\ \times g^{(4)}_{\chi,J_1,J_2}\left[X, \vec{k}_1; Y, \vec{k}_2; Z, \vec{k}_3; x, y, z, w\right] \end{aligned} \tag{A.5}$$

where

$$\begin{aligned} g^{(4)}_{\chi,J_1,J_2}\left[X, \vec{k}_1; Y, \vec{k}_2; Z, \vec{k}_3; x, y, z, w\right] := \frac{1}{2E_{X,\vec{k}_1}} \frac{1}{2E_{Y,\vec{k}_2}} \frac{1}{2E_{Z,\vec{k}_3}} \\ \times \left\langle \Omega \middle| \chi(x) \middle| X, \vec{k}_1 \right\rangle \left\langle X, \vec{k}_1 \middle| J_2(y) \middle| Y, \vec{k}_2 \right\rangle \\ \times \left\langle Y, \vec{k}_2 \middle| J_1(z) \middle| Z, \vec{k}_3 \right\rangle \left\langle Z, \vec{k}_3 \middle| \chi^\dagger(w) \middle| \Omega \right\rangle. \end{aligned} \tag{3.79}$$

Then as before we can use translational invariance

$$\begin{aligned} G^{(4)}_{\chi,J_1,J_2}(x, y, z, w) = \sum_{X,Y,Z} \int \frac{d^3k_1}{(2\pi)^3} \int \frac{d^3k_2}{(2\pi)^3} \int \frac{d^3k_3}{(2\pi)^3} e^{ik_1\cdot x} e^{i(k_2-k_1)\cdot y} e^{i(k_3-k_2)\cdot z} e^{-ik_3\cdot w} \\ \times g^{(4)}_{\chi,J_1,J_2}\left[X, \vec{k}_1; Y, \vec{k}_2; Z, \vec{k}_3, 0, 0, 0, 0\right]. \end{aligned} \tag{A.6}$$

The momentum projected form of this function then has three momenta to be specified

$$\begin{aligned} G^{(4)}_{\chi,J_1,J_2}(x_4, y_4, z_4, w_4, \vec{p}, \vec{q}_1, \vec{q}_2) = \int d^3x \int d^3y \int d^3z e^{-i\vec{p}\cdot(\vec{x}-\vec{w})} e^{i\vec{q}_2\cdot(\vec{y}-\vec{w})} e^{i\vec{q}_1\cdot(\vec{z}-\vec{w})} \\ \times G^{(4)}_{\chi,J_1,J_2}(x, y, z, w) \end{aligned} \tag{3.80}$$

where we note the careful choice of momentum projections, which after integration becomes

$$\begin{aligned} G^{(4)}_{\chi,J_1,J_2}(x_4, y_4, z_4, w_4, \vec{p}, \vec{q}_1, \vec{q}_2) = \sum_{X,Y,Z} e^{-E_{X,\vec{p}}(x_4-w_4)} e^{-\left(E_{Y,(\vec{p}-\vec{q}_1)} - E_{X,\vec{p}}\right)(y_4-w_4)} \\ \times e^{-\left(E_{Y,(\vec{p}-\vec{q}_1-\vec{q}_2)} - E_{Y,(\vec{p}-\vec{q}_1)}\right)(z_4-w_4)} \\ \times g^{(4)}_{\chi,J_1,J_2}\left[X, \vec{p}; Y, (\vec{p}-\vec{q}_1); Y, (\vec{p}-\vec{q}_1-\vec{q}_2); 0, 0, 0, 0\right] \end{aligned} \tag{A.7}$$

As expected we have an expression defined entirely in terms of differences of our temporal variables and momentum.

Appendix B

Additional Plots

B.1 Compton Amplitude

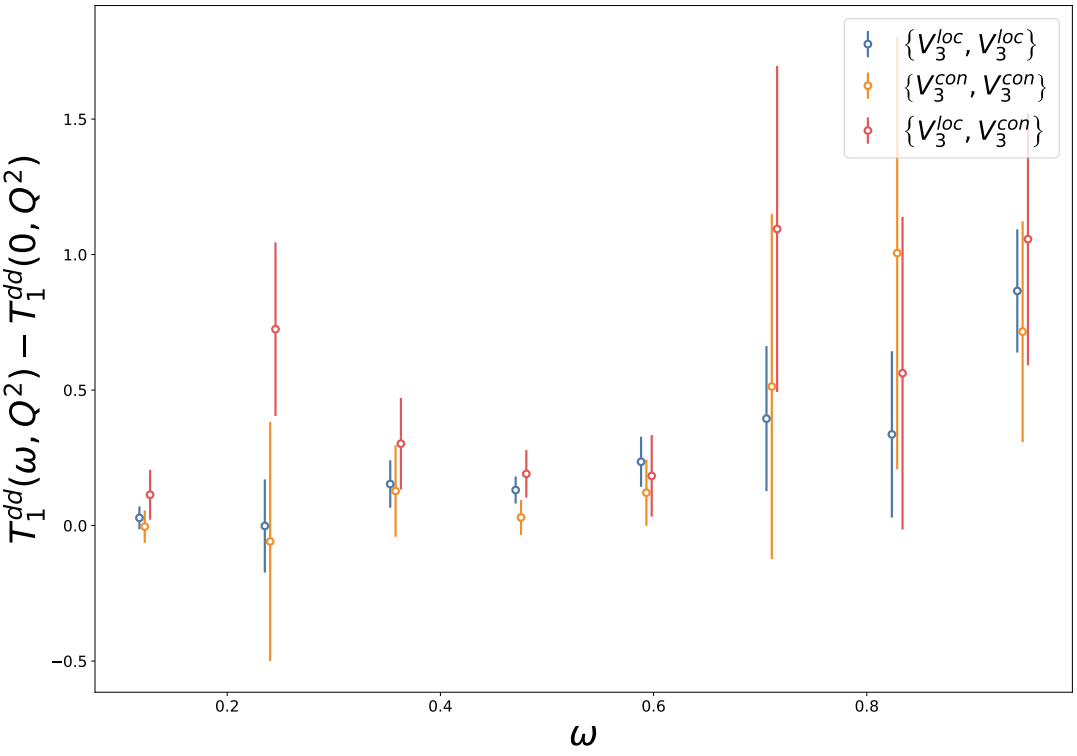

Figure B.1: Operator comparison of the subtracted Compton amplitude $T_1^{dd}(\omega, Q^2) - T_1^{dd}(0, Q^2)$ for $\vec{q} = (4, 1, 0)$ for a set of different currents. Note that there is a large difference in the number of sources between the V_3^{loc} and the other currents (Table 7.2).

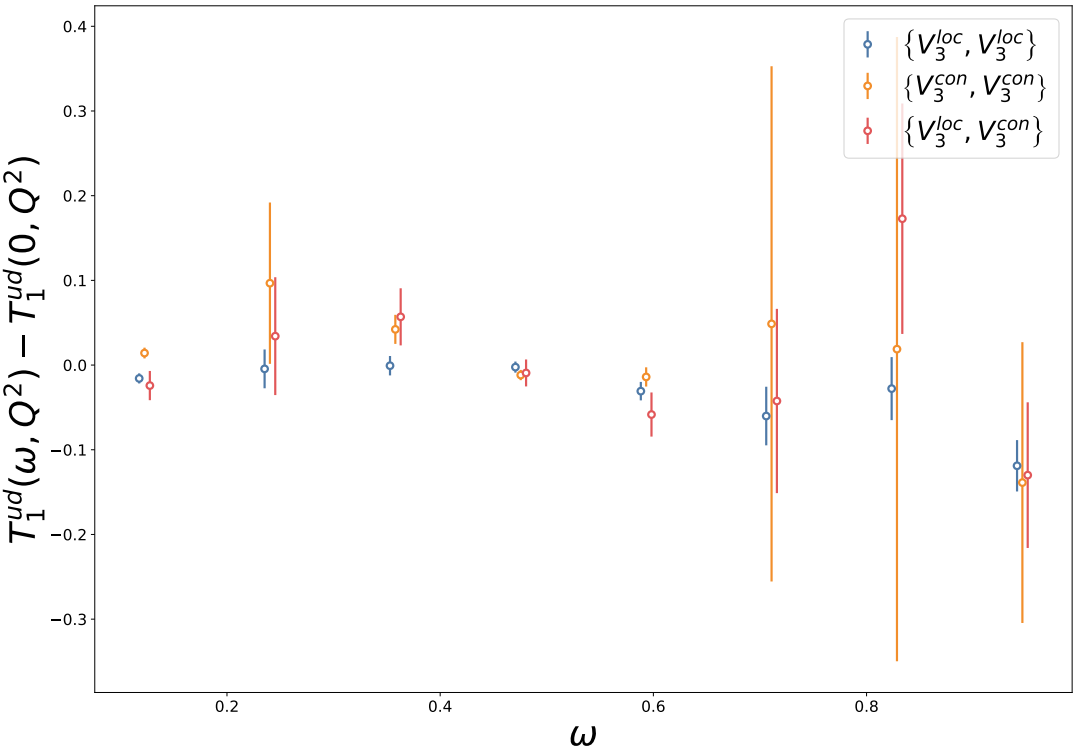

Figure B.2: Operator comparison of the subtracted Compton amplitude $T_1^{ud}(\omega, Q^2) - T_1^{ud}(0, Q^2)$ for $\vec{q} = (4, 1, 0)$ for a set of different currents. Note that there is a large difference in the number of sources between the V_3^{loc} and the other currents (Table 7.2).

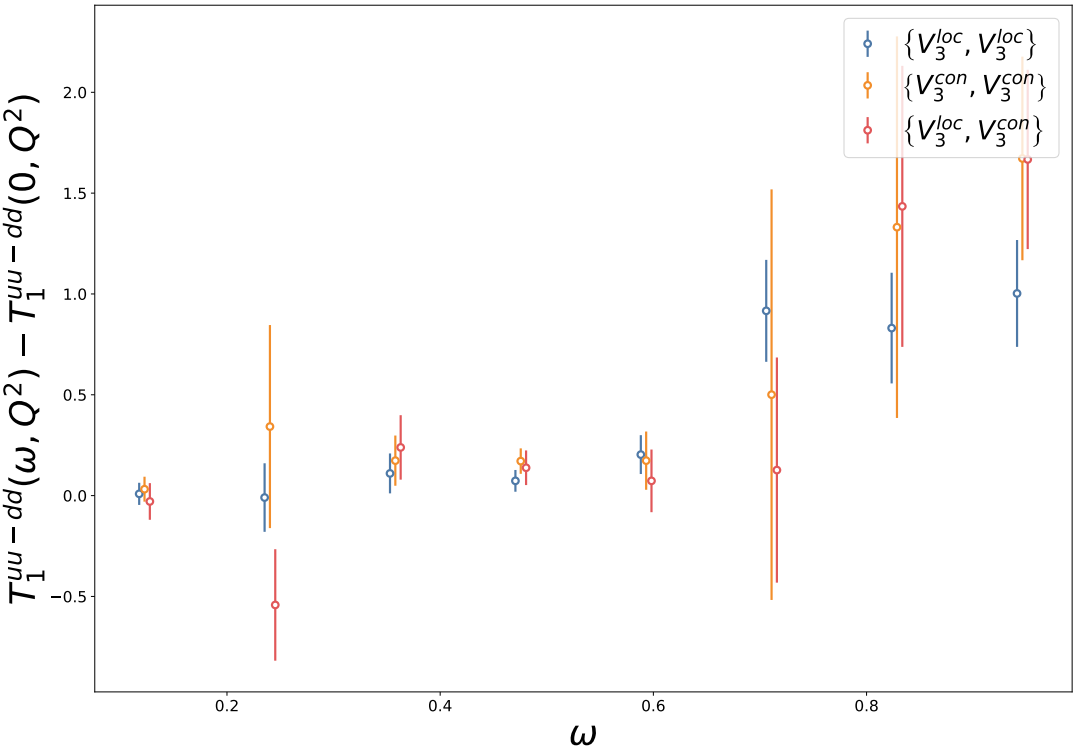

Figure B.3: Operator comparison of the subtracted Compton amplitude $T_1^{uu-dd}(\omega, Q^2) - T_1^{uu-dd}(0, Q^2)$ for $\vec{q} = (4, 1, 0)$ for a set of different currents. Note that there is a large difference in the number of sources between the V_3^{loc} and the other currents (Table 7.2).

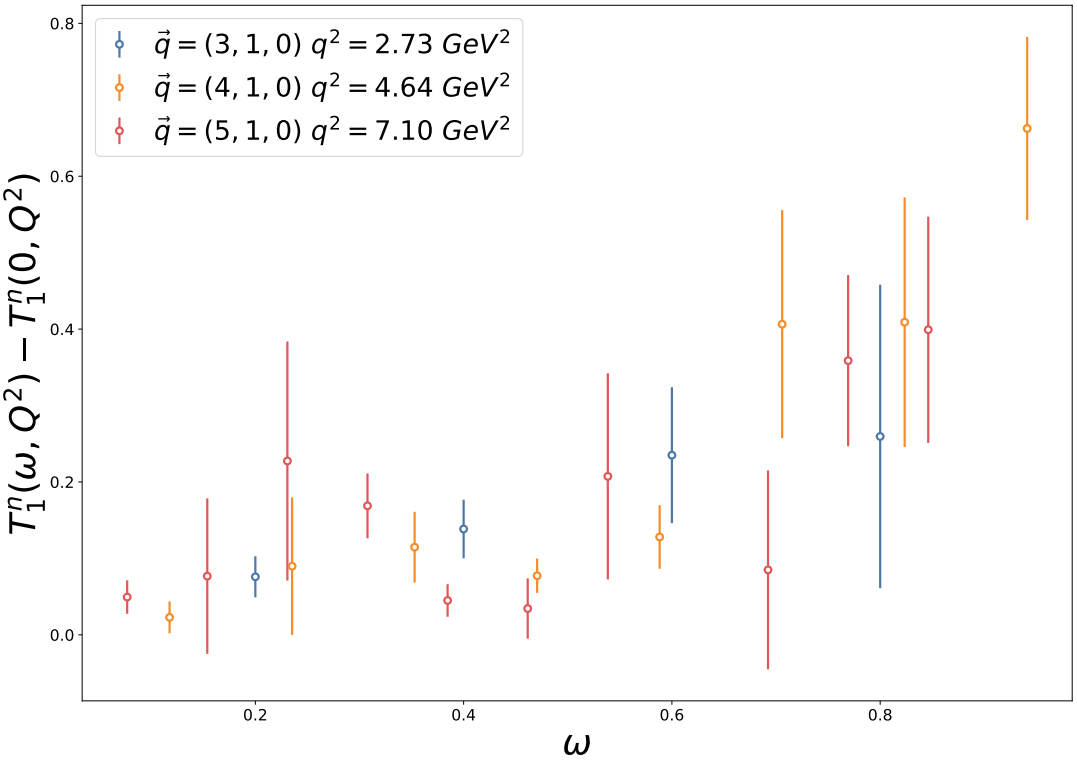

Figure B.4: The reconstructed subtracted neutron Compton amplitude $T_1^n(\omega, Q^2) - T_1^n(0, Q^2)$. The points are the high statistics $N_s = \mathcal{O}(10000)$ simulations from Table 7.2.

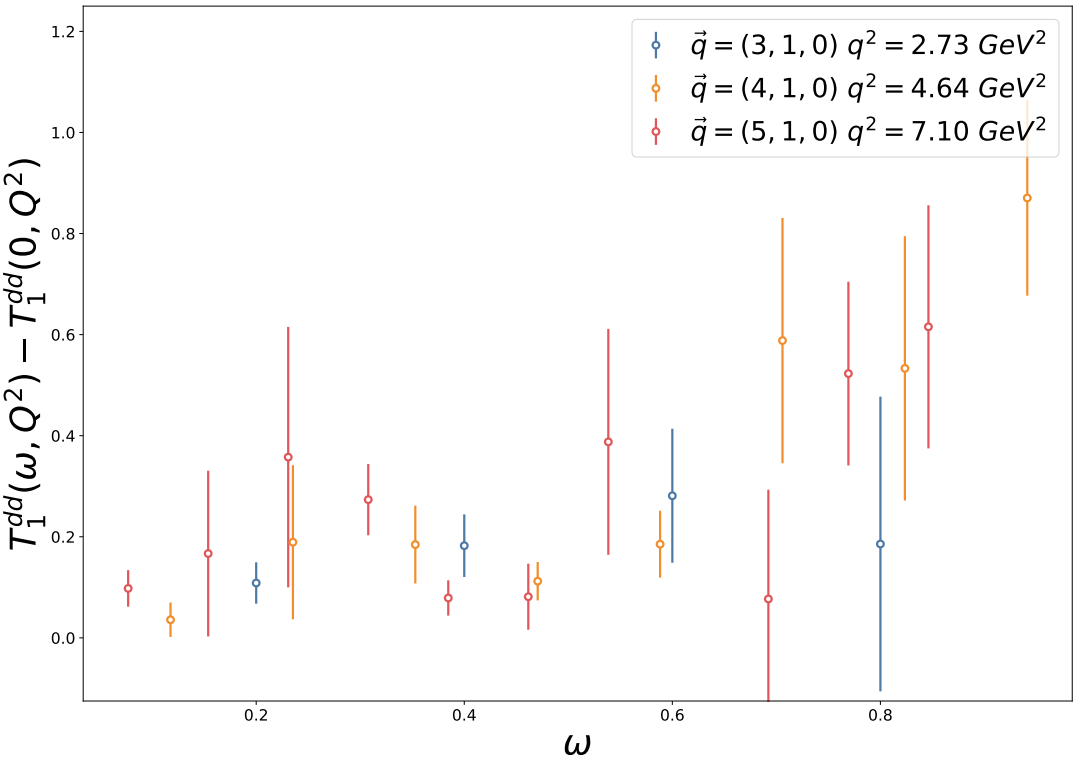

Figure B.5: The subtracted Compton amplitude $T_1^{dd}(\omega, Q^2) - T_1^{dd}(0, Q^2)$. The points are the high statistics $N_s = \mathcal{O}(10000)$ simulations from Table 7.2.

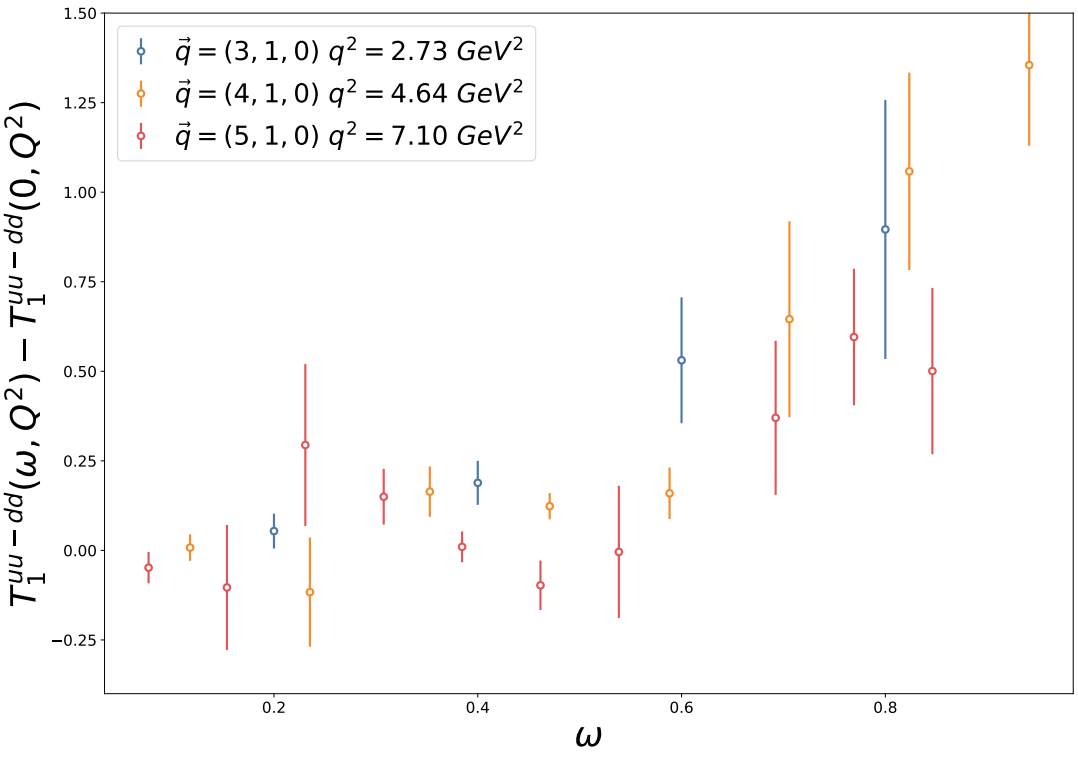

Figure B.6: The subtracted Compton amplitude $T_1^{uu-dd}(\omega, Q^2) - T_1^{uu-dd}(0, Q^2)$. The points are the high statistics $N_s = \mathcal{O}(10000)$ simulations from Table 7.2.

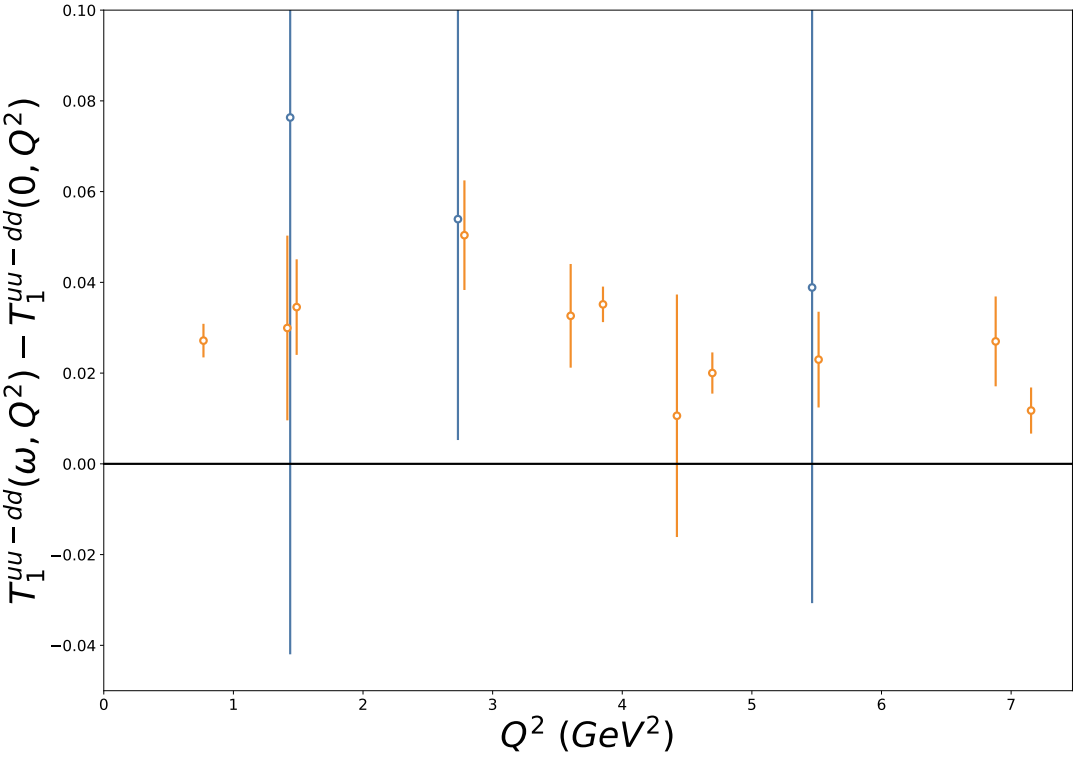

(a) $\omega = 0.2$

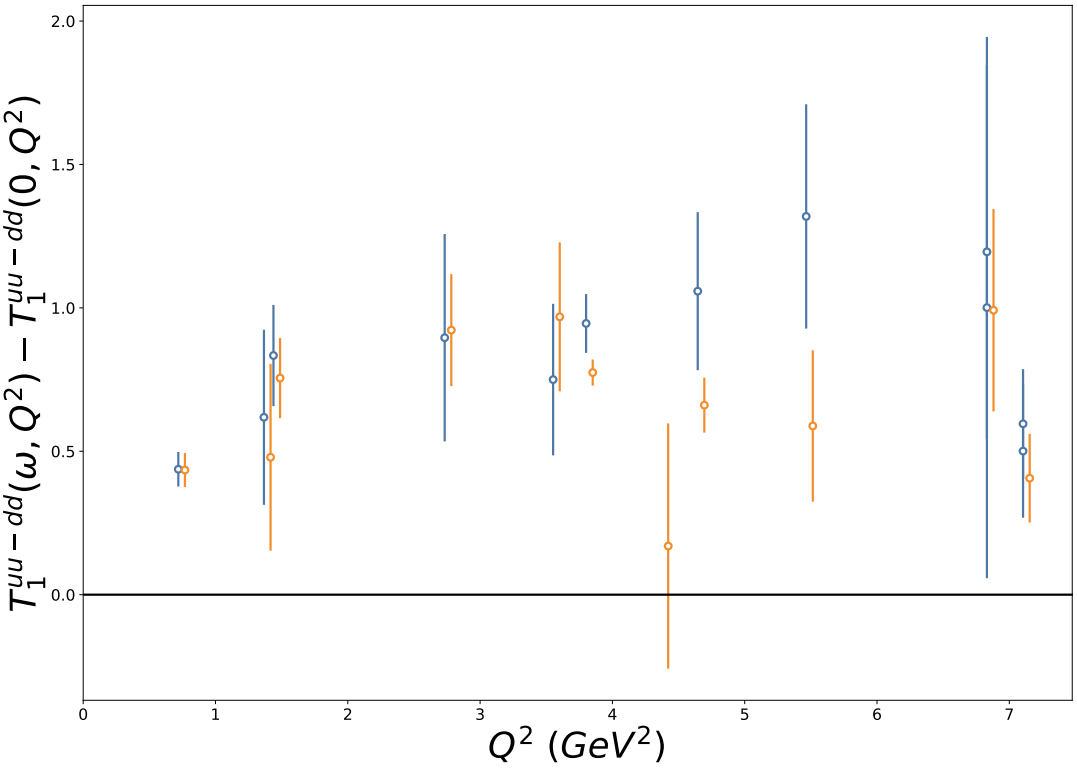

(b) $\omega = 0.8$

Figure B.7: The scaling at constant ω of the subtracted Compton amplitude $T_1^{dd}(\omega, Q^2) - T_1^{dd}(0, Q^2)$ for $\omega = 0.2$ (a) and $\omega = 0.8$ (b). These points include direct calculations at these ω (blue), whose ω are within 10.0% of this value. The constrained fit values for each simulation have been used to generate points (orange) at these ω, offset slightly for clarity.

Appendix C

Conventions

C.1 Euclidianisation

With our work with Euclidean space path integrals on the lattice we often wish to compare our results to those of QFT or GFT in Minkowski space. Here we present the convention used in the Wick rotation in our work. Our aim is to convert the metric $g_{\mu\nu}$ with signature $(+,-,-,-)$ to $\delta_{\mu\nu}$ with signature $(+,+,+,+)$. We note carefully that we have used the metric of signature $(+,-,-,-)$ as opposed to the one with $(-,+,+,+)$ for all our definitions. We start with a Wick rotation as described in §3.1

$$x^{\mu}_{(M)} := \left(x^0_{(M)}, \quad \vec{x}_{(M)}\right) \to \left(\quad \vec{x}_{(M)}, ix^0_{(M)}\right) = \left(\vec{x}^{\,(E)}, x_4^{(E)}\right) =: x_{\mu}^{(E)} \tag{C.1}$$

$$x_{\mu}^{(M)} \ = \left(x^0_{(M)}, -\vec{x}_{(M)}\right) \to \left(-\vec{x}_{(M)}, ix^0_{(M)}\right) \tag{C.2}$$

and for Dirac matrices

$$\gamma_{\mu}^{(M)} := \left(\gamma_0^{(M)}, \vec{\gamma}^{(M)}\right) \to \left(i\vec{\gamma}^{(M)}, \gamma_0^{(M)}\right) =: \gamma_{\mu}^{(E)}. \tag{C.3}$$

Explicitly transformations affect vectors in the following way

$$x_4^{(E)} = ix_0^{(M)} \tag{C.4}$$

$$x_4^{(E)} = ix^0_{(M)} \tag{C.5}$$

$$x_i^{(E)} = -x_i^{(M)} \tag{C.6}$$

$$x_i^{(E)} = x^i_{(M)} \tag{C.7}$$

for transformation from Minkowski into Euclidean, and

$$x_0^{(M)} = -ix_4^{(E)} \tag{C.8}$$

$$x^0_{(M)} = -ix_4^{(E)} \tag{C.9}$$

$$x_i^{(M)} = -x_i^{(E)} \tag{C.10}$$

$$x^i_{(M)} = x_i^{(E)} \tag{C.11}$$

for transformation from Euclidean into Minkowski. The Dirac matrices meanwhile transform

$$\gamma_0^{(M)} = \gamma_4^{(E)} \tag{C.12}$$

$$\gamma^0_{(M)} = \gamma_4^{(E)} \tag{C.13}$$

$$\gamma_i^{(M)} = -i\gamma_i^{(E)} \tag{C.14}$$

$$\gamma^i_{(M)} = \quad i\gamma_i^{(E)} \tag{C.15}$$

$$\tag{C.16}$$

from Euclidean into Minkowski, and

$$\gamma_4^{(E)} = \gamma_0^{(M)} \tag{C.17}$$
$$\gamma_4^{(E)} = \gamma^0_{(M)} \tag{C.18}$$
$$\gamma_i^{(E)} = \quad i\gamma_i^{(M)} \tag{C.19}$$
$$\gamma_i^{(E)} = -i\gamma^i_{(M)} \tag{C.20}$$

from Minkowski to Euclidean. The fifth gamma matrix γ_5 is defined to transform

$$\gamma_5^{(M)} = \gamma_5^{(E)} \tag{C.21}$$

as

$$\gamma_5^{(M)} := i\gamma_0^{(M)}\gamma_2^{(M)}\gamma_3^{(M)} \tag{C.22}$$
$$\gamma_5^{(E)} := \gamma_1^{(E)}\gamma_2^{(E)}\gamma_3^{(E)}\gamma_4^{(E)} \tag{C.23}$$

For explicit gamma matrices in each space see §C.1.2. Our convention has sign change for dot products under transformation

$$\begin{aligned}(q\cdot x)^{(M)} &:= q_\mu x^\mu \\ &\to \left(-\vec{q}^{(M)}, iq_0^{(M)}\right)\cdot\left(\vec{x}^{(M)}, ix_0^{(M)}\right) \\ &= -(q\cdot x)^{(E)}\end{aligned} \tag{C.24}$$

Noting all but the first dot product is in Euclidean space and hence uses the $\delta_{\mu\nu}$ metric.

We now have the necessary pieces to work out all the resulting transformation properties. We will start by working out the transformation properties of the tangent plane in §C.1.1, followed by the various parts of the Clifford algebra §C.1.2, and then the field strength tensor §C.1.3. We then use all these piece to work out the transformation properties of matrix elements we are interested in, namely the vector §C.1.4, gluon §C.1.5, and Compton amplitude §C.1.6.

C.1.1 Derivatives

We start with the tangent space Wick rotation, first with partial derivatives

$$\partial_0^{(M)} = \frac{\partial}{\partial x^0_{(M)}} = -\frac{\partial}{\partial i x^0_{(E)}} = i\frac{\partial}{\partial x^4_{(E)}} = i\partial_4^{(E)} \tag{C.25}$$
$$\partial^0_{(M)} = i\partial_4^{(E)} \tag{C.26}$$
$$\partial_i^{(M)} = \frac{\partial}{\partial x^i_{(M)}} = \frac{\partial}{\partial x^i_{(E)}} = \partial_i^{(E)} \tag{C.27}$$
$$\partial^i_{(M)} = -\partial_i^{(E)}. \tag{C.28}$$

Taking the partial derivative in combination with the transformation law of vectors we can work out how the covariant derivative

$$\mathcal{D}_\mu^{(M)} := \partial_\mu^{(M)} - igA_\mu^{(M)} \tag{C.29}$$
$$\mathcal{D}_\mu^{(E)} := \partial_\mu^{(E)} + igA_\mu^{(E)} \tag{C.30}$$
$$\tag{C.31}$$

where because $A_\mu^{(M)}$ transforms like our arbitrary vectors

$$\begin{aligned}\mathcal{D}_0^{(M)} &= \partial_0^{(M)} - igA_0^{(M)} \\ &= i\partial_4^{(E)} - gA_4^{(E)} \\ &= i\partial_4^{(E)} + i^2 gA_4^{(E)} \\ &= i\left(\partial_4^{(E)} + igA_4^{(E)}\right) \\ &=: i\mathcal{D}_4^{(E)}\end{aligned} \tag{C.32}$$

and

$$\begin{aligned}\mathcal{D}_i^{(M)} &= \partial_i^{(M)} - igA_i^{(M)} \\ &= \partial_i^{(E)} + igA_i^{(E)} \\ &= \mathcal{D}_i^{(E)}.\end{aligned} \tag{C.33}$$

Another transformation we can now calculate is a space–time integrals, that like derivatives transform in the tangent space. A four dimensional integrals transforms like

$$\int d^4x_{(M)} = i\int d^4x_{(E)} \tag{C.34}$$

C.1.2 Clifford Algebra

The only part of the Clifford algebra we still need to transform is the anti commuting $\sigma_{\mu\nu}$. We define it in both spaces by

$$\sigma_{\mu\nu}^{(M)} := \frac{i}{2}\left[\gamma_\mu^{(M)}, \gamma_\nu^{(M)}\right] \tag{C.35}$$

$$\sigma_{\mu\nu}^{(E)} := \frac{i}{2}\left[\gamma_\mu^{(E)}, \gamma_\nu^{(E)}\right]. \tag{C.36}$$

Due to the skew symmetry one only needs to calculate the transformation of two possible cases

$$\sigma_{0i}^{(M)} = -i\sigma_{4i}^{(E)} \tag{C.37}$$

$$\sigma_{ij}^{(M)} = -\sigma_{ij}^{(E)} \tag{C.38}$$

which means their reverse transformations are

$$\sigma_{4i}^{(E)} = i\sigma_{0i}^{(M)} \tag{C.39}$$

$$\sigma_{ij}^{(E)} = -\sigma_{ij}^{(M)}. \tag{C.40}$$

In our case we often see a contracted vector with the tensor

$$\begin{aligned}\sigma_{0\alpha}^{(M)} q_{(M)}^\alpha &= \sigma_{0i}^{(M)} q_{(M)}^i \\ &= -i\sigma_{4i}^{(E)} q_i^{(E)}\end{aligned} \tag{C.41}$$

and

$$\begin{aligned}\sigma_{i\alpha}^{(M)} q_{(M)}^\alpha &= \sigma_{ij}^{(M)} q_{(M)}^j + \sigma_{i0}^{(M)} q_{(M)}^0 \\ &= -\sigma_{ij}^{(E)} q_j^{(E)} + (-i)^2 \sigma_{i4}^{(E)} q_4^{(M)} \\ &= -\sigma_{i\alpha}^{(E)} q_\alpha^{(E)}.\end{aligned} \tag{C.42}$$

Then we note γ_5 transforms to it's counterpart so pseudo–vectors $\gamma_\mu\gamma_5$ transform like the vector counterparts.

C.1.3 Field Strength Tensor

To calculate how the field strength tensor

$$F_{\mu\nu}^{(M)} := i\Big[\mathcal{D}_{\mu}^{(M)}, \mathcal{D}_{\nu}^{(M)}\Big] \tag{C.43}$$

we divide into different parts, which because of the skew symmetry of indices is just two different cases just like $\sigma_{\mu\nu}$

$$F_{0i}^{(M)} = i\Big[\mathcal{D}_{0}^{(M)}, \mathcal{D}_{i}^{(M)}\Big] = i^2\Big[\mathcal{D}_{4}^{(E)}, \mathcal{D}_{i}^{(E)}\Big] = iF_{4i}^{(E)} \tag{C.44}$$

and

$$F_{ij}^{(M)} = i\Big[\mathcal{D}_{i}^{(M)}, \mathcal{D}_{j}^{(M)}\Big] = i\Big[\mathcal{D}_{i}^{(E)}, \mathcal{D}_{j}^{(E)}\Big] = F_{ij}^{(E)} \tag{C.45}$$

where we define

$$F_{\mu\nu}^{(E)} := i\Big[\mathcal{D}_{\mu}^{(E)}, \mathcal{D}_{\nu}^{(E)}\Big]. \tag{C.46}$$

Using this we can then figure out how the photonic (or implicitly colour traced gluonic) E and B fields transform

$$E_i^{(M)} := F_{0i}^{(M)} = iF_{4i}^{(E)} = iE_i^{(E)} \tag{C.47}$$

$$B_i^{(M)} := -\frac{1}{2}\epsilon_{ijk}F_{(M)}^{jk} = (-1)^3\frac{1}{2}\epsilon_{ijk}F_{(E)}^{jk} = B_i^{(E)}. \tag{C.48}$$

For the gluonic EMT operator

$$T_{\mu\nu}^{(M)} := -F_{\mu\alpha}F_{\nu}{}^{\alpha} \tag{C.49}$$

we consider only three different combinations, using the anti symmetric property of $F_{\mu\nu}$

$$T_{00}^{(M)} = -F_{0\alpha}^{(M)}(F_0{}^{\alpha})^{(M)} = (-1)^2\Big(F_{0i}^{(M)}\Big)^2 = -\Big(F_{4i}^{(E)}\Big)^2 =: T_{44}^{(E)} \tag{C.50}$$

$$T_{ii}^{(M)} = -F_{i\alpha}^{(M)}(F_i{}^{\alpha})^{(M)} = (-1)^2\Big(F_{ij}^{(M)}\Big)^2 - \Big(F_{i0}^{(M)}\Big)^2 = \Big(F_{ij}^{(E)}\Big)^2 - i^2\Big(F_{i0}^{(E)}\Big)^2 = -T_{ii}^{(E)} \tag{C.51}$$

$$T_{i0}^{(M)} = -F_{i\alpha}^{(M)}(F_4{}^{\alpha})^{(M)} = (-1)^2F_{ij}^{(M)}F_{0j}^{(M)} = iF_{ij}^{(E)}F_{4j}^{(E)} = iF_{i\alpha}^{(E)}F_{4\alpha}^{(E)} = -iT_{i4}^{(E)} \tag{C.52}$$

C.1.4 Vector Form Factor

By defining the matrix elements of form factors carefully, the form factors themselves are the same, whether from a Minkowski or Euclidean form factor (In fact that is the motivation for our normalisation choice (3.61)). Consider a nucleon vector form factor

$$\big\langle p'\big|\gamma_\mu\big|p\big\rangle^{(M)} = \overline{u}(p')\left[\gamma_\mu^{(M)}F_1(t) + \frac{i\sigma_{\mu\alpha}^{(M)}q_{(M)}^{\alpha}}{2m}F_2(t)\right]u(p) \tag{C.53}$$

we then look at the temporal and spatial components separately, and equate them after wick rotation.

$$\big\langle p'\big|\gamma_0\big|p\big\rangle^{(M)} = \big\langle p'\big|\gamma_4\big|p\big\rangle^{(E)} \tag{C.54}$$

$$= \overline{u}(p')\left[\gamma_4^{(E)}F_1(t) - i\frac{i\sigma_{4\alpha}^{(E)}q_{\alpha}^{(E)}}{2m}F_2(t)\right]u(p) \tag{C.55}$$

$$= \overline{u}(p')\left[\gamma_4^{(E)}F_1(t) + \frac{\sigma_{4\alpha}^{(E)}q_{\alpha}^{(E)}}{2m}F_2(t)\right]u(p) \tag{C.56}$$

for the temporal and

$$\langle p'|\gamma_i|p\rangle^{(M)} = -i\langle p'|\gamma_i|p\rangle^{(E)} \tag{C.57}$$

$$= \overline{u}(p')\left[-i\gamma_i^{(E)}F_1(t) - \frac{i\sigma_{i\alpha}^{(E)}q_\alpha^{(E)}}{2m}F_2(t)\right]u(p) \tag{C.58}$$

which corresponds to

$$\langle p'|\gamma_i|p\rangle^{(E)} = \overline{u}(p')\left[\gamma_i^{(E)}F_1(t) + \frac{\sigma_{i\alpha}^{(E)}q_\alpha^{(E)}}{2m}F_2(t)\right]u(p). \tag{C.59}$$

Hence we as both temporal and spatial transform in the same manner we can say that

$$\langle p'|\gamma_\mu|p\rangle^{(E)} = \overline{u}(p')\left[\gamma_\mu^{(E)}F_1(t) + \frac{\sigma_{\mu\alpha}^{(E)}q_\alpha^{(E)}}{2m}F_2(t)\right]u(p). \tag{C.60}$$

C.1.5 Gluon Form Factor

We perform the same steps of matching as for the vector form factors for the gluon EMT GFFs. Consider the form factor of a symmetric tensor $T_{\mu\nu}$, which in Minkowski space has general form

$$\begin{aligned}\langle N|T_{\mu\nu}|N\rangle^{(M)} = \frac{1}{2}\overline{u}(p')\Bigg[&\gamma_\mu^{(M)}P_\nu^{(M)}A(t)\\ &+\frac{i\sigma_{\mu\alpha}^{(M)}q_{(M)}^\alpha P_\nu^{(M)}}{2m}B(t)\\ &+\frac{q_\mu^{(M)}q_\nu^{(M)}}{m}C(t) + (\mu\leftrightarrow\nu)\Bigg]u(p)\end{aligned} \tag{C.61}$$

Now we wish to look at the transformation of this to Euclidean space component by component

$$\langle N|T_{00}|N\rangle^{(M)} = \left\langle N\middle|T_{44}^{(E)}\middle|N\right\rangle \tag{C.62}$$

$$= \overline{u}(p')\left[-i\gamma_4^{(E)}P_4^{(E)}A(t) + \frac{i^3\sigma_{4\alpha}^{(E)}q_\alpha^{(E)}P_4^{(E)}}{2m}B(t) - \frac{q_4^{(E)}q_4^{(E)}}{m}C(t)\right]u(p) \tag{C.63}$$

$$= \overline{u}(p')\left[-i\gamma_4^{(E)}P_4^{(E)}A(t) - \frac{i\sigma_{4\alpha}^{(E)}q_\alpha^{(E)}P_4^{(E)}}{2m}B(t) - \frac{q_4^{(E)}q_4^{(E)}}{m}C(t)\right]u(p) \tag{C.64}$$

$$\left\langle N\middle|T_{ii}^{(M)}\middle|N\right\rangle = -\left\langle N\middle|T_{ii}^{(E)}\middle|N\right\rangle \tag{C.65}$$

$$= \overline{u}(p')\left[i\gamma_i^{(E)}P_i^{(E)}A(t) + \frac{i\sigma_{i\alpha}^{(E)}q_\alpha^{(E)}P_i^{(E)}}{2m}B(t) + \frac{q_i^{(E)}q_i^{(E)}}{m}C(t)\right]u(p) \tag{C.66}$$

$$\begin{aligned}\left\langle N\middle|T_{0i}^{(M)}\middle|N\right\rangle &= -i\left\langle N\middle|T_{0i}^{(E)}\middle|N\right\rangle \\ &= \frac{1}{2}\overline{u}(p')\left[\left(-\gamma_4^{(E)}P_i^{(E)}+(-i)^2\gamma_i^{(E)}P_4^{(E)}\right)A(t)\right. \\ &\quad + \frac{i(-i)(-1)\sigma_{4\alpha}^{(E)}q_\alpha^{(E)}P_i^{(E)}+i(-1)(-i)\sigma_{i\alpha}^{(E)}q_\alpha^{(E)}P_4^{(E)}}{2m}B(t) \\ &\quad \left.+\frac{2iq_4^{(E)}q_i^{(E)}}{m}C(t)\right]u(p) \\ &= \frac{1}{2}\overline{u}(p')\left[\left(-\gamma_4^{(E)}P_i^{(E)}-\gamma_i^{(E)}P_4^{(E)}\right)A(t)\right. \\ &\quad - \frac{\sigma_{4\alpha}^{(E)}q_\alpha^{(E)}P_i^{(E)}+\sigma_{i\alpha}^{(E)}q_\alpha^{(E)}P_4^{(E)}}{2m}B(t) \\ &\quad \left.+\frac{2iq_4^{(E)}q_i^{(E)}}{m}C(t)\right.. \end{aligned} \tag{C.67}$$

Then for the components we are interested in it is clear that

$$\begin{aligned}\left\langle N\middle|T_{\mu\nu}^{(E)}\middle|N\right\rangle = \frac{1}{2}\overline{u}(p')\left[-i\gamma_\mu^{(E)}P_\nu^{(E)}A(t)-\frac{i\sigma_{\mu\alpha}^{(E)}q_\alpha^{(E)}P_\nu^{(E)}}{2m}B(t)\right. \\ \left.-\frac{q_\mu^{(E)}q_\nu^{(E)}}{m}C(t)+(\mu\leftrightarrow\nu)\right]u(p)\end{aligned} \tag{C.68}$$

C.1.6 Compton Amplitude

First we determine the equivalent to $T_{\mu\nu}^{(M)}(p,q,\rho)$ in Euclidean space starting with the Minkowski definition

$$T_{\mu\nu}^{(M)}(p,q,\rho) := i\rho_{s's}\left\langle p,s'\middle|\int d^4x^{(M)}e^{i(q\cdot x)^{(M)}}T\left\{J_\mu^{(M)}\left(x^{(M)}\right)J_\nu^{(M)}(0)\right\}\middle|p,s\right\rangle. \tag{C.69}$$

The next step is to convert elements on the RHS to Euclidean

$$T_{\mu\nu}^{(M)}(p,q,\rho) = ic_\mu c_\nu\rho_{s's}\left\langle p,s'\middle|i\int d^4x^{(E)}e^{-i(q\cdot x)^{(E)}}T\left\{J_\mu^{(E)}(0)J_\nu^{(E)}\left(x^{(E)}\right)\right\}\middle|p,s\right\rangle \tag{C.70}$$

where c_μ is the factor such that $J_\mu^{(M)} = c_\mu J_\mu^{(E)}$ and we have used translational invariance $J(x) = e^{-ip\cdot x}J(0)e^{ip\cdot x}$. Then we use crossing symmetry

$$T_{\mu\nu}^{(M)}(p,q,\rho) = -c_\mu c_\nu\rho_{s's}T_{\nu\mu}^{(E)}(p,q,\rho) \tag{C.71}$$

for

$$T_{\mu\nu}^{(E)}(p,q,\rho) := \rho_{s's}\left\langle p,s'\middle|\int d^4x^{(E)}e^{i(q\cdot x)^{(E)}}T\left\{J_\mu^{(E)}\left(x^{(E)}\right)J_\nu^{(E)}(0)\right\}\middle|p,s\right\rangle. \tag{C.72}$$

Take $\mu=\nu=4$, which has $c_4=1$, and work out how the coefficient in front of T_1 where

$$-1+\frac{\left(q_0^{(M)}\right)^2}{q^2} = -1+\frac{\left(q_4^{(E)}\right)^2}{q^2} \implies -g_{\mu\nu}+\frac{q_\mu q_\nu}{q^2}\to\delta_{\mu\nu}-\frac{q_\mu q_\nu}{q^2}. \tag{C.73}$$

The same step can be done for T_2 where

$$\frac{1}{\nu^{(M)}}\left(p_0^{(M)}-\frac{1}{2}\omega q_0^{(M)}\right)\left(p_0^{(M)}-\frac{1}{2}\omega q_0^{(M)}\right) \tag{C.74}$$

is equivalent to

$$-(-i)^2\frac{1}{\nu^{(E)}}\left(p_4^{(E)}-\frac{1}{2}\omega q_4^{(E)}\right)\left(p_4^{(E)}-\frac{1}{2}\omega q_4^{(E)}\right) \tag{C.75}$$

which implies

$$\frac{\left(p_\mu-\frac{1}{2}\omega q_\mu\right)\left(p_\nu-\frac{1}{2}\omega q_\nu\right)}{\nu}\to-\frac{\left(p_\mu-\frac{1}{2}\omega q_\mu\right)\left(p_\nu-\frac{1}{2}\omega q_\nu\right)}{\nu} \tag{C.76}$$

This gives us for the first two structure functions

$$T_{\mu\nu}^{(M)}(p,q)=\left(-g_{\mu\nu}+\frac{q_\mu^{(M)}q_\nu^{(M)}}{\left(q^{(M)}\right)^2}\right)T_1+\frac{\left(p_\mu^{(M)}-\frac{1}{2}\omega q_\mu^{(M)}\right)\left(p_\nu^{(M)}-\frac{1}{2}\omega q_\nu^{(M)}\right)}{\nu^{(M)}}T_2 \tag{C.77}$$

$$T_{\mu\nu}^{(E)}(p,q)=\left(\delta_{\mu\nu}-\frac{q_\mu^{(E)}q_\nu^{(E)}}{\left(q^{(E)}\right)^2}\right)T_1-\frac{\left(p_\mu^{(E)}-\frac{1}{2}\omega q_\mu^{(E)}\right)\left(p_\nu^{(E)}-\frac{1}{2}\omega q_\nu^{(E)}\right)}{\nu^{(E)}}T_2. \tag{C.78}$$

The other structure functions follow in the same way, but are not necessary for this work. As the structure functions are the same between the spaces with these definitions, the Minkowski relationships to the hadron tensor and hence the parton model apply to the structure functions determined from the Euclidean Compton amplitude.

C.2 Various Definitions

C.2.1 Parity Projector

$$\Gamma^{\pm}:=\frac{1}{2}(I\pm\gamma_4) \tag{C.79}$$

C.2.2 Spin Projector

$$\Gamma_{\hat{s}}=i\vec{\gamma}\cdot\hat{s}\gamma_5 \tag{C.80}$$

where the polarisation vector ϵ for spinor $u(p,\sigma)$ is then defined as

$$\epsilon=\left(\sigma\left[\hat{s}+\frac{\vec{p}\cdot\hat{s}}{m(E+m)}\vec{p}\right],i\sigma\frac{\vec{p}\cdot\hat{s}}{m}\right). \tag{C.81}$$

This convention then satisfies

$$p\cdot s=0 \tag{C.82}$$

$$s^2=1 \tag{C.83}$$

C.2.3 γ_4–Hermiticity

A operator $\mathcal{O}$ is γ_4–Hermitian if

$$(\gamma_4\mathcal{O})^\dagger=\gamma_4\mathcal{O}. \tag{C.84}$$

C.2.4 γ_5–Hermiticity

A operator $\mathcal{O}$ is γ_5–Hermitian if

$$(\gamma_5\mathcal{O})^\dagger=\gamma_5\mathcal{O}. \tag{C.85}$$

C.3 Special Unitary Group

The special unitary group $SU(N)$ of degree N is a non–abelian Lie group of $N \times N$ unitary matrices with determinant 1. The lie algebra in the fundamental representation is represented by $N^2 - 1$ traceless Hermitian matrices whose generators are denoted t^i_{ab} for i ranging over all $N^2 - 1$ generators. The non–abelian nature gives rise to the structure constants defined in terms of commutators of the generators

$$if^{ijk}t^i = \left[t^j, t^k\right]. \tag{C.86}$$

For $N = 2$ the generators are the Pauli matrices and for $N = 3$ the Gell–Mann matrices.

C.4 Gordon Identity

The (vector) Gordon identity for Minkowski space reads

$$\overline{u}(p')\gamma_\mu u(p) = \overline{u}(p')\left[\frac{i\sigma_{\mu\alpha}q^\alpha}{2m} + \frac{P_\mu}{m}\right]u(p) \tag{C.87}$$

which we no derive for Euclidean space. Starting with the σ term

$$\overline{u}(p')i\sigma_{\mu\alpha}q_\alpha u(p) = -\frac{1}{2}\overline{u}\left[\gamma_\mu \not{q} - \not{q}\gamma_\mu\right]u(p). \tag{C.88}$$

We can use the anti–commutator to rewrite this as

$$\overline{u}(p')i\sigma_{\mu\alpha}q_\alpha u(p) = -\frac{1}{2}\overline{u}\left[\left\{\gamma_\mu, \not{q}\right\} - 2\not{q}\gamma_\mu\right]u(p) \tag{C.89}$$

$$= -\frac{1}{2}\overline{u}\left[2q_\mu - 2\not{q}\gamma_\mu\right]u(p). \tag{C.90}$$

We then rewrite the latter term

$$\overline{u}(p')\not{q}\gamma_\mu u(p) = \overline{u}(p')\left[\not{p}'\gamma_\mu - \not{p}\gamma_\mu\right]u(p) \tag{C.91}$$

$$= \overline{u}(p')\left[\not{p}'\gamma_\mu - \left\{\not{p}, \gamma_\mu\right\} + \gamma_\mu\not{p}\right]u(p) \tag{C.92}$$

$$= \overline{u}(p')\left[\not{p}'\gamma_\mu - 2p_\mu + \gamma_\mu\not{p}\right]u(p) \tag{C.93}$$

which combined with the *Klein–Gordon* equation $\not{p}u(p) = imu(p)$ gives

$$\overline{u}(p')\not{q}\gamma_\mu u(p) = \overline{u}(p')\left[2im\gamma_\mu - 2p_\mu\right]u(p). \tag{C.94}$$

Substituting this into (C.90) we then have

$$\overline{u}(p')(p')i\sigma_{\mu\alpha}q_\alpha u(p)(p) = -\overline{u}(p')\left[2P_\mu - 2im\gamma_\mu\right]u(p) \tag{C.95}$$

which after rearranging gives us the *Euclidean Gordon identity*

$$\boxed{\overline{u}(p')i\gamma_\mu u(p) = \overline{u}(p')\left[\frac{i\sigma_{\mu\alpha}q_\alpha}{2m} + \frac{P_\mu}{m}\right]u(p)} \tag{C.96}$$

Appendix D

F Functions

The 'F' functions are convenient for determining the traces of matrix elements encountered in lattice QCD calculations. Consider the matrix element part of two (3.72) and three–point (3.75) correlators

$$g_{\chi}^{(2)}\left[X,\vec{p}\right] = \frac{1}{2E_{X,\vec{p}}}\Big\langle\Omega\Big|\chi(0)\Big|X,\vec{p}\Big\rangle\Big\langle X,\vec{p}\Big|\chi^{\dagger}(0)\Big|\Omega\Big\rangle \tag{D.1}$$

$$g_{\chi J\chi^{\dagger}}^{(3)}\left[X,\vec{p}',X,\vec{p}\right] = \frac{1}{2E_{X,\vec{p}'}}\frac{1}{2E_{X,\vec{p}}}\Big\langle\Omega\Big|\chi(0)\Big|X,\vec{p}'\Big\rangle\Big\langle X,\vec{p}'\Big|J(0)\Big|X,\vec{p}\Big\rangle\Big\langle X,\vec{p}\Big|\chi^{\dagger}(0)\Big|\Omega\Big\rangle. \tag{D.2}$$

The two matrix elements in (D.1) are then projected onto the parity and spin of interest using a projection matrix Γ

$$F_2(\Gamma) := \Gamma_{\alpha\beta}\Big\langle\Omega\Big|\chi_{\beta}(0)\Big|X,\vec{p}\Big\rangle\Big\langle X,\vec{p}\Big|\chi_{\alpha}^{\dagger}(0)\Big|\Omega\Big\rangle \tag{D.3}$$

$$= \frac{1}{4}\operatorname{tr}\left[\Gamma\left(-i\not{p}+m_X\right)\right]. \tag{D.4}$$

To simplify the calculations we drop explicit state X labelling throughout this chapter. The F_2 function for positive parity §C.2.1 then is

$$F_2\left(\Gamma^{+}\right) = \frac{1}{2}\left(m+E_{\vec{p}}\right). \tag{D.5}$$

For three–point functions we define F_3 by

$$F_3(\Gamma,J) := 2\Gamma_{\alpha\beta}\Big\langle\Omega\Big|\chi_{\beta}(0)\Big|\vec{p}'\Big\rangle\langle\vec{p}'|J(0)|\vec{p}\rangle\Big\langle\vec{p}\Big|\chi_{\alpha}^{\dagger}(0)\Big|\Omega\Big\rangle \tag{D.6}$$

$$F_3(\Gamma,J) \;= \frac{1}{2}\operatorname{tr}\left[\Gamma\left(-i\not{p}'+m\right)J\left(-i\not{p}+m\right)\right]. \tag{D.7}$$

Note that this differs from the usual definition by a factor of 2. The resultant basis for F_3 functions can then be constructed in full, we present the part of interest to §9.2

$$F_3(I,I) = m^2 - p'\cdot p = -2P^2 = \frac{1}{2}Q^2 + 2m^2 \tag{D.8}$$

$$F_3(I,\gamma_\mu) = -2imP_\mu \tag{D.9}$$

$$F_3(I,\sigma_{\mu\nu}) = -i\left[p'_\mu p_\nu - p'_\nu p_\mu\right] = -i\left[q_\mu P_\nu - P_\mu q_\nu\right] \tag{D.10}$$

$$F_3(\gamma_\mu,I) = -2imP_\mu \tag{D.11}$$

$$F_3(\gamma_\mu,\gamma_\nu) = -\left[p'_\mu p_\nu + p_\mu p'_\nu + \delta_{\mu\nu}\frac{Q^2}{2}\right] = -2\left[P_\mu P_\nu - \frac{1}{4}\left(q_\mu q_\nu - \delta_{\mu\nu}Q^2\right)\right] \tag{D.12}$$

$$F_3(\gamma_\mu,\sigma_{\nu\alpha}) = m\left[\delta_{\mu\alpha}q_\nu - \delta_{\mu\nu}q_\alpha\right] \tag{D.13}$$

Using these we can then construct our F_3 basis in terms of our projectors, first the unpolarised projector

$$F_3\big(\Gamma^+, I\big) = \big(E' + m\big)(E + m) - \vec{p}' \cdot \vec{p} \tag{D.14}$$
$$F_3\big(\Gamma^+, \gamma_i\big) = -i\left[(E + m)p'_i + \big(E' + m\big)p_i\right] \tag{D.15}$$
$$F_3\big(\Gamma^+, \gamma_4\big) = \big(E' + m\big)(E + m) + \vec{p}' \cdot \vec{p} \tag{D.16}$$
$$F_3\big(\Gamma^+, \sigma_{4i}\big) = -\left[(E + m)p'_i - \big(E' + m\big)p_i\right] \tag{D.17}$$
$$F_3\big(\Gamma^+, \sigma_{ij}\big) = i\epsilon_{ijk}\big(\vec{p} \times \vec{p}'\big)_k \tag{D.18}$$

where E' and E are shorthand for $E(\vec{p}')$ and $E(\vec{p})$ respectively. The polarised projector then yields

$$F_3\big(\Gamma^+\Gamma_{\hat{s}}, I\big) = -i\big(\vec{p} \times \vec{p}'\big) \cdot \hat{s} \tag{D.19}$$
$$F_3\big(\Gamma^+\Gamma_{\hat{s}}, \gamma_i\big) = \left[(E + m)\big(\vec{p}' \times \hat{s}\big)_i + \big(E' + m\big)(\vec{p} \times \hat{s})_i\right] \tag{D.20}$$
$$F_3\big(\Gamma^+\Gamma_{\hat{s}}, \gamma_4\big) = i\big(\vec{p} \times \vec{p}'\big) \cdot \hat{s} \tag{D.21}$$
$$F_3\big(\Gamma^+\Gamma_{\hat{s}}, \sigma_{4i}\big) = -i\left[(E + m)\big(\vec{p}' \times \hat{s}\big)_i + \big(E' + m\big)(\vec{p} \times \hat{s})_i\right] \tag{D.22}$$
$$F_3\big(\Gamma^+\Gamma_{\hat{s}}, \sigma_{ij}\big) = \epsilon_{ijk}\big(\big(E' + m\big)(E + m)s_k - p_k\big(\vec{p}' \cdot \hat{s}\big) - p'_k(\vec{p} \cdot \hat{s}) + s_k\big(\vec{p} \cdot \vec{p}'\big)\big). \tag{D.23}$$

In the FHT the first and last matrix element of (D.2) are cancelled exactly leaving us with just the middle element, the element we are always trying to extract and hence the 'F' functions aren't required. When using regular three point function techniques such as in §9.2 we use combinations of F_2 and F_3 to determine our results.

We can work out arbitrary form factor coefficients by using (D.14)–(D.23). For (9.15) in terms of projections §C.2.1 and §C.2.2 this becomes

$$\begin{aligned} F_3\big(\Gamma^+, 2T_{4i}\big) = &\left\{-P_4\left[(E + m)p'_i + \big(E' + m\big)p_i\right] - iP_i\left[\big(E' + m\big)(E + m) + \vec{p}' \cdot \vec{p}\right]\right\} A_{20}\big(Q^2\big) \\ &+ \frac{1}{2m}\left\{-iP_i\vec{q} \cdot \left[(E + m)\vec{p}' - \big(E' + m\big)\vec{p}\right] - iP_4q_4\left[(E + m)p'_i - \big(E' + m\big)p_i\right]\right\} B_{20}\big(Q^2\big) \\ &+ \left\{\frac{q_4q_i}{m}\left[\big(E' + m\big)(E + m) - \vec{p}' \cdot \vec{p}\right]\right\} C_{20}\big(Q^2\big) \end{aligned} \tag{D.24}$$

$$\begin{aligned} F_3\big(\Gamma^+, 2T_{4i}\big) = &\left\{-P_4\left[(E + m)p'_i + \big(E' + m\big)p_i\right] - iP_i\left[\big(E' + m\big)(E + m) + \vec{p}' \cdot \vec{p}\right]\right\} A_{20}\big(Q^2\big) \\ &+ \frac{1}{2m}\left\{-iP_i\vec{q} \cdot \left[(E + m)\vec{p}' - \big(E' + m\big)\vec{p}\right] - iP_4q_4\left[(E + m)p'_i - \big(E' + m\big)p_i\right]\right\} B_{20}\big(Q^2\big) \\ &+ \left\{\frac{q_4q_i}{m}\left[\big(E' + m\big)(E + m) - \vec{p}' \cdot \vec{p}\right]\right\} C_{20}\big(Q^2\big) \end{aligned} \tag{D.25}$$

$$\begin{aligned} F_3\big(\Gamma^+\Gamma_{\hat{s}}, 2T_{4i}\big) = &\left\{-iP_4\left[(E + m)\big(\vec{p}' \times \hat{s}\big)_i + \big(E' + m\big)(\vec{p} \times \hat{s})_i\right] + P_i\big(\vec{p} \times \vec{p}'\big) \cdot \hat{s}\right\} A_{20}\big(Q^2\big) \\ &+ \Big\{-P_i\left[(E + m)\big(\vec{p} \times \vec{p}'\big) \cdot \hat{s} + \big(E' + m\big)\big(\vec{p} \times \vec{p}'\big) \cdot \hat{s}\right] \\ &\quad -iP_4\left[\big(E' + m\big)(E + m) + \vec{p} \cdot \vec{p}'\right](\vec{q} \times \hat{s})_i - iP_4\big(\vec{p} \times \vec{p}'\big)_i(\vec{q} \cdot \hat{s}) \\ &\quad -P_i\left[(E + m)\big(\vec{p} \times \vec{p}'\big) \cdot \hat{s} - \big(E' + m\big)\big(\vec{p} \times \vec{p}'\big) \cdot \hat{s}\right]\Big\} B_{20}\big(Q^2\big) \\ &+ \left\{\frac{q_4q_i}{m}\big(\vec{p} \times \vec{p}'\big) \cdot \hat{s}\right\} C_{20}\big(Q^2\big) \end{aligned} \tag{D.26}$$

$$\begin{aligned} F_3\big(\Gamma^+, T_{44} - \tfrac{1}{3}T_{ii}\big) = &\left\{-iP_4\big(E' + m\big)(E + m) + \vec{p}' \cdot \vec{p} + \frac{1}{3}\vec{P} \cdot \left[(E + m)\vec{p}' + \big(E' + m\big)\vec{p}\right]\right\} A_{20}\big(Q^2\big) \\ &+ \left\{\frac{i}{2m}\left(P_4\vec{q} - \frac{1}{3}q_4\vec{P}\right) \cdot \left[(E + m)\vec{p}' - \big(E' + m\big)\vec{p}\right]\right\} B_{20}\big(Q^2\big) \\ &+ \left\{\frac{1}{m}\left(-q_4^2 - \frac{1}{3}\vec{q}^2\right)\big(\vec{p} \times \vec{p}'\big) \cdot \hat{s}\right\} C_{20}\big(Q^2\big) \end{aligned} \tag{D.27}$$

and

$$
\begin{aligned}
{}_{F_3\left(\Gamma^+\Gamma_{\hat{s}},T_{44}-\frac{1}{3}T_{ii}\right)} = & \left\{\left[P_4+\frac{i}{6}\big((E+m)+\big(E'+m\big)\big)\right]\big(\vec{p}\times\vec{p}'\big)\cdot\hat{s}\right\}A_{20}\big(Q^2\big) \\
& +\left\{\frac{i}{2m}\left[P_4q_4-\frac{1}{3}\big(q_4^2+\big(E'+m\big)(E+m)+\vec{p}\cdot\vec{p}'\big)\right]\big(\vec{p}\times\vec{p}'\big)\cdot\hat{s}\right\}B_{20}\big(Q^2\big) \\
& +\left\{\frac{i}{m}\left[q_4^2-\frac{1}{3}\vec{q}^2\right]\big(\vec{p}\times\vec{p}'\big)\cdot\hat{s}\right\}C_{20}\big(Q^2\big).
\end{aligned}
\tag{D.28}
$$

Appendix E

Lattice Configurations

Here we summarise the lattices generated and used throughout this work. First we look at the quenched lattices generated specifically for gluonic studies §9 in §E.1, followed by a summary of the dynamical trajectories used throughout the rest of the work §E.2.

E.1 Quenched

The quenched lattices, those with $\det(\mathcal{D}) = 1$ in (3.37) have been generated using Chroma software library [196]. 2000 such lattices were generated as summarised in Table E.1, built to compare directly to [183].

β	$\frac{1}{a^4}L^3 \times T$	$a\,(fm)$	N_{cfg}
6.0	$24^3 \times 48$	0.1	2000

Table E.1: Parameters of quenched gauge–field ensembles used. Lattice have extend L in three directions and T in the direction chosen to represent the time direction.

E.2 Dynamical

The QCDSF/UKQCD ensembles are summarised in Table E.2. These have all been generated using $N_f = 2 + 1$ dynamical flavours, with two degenerate light quark flavours u and d, and one separate flavour s, using the BQCD lattice QCD program [325].

As described in §3.4, all ensembles have been generated to keep the average quark mass

$$\overline{m} = \frac{1}{3}(2m_l + m_s) \tag{3.58}$$

constant. This has one advantage over fixing the strange mass to the physical mass in that flavour breaking expansions are constrained. In addition flavour singlet quantities exhibit no leading order effects. As a consequence of this choice, the $SU(3)_{flavour}$ symmetric point has been chosen, where the pion and kaon have mass of the 'centre of multiplet mass'

$$X_\pi^2 = \frac{1}{3}(2m_K^2 + m_\pi^2) \tag{E.1}$$

which is invariant on our trajectory to the physical point, where we have used that charge conjugate mesons have the same masses for pure QCD. The ensembles are all made up of non–perturbatively $\mathcal{O}(a)$ improved Wilson fermions as described in §3.2.4 with tree–level Symanzik improved gluons and stout smeared fermion action. The lattice spacing a has been set using a number of singlet quantities [137, 139–141] as described in §3.4.

β	c_{SW}	κ_l	κ_s	$\frac{1}{a^4}L^3 \times T$	$a\ (fm)$	$m_\pi\ (MeV)$	N_{cfg}
5.5	2.65	0.1209	0.1209	$24^3 \times 48$	0.074(2)	≈ 470	2988
5.5	2.65	0.1209	0.1209	$32^3 \times 64$	0.074(2)	≈ 470	1763
5.65	2.48	0.122005	0.122005	$48^3 \times 96$	0.068(3)	≈ 470	530
5.4	2.79	0.11993	0.11993	$32^3 \times 64$	0.082(2)	≈ 400	1067

Table E.2: Parameters of dynamical gauge–field ensembles used in this work.

Appendix F

Further Compton Amplitude Discussion

F.1 Averaged Propagators

To isolate the second order energy shift a ratio was used (5.25), removing odd energy shift terms at the hadron level. Another way of removing the odd energy shift terms is at the propagator level, by averaging λ and $-\lambda$ propagator prior to subtraction, all odd energy shift terms are removed and the ratio to extract the equivalent energy shifts as (5.25) becomes (5.20).

A consequence of removing odd λ terms at the propagator level is that higher twist effects involving more than one quark line have been cancelled. It was thought that by removing these terms the signal could be improved, for use in extracting PDFs. However in the resultant comparison Figure F.1, we do not see any significant differences and no increase in precision. Thus we shall use the basic ratio technique for all our extractions.

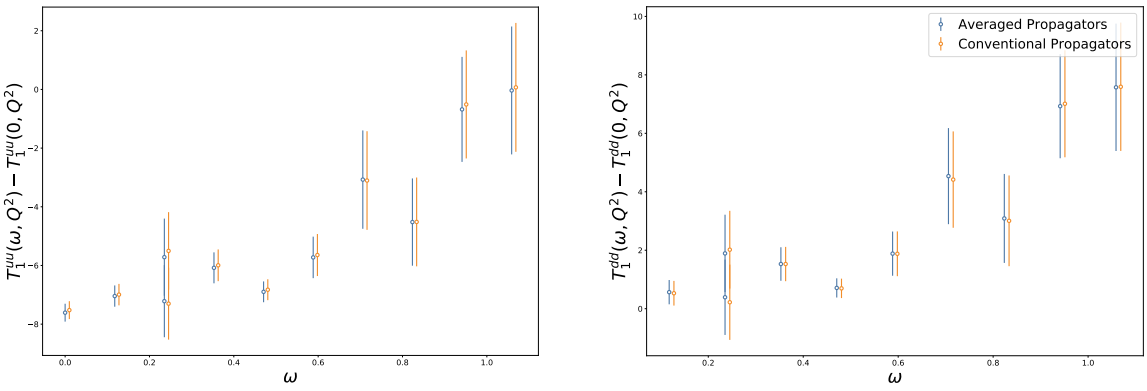

(a) u (b) d

Figure F.1: A comparison of average propagator (blue) and the regular method of §7.1.3 (orange) extraction of the unsubtracted Compton amplitude T_1 for u (a) and d (b) flavours. The data points have been offset slightly for clarity. The data is taken from a subset $N_{cfg} = 1755$ of the $\beta = 5.5$, $SU(3)_{flav}$ symmetric ensemble of §E.2, with $N_s = 3460$ sources corresponding to $N_{s/cfg} = 2.0$ random sources on each trajectory.

F.2 Experimental Deep Inelastic Scattering

In lepton–Hadron to lepton–X or lepton–Hadron scattering the differential cross section is given by

$$\frac{d\sigma}{d\Omega dE'} \tag{F.1}$$

where Ω is the solid angle, and E' is the outgoing measured lepton energy. So the cross section is binned in terms of angle and energy. This cross section might be modified by effects such as bremsstrahlung, vertex corrections, loop diagrams and radiative corrections. We shall take inclusive lepton scattering as our example. Kinematically appropriate variables to determine the scattering are then the in–going E and outgoing E' lepton energy and their corresponding scattering angle θ. The virtual exchanged photon polarisation ϵ and flux Γ is also measured.

Note that all these quantities are determined entirely from the lepton. From these quantities the scattering process can be determined such as (2.53)

$$y = \frac{E - E'}{E} \tag{F.2}$$

and

$$Q^2 = 4EE' \cos^2 \frac{\theta}{2}. \tag{F.3}$$

From these kinematics invariant mass W and Bjorken x can also be inferred

$$W^2 = m^2 + Q^2 \frac{1 - x}{x}. \tag{F.4}$$

For our example in inclusive scattering we work with the so called reduced scattering cross section

$$\sigma_r = \frac{d\sigma}{\Gamma} \tag{F.5}$$

which we can further divide into transverse and longitudinal parts via the virtual photon polarisation ϵ

$$\sigma_r = \sigma_L + \epsilon\sigma_T. \tag{F.6}$$

Finally these two cross section can be related to the hadron tensor structure functions

$$F_1 = \frac{8\pi^2\alpha}{W^2 - M^2}\sigma_T \tag{F.7}$$

$$F_L = \frac{1}{x}\frac{4\pi^2\alpha}{W^2 - M^2}\sigma_L \tag{F.8}$$

where F_L is defined as

$$F_L = 2xF_1 - F_2. \tag{F.9}$$

This form is used as in terms of x and Q^2 as the cross section can be written in terms of the natural units for F as

$$\frac{d\sigma}{dQ^2 dx} = \frac{4\pi\alpha^2}{Q^4}\left[\left(1 + (1 - y)^2\right)F_2 + \frac{1 - y}{x}F_L\right]. \tag{F.10}$$

The reduced cross section (F.6) can be rewritten using the so called R function

$$\sigma_r \ = \sigma_L(1 + \epsilon R) \tag{F.11}$$

$$R := \frac{\sigma_T}{\sigma_L}. \tag{F.12}$$

Either R is calculated directly by running experiments at constant Q^2 and x (W^2) and differing ϵ or a model for R is used and F_2 can be extracted directly by

$$\sigma_r = \frac{4\pi^2\alpha}{1 - x}\frac{\rho^2}{Q^2}\frac{1 + \epsilon R}{1 + R} \tag{F.13}$$

where the commonly used ρ is defined by

$$\rho^2 := 1 + \frac{4m^2x^2}{Q^2}. \tag{F.14}$$

This theory was used to reconstruct F_2 in the JLAB data of Figure 2.9.

Bibliography

[1] A. H. Becquerel. *Comptes rendus de l'Académie des sciences*, 122:420–421;501–503;689–694. [Cited in §2]

[2] E. Rutherford. "The scattering of alpha and beta particles by matter and the structure of the atom". *Phil. Mag. Ser.6*, 21:669–688, 1911. doi:10.1080/14786440508637080. [Cited in §2]

[3] M. Gell-Mann. "A Schematic Model of Baryons and Mesons". *Phys. Lett.*, 8:214–215, 1964. doi:10.1016/S0031-9163(64)92001-3. [Cited in §2]

[4] H. Fritzsch and M. Gell-Mann. "Current algebra: Quarks and what else?". *eConf*, C720906V2:135–165, 1972. arXiv:hep-ph/hep-ph/0208010. [Cited in §2]

[5] H. Fritzsch et al. "Advantages of the Color Octet Gluon Picture". *Phys. Lett.*, 47B:365–368, 1973. doi:10.1016/0370-2693(73)90625-4. [Cited in §2]

[6] S. L. Glashow. "Partial Symmetries of Weak Interactions". *Nucl. Phys.*, 22:579–588, 1961. doi:10.1016/0029-5582(61)90469-2. [Cited in §2]

[7] F. Englert and R. Brout. "Broken Symmetry and the Mass of Gauge Vector Mesons". *Phys. Rev. Lett.*, 13:321–323, 1964. doi:10.1103/PhysRevLett.13.321. [,157(1964)]. [Cited in §2]

[8] P. W. Higgs. "Broken Symmetries and the Masses of Gauge Bosons". *Phys. Rev. Lett.*, 13:508–509, 1964. doi:10.1103/PhysRevLett.13.508. [,160(1964)]. [Cited in §2]

[9] G. S. Guralnik et al. "Global Conservation Laws and Massless Particles". *Phys. Rev. Lett.*, 13:585–587, 1964. doi:10.1103/PhysRevLett.13.585. [,162(1964)]. [Cited in §2]

[10] S. Weinberg. "A Model of Leptons". *Phys. Rev. Lett.*, 19:1264–1266, 1967. doi:10.1103/PhysRevLett.19.1264. [Cited in §2]

[11] A. Salam. "Weak and Electromagnetic Interactions". *Conf. Proc.*, C680519:367–377, 1968. [Cited in §2]

[12] C.-N. Yang and R. L. Mills. "Conservation of Isotopic Spin and Isotopic Gauge Invariance". *Phys. Rev.*, 96:191–195, 1954. doi:10.1103/PhysRev.96.191. [,150(1954)]. [Cited in §2 and §2.1]

[13] F. J. Hasert et al. "Search for Elastic ν_μ Electron Scattering". *Phys. Lett.*, 46B:121–124, 1973. doi:10.1016/0370-2693(73)90494-2. [,5.11(1973)]. [Cited in §2]

[14] F. J. Hasert et al. "Observation of Neutrino Like Interactions Without Muon Or Electron in the Gargamelle Neutrino Experiment". *Phys. Lett.*, 46B:138–140, 1973. doi:10.1016/0370-2693(73)90499-1. [,5.15(1973)]. [Cited in §2]

[15] F. J. Hasert et al. "Observation of Neutrino Like Interactions Without Muon Or Electron in the Gargamelle Neutrino Experiment". *Phys. Lett.*, 46B:138–140, 1973. doi:10.1016/0370-2693(73)90499-1. [,5.15(1973)]. [Cited in §2]

[16] G. Arnison et al. "Experimental Observation of Isolated Large Transverse Energy Electrons with Associated Missing Energy at s**(1/2) = 540-GeV". *Phys. Lett.*, 122B:103–116, 1983. doi:10.1016/0370-2693(83)91177-2. [,611(1983)]. [Cited in §2]

[17] G. Arnison et al. "Experimental Observation of Lepton Pairs of Invariant Mass Around 95-GeV/c**2 at the CERN SPS Collider". *Phys. Lett.*, 126B:398–410, 1983. doi:10.1016/0370-2693(83)90188-0. [,7.55(1983)]. [Cited in §2]

[18] P. Bagnaia et al. "Evidence for Z0 —> e+ e- at the CERN anti-p p Collider". *Phys. Lett.*, 129B: 130–140, 1983. doi:10.1016/0370-2693(83)90744-X. [,7.69(1983)]. [Cited in §2]

[19] M. Banner et al. "Observation of Single Isolated Electrons of High Transverse Momentum in Events with Missing Transverse Energy at the CERN anti-p p Collider". *Phys. Lett.*, 122B: 476–485, 1983. doi:10.1016/0370-2693(83)91605-2. [,7.45(1983)]. [Cited in §2]

[20] R. Brandelik et al. "Evidence for Planar Events in e+ e- Annihilation at High-Energies". *Phys. Lett.*, 86B:243–249, 1979. doi:10.1016/0370-2693(79)90830-X. [Cited in §2]

[21] D. P. Barber et al. "Discovery of Three Jet Events and a Test of Quantum Chromodynamics at PETRA Energies". *Phys. Rev. Lett.*, 43:830, 1979. doi:10.1103/PhysRevLett.43.830. [Cited in §2]

[22] C. Berger et al. "Evidence for Gluon Bremsstrahlung in e+ e- Annihilations at High-Energies". *Phys. Lett.*, 86B:418–425, 1979. doi:10.1016/0370-2693(79)90869-4. [Cited in §2]

[23] W. Bartel et al. "Observation of Planar Three Jet Events in e+ e- Annihilation and Evidence for Gluon Bremsstrahlung". *Phys. Lett.*, 91B:142–147, 1980. doi:10.1016/0370-2693(80)90680-2. [Cited in §2]

[24] R. Brandelik et al. "Evidence for a Spin One Gluon in Three Jet Events". *Phys. Lett.*, 97B: 453–458, 1980. doi:10.1016/0370-2693(80)90639-5. [Cited in §2]

[25] C. Berger et al. "A Study of Multi-Jet Events in e+ e- Annihilation". *Phys. Lett.*, 97B:459–464, 1980. doi:10.1016/0370-2693(80)90640-1. [Cited in §2]

[26] J. E. Augustin et al. "Discovery of a Narrow Resonance in e^+e^- Annihilation". *Phys. Rev. Lett.*, 33:1406–1408, 1974. doi:10.1103/PhysRevLett.33.1406. [Adv. Exp. Phys.5,141(1976)]. [Cited in §2]

[27] J. J. Aubert et al. "Experimental Observation of a Heavy Particle J". *Phys. Rev. Lett.*, 33: 1404–1406, 1974. doi:10.1103/PhysRevLett.33.1404. [Cited in §2]

[28] S. Abachi et al. "Search for high mass top quark production in $p\bar{p}$ collisions at $\sqrt{s} = 1.8$ TeV". *Phys. Rev. Lett.*, 74:2422–2426, 1995. doi:10.1103/PhysRevLett.74.2422. arXiv:hep-ex/hep-ex/9411001. [Cited in §2]

[29] F. Abe et al. "Observation of top quark production in $\bar{p}p$ collisions". *Phys. Rev. Lett.*, 74: 2626–2631, 1995. doi:10.1103/PhysRevLett.74.2626. arXiv:hep-ex/hep-ex/9503002. [Cited in §2]

[30] S. Chatrchyan et al. "Observation of a New Boson at a Mass of 125 GeV with the CMS Experiment at the LHC". *Phys. Lett.*, B716:30–61, 2012. doi:10.1016/j.physletb.2012.08.021. arXiv:hep-ex/1207.7235. [Cited in §2]

[31] G. Aad et al. "Observation of a new particle in the search for the Standard Model Higgs boson with the ATLAS detector at the LHC". *Phys. Lett.*, B716:1–29, 2012. doi:10.1016/j.physletb.2012.08.020. arXiv:hep-ex/1207.7214. [Cited in §2]

[32] Q. R. Ahmad et al. "Measurement of the rate of $\nu_e + d \rightarrow p + p + e^-$ interactions produced by ^8B solar neutrinos at the Sudbury Neutrino Observatory". *Phys. Rev. Lett.*, 87: 071301, 2001. doi:10.1103/PhysRevLett.87.071301. arXiv:nucl-ex/nucl-ex/0106015. [Cited in §2]

[33] F. P. An et al. "Observation of electron-antineutrino disappearance at Daya Bay". *Phys. Rev. Lett.*, 108:171803, 2012. doi:10.1103/PhysRevLett.108.171803. arXiv:hep-ex/1203.1669. [Cited in §2]

[34] J. K. Ahn et al. "Observation of Reactor Electron Antineutrino Disappearance in the RENO Experiment". *Phys. Rev. Lett.*, 108:191802, 2012. doi:10.1103/PhysRevLett.108.191802. arXiv:hep-ex/1204.0626. [Cited in §2]

[35] K. Abe et al. "Evidence of Electron Neutrino Appearance in a Muon Neutrino Beam". *Phys. Rev.*, D88(3):032002, 2013. doi:10.1103/PhysRevD.88.032002. arXiv:hep-ex/1304.0841. [Cited in §2]

[36] G. Senjanovic. "Natural Philosophy versus Philosophy of Naturalness". 2020. arXiv:hep-ph/2001.10988. [Cited in §2]

[37] J. H. Christenson et al. "Evidence for the 2π Decay of the K_2^0 Meson". *Phys. Rev. Lett.*, 13: 138–140, 1964. doi:10.1103/PhysRevLett.13.138. [Cited in §2]

[38] A. Alavi-Harati et al. "Observation of direct CP violation in $K_{S,L} \rightarrow \pi\pi$ decays". *Phys. Rev. Lett.*, 83:22–27, 1999. doi:10.1103/PhysRevLett.83.22. arXiv:hep-ex/hep-ex/9905060. [Cited in §2]

[39] V. Fanti et al. "A New measurement of direct CP violation in two pion decays of the neutral kaon". *Phys. Lett.*, B465:335–348, 1999. doi:10.1016/S0370-2693(99)01030-8. arXiv:hep-ex/hep-ex/9909022. [Cited in §2]

[40] R. Aaij et al. "First observation of CP violation in the decays of B_s^0 mesons". *Phys. Rev. Lett.*, 110(22):221601, 2013. doi:10.1103/PhysRevLett.110.221601. arXiv:hep-ex/1304.6173. [Cited in §2]

[41] S. Bifani et al. "Review of Lepton Universality tests in B decays". *J. Phys.*, G46(2):023001, 2019. doi:10.1088/1361-6471/aaf5de. arXiv:hep-ex/1809.06229. [Cited in §2]

[42] M. Tanabashi et al. "Review of Particle Physics". *Phys. Rev.*, D98(3):030001, 2018. doi:10.1103/PhysRevD.98.030001. [Cited in §2.2 and §8.2]

[43] M. Baak et al. "The global electroweak fit at NNLO and prospects for the LHC and ILC". *Eur. Phys. J.*, C74:3046, 2014. doi:10.1140/epjc/s10052-014-3046-5. arXiv:hep-ph/1407.3792. [Cited in §2.2]

[44] N. Brambilla et al. "Extraction of alpha(s) from radiative Upsilon(1S) decays". *Phys. Rev.*, D75:074014, 2007. doi:10.1103/PhysRevD.75.074014. arXiv:hep-ph/hep-ph/0702079. [Cited in §2.2]

[45] C. Adloff et al. "Measurement and QCD analysis of jet cross-sections in deep inelastic positron - proton collisions at s**(1/2) of 300-GeV". *Eur. Phys. J.*, C19:289–311, 2001. doi:10.1007/s100520100621. arXiv:hep-ex/hep-ex/0010054. [Cited in §2.2]

[46] J. Breitweg et al. "Measurement of dijet production in neutral current deep inelastic scattering at high Q**2 and determination of alpha(s)". *Phys. Lett.*, B507:70–88, 2001. doi:10.1016/S0370-2693(01)00421-X. arXiv:hep-ex/hep-ex/0102042. [Cited in §2.2]

[47] S. Chekanov et al. "Inclusive jet cross-sections in the Breit frame in neutral current deep inelastic scattering at HERA and determination of alpha(s)". *Phys. Lett.*, B547:164–180, 2002. doi:10.1016/S0370-2693(02)02763-6. arXiv:hep-ex/hep-ex/0208037. [Cited in §2.2]

[48] S. Chekanov et al. "Scaling violations and determination of alpha(s) from jet production in gamma p interactions at HERA". *Phys. Lett.*, B560:7–23, 2003. doi:10.1016/S0370-2693(03)00380-0. arXiv:hep-ex/hep-ex/0212064. [Cited in §2.2]

[49] V. M. Abazov et al. "Determination of the strong coupling constant from the inclusive jet cross section in $p\bar{p}$ collisions at sqrt(s)=1.96 TeV". *Phys. Rev.*, D80:111107, 2009. doi:10.1103/PhysRevD.80.111107. arXiv:hep-ex/0911.2710. [Cited in §2.2]

[50] V. M. Abazov et al. "Measurement of angular correlations of jets at $\sqrt{s} = 1.96$ TeV and determination of the strong coupling at high momentum transfers". *Phys. Lett.*, B718:56–63, 2012. doi:10.1016/j.physletb.2012.10.003. arXiv:hep-ex/1207.4957. [Cited in §2.2]

[51] S. Chatrchyan et al. "Measurement of the ratio of the inclusive 3-jet cross section to the inclusive 2-jet cross section in pp collisions at $\sqrt{s}$ = 7 TeV and first determination of the strong coupling constant in the TeV range". *Eur. Phys. J.*, C73(10):2604, 2013. doi:10.1140/epjc/s10052-013-2604-6. arXiv:hep-ex/1304.7498. [Cited in §2.2]

[52] V. Khachatryan et al. "Constraints on parton distribution functions and extraction of the strong coupling constant from the inclusive jet cross section in pp collisions at $\sqrt{s} = 7$ TeV". *Eur. Phys. J.*, C75(6):288, 2015. doi:10.1140/epjc/s10052-015-3499-1. arXiv:hep-ex/1410.6765. [Cited in §2.2]

[53] V. Khachatryan et al. "Measurement of the inclusive 3-jet production differential cross section in proton–proton collisions at 7 TeV and determination of the strong coupling constant in the TeV range". *Eur. Phys. J.*, C75(5):186, 2015. doi:10.1140/epjc/s10052-015-3376-y. arXiv:hep-ex/1412.1633. [Cited in §2.2]

[54] S. Bethke et al. "Determination of the Strong Coupling alpha(s) from hadronic Event Shapes with O(alpha**3(s)) and resummed QCD predictions using JADE Data". *Eur. Phys. J.*, C64:351–360, 2009. doi:10.1140/epjc/s10052-009-1149-1. arXiv:hep-ex/0810.1389. [Cited in §2.2]

[55] G. Dissertori et al. "Determination of the strong coupling constant using matched NNLO+NLLA predictions for hadronic event shapes in e+e- annihilations". *JHEP*, 08:036, 2009. doi:10.1088/1126-6708/2009/08/036. arXiv:hep-ph/0906.3436. [Cited in §2.2]

[56] G. Abbiendi et al. "Determination of $alpha_s$ using OPAL hadronic event shapes at $\sqrt{s} = 91$ - 209 GeV and resummed NNLO calculations". *Eur. Phys. J.*, C71:1733, 2011. doi:10.1140/epjc/s10052-011-1733-z. arXiv:hep-ex/1101.1470. [Cited in §2.2]

[57] E. Gardi et al. "Can the QCD running coupling have a causal analyticity structure?". *JHEP*, 07:007, 1998. doi:10.1088/1126-6708/1998/07/007. arXiv:hep-ph/hep-ph/9806462. [Cited in §2.2]

[58] A. Deur et al. "The QCD Running Coupling". *Prog. Part. Nucl. Phys.*, 90:1–74, 2016. doi:10.1016/j.ppnp.2016.04.003. arXiv:hep-ph/1604.08082. [Cited in §2.2]

[59] M. N. Rosenbluth. "High Energy Elastic Scattering of Electrons on Protons". *Phys. Rev.*, 79:615–619, 1950. doi:10.1103/PhysRev.79.615. [Cited in §2.2 and §2.3.5]

[60] R. Hofstadter et al. "High-Energy Electron Scattering and Nuclear Structure Determinations". *Phys. Rev.*, 92(4):978, 1953. doi:10.1103/PhysRev.92.978. [Cited in §2.2]

[61] R. Hofstadter and R. W. McAllister. "Electron Scattering From the Proton". *Phys. Rev.*, 98: 217–218, 1955. doi:10.1103/PhysRev.98.217. [Cited in §2.2]

[62] M. R. Yearian and R. Hofstadter. "Magnetic Form Factor of the Neutron". *Phys. Rev.*, 110 (2):552, 1958. doi:10.1103/PhysRev.110.552. [Cited in §2.2]

[63] R. P. Feynman. "The behavior of hadron collisions at extreme energies". *Conf. Proc.*, C690905:237–258, 1969. [Cited in §2.2 and §2.3]

[64] P. Hagler. "Hadron structure from lattice quantum chromodynamics". *Phys. Rept.*, 490:49–175, 2010. doi:10.1016/j.physrep.2009.12.008. arXiv:hep-lat/0912.5483. [Cited in §2.2, §9.1.1, §9.2.2, and §9.3.6]

[65] X. Ji. "the nucleon structure functions from deep-inelastic scattering with electroweak currents". *Nuclear Physics B*, 402(1-2):217–250, August 1993. doi:10.1016/0550-3213(93)90642-3. [Cited in §2.3.1]

[66] E. D. Bloom et al. "High-Energy Inelastic e p Scattering at 6-Degrees and 10-Degrees". *Phys. Rev. Lett.*, 23:930–934, 1969. doi:10.1103/PhysRevLett.23.930. [Cited in §2.3.2]

[67] M. Breidenbach et al. "Observed Behavior of Highly Inelastic electron-Proton Scattering". *Phys. Rev. Lett.*, 23:935–939, 1969. doi:10.1103/PhysRevLett.23.935. [Cited in §2.3.2]

[68] J. S. Poucher et al. "High-Energy Single-Arm Inelastic e - p and e - d Scattering at 6-Degrees and 10-Degrees". *Phys. Rev. Lett.*, 32:118, 1974. doi:10.1103/PhysRevLett.32.118. [Cited in §2.3.2]

[69] C. G. Callan and D. J. Gross. "Crucial Test of a Theory of Currents". *Phys. Rev. Lett.*, 21: 311–313, 1968. doi:10.1103/PhysRevLett.21.311. [Cited in §2.3.2]

[70] F. D. Aaron et al. "Combined Measurement and QCD Analysis of the Inclusive e+- p Scattering Cross Sections at HERA". *JHEP*, 01:109, 2010. doi:10.1007/JHEP01(2010)109. arXiv:hep-ex/0911.0884. [Cited in §2.7]

[71] S. Habib. "Combined measurement and QCD analysis of the inclusive e+- p scattering cross sections at HERA". *PoS*, DIS2010:035, 2010. doi:10.22323/1.106.0035. [Cited in §2.7]

[72] A. C. Benvenuti et al. "A High Statistics Measurement of the Proton Structure Functions F(2) (x, Q**2) and R from Deep Inelastic Muon Scattering at High Q**2". *Phys. Lett.*, B223: 485–489, 1989. doi:10.1016/0370-2693(89)91637-7. [Cited in §2.7]

[73] M. R. Adams et al. "Proton and deuteron structure functions in muon scattering at 470-GeV". *Phys. Rev.*, D54:3006–3056, 1996. doi:10.1103/PhysRevD.54.3006. [Cited in §2.7]

[74] M. Arneodo et al. "Measurement of the proton and deuteron structure functions, F2(p) and F2(d), and of the ratio sigma-L / sigma-T". *Nucl. Phys.*, B483:3–43, 1997. doi:10.1016/S0550-3213(96)00538-X. arXiv:hep-ph/hep-ph/9610231. [Cited in §2.7 and §2.9]

[75] L. W. Whitlow et al. "A COMBINED ANALYSIS OF SLAC EXPERIMENTS ON DEEP INELASTIC e p AND e d SCATTERING". *Nucl. Phys. Proc. Suppl.*, 16:215–216, 1990. doi:10.1016/0920-5632(90)90480-I. [Cited in §2.7 and §2.9]

[76] D. Allasia et al. "Q**2 Dependence of the Proton and Neutron Structure Functions from Neutrino and anti-neutrinos Scattering in Deuterium". *Z. Phys.*, C28:321, 1985. doi:10.1007/BF01413595. [Cited in §2.7]

[77] J. J. Aubert et al. "A Detailed Study of the Proton Structure Functions in Deep Inelastic Muon - Proton Scattering". *Nucl. Phys.*, B259:189, 1985. doi:10.1016/0550-3213(85)90635-2. [Cited in §2.7]

[78] F. D. Aaron et al. "Inclusive Deep Inelastic Scattering at High Q^2 with Longitudinally Polarised Lepton Beams at HERA". *JHEP*, 09:061, 2012. doi:10.1007/JHEP09(2012)061. arXiv:hep-ex/1206.7007. [Cited in §2.7]

[79] S. P. Malace et al. "Applications of quark-hadron duality in F(2) structure function". *Phys. Rev.*, C80:035207, 2009. doi:10.1103/PhysRevC.80.035207. arXiv:nucl-ex/0905.2374. [Cited in §2.3.2]

[80] I. Niculescu et al. "Direct observation of quark-hadron duality in the free neutron F_2 structure function". *Phys. Rev.*, C91(5):055206, 2015. doi:10.1103/PhysRevC.91.055206. arXiv:hep-ex/1501.02203. [Cited in §2.3.2]

[81] M. E. Christy and W. Melnitchouk. "Unpolarized structure functions at Jefferson Lab". *J. Phys. Conf. Ser.*, 299:012004, 2011. doi:10.1088/1742-6596/299/1/012004. arXiv:nucl-ex/1104.0239. [Cited in §2.9]

[82] M. Osipenko et al. "A Kinematically complete measurement of the proton structure function F(2) in the resonance region and evaluation of its moments". *Phys. Rev.*, D67: 092001, 2003. doi:10.1103/PhysRevD.67.092001. arXiv:hep-ph/hep-ph/0301204. [Cited in §2.9]

[83] Y. Liang et al. "Measurement of R = sigma(L) / sigma(T) and the separated longitudinal and transverse structure functions in the nucleon resonance region". 2004. arXiv:nucl-ex/nucl-ex/0410027. [Cited in §2.9]

[84] H. Abramowicz and A. Levy. "The ALLM parameterization of sigma(tot)(gamma* p): An Update". 1997. arXiv:hep-ph/hep-ph/9712415. [Cited in §2.9]

[85] A. Accardi et al. "Constraints on large-x parton distributions from new weak boson production and deep-inelastic scattering data". *Phys. Rev.*, D93(11):114017, 2016. doi:10.1103/PhysRevD.93.114017. arXiv:hep-ph/1602.03154. [Cited in §2.11]

[86] J. F. Owens et al. "Global parton distributions with nuclear and finite-Q^2 corrections". *Phys. Rev.*, D87(9):094012, 2013. doi:10.1103/PhysRevD.87.094012. arXiv:hep-ph/1212.1702. [Cited in §2.11]

[87] V. N. Gribov and L. N. Lipatov. "Deep inelastic e p scattering in perturbation theory". *Sov. J. Nucl. Phys.*, 15:438–450, 1972. [Yad. Fiz.15,781(1972)]. [Cited in §2.11]

[88] G. Altarelli and G. Parisi. "Asymptotic Freedom in Parton Language". *Nucl. Phys.*, B126: 298–318, 1977. doi:10.1016/0550-3213(77)90384-4. [Cited in §2.11]

[89] Y. L. Dokshitzer. "Calculation of the Structure Functions for Deep Inelastic Scattering and e+ e- Annihilation by Perturbation Theory in Quantum Chromodynamics.". *Sov. Phys. JETP*, 46:641–653, 1977. [Zh. Eksp. Teor. Fiz.73,1216(1977)]. [Cited in §2.11]

[90] D. J. Gross and C. H. Llewellyn Smith. "High-energy neutrino - nucleon scattering, current algebra and partons". *Nucl. Phys.*, B14:337–347, 1969. doi:10.1016/0550-3213(69)90213-2. [Cited in §2.3.2]

[91] S. L. Adler. "Sum rules giving tests of local current commutation relations in high-energy neutrino reactions". *Phys. Rev.*, 143:1144–1155, 1966. doi:10.1103/PhysRev.143.1144. [,183(1965)]. [Cited in §2.3.2]

[92] K. Gottfried. "Sum rule for high-energy electron - proton scattering". *Phys. Rev. Lett.*, 18: 1174, 1967. doi:10.1103/PhysRevLett.18.1174. [Cited in §2.3.2]

[93] J. Erler et al. "The Weak charge of the proton and new physics". *Phys. Rev.*, D68: 016006, 2003. doi:10.1103/PhysRevD.68.016006. arXiv:hep-ph/hep-ph/0302149. [Cited in §2.3.4]

[94] A. Sibirtsev et al. "gamma-Z corrections to forward-angle parity-violating e-p scattering". *Phys. Rev.*, D82:013011, 2010. doi:10.1103/PhysRevD.82.013011. arXiv:hep-ph/1002.0740. [Cited in §2.3.4]

[95] M. Gorchtein et al. "Model-dependence of the γZ dispersion correction to the parity-violating asymmetry in elastic ep scattering". *Phys. Rev.*, C84:015502, 2011. doi:10.1103/PhysRevC.84.015502. arXiv:nucl-th/1102.3910. [Cited in §2.3.4]

[96] P. G. Blunden et al. "New formulation of gamma-Z box corrections to the weak charge of the proton". *Phys. Rev. Lett.*, 107:081801, 2011. doi:10.1103/PhysRevLett.107.081801. arXiv:hep-ph/1102.5334. [Cited in §2.3.4]

[97] P. G. Blunden et al. "$\gamma - Z$ box corrections to weak charges of heavy nuclei in atomic parity violation". *Phys. Rev. Lett.*, 109:262301, 2012. doi:10.1103/PhysRevLett.109.262301. arXiv:hep-ph/1208.4310. [Cited in §2.3.4]

[98] B. C. Rislow and C. E. Carlson. "Modification of electromagnetic structure functions for the γZ-box diagram". *Phys. Rev.*, D88:013018, 2013. doi:10.1103/PhysRevD.88.013018. arXiv:hep-ph/1304.8113. [Cited in §2.3.4]

[99] N. L. Hall et al. "Quark–hadron duality constraints on γZ box corrections to parity-violating elastic scattering". *Phys. Lett.*, B753:221–226, 2016. doi:10.1016/j.physletb.2015.11.081. arXiv:nucl-th/1504.03973. [Cited in §2.3.4 and §7.2]

[100] D. Androic et al. "First Determination of the Weak Charge of the Proton". *Phys. Rev. Lett.*, 111(14):141803, 2013. doi:10.1103/PhysRevLett.111.141803. arXiv:nucl-ex/1307.5275. [Cited in §2.3.4]

[101] D. Androic et al. "Early results from the Q_{weak} experiment". *EPJ Web Conf.*, 66:05002, 2014. doi:10.1051/epjconf/20146605002. arXiv:nucl-ex/1311.6437. [Cited in §2.3.4]

[102] D. Androić et al. "Precision measurement of the weak charge of the proton". *Nature*, 557 (7704):207–211, 2018. doi:10.1038/s41586-018-0096-0. arXiv:nucl-ex/1905.08283. [Cited in §2.3.4]

[103] L. Andivahis et al. "Measurements of the electric and magnetic form-factors of the proton from Q**2 = 1.75-GeV/c**2 to 8.83-GeV/c**2". *Phys. Rev.*, D50:5491–5517, 1994. doi:10.1103/PhysRevD.50.5491. [Cited in §2.3.5 and §2.16]

[104] M. E. Christy et al. "Measurements of electron proton elastic cross-sections for 0.4 < Q**2 < 5.5 (GeV/c)**2". *Phys. Rev.*, C70:015206, 2004. doi:10.1103/PhysRevC.70.015206. arXiv:nucl-ex/nucl-ex/0401030. [Cited in §2.3.5 and §2.16]

[105] I. A. Qattan et al. "Precision Rosenbluth measurement of the proton elastic form-factors". *Phys. Rev. Lett.*, 94:142301, 2005. doi:10.1103/PhysRevLett.94.142301. arXiv:nucl-ex/nucl-ex/0410010. [Cited in §2.3.5 and §2.16]

[106] M. K. Jones et al. "G(E(p)) / G(M(p)) ratio by polarization transfer in polarized e p —> e polarized p". *Phys. Rev. Lett.*, 84:1398–1402, 2000. doi:10.1103/PhysRevLett.84.1398. arXiv:nucl-ex/nucl-ex/9910005. [Cited in §2.3.5 and §2.16]

[107] O. Gayou et al. "Measurement of G(Ep) / G(Mp) in polarized-e p —> e polarized-p to Q**2 = 5.6-GeV**2". *Phys. Rev. Lett.*, 88:092301, 2002. doi:10.1103/PhysRevLett.88.092301. arXiv:nucl-ex/nucl-ex/0111010. [Cited in §2.3.5 and §2.16]

[108] V. Punjabi et al. "Proton elastic form-factor ratios to Q**2 = 3.5-GeV**2 by polarization transfer". *Phys. Rev.*, C71:055202, 2005. doi:10.1103/PhysRevC.71.055202, 10.1103/PhysRevC.71.069902. arXiv:nucl-ex/nucl-ex/0501018. [Erratum: Phys. Rev.C71,069902(2005)]. [Cited in §2.3.5 and §2.16]

[109] A. J. R. Puckett et al. "Recoil Polarization Measurements of the Proton Electromagnetic Form Factor Ratio to Q**2 = 8.5 GeV**2". *Phys. Rev. Lett.*, 104: 242301, 2010. doi:10.1103/PhysRevLett.104.242301. arXiv:nucl-ex/1005.3419. [Cited in §2.3.5 and §2.16]

[110] A. J. R. Puckett et al. "Final Analysis of Proton Form Factor Ratio Data at Q**2 = 4.0, 4.8 and 5.6 GeV**2". *Phys. Rev.*, C85:045203, 2012. doi:10.1103/PhysRevC.85.045203. arXiv:nucl-ex/1102.5737. [Cited in §2.3.5 and §2.16]

[111] I. C. Cloet et al. "Revealing dressed-quarks via the proton's charge distribution". *Phys. Rev. Lett.*, 111:101803, 2013. doi:10.1103/PhysRevLett.111.101803. arXiv:nucl-th/1304.0855. [Cited in §2.3.5]

[112] A. J. Chambers et al. "Electromagnetic form factors at large momenta from lattice QCD". *Phys. Rev.*, D96(11):114509, 2017. doi:10.1103/PhysRevD.96.114509. arXiv:hep-lat/1702.01513. [Cited in §2.3.5, §4, §4.2.1, §5.2.1, and §6]

[113] I. A. Rachek et al. "Measurement of the two-photon exchange contribution to the elastic $e^{\pm}p$ scattering cross sections at the VEPP-3 storage ring". *Phys. Rev. Lett.*, 114(6):062005, 2015. doi:10.1103/PhysRevLett.114.062005. arXiv:nucl-ex/1411.7372. [Cited in §2.3.5]

[114] D. Adikaram et al. "Towards a resolution of the proton form factor problem: new electron and positron scattering data". *Phys. Rev. Lett.*, 114:062003, 2015. doi:10.1103/PhysRevLett.114.062003. arXiv:nucl-ex/1411.6908. [Cited in §2.3.5]

[115] B. S. Henderson et al. "Hard Two-Photon Contribution to Elastic Lepton-Proton Scattering: Determined by the OLYMPUS Experiment". *Phys. Rev. Lett.*, 118(9):092501, 2017. doi:10.1103/PhysRevLett.118.092501. arXiv:nucl-ex/1611.04685. [Cited in §2.3.5]

[116] Y. C. Chen et al. "Partonic calculation of the two photon exchange contribution to elastic electron proton scattering at large momentum transfer". *Phys. Rev. Lett.*, 93:122301, 2004. doi:10.1103/PhysRevLett.93.122301. arXiv:hep-ph/hep-ph/0403058. [Cited in §2.3.5]

[117] A. V. Afanasev et al. "The Two-photon exchange contribution to elastic electron-nucleon scattering at large momentum transfer". *Phys. Rev.*, D72:013008, 2005. doi:10.1103/PhysRevD.72.013008. arXiv:hep-ph/hep-ph/0502013. [Cited in §2.3.5]

[118] P. G. Blunden et al. "Two-photon exchange in elastic electron-nucleon scattering". *Phys. Rev.*, C72:034612, 2005. doi:10.1103/PhysRevC.72.034612. arXiv:nucl-th/nucl-th/0506039. [Cited in §2.3.5]

[119] S. Kondratyuk et al. "Delta resonance contribution to two-photon exchange in electron-proton scattering". *Phys. Rev. Lett.*, 95:172503, 2005. doi:10.1103/PhysRevLett.95.172503. arXiv:nucl-th/nucl-th/0506026. [Cited in §2.3.5]

[120] Yu. M. Bystritskiy et al. "Structure function method applied to polarized and unpolarized electron-proton scattering: A solution of the GE(p)/GM(p) discrepancy". *Phys. Rev.*, C75:015207, 2007. doi:10.1103/PhysRevC.75.015207. arXiv:hep-ph/hep-ph/0603132. [Cited in §2.3.5]

[121] E. A. Kuraev et al. "Charge asymmetry for electron (positron)-proton elastic scattering at large angle". *Phys. Rev.*, C78:015205, 2008. doi:10.1103/PhysRevC.78.015205. arXiv:hep-ph/0710.3699. [Cited in §2.3.5]

[122] K. G. Wilson. "confinement of quarks". *Phys. Rev. D*, 10:2445–2459, Oct 1974. doi:10.1103/PhysRevD.10.2445. [Cited in §3]

[123] R. P. Feynman. "space-time approach to non-relativistic quantum mechanics". *Reviews of Modern Physics*, 20(2):367–387, April 1948. doi:10.1103/revmodphys.20.367. [Cited in §3]

[124] C. Gattringer and C. B. Lang. "Quantum chromodynamics on the lattice". *Lect. Notes Phys.*, 788:1–343, 2010. doi:10.1007/978-3-642-01850-3. [Cited in §3 and §5.2.2]

[125] I. Montvay and G. Münster. *Quantum Fields on a Lattice*. Cambridge University Press, 1994. doi:10.1017/cbo9780511470783. [Cited in §3]

[126] J. Engels et al. "Determination of anisotropy coefficients for SU(3) gauge actions from the integral and matching methods". *Nucl. Phys.*, B564:303–324, 2000. doi:10.1016/S0550-3213(99)00522-2. arXiv:hep-lat/hep-lat/9905002. [Cited in §3.2.1]

[127] P. T. Matthews and A. Salam. "the green's functions of quantised fields". *Il Nuovo Cimento*, 12(4):563–565, October 1954. doi:10.1007/bf02781302. [Cited in §3.2.2]

[128] P. T. Matthews and A. Salam. "propagators of quantized field". *Il Nuovo Cimento*, 2(1): 120–134, July 1955. doi:10.1007/bf02856011. [Cited in §3.2.2]

[129] S. Duane et al. "hybrid monte carlo". *Physics Letters B*, 195(2):216–222, September 1987. doi:10.1016/0370-2693(87)91197-x. [Cited in §3.2.2]

[130] S. Aoki et al. "FLAG Review 2019". 2019. arXiv:hep-lat/1902.08191. [Cited in §3.2.2 and §7.2]

[131] H. B. Nielsen and M. Ninomiya. "Absence of Neutrinos on a Lattice. 1. Proof by Homotopy Theory". pages 533–555, 11 1980. doi:10.1016/0550-3213(82)90011-6. [Erratum: Nucl.Phys.B 195, 541 (1982)]. [Cited in §3.2.3]

[132] H. B. Nielsen and M. Ninomiya. "Absence of Neutrinos on a Lattice. 2. Intuitive Topological Proof". *Nucl. Phys. B*, 193:173–194, 1981. doi:10.1016/0550-3213(81)90524-1. [Cited in §3.2.3]

[133] H. B. Nielsen and M. Ninomiya. "No Go Theorem for Regularizing Chiral Fermions". *Phys. Lett. B*, 105:219–223, 1981. doi:10.1016/0370-2693(81)91026-1. [Cited in §3.2.3]

[134] K. Symanzik. "continuum limit and improved action in lattice theories". *Nuclear Physics B*, 226(1):187–204, September 1983. doi:10.1016/0550-3213(83)90468-6. [Cited in §3.2.4]

[135] B. Sheikholeslami and R. Wohlert. "improved continuum limit lattice action for QCD with wilson fermions". *Nuclear Physics B*, 259(4):572–596, September 1985. doi:10.1016/0550-3213(85)90002-1. [Cited in §3.2.4]

[136] M. Luscher and P. Weisz. "On-Shell Improved Lattice Gauge Theories". *Commun. Math. Phys.*, 97:59, 1985. doi:10.1007/BF01206178. [Erratum: Commun. Math. Phys.98,433(1985)]. [Cited in §3.2.4]

[137] W. Bietenholz et al. "Flavour blindness and patterns of flavour symmetry breaking in lattice simulations of up, down and strange quarks". *Phys. Rev.*, D84: 054509, 2011. doi:10.1103/PhysRevD.84.054509. arXiv:hep-lat/1102.5300. [Cited in §3.2.4, §3.4, §3.6.1, and §E.2]

[138] M. Gockeler et al. "Perturbative renormalisation of the second moment of generalised parton distributions". *Nucl. Phys.*, B717:304–323, 2005. doi:10.1016/j.nuclphysb.2005.04.005. arXiv:hep-lat/hep-lat/0410009. [Cited in §3.3]

[139] W. Bietenholz et al. "Tuning the strange quark mass in lattice simulations". *Phys. Lett.*, B690:436–441, 2010. doi:10.1016/j.physletb.2010.05.067. arXiv:hep-lat/1003.1114. [Cited in §3.4, §3.6.1, and §E.2]

[140] R. Horsley et al. "SU(3) flavour symmetry breaking and charmed states". *PoS*, LATTICE2013:249, 2014. doi:10.22323/1.187.0249. arXiv:hep-lat/1311.5010. [Cited in §3.4, §3.6.1, and §E.2]

[141] V. G. Bornyakov et al. "Wilson flow and scale setting from lattice QCD". 2015. arXiv:hep-lat/1508.05916. [Cited in §3.4, §3.6.1, and §E.2]

[142] U. Aglietti et al. "Model independent determination of the shape function for inclusive B decays and of the structure functions in DIS". *Phys. Lett.*, B432:411–420, 1998. doi:10.1016/S0370-2693(98)00677-7. arXiv:hep-ph/hep-ph/9804416. [Cited in §3.5.2]

[143] K.-F. Liu. "Parton degrees of freedom from the path integral formalism". *Phys. Rev.*, D62:074501, 2000. doi:10.1103/PhysRevD.62.074501. arXiv:hep-ph/hep-ph/9910306. [Cited in §3.5.2]

[144] S. R. Beane et al. "High Statistics Analysis using Anisotropic Clover Lattices: (I) Single Hadron Correlation Functions". *Phys. Rev.*, D79:114502, 2009. doi:10.1103/PhysRevD.79.114502. arXiv:hep-lat/0903.2990. [Cited in §3.6]

[145] C. R. Allton et al. "Gauge invariant smearing and matrix correlators using Wilson fermions at Beta = 6.2". *Phys. Rev.*, D47:5128–5137, 1993. doi:10.1103/PhysRevD.47.5128. arXiv:hep-lat/hep-lat/9303009. [Cited in §3.6]

[146] B. J. Owen et al. "Variational Approach to the Calculation of gA". *Phys. Lett.*, B723:217–223, 2013. doi:10.1016/j.physletb.2013.04.063. arXiv:hep-lat/1212.4668. [Cited in §3.6 and §4.3.1]

[147] F. M. Stokes et al. "Parity-expanded variational analysis for nonzero momentum". *Phys. Rev.*, D92(11):114506, 2015. doi:10.1103/PhysRevD.92.114506. arXiv:hep-lat/1302.4152. [Cited in §3.6, §3.6.1, and §4.3.1]

[148] C. Alexandrou et al. "Novel analysis method for excited states in lattice QCD: The nucleon case". *Phys. Rev.*, D91(1):014506, 2015. doi:10.1103/PhysRevD.91.014506. arXiv:hep-lat/1411.6765. [Cited in §3.6 and §4.3.1]

[149] J. Dragos et al. "Nucleon matrix elements using the variational method in lattice QCD". *Phys. Rev.*, D94(7):074505, 2016. doi:10.1103/PhysRevD.94.074505. arXiv:hep-lat/1606.03195. [Cited in §3.6 and §4.3.1]

[150] F. M. Stokes et al. "Electromagnetic Form Factors of Excited Nucleons via Parity-Expanded Variational Analysis". *PoS*, LATTICE2016:161, 2016. doi:10.22323/1.256.0161. arXiv:hep-lat/1701.07177. [Cited in §3.6, §3.6.1, and §4.3.1]

[151] G. S. Bali et al. "Novel quark smearing for hadrons with high momenta in lattice QCD". *Phys. Rev.*, D93(9):094515, 2016. doi:10.1103/PhysRevD.93.094515. arXiv:hep-lat/1602.05525. [Cited in §3.6]

[152] W. Detmold et al. "phase unwrapping and one-dimensional sign problems". *Physical Review D*, 98(7), October 2018. doi:10.1103/physrevd.98.074511. [Cited in §3.6]

[153] P. Göttinger. "das verhalten von atomen im magnetischen drehfeld". *Zeitschrift für Physik*, 73(3-4):169–184, 1932. ISSN 1434-6001. doi:10.1007/BF01351211. [Cited in §4]

[154] W. Pauli. *Die allgemeinen Prinzipien der Wellenmechanik*. Springer Berlin Heidelberg, 1933. [Cited in §4]

[155] H. Hellmann. *Einführung in die Quantenchemie*. Leipzig und Wien, Franz Deuticke, 1937. [Cited in §4]

[156] R. P. Feynman. "forces in molecules". *Phys. Rev.*, 56(4):340–343, aug 1939. doi:10.1103/physrev.56.340. [Cited in §4 and §4.1]

[157] H. Ohki et al. "Nucleon sigma term and strange quark content from lattice QCD with exact chiral symmetry". *Phys. Rev.*, D78:054502, 2008. doi:10.1103/PhysRevD.78.054502. arXiv:hep-lat/0806.4744. [Cited in §4 and §5.2.1]

[158] K. I. Ishikawa et al. "SU(2) and SU(3) chiral perturbation theory analyses on baryon masses in 2+1 flavor lattice QCD". *Phys. Rev.*, D80:054502, 2009. doi:10.1103/PhysRevD.80.054502. arXiv:hep-lat/0905.0962. [Cited in §4 and §5.2.1]

[159] J. Martin Camalich et al. "The lowest-lying baryon masses in covariant SU(3)-flavor chiral perturbation theory". *Phys. Rev.*, D82:074504, 2010. doi:10.1103/PhysRevD.82.074504. arXiv:hep-lat/1003.1929. [Cited in §4 and §5.2.1]

[160] S. Durr et al. "Sigma term and strangeness content of octet baryons". *Phys. Rev.*, D85: 014509, 2012. doi:10.1103/PhysRevD.85.014509, 10.1103/PhysRevD.93.039905. arXiv:hep-lat/1109.4265. [Erratum: Phys. Rev.D93,no.3,039905(2016)]. [Cited in §4, §5.2.1, and §6]

[161] R. Horsley et al. "Hyperon sigma terms for 2+1 quark flavours". *Phys. Rev.*, D85:034506, 2012. doi:10.1103/PhysRevD.85.034506. arXiv:hep-lat/1110.4971. [Cited in §4, §5.2.1, and §6]

[162] S. Dinter et al. "Sigma terms and strangeness content of the nucleon with $N_f = 2 + 1 + 1$ twisted mass fermions". *JHEP*, 08:037, 2012. doi:10.1007/JHEP08(2012)037. arXiv:hep-lat/1202.1480. [Cited in §4, §5.2.1, and §6]

[163] G. S. Bali et al. "Nucleon mass and sigma term from lattice QCD with two light fermion flavors". *Nucl. Phys.*, B866:1–25, 2013. doi:10.1016/j.nuclphysb.2012.08.009. arXiv:hep-lat/1206.7034. [Cited in §4 and §5.2.1]

[164] H. Ohki et al. "Nucleon strange quark content from $N_f = 2+1$ lattice QCD with exact chiral symmetry". *Phys. Rev.*, D87:034509, 2013. doi:10.1103/PhysRevD.87.034509. arXiv:hep-lat/1208.4185. [Cited in §4 and §5.2.1]

[165] P. E. Shanahan et al. "Sigma terms from an SU(3) chiral extrapolation". *Phys. Rev.*, D87:074503, 2013. doi:10.1103/PhysRevD.87.074503. arXiv:nucl-th/1205.5365. [Cited in §4, §5.2.1, and §6]

[166] P. Junnarkar and A. Walker-Loud. "Scalar strange content of the nucleon from lattice QCD". *Phys. Rev.*, D87:114510, 2013. doi:10.1103/PhysRevD.87.114510. arXiv:hep-lat/1301.1114. [Cited in §4 and §5.2.1]

[167] C. Alexandrou et al. "Baryon spectrum with $N_f = 2 + 1 + 1$ twisted mass fermions". *Phys. Rev.*, D90(7):074501, 2014. doi:10.1103/PhysRevD.90.074501. arXiv:hep-lat/1406.4310. [Cited in §4 and §5.2.1]

[168] S. Durr et al. "Lattice computation of the nucleon scalar quark contents at the physical point". *Phys. Rev. Lett.*, 116(17):172001, 2016. doi:10.1103/PhysRevLett.116.172001. arXiv:hep-lat/1510.08013. [Cited in §4 and §5.2.1]

[169] C. Alexandrou and C. Kallidonis. "Low-lying baryon masses using $N_f = 2$ twisted mass clover-improved fermions directly at the physical pion mass". *Phys. Rev.*, D96 (3):034511, 2017. doi:10.1103/PhysRevD.96.034511. arXiv:hep-lat/1704.02647. [Cited in §4 and §5.2.1]

[170] C. Bernard et al. "lattice quantum-chromodynamics calculation of some baryon magnetic moments". *Physical Review Letters*, 49(15):1076–1079, October 1982. doi:10.1103/physrevlett.49.1076. [Cited in §4 and §6]

[171] G. Martinelli et al. "the proton and neutron magnetic moments in lattice QCD". *Physics Letters B*, 116(6):434–436, October 1982. doi:10.1016/0370-2693(82)90162-9. [Cited in §4 and §6]

[172] F. Fucito et al. "first evaluation of in lattice QCD in the quenched approximation". *Physics Letters B*, 115(2):148–150, August 1982. doi:10.1016/0370-2693(82)90816-4. [Cited in §4 and §6]

[173] M. Engelhardt. "Neutron electric polarizability from unquenched lattice QCD using the background field approach". *Phys. Rev.*, D76:114502, 2007. doi:10.1103/PhysRevD.76.114502. arXiv:hep-lat/0706.3919. [Cited in §4 and §6]

[174] W. Detmold et al. "Extracting Electric Polarizabilities from Lattice QCD". *Phys. Rev.*, D79:094505, 2009. doi:10.1103/PhysRevD.79.094505. arXiv:hep-lat/0904.1586. [Cited in §4 and §6]

[175] W. Detmold et al. "Extracting Nucleon Magnetic Moments and Electric Polarizabilities from Lattice QCD in Background Electric Fields". *Phys. Rev.*, D81:054502, 2010. doi:10.1103/PhysRevD.81.054502. arXiv:hep-lat/1001.1131. [Cited in §4 and §6]

[176] T. Primer et al. "Magnetic properties of the nucleon in a uniform background field". *Phys. Rev.*, D89(3):034508, 2014. doi:10.1103/PhysRevD.89.034508. arXiv:hep-lat/1307.1509. [Cited in §4 and §6]

[177] R. Bignell et al. "Neutron magnetic polarizability with Landau mode operators". *Phys. Rev.*, D98(3):034504, 2018. doi:10.1103/PhysRevD.98.034504. arXiv:hep-lat/1804.06574. [Cited in §4 and §6]

[178] Z. Davoudi and W. Detmold. "Implementation of general background electromagnetic fields on a periodic hypercubic lattice". *Phys. Rev.*, D92(7):074506, 2015. doi:10.1103/PhysRevD.92.074506. arXiv:hep-lat/1507.01908. [Cited in §4]

[179] A. Agadjanov et al. "Nucleon in a periodic magnetic field". *Phys. Rev.*, D95(3):031502, 2017. doi:10.1103/PhysRevD.95.031502. arXiv:hep-lat/1610.05545. [Cited in §4 and §8]

[180] G. S. Bali and G. Endrődi. "hadronic vacuum polarization and muong-2from magnetic susceptibilities on the lattice". *Physical Review D*, 92(5), September 2015. doi:10.1103/physrevd.92.054506. arXiv:arXiv:1506.08638. [Cited in §4 and §6]

[181] B. C. Tiburzi et al. "double- β decay matrix elements from lattice quantum chromodynamics". *Physical Review D*, 96(5), September 2017. doi:10.1103/physrevd.96.054505. arXiv:arXiv:1702.02929. [Cited in §4 and §6]

[182] P. E. Shanahan et al. "isotensor axial polarizability and lattice QCD input for nuclear double- β decay phenomenology". *Physical Review Letters*, 119(6), August 2017. doi:10.1103/physrevlett.119.062003. arXiv:arXiv:1701.03456. [Cited in §4 and §6]

[183] R. Horsley et al. "a lattice study of the glue in the nucleon". *Physics Letters B*, 714(2-5):312–316, August 2012. doi:10.1016/j.physletb.2012.07.004. [Cited in §4, §6, §9.2, §9.2.1, §9.3.2, §9.3.2, §9.3.2, §9.3.2, and §E.1]

[184] A. Chambers et al. "feynman-hellmann approach to the spin structure of hadrons". *Physical Review D*, 90(1), July 2014. doi:10.1103/physrevd.90.014510. [Cited in §4, §5.2.1, §5.4, §5.6, and §6]

[185] A. J. Chambers et al. "Disconnected contributions to the spin of the nucleon". *Phys. Rev.*, D92(11):114517, 2015. doi:10.1103/PhysRevD.92.114517. arXiv:hep-lat/1508.06856. [Cited in §4, §5.2.2, and §6]

[186] A. J. Chambers et al. "A novel approach to nonperturbative renormalization of singlet and nonsinglet lattice operators". *Phys. Lett.*, B740:30–35, 2015. doi:10.1016/j.physletb.2014.11.033. arXiv:hep-lat/1410.3078. [Cited in §4, §5.2.1, §6, and §7.1.2]

[187] J. Ruiz de Elvira et al. "Feynman–Hellmann theorem for resonances and the quest for QCD exotica". *Eur. Phys. J.*, C77(10):659, 2017. doi:10.1140/epjc/s10052-017-5237-3. arXiv:hep-lat/1706.09015. [Cited in §4 and §6]

[188] C. Bouchard et al. "On the Feynman-Hellmann Theorem in Quantum Field Theory and the Calculation of Matrix Elements". *Phys. Rev.*, D96(1):014504, 2017. doi:10.1103/PhysRevD.96.014504. arXiv:hep-lat/1612.06963. [Cited in §4 and §5.2.3]

[189] C. C. Chang et al. "Nucleon axial coupling from Lattice QCD". *EPJ Web Conf.*, 175:01008, 2018. doi:10.1051/epjconf/201817501008. arXiv:hep-lat/1710.06523. [Cited in §4]

[190] E. Berkowitz et al. "An accurate calculation of the nucleon axial charge with lattice QCD". 2017. arXiv:hep-lat/1704.01114. [Cited in §4]

[191] A. S. Gambhir et al. "The Stochastic Feynman-Hellmann Method". *PoS*, LATTICE2018:126, 2019. doi:10.22323/1.334.0126. arXiv:hep-lat/1905.03355. [Cited in §4]

[192] S. Singh and C. A. Singh. "extensions of the feynman-hellman theorem and applications". *American Journal of Physics*, 57(10):894–899, 1989. doi:10.1119/1.15842. [Cited in §4 and §4.1.2]

[193] A. J. Chambers. *Hadron structure and the Feynman-Hellmann theorem in lattice quantum chromodynamics*. PhD thesis, University of Adelaide, School of Physical Sciences, 2018. http://hdl.handle.net/2440/114262. [Cited in §4.2.1 and §5.2.2]

[194] L. H. Karsten and J. Smit. "Lattice Fermions: Species Doubling, Chiral Invariance, and the Triangle Anomaly". *Nucl. Phys.*, B183:103, 1981. doi:10.1016/0550-3213(81)90549-6. [,495(1980)]. [Cited in §5.2.2]

[195] M. Bochicchio et al. "Chiral Symmetry on the Lattice with Wilson Fermions". *Nucl. Phys.*, B262:331, 1985. doi:10.1016/0550-3213(85)90290-1. [Cited in §5.2.2]

[196] R. G. Edwards and B. Joo. "The Chroma software system for lattice QCD". *Nucl. Phys. Proc. Suppl.*, 140:832, 2005. doi:10.1016/j.nuclphysbps.2004.11.254. arXiv:hep-lat/hep-lat/0409003. [,832(2004)]. [Cited in §5.2.2, §5.2.3, and §E.1]

[197] R. Babich et al. "Exploring strange nucleon form factors on the lattice". *Phys. Rev.*, D85:054510, 2012. doi:10.1103/PhysRevD.85.054510. arXiv:hep-lat/1012.0562. [Cited in §5.2.2]

[198] G. S. Bali et al. "Strangeness Contribution to the Proton Spin from Lattice QCD". *Phys. Rev. Lett.*, 108:222001, 2012. doi:10.1103/PhysRevLett.108.222001. arXiv:hep-lat/1112.3354. [Cited in §5.2.2]

[199] M. Engelhardt. "Strange quark contributions to nucleon mass and spin from lattice QCD". *Phys. Rev.*, D86:114510, 2012. doi:10.1103/PhysRevD.86.114510. arXiv:hep-lat/1210.0025. [Cited in §5.2.2]

[200] A. Abdel-Rehim et al. "Disconnected quark loop contributions to nucleon observables in lattice QCD". *Phys. Rev.*, D89(3):034501, 2014. doi:10.1103/PhysRevD.89.034501. arXiv:hep-lat/1310.6339. [Cited in §5.2.2]

[201] M. Deka et al. "Lattice study of quark and glue momenta and angular momenta in the nucleon". *Phys. Rev.*, D91(1):014505, 2015. doi:10.1103/PhysRevD.91.014505. arXiv:hep-lat/1312.4816. [Cited in §5.2.2]

[202] S. Heybrock et al. "Lattice QCD with Domain Decomposition on Intel Xeon Phi Co-Processors". In *The International Conference for High Performance Computing, Networking, Storage, and Analysis: SC14: HPC matters (SC) New Orleans, LA, USA, November 16-21, 2014*, 2014. doi:10.1109/SC.2014.11. arXiv:hep-lat/1412.2629. [Cited in §5.2.3]

[203] C. Alexandrou et al. "Updated Lattice Results for Parton Distributions". *Phys. Rev.*, D96(1):014513, 2017. doi:10.1103/PhysRevD.96.014513. arXiv:hep-lat/1610.03689. [Cited in §5.2.3 and §7]

[204] B. Joó et al. "Parton Distribution Functions from Ioffe time pseudo-distributions". 2019. arXiv:hep-lat/1908.09771. [Cited in §5.2.3 and §7]

[205] S.-L. Zhu and M. J. Ramsey-Musolf. "The Off diagonal Goldberger-Treiman relation and its discrepancy". *Phys. Rev.*, D66:076008, 2002. doi:10.1103/PhysRevD.66.076008. arXiv:hep-ph/hep-ph/0207304. [Cited in §6, §6.2, §6.2, and §??]

[206] J. C. Alder et al. "Pi0 electroproduction at the first resonance at momentum transfers q-squared=0.6, 1.0 and 1.56 gev-squared". *Nucl. Phys.*, B46:573–592, 1972. doi:10.1016/0550-3213(72)90087-9. [Cited in §6.2]

[207] K. M. Graczyk et al. "Electroweak form factors of the Delta(1232) resonance". *Phys. Rev.*, D90(9):093001, 2014. doi:10.1103/PhysRevD.90.093001. arXiv:hep-ph/1407.5445. [Cited in §6.2]

[208] C. Alexandrou et al. "The Axial N to Delta transition form factors from Lattice QCD". *Phys. Rev. Lett.*, 98:052003, 2007. doi:10.1103/PhysRevLett.98.052003. arXiv:hep-lat/hep-lat/0607030. [Cited in §6.2 and §6.3]

[209] H. F. Jones and M. D. Scadron. "Multipole gamma N Delta form-factors and resonant photoproduction and electroproduction". *Annals Phys.*, 81:1–14, 1973. doi:10.1016/0003-4916(73)90476-4. [Cited in §6.2]

[210] D. B. Leinweber et al. "Baryon octet to decuplet electromagnetic transitions". *Phys. Rev.*, D48:2230–2249, 1993. doi:10.1103/PhysRevD.48.2230. arXiv:hep-lat/hep-lat/9212016. [Cited in §6.2]

[211] C. Alexandrou et al. "Nucleon to delta electromagnetic transition form factors in lattice QCD". *Phys. Rev.*, D77:085012, 2008. doi:10.1103/PhysRevD.77.085012. arXiv:hep-lat/0710.4621. [Cited in §6.2]

[212] M. L. Goldberger and S. B. Treiman. "Decay of the pi meson". *Phys. Rev.*, 110:1178–1184, 1958. doi:10.1103/PhysRev.110.1178. [Cited in §6.2]

[213] C. Alexandrou et al. "Nucleon to Delta transition form factors with $N_F = 2+1$ domain wall fermions". *Phys. Rev.*, D83:014501, 2011. doi:10.1103/PhysRevD.83.014501. arXiv:hep-lat/1011.3233. [Cited in §6.3 and §??]

[214] T. R. Hemmert et al. "NN, nδ couplings and the quark model". *Physical Review D*, 51(1): 158–167, January 1995. doi:10.1103/physrevd.51.158. [Cited in §6.3 and §??]

[215] S. J. Barish et al. "Study of Neutrino Interactions in Hydrogen and Deuterium: Inelastic Charged Current Reactions". *Phys. Rev.*, D19:2521, 1979. doi:10.1103/PhysRevD.19.2521. [Cited in §6.3, §6.3, and §??]

[216] M. Rafi Alam et al. "Weak charged and neutral current induced one pion production off the nucleon". *Int. J. Mod. Phys.*, E25(02):1650010, 2016. doi:10.1142/S0218301316500105. arXiv:hep-ph/1509.08622. [Cited in §6.3 and §??]

[217] V. Braun et al. "Ioffe - time distributions instead of parton momentum distributions in description of deep inelastic scattering". *Phys. Rev.*, D51:6036–6051, 1995. doi:10.1103/PhysRevD.51.6036. arXiv:hep-ph/hep-ph/9410318. [Cited in §7]

[218] X. Ji. "Parton Physics on a Euclidean Lattice". *Phys. Rev. Lett.*, 110:262002, 2013. doi:10.1103/PhysRevLett.110.262002. arXiv:hep-ph/1305.1539. [Cited in §7]

[219] A. V. Radyushkin. "Quasi-parton distribution functions, momentum distributions, and pseudo-parton distribution functions". *Phys. Rev.*, D96(3):034025, 2017. doi:10.1103/PhysRevD.96.034025. arXiv:hep-ph/1705.01488. [Cited in §7]

[220] H.-W. Lin et al. "Flavor Structure of the Nucleon Sea from Lattice QCD". *Phys. Rev.*, D91:054510, 2015. doi:10.1103/PhysRevD.91.054510. arXiv:hep-ph/1402.1462. [Cited in §7]

[221] J.-W. Chen et al. "Nucleon Helicity and Transversity Parton Distributions from Lattice QCD". *Nucl. Phys.*, B911:246–273, 2016. doi:10.1016/j.nuclphysb.2016.07.033. arXiv:hep-ph/1603.06664. [Cited in §7]

[222] C. Alexandrou et al. "Light-Cone Parton Distribution Functions from Lattice QCD". *Phys. Rev. Lett.*, 121(11):112001, 2018. doi:10.1103/PhysRevLett.121.112001. arXiv:hep-lat/1803.02685. [Cited in §7]

[223] J.-W. Chen et al. "Lattice Calculation of Parton Distribution Function from LaMET at Physical Pion Mass with Large Nucleon Momentum". 2018. arXiv:hep-lat/1803.04393. [Cited in §7]

[224] J. Green et al. "Nonperturbative Renormalization of Nonlocal Quark Bilinears for Parton Quasidistribution Functions on the Lattice Using an Auxiliary Field". *Phys. Rev. Lett.*, 121(2):022004, 2018. doi:10.1103/PhysRevLett.121.022004. arXiv:hep-lat/1707.07152. [Cited in §7]

[225] C. Alexandrou et al. "A complete non-perturbative renormalization prescription for quasi-PDFs". *Nucl. Phys.*, B923:394–415, 2017. doi:10.1016/j.nuclphysb.2017.08.012. arXiv:hep-lat/1706.00265. [Cited in §7]

[226] J.-W. Chen et al. "Parton distribution function with nonperturbative renormalization from lattice QCD". *Phys. Rev.*, D97(1):014505, 2018. doi:10.1103/PhysRevD.97.014505. arXiv:hep-lat/1706.01295. [Cited in §7]

[227] K. Orginos et al. "Lattice QCD exploration of parton pseudo-distribution functions". *Phys. Rev.*, D96(9):094503, 2017. doi:10.1103/PhysRevD.96.094503. arXiv:hep-ph/1706.05373. [Cited in §7]

[228] B. Joó et al. "Pion Valence Structure from Ioffe Time Pseudo-Distributions". 2019. arXiv:hep-lat/1909.08517. [Cited in §7]

[229] T. Liu et al. "Will the up and down quarks always spin opposite in the proton?". 2019. arXiv:hep-ph/1909.13818. [Cited in §7]

[230] I. Balitsky et al. "Gluon Pseudo-Distributions at Short Distances: Forward Case". 2019. arXiv:hep-ph/1910.13963. [Cited in §7]

[231] Y.-Q. Ma and J.-W. Qiu. "Exploring Partonic Structure of Hadrons Using ab initio Lattice QCD Calculations". *Phys. Rev. Lett.*, 120(2):022003, 2018. doi:10.1103/PhysRevLett.120.022003. arXiv:hep-ph/1709.03018. [Cited in §7]

[232] C. Monahan. "Recent Developments in x-dependent Structure Calculations". *PoS*, LATTICE2018:018, 2018. doi:10.22323/1.334.0018. arXiv:hep-lat/1811.00678. [Cited in §7]

[233] G. S. Bali et al. "Pion distribution amplitude from Euclidean correlation functions". *Eur. Phys. J.*, C78(3):217, 2018. doi:10.1140/epjc/s10052-018-5700-9. arXiv:hep-lat/1709.04325. [Cited in §7]

[234] G. S. Bali et al. "Pion distribution amplitude from Euclidean correlation functions: Exploring universality and higher-twist effects". *Phys. Rev.*, D98(9):094507, 2018. doi:10.1103/PhysRevD.98.094507. arXiv:hep-lat/1807.06671. [Cited in §7 and §7.4]

[235] W. Detmold and C. J. D. Lin. "Deep-inelastic scattering and the operator product expansion in lattice QCD". *Phys. Rev.*, D73:014501, 2006. doi:10.1103/PhysRevD.73.014501. arXiv:hep-lat/hep-lat/0507007. [Cited in §7]

[236] W. Detmold et al. "Moments of pion distribution amplitude using operator product expansion on the lattice". *PoS*, LATTICE2018:106, 2018. doi:10.22323/1.334.0106. arXiv:hep-lat/1810.12194. [Cited in §7]

[237] K.-F. Liu and S.-J. Dong. "Origin of difference between anti-d and anti-u partons in the nucleon". *Phys. Rev. Lett.*, 72:1790–1793, 1994. doi:10.1103/PhysRevLett.72.1790. arXiv:hep-ph/hep-ph/9306299. [Cited in §7]

[238] M. Gockeler et al. "Polarized and unpolarized nucleon structure functions from lattice QCD". *Phys. Rev.*, D53:2317–2325, 1996. doi:10.1103/PhysRevD.53.2317. arXiv:hep-lat/hep-lat/9508004. [Cited in §7 and §9.2]

[239] M. Gockeler et al. "Lattice operators for moments of the structure functions and their transformation under the hypercubic group". *Phys. Rev.*, D54:5705–5714, 1996. doi:10.1103/PhysRevD.54.5705. arXiv:hep-lat/hep-lat/9602029. [Cited in §7 and §9.2]

[240] S. Capitani et al. "Towards a nonperturbative calculation of DIS Wilson coefficients". *Nucl. Phys. Proc. Suppl.*, 73:288–290, 1999. doi:10.1016/S0920-5632(99)85050-6. arXiv:hep-lat/hep-lat/9809171. [,288(1998)]. [Cited in §7]

[241] Z. Davoudi and M. J. Savage. "Restoration of Rotational Symmetry in the Continuum Limit of Lattice Field Theories". *Phys. Rev.*, D86:054505, 2012. doi:10.1103/PhysRevD.86.054505. arXiv:hep-lat/1204.4146. [Cited in §7]

[242] X.-d. Ji and C.-w. Jung. "Studying hadronic structure of the photon in lattice QCD". *Phys. Rev. Lett.*, 86:208, 2001. doi:10.1103/PhysRevLett.86.208. arXiv:hep-lat/hep-lat/0101014. [Cited in §7]

[243] V. Braun and D. Müller. "Exclusive processes in position space and the pion distribution amplitude". *Eur. Phys. J. C*, 55:349–361, 2008. doi:10.1140/epjc/s10052-008-0608-4. arXiv:hep-ph/0709.1348. [Cited in §7]

[244] A. J. Chambers et al. "Nucleon Structure Functions from Operator Product Expansion on the Lattice". *Phys. Rev. Lett.*, 118(24):242001, 2017. doi:10.1103/PhysRevLett.118.242001. arXiv:hep-lat/1703.01153. [Cited in §7 and §7.2]

[245] M. Gockeler et al. "A Lattice determination of moments of unpolarised nucleon structure functions using improved Wilson fermions". *Phys. Rev.*, D71: 114511, 2005. doi:10.1103/PhysRevD.71.114511. arXiv:hep-ph/hep-ph/0410187. [Cited in §7.2, §9.3.2, and §9.3.2]

[246] V. M. Braun et al. "Moments of pseudoscalar meson distribution amplitudes from the lattice". *Phys. Rev.*, D74:074501, 2006. doi:10.1103/PhysRevD.74.074501. arXiv:hep-lat/hep-lat/0606012. [Cited in §7.2]

[247] R. Arthur et al. "Lattice Results for Low Moments of Light Meson Distribution Amplitudes". *Phys. Rev.*, D83:074505, 2011. doi:10.1103/PhysRevD.83.074505. arXiv:hep-lat/1011.5906. [Cited in §7.2]

[248] V. M. Braun et al. "Second Moment of the Pion Light-cone Distribution Amplitude from Lattice QCD". *Phys. Rev.*, D92(1):014504, 2015. doi:10.1103/PhysRevD.92.014504. arXiv:hep-lat/1503.03656. [Cited in §7.2]

[249] G. S. Bali et al. "Second moment of the pion distribution amplitude with the momentum smearing technique". *Phys. Lett.*, B774:91–97, 2017. doi:10.1016/j.physletb.2017.08.077. arXiv:hep-lat/1705.10236. [Cited in §7.2]

[250] M. E. Peskin and D. V. Schroeder. *An Introduction to quantum field theory*. Addison-Wesley, Reading, USA, 1995. ISBN 9780201503975, 0201503972. `http://www.slac.stanford.edu/~mpeskin/QFT.html`. [Cited in §7.2]

[251] A. Hannaford-Gunn et al. "Scaling and higher twist in the nucleon Compton amplitude". 2020. arXiv:hep-lat/2001.05090. [Cited in §7.2.1 and §7.5]

[252] S. Alekhin et al. "Parton distribution functions, α_s, and heavy-quark masses for LHC Run II". *Phys. Rev.*, D96(1):014011, 2017. doi:10.1103/PhysRevD.96.014011. arXiv:hep-ph/1701.05838. [Cited in §7.10]

[253] C. Alexandrou et al. "Nucleon form factors and moments of generalized parton distributions using $N_f = 2 + 1 + 1$ twisted mass fermions". *Phys. Rev.*, D88(1):014509, 2013. doi:10.1103/PhysRevD.88.014509. arXiv:hep-lat/1303.5979. [Cited in §7.10]

[254] A. Abdel-Rehim et al. "Nucleon and pion structure with lattice QCD simulations at physical value of the pion mass". *Phys. Rev.*, D92(11):114513, 2015. doi:10.1103/PhysRevD.92.114513, 10.1103/PhysRevD.93.039904. arXiv:hep-lat/1507.04936. [Erratum: Phys. Rev.D93,no.3,039904(2016)]. [Cited in §7.10]

[255] Y. Aoki et al. "Nucleon isovector structure functions in (2+1)-flavor QCD with domain wall fermions". *Phys. Rev.*, D82:014501, 2010. doi:10.1103/PhysRevD.82.014501. arXiv:hep-lat/1003.3387. [Cited in §7.10]

[256] G. S. Bali et al. "The moment $\langle x \rangle_{u-d}$ of the nucleon from $N_f = 2$ lattice QCD down to nearly physical quark masses". *Phys. Rev.*, D90(7):074510, 2014. doi:10.1103/PhysRevD.90.074510. arXiv:hep-lat/1408.6850. [Cited in §7.10]

[257] J. D. Bratt et al. "Nucleon structure from mixed action calculations using 2+1 flavors of asqtad sea and domain wall valence fermions". *Phys. Rev.*, D82: 094502, 2010. doi:10.1103/PhysRevD.82.094502. arXiv:hep-lat/1001.3620. [Cited in §7.10, §9, and §9.1]

[258] J. R. Green et al. "Nucleon Structure from Lattice QCD Using a Nearly Physical Pion Mass". *Phys. Lett.*, B734:290–295, 2014. doi:10.1016/j.physletb.2014.05.075. arXiv:hep-lat/1209.1687. [Cited in §7.10]

[259] E. Moffat et al. "What are the low-Q and large-x boundaries of collinear QCD factorization theorems?". *Phys. Rev.*, D95(9):096008, 2017. doi:10.1103/PhysRevD.95.096008. arXiv:hep-ph/1702.03955. [Cited in §7.4]

[260] V. M. Braun et al. "Power corrections and renormalons in parton quasidistributions". *Phys. Rev.*, D99(1):014013, 2019. doi:10.1103/PhysRevD.99.014013. arXiv:hep-ph/1810.00048. [Cited in §7.4]

[261] R. Horsley et al. "Structure functions from the Compton amplitude". 2020. arXiv:hep-lat/2001.05366. [Cited in §7.5]

[262] R. L. Heimann. "Spin dependent high frequency inelastic electron scattering and helicity flip couplings". *Nucl. Phys.*, B64:429–463, 1973. doi:10.1016/0550-3213(73)90635-4. [Cited in §7.5 and §8]

[263] X.-D. Ji. "Deeply virtual Compton scattering". *Phys. Rev.*, D55:7114–7125, 1997. doi:10.1103/PhysRevD.55.7114. arXiv:hep-ph/hep-ph/9609381. [Cited in §7.5]

[264] A. H. Gunn. "generalised parton distributions from lattice feynman-hellmann techniques". Master's thesis, University of Adelaide, School of Physical Sciences, In Preparation. [Cited in §7.5]

[265] F. E. Low. "Scattering of light of very low frequency by systems of spin 1/2". *Phys. Rev.*, 96: 1428–1432, 1954. doi:10.1103/PhysRev.96.1428. [Cited in §8]

[266] M. Gell-Mann and M. L. Goldberger. "Scattering of low-energy photons by particles of spin 1/2". *Phys. Rev.*, 96:1433–1438, 1954. doi:10.1103/PhysRev.96.1433. [Cited in §8]

[267] J. C. Collins. "Renormalization of the Cottingham Formula". *Nucl. Phys.*, B149:90–100, 1979. doi:10.1016/j.nuclphysb.2016.12.017, 10.1016/0550-3213(79)90158-5. [Erratum: Nucl. Phys.B915,392(2017)]. [Cited in §8 and §8.2]

[268] R. J. Hill and G. Paz. "Model independent analysis of proton structure for hydrogenic bound states". *Phys. Rev. Lett.*, 107:160402, 2011. doi:10.1103/PhysRevLett.107.160402. arXiv:hep-ph/1103.4617. [Cited in §8]

[269] R. J. Hill and G. Paz. "Nucleon spin-averaged forward virtual Compton tensor at large Q^2". *Phys. Rev.*, D95(9):094017, 2017. doi:10.1103/PhysRevD.95.094017. arXiv:hep-ph/1611.09917. [Cited in §8 and §8.3]

[270] H. Harari. "SUPERCONVERGENT DISPERSION RELATIONS AND ELECTROMAGNETIC MASS DIFFERENCES". *Phys. Rev. Lett.*, 17:1303–1306, 1966. doi:10.1103/PhysRevLett.17.1303. [Cited in §8 and §8.1]

[271] H. D. I. Abarbanel and S. Nussinov. "Implications of Regge Behavior for Processes Involving Photons". *Phys. Rev.*, 158:1462–1466, 1967. doi:10.1103/PhysRev.158.1462. [Cited in §8]

[272] A. I. L'vov. "Electric polarizability of nuclei and a longitudinal sum rule". *Nucl. Phys.*, A638: 756–764, 1998. doi:10.1016/S0375-9474(98)00434-5. arXiv:nucl-th/nucl-th/9804033. [Cited in §8]

[273] J. Sucher. "Sign of the Static Electric Polarizability in Relativistic Quantum Theory". *Phys. Rev.*, D6:1798–1800, 1972. doi:10.1103/PhysRevD.6.1798. [Cited in §8]

[274] J. Bernabeu and R. Tarrach. "Unsubtracted Dispersion Relation for the Longitudinal Compton Amplitude?". *Phys. Lett.*, 55B:183–186, 1975. doi:10.1016/0370-2693(75)90438-4. [Cited in §8]

[275] G. N. Watson and J. W. Nicholson. "the diffraction of electric waves by the earth". *Proceedings of the Royal Society of London. Series A, Containing Papers of a Mathematical and Physical Character*, 95(666):83–99, 1918. doi:10.1098/rspa.1918.0050. arXiv:https://royalsocietypublishing.org/doi/pdf/10.1098/rspa.1918.0050. [Cited in §8.1]

[276] A. Sommerfeld. *Vorlesungen ueber theoretische Physik*. 10 1942. ISBN 9783871443749. [Cited in §8.1]

[277] T. Regge. "Introduction to complex orbital momenta". *Nuovo Cim.*, 14:951, 1959. doi:10.1007/BF02728177. [Cited in §8.1]

[278] T. Regge. "Bound states, shadow states and Mandelstam representation". *Nuovo Cim.*, 18: 947–956, 1960. doi:10.1007/BF02733035. [Cited in §8.1]

[279] A. Aktas et al. "Measurement and QCD analysis of the diffractive deep-inelastic scattering cross-section at HERA". *Eur. Phys. J.*, C48:715–748, 2006. doi:10.1140/epjc/s10052-006-0035-3. arXiv:hep-ex/hep-ex/0606004. [Cited in §8.1]

[280] M. Trzebinski. "Diffractive Physics at the LHC". *Ukr. J. Phys.*, 64(8):772, 2019. doi:10.15407/ujpe64.8.772. arXiv:hep-ph/1909.10830. [Cited in §8.1]

[281] V. N. Gribov and I. Ya. Pomeranchuk. "Restriction on the amplitudes of various processes". *Phys. Lett.*, 2:239, 1962. doi:10.1016/0031-9163(62)90244-5. [Cited in §8.1]

[282] J. Gasser and H. Leutwyler. "Implications of Scaling for the Proton - Neutron Mass - Difference". *Nucl. Phys.*, B94:269–310, 1975. doi:10.1016/0550-3213(75)90493-9. [Cited in §8.1]

[283] I. Caprini et al. "Regge analysis of the pi pi scattering amplitude". *Eur. Phys. J.*, C72:1860, 2012. doi:10.1140/epjc/s10052-012-1860-1. arXiv:hep-ph/1111.7160. [Cited in §8.1]

[284] J. Gasser et al. "Cottingham formula and nucleon polarisabilities". *Eur. Phys. J.*, C75(8):375, 2015. doi:10.1140/epjc/s10052-015-3580-9. arXiv:hep-ph/1506.06747. [Cited in §8.1]

[285] S. J. Brodsky et al. "Local Two-Photon Couplings and the J=0 Fixed Pole in Real and Virtual Compton Scattering". *Phys. Rev.*, D79:033012, 2009. doi:10.1103/PhysRevD.79.033012. arXiv:hep-ph/0812.0395. [Cited in §8.1]

[286] D. Müller and K. M. Semenov-Tian-Shansky. "$J = 0$ fixed pole and D-term form factor in deeply virtual Compton scattering". *Phys. Rev.*, D92(7):074025, 2015. doi:10.1103/PhysRevD.92.074025. arXiv:hep-ph/1507.02164. [Cited in §8.1]

[287] A. Walker-Loud et al. "The Electromagnetic Self-Energy Contribution to $M_p - M_n$ and the Isovector Nucleon Magnetic Polarizability". *Phys. Rev. Lett.*, 108: 232301, 2012. doi:10.1103/PhysRevLett.108.232301. arXiv:nucl-th/1203.0254. [Cited in §8.2, §??, and §8.1]

[288] W. N. Cottingham. "The neutron proton mass difference and electron scattering experiments". *Annals Phys.*, 25:424–432, 1963. doi:10.1016/0003-4916(63)90023-X. [Cited in §8.2]

[289] J. Gasser and H. Leutwyler. "Quark Masses". *Phys. Rept.*, 87:77–169, 1982. doi:10.1016/0370-1573(82)90035-7. [Cited in §?? and §8.1]

[290] F. B. Erben et al. "Dispersive estimate of the electromagnetic charge symmetry violation in the octet baryon masses". *Phys. Rev.*, C90(6):065205, 2014. doi:10.1103/PhysRevC.90.065205. arXiv:nucl-th/1408.6628. [Cited in §?? and §8.1]

[291] W. E. Lamb and R. C. Retherford. "Fine Structure of the Hydrogen Atom by a Microwave Method". *Phys. Rev.*, 72:241–243, 1947. doi:10.1103/PhysRev.72.241. [Cited in §8.3]

[292] P. J. Mohr et al. "CODATA Recommended Values of the Fundamental Physical Constants: 2006". *Rev. Mod. Phys.*, 80:633–730, 2008. doi:10.1103/RevModPhys.80.633. arXiv:physics.atom-ph/0801.0028. [Cited in §8.3]

[293] R. Pohl et al. "The size of the proton". *Nature*, 466:213–216, 2010. doi:10.1038/nature09250. [Cited in §8.3]

[294] C. E. Carlson and M. Vanderhaeghen. "Higher order proton structure corrections to the Lamb shift in muonic hydrogen". *Phys. Rev.*, A84:020102, 2011. doi:10.1103/PhysRevA.84.020102. arXiv:hep-ph/1101.5965. [Cited in §8.3]

[295] S. Capitani et al. "Renormalization and off-shell improvement in lattice perturbation theory". *Nucl. Phys.*, B593:183–228, 2001. doi:10.1016/S0550-3213(00)00590-3. arXiv:hep-lat/hep-lat/0007004. [Cited in §8.4]

[296] C. Aubin et al. "Finite-volume effects in the muon anomalous magnetic moment on the lattice". *Phys. Rev.*, D93(5):054508, 2016. doi:10.1103/PhysRevD.93.054508. arXiv:hep-lat/1512.07555. [Cited in §8.4]

[297] M. V. Polyakov and P. Schweitzer. "Forces inside hadrons: pressure, surface tension, mechanical radius, and all that". *Int. J. Mod. Phys.*, A33(26): 1830025, 2018. doi:10.1142/S0217751X18300259. arXiv:hep-ph/1805.06596. [Cited in §9, §9.1, and §9.1]

[298] P. Hagler et al. "Nucleon Generalized Parton Distributions from Full Lattice QCD". *Phys. Rev.*, D77:094502, 2008. doi:10.1103/PhysRevD.77.094502. arXiv:hep-lat/0705.4295. [Cited in §9]

[299] W. Detmold et al. "off-forward gluonic structure of vector mesons". *Physical Review D*, 95 (11), June 2017. doi:10.1103/physrevd.95.114515. arXiv:arXiv:1703.08220. [Cited in §9]

[300] W. Detmold and P. Shanahan. "erratum: Gluonic transversity from lattice QCD [phys. rev. d 94 , 014507 (2016)]". *Physical Review D*, 95(7), April 2017. doi:10.1103/physrevd.95.079902. arXiv:arXiv:1606.04505. [Cited in §9]

[301] C. Alexandrou et al. "Nucleon Spin and Momentum Decomposition Using Lattice QCD Simulations". *Phys. Rev. Lett.*, 119(14):142002, 2017. doi:10.1103/PhysRevLett.119.142002. arXiv:hep-lat/1706.02973. [Cited in §9]

[302] P. E. Shanahan and W. Detmold. "Gluon gravitational form factors of the nucleon and the pion from lattice QCD". *Phys. Rev.*, D99(1):014511, 2019. doi:10.1103/PhysRevD.99.014511. arXiv:hep-lat/1810.04626. [Cited in §9]

[303] P. E. Shanahan and W. Detmold. "Pressure Distribution and Shear Forces inside the Proton". *Phys. Rev. Lett.*, 122(7):072003, 2019. doi:10.1103/PhysRevLett.122.072003. arXiv:nucl-th/1810.07589. [Cited in §9]

[304] A. Accardi et al. "Electron Ion Collider: The Next QCD Frontier". *Eur. Phys. J.*, A52(9):268, 2016. doi:10.1140/epja/i2016-16268-9. arXiv:nucl-ex/1212.1701. [Cited in §9.1 and §9.1.1]

[305] M. V. Polyakov. "Generalized parton distributions and strong forces inside nucleons and nuclei". *Phys. Lett.*, B555:57–62, 2003. doi:10.1016/S0370-2693(03)00036-4. arXiv:hep-ph/hep-ph/0210165. [Cited in §9.1]

[306] X.-D. Ji. "Gauge-Invariant Decomposition of Nucleon Spin". *Phys. Rev. Lett.*, 78: 610–613, 1997. doi:10.1103/PhysRevLett.78.610. arXiv:hep-ph/hep-ph/9603249. [Cited in §9.1.1]

[307] X. Ji. "gauge-invariant decomposition of nucleon spin". *Physical Review Letters*, 78(4):610–613, jan 1997. doi:10.1103/physrevlett.78.610. [Cited in §9.1.1]

[308] R. L. Jaffe and A. Manohar. "The G(1) Problem: Fact and Fantasy on the Spin of the Proton". *Nucl. Phys.*, B337:509–546, 1990. doi:10.1016/0550-3213(90)90506-9. [Cited in §9.1.1]

[309] X.-S. Chen et al. "Do gluons carry half of the nucleon momentum?". *Phys. Rev. Lett.*, 103:062001, 2009. doi:10.1103/PhysRevLett.103.062001. arXiv:hep-ph/0904.0321. [Cited in §9.1.1]

[310] C. Lorce. "Geometrical approach to the proton spin decomposition". *Phys. Rev.*, D87(3):034031, 2013. doi:10.1103/PhysRevD.87.034031. arXiv:hep-ph/1205.6483. [Cited in §9.1.1]

[311] M. Engelhardt. "Quark orbital dynamics in the nucleon - from Ji to Jaffe-Manohar orbital angular momentum". *PoS*, LATTICE2016:138, 2016. doi:10.22323/1.256.0138. [Cited in §9.1.1]

[312] X. Ji et al. "Physics of the Gluon-Helicity Contribution to Proton Spin". *Phys. Rev. Lett.*, 111:112002, 2013. doi:10.1103/PhysRevLett.111.112002. arXiv:hep-ph/1304.6708. [Cited in §9.1.1]

[313] Y.-B. Yang et al. "Glue Spin of the Proton". *PoS*, LATTICE2015:129, 2016. doi:10.22323/1.251.0129. arXiv:hep-ph/1603.05256. [Cited in §9.1.1]

[314] J. Ashman et al. "An Investigation of the Spin Structure of the Proton in Deep Inelastic Scattering of Polarized Muons on Polarized Protons". *Nucl. Phys.*, B328:1, 1989. doi:10.1016/0550-3213(89)90089-8. [,351(1989)]. [Cited in §9.1.1]

[315] V. Yu. Alexakhin et al. "The Deuteron Spin-dependent Structure Function g1(d) and its First Moment". *Phys. Lett.*, B647:8–17, 2007. doi:10.1016/j.physletb.2006.12.076. arXiv:hep-ex/hep-ex/0609038. [Cited in §9.1.1]

[316] E. Leader and M. Anselmino. "A crisis in the parton model: Where, oh where is the proton's spin?". *Z. Phys.*, C41:239, 1988. doi:10.1063/1.38312, 10.1007/BF01566922. [AIP Conf. Proc.187,764(2008)]. [Cited in §9.1.1]

[317] A. Deur et al. "The Spin Structure of the Nucleon". *Rept. Prog. Phys.*, 82(076201), 2019. doi:10.1088/1361-6633/ab0b8f. arXiv:hep-ph/1807.05250. [Cited in §9.1.1]

[318] M. Baake et al. "Structure and Representations of the Symmetry Group of the Four-dimensional Cube". *J. Math. Phys.*, 23:944, 1982. doi:10.1063/1.525461. [Erratum: J. Math. Phys.23,2595(1982)]. [Cited in §9.2]

[319] M. Lüscher. "Properties and uses of the Wilson flow in lattice QCD". *JHEP*, 08:071, 2010. doi:10.1007/JHEP08(2010)071, 10.1007/JHEP03(2014)092. arXiv:hep-lat/1006.4518. [Erratum: JHEP03,092(2014)]. [Cited in §9.2]

[320] A. M. Ferrenberg and R. H. Swendsen. "New Monte Carlo Technique for Studying Phase Transitions". *Phys. Rev. Lett.*, 61:2635–2638, 1988. doi:10.1103/PhysRevLett.61.2635. [Cited in §9.2.1]

[321] A. M. Ferrenberg and R. H. Swendsen. "Optimized Monte Carlo analysis". *Phys. Rev. Lett.*, 63:1195–1198, 1989. doi:10.1103/PhysRevLett.63.1195. [Cited in §9.2.1]

[322] A. Li et al. "Reweighting method in finite density lattice QCD". *PoS*, LAT2006:030, 2006. doi:10.22323/1.032.0030. arXiv:hep-lat/hep-lat/0612011. [Cited in §9.2.1]

[323] J. M. Bickerton. *Transverse Properties of Hadron Structure Using Lattice QCD*. PhD thesis, University of Adelaide, School of Physical Sciences, In Preparation. [Cited in §9.3.1]

[324] S. Alekhin et al. "The ABM parton distributions tuned to LHC data". *Phys. Rev.*, D89(5):054028, 2014. doi:10.1103/PhysRevD.89.054028. arXiv:hep-ph/1310.3059. [Cited in §9.3.2]

[325] T. R. Haar et al. "An update on the BQCD Hybrid Monte Carlo program". *EPJ Web Conf.*, 175:14011, 2018. doi:10.1051/epjconf/201817514011. arXiv:hep-lat/1711.03836. [Cited in §E.2]